PHOTOPHYSICAL, NONLINEAR OPTICAL AND PHOTODYNAMIC THERAPY ACTIVITY OF PHTHALOCYANINE–NANOPARTICLES CONJUGATES

A thesis submitted in fulfillment of the requirements for the degree of

DOCTOR OF PHILOSOPHY

Of

RHODES UNIVERSITY

By

OLUYINKA DAVID OLUWOLE

OCTOBER 2016

To God Almighty, my strength in ages–past, present and the future, for always coming through for me when I least expected: "For You formed my inward parts; You wove me in my mother's womb.....How precious also are Your thoughts to me, O God! How vast is the sum of them!" (Psalm 139:13,17),

Ndiyabulela KuThixo;

To my Mom, Princess Caroline O. Oluwole, and to my Folks – Mobolaji, Fola, Bolarinwa, Adeola, Foluso and my late Dad (Prince Timothy O. Oluwole – May his memory be blessed).

ACKNOWLEDGEMENTS

My sincere appreciation goes to Distinguished Professor Tebello Nyokong for her unrelenting guidance, support, tutelage, and encouragement throughout the programme and for many opportunities she afforded me–***Kealeboha***.

To my Russian hosts; Prof. Yulia and Dr. Alexander, I'm grateful for the special treats whilst I was with you and the research done under your supervision–***Spasiba***. Dr. Earl and Shane, thank you for the cancer cells culture training.

To my parents, I am indeed short of words to express my immeasurable gratitude to you. You've been an ever–present source of joy and support. Your patience and understanding will forever be treasured and venerated–***Mo'dupe***.

To my senior colleagues, Drs: Rachael, Kay, Dayo, Phindi, Sarah, Ola, Edward, Audacity and Stephen–Thank you for all the assistance. To my S22 colleagues present and past, thank you for all the fascinating and joyous time that we shared. To Ps.: Tends, Emmanuel, Awotunde, Agbale, Bryan and David; and mentors: Profs: Ololade and Akinleye–thank you for all the encouragements.

To the BSG@RU (Lesedi, Madam Odun, Madam Bola, Mr. Christtestimony, Nnamdi, Refiloe, Maureen, Sixolile, Siwa, Nwaji, Anneline, Clement, Mhlangulele, and others), thank you for being true friends and for your steadfastness of faith in God. Rudo, Banky, Munya, Clinton, Kingsley, Kunle, Ayodele, and Adeyemi: thank you for the awesome friendship and kindness.

Special thanks to the amazing members of staff in the Chemistry Department (support and academic) and the E.M.U. (Shirley and Marvin).

Financial support from the Department of Science and Technology (DST)/MINTEK, South Africa is gratefully acknowledged.

Finally, if my hair could turn to many tongues in professing the greatness and splendor of my Creator, it can't quantify the work of my *Abba Father* in whose Will I was made and have my existence. Thank You God for everything You've been and will be to me. "Those who go out weeping, carrying seed to sow, will return with songs of joy, carrying sheaves with them. Weeping may last through the night, but joy comes with the morning (Psalm 126:6, 30:5b)".

Keep living in the atmosphere of God's greatness.....**David O. Oluwole@2016**

This thesis reports on the syntheses and characterization of symmetrical and asymmetrical mononuclear and multinuclear phthalocyanines (Pcs) with different ring substituents (carboxylic acid, phenoxy acetic acid, diol, di–thiol, *tert*–butyl and butoxy). The syntheses of different nanoparticles (NPs) were also undertaken in this research work. The Pcs were covalently linked or mixed with NPs, human serum albumin (HSA) and chitosan. The Pcs and their conjugates were characterized with different analytical techniques.

The photophysics and photochemistry of the MPcs were assessed when alone and in conjugates. The Pc macrocycles with relatively light metal (Al) exhibited high fluorescence quantum yields (Φ_F) and lifetimes (τ_F) in comparison to their heavy metal analogues (Zn and In) which depicted low Φ_F and τ_F values. In general, the Φ_F and τ_F values of the MPcs in conjugates were relatively unchanged. The Pc macrocycles with heavy metal (Zn or In) exhibited high triplet quantum yields (Φ_T) and short lifetimes (τ_T) in comparison to their relatively light metal analogues (Al). The MPcs conjugates with zinc oxide/silica nanoparticles (ZnO/SiNPs) and quantum dots (QDs) afforded significantly higher Φ_T and τ_T in comparison to their chitosan, HSA and SiNPs counterparts. The singlet oxygen quantum yields (Φ_Δ) of some of the MPcs were not consistent with the expected trends due to mismatch between the Φ_T and Φ_Δ values of the MPcs. Similar trends were seen in the conjugates. The low Φ_Δ values could be adduced to inefficiency in the energy transfer between the excited triplet state of the photosensitizers and the ground state molecular oxygen.

The mononuclear and multinuclear Pcs showed fascinating nonlinear optical (NLO) properties and their conjugates with QDs showed improved NLO activity.

The *in vitro* cytotoxicity of the passivated QDs were relatively innocuous at low concentrations and reduced cytocidal activity was observed when the QDs were further encapsulated with Pcs. The MPcs and their conjugates showed no dark cytotoxicity at low concentrations but relative cytocidal activity was observed at

elevated doses. The photodynamic therapy studies (PDT) of the MPcs and the conjugates showed significant activity at the tested concentrations. Reduced PDT activity was observed in the conjugates in comparison to the MPcs except for the conjugates of zinc(II) 2(3)–mono–2–(4–oxy)phenoxy)acetic acid phthalocyanine (**10**) with AgAuNPs–Cyst which showed similar activity as compound **10** alone but with minimal dark cytotoxicity which is essential for PDT.

CONTENTS **PAGES**

^{1}H NMR	=	Proton Nuclear Magnetic Resonance
2PA	=	2–Photon Absorption
A.U.	=	Absorbance Unit
ADMA	=	tetrasodium α,α–(anthracene–9,10–diyl) dimethylmalonate
APTES	=	3–Aminopropyltriethoxysilane
BET	=	Brunauer–Emmet–Teller
BV	=	Blue Valence
$CDCl_3$	=	Deuterated Chloroform
COSY	=	Correlated Spectroscopy
Cyst	=	Cysteamine
DABCO	=	1,4–Diazabicyclo–octane
DBU	=	1,8–Diazabicyclo–[5.4.0]–undec–7–ene
DCC	=	Dicyclohexylcarbodiimide
DCM	=	Dichloromethane
DHLA	=	Dihydrolipoic Acid
DMAP	=	Dimethylaminopyridine
DMF	=	Dimethylformamide
DMSO	=	Dimethyl Sulfoxide
DMSO-d_6	=	Deuterated Dimethylsulfoxide
DPBF	=	1,3–Diphenylisobenzofuran
DPE	=	Diphenyl Ether
EDC	=	N–(3–Dimethylaminopropyl)–N′–ethylcarbodiimide
ET	=	Energy Transfer
FCA	=	Free–Carrier Absorption
Flu	=	Fluorescence
FRET	=	Förster Resonance Energy Transfer
FT–IR	=	Fourier Transform Infrared

FWHM	=	Full Width at Half–Maximum
GSH	=	Glutathione
H_2Pc	=	Metal Free Phthalocyanine
HOMO	=	Highest Occupied Molecular Orbital
HSA	=	Human Serum Albumin
IC	=	Internal Conversion
ISC	=	Intersystem Crossing
LUMO	=	Lowest Unoccupied Molecular Orbital
MALDI	=	Matrix–Assisted Laser Desorption/Ionization
MPA	=	Mercaptopropionic Acid
MPcs	=	Metallophthalocyanines
MS	=	Mass Spectrometer
MSA	=	Mercaptosuccinic Acid
Nd–YAG	=	Neodymium–doped Yttrium Aluminum Garnet
NHS	=	N–Hydroxysuccinimide
NIR	=	Near Infrared
NLA	=	Nonlinear Absorption
NLO	=	Nonlinear Optics
NPs	=	Nanoparticles
OA	=	Oleic Acid
ODE	=	1–Octadecene
OLM	=	Oleylamine
Pcs	=	Phthalocyanines
PDT	=	Photodynamic Therapy
Pho	=	Phosphorescence
QDs	=	Quantum Dots
ROS	=	Reactive Oxygen Species

RSA	=	Reverse Saturable Absorption
RV	=	Red Valence
SA	=	Saturable Absorption
SiNPs	=	Silica Nanoparticles
SOMO	=	Semi Occupied Molecular Orbital
TCSPC	=	Time Correlated Single Photon Counting
TEM	=	Transmission Electron Microscope
TEOS	=	Tetraethyl orthosilicate
TGA	=	Thioglycolic Acid
TOPO	=	Triocylphosphine Oxide
UV–Vis	=	Ultraviolet–Visible
VR	=	Vibrational Relaxation
XPS	=	X–ray Photoelectron Spectroscopy
XRD	=	X–ray Diffractometer

α	=	Non–peripheral Position
Φ_{Δ}	=	Singlet Oxygen Quantum Yield
Φ_{F}	=	Fluorescence Quantum Yield
Φ_{pd}	=	Photodegradation Quantum Yield
Φ_{T}	=	Triplet Quantum Yield
$^1O_2$	=	Singlet Oxygen
$^3O_2$	=	Molecular Oxygen
I_{in}	=	Input Fluence
I_{lim}	=	Limiting Intensity
$Im[X^{(3)}]$=		Imaginary component of the third order susceptibility
I_o	=	On–Focus Intensity
I_{out}	=	Output Fluence
K	=	Triplet State Absorption Rate Constant
N	=	Number Density
S_{Δ}	=	Energy Transfer efficiency
S_0	=	Singlet ground state
S_1	=	Singlet excited state
t	=	Time
T_1	=	Triplet excited state
W_o	=	Beam Waist
z	=	Sample Position
z_o	=	Rayleigh Length
β	=	Peripheral Position
β_{eff}	=	Effective Nonlinear Absorption Coefficient
ε_o	=	Permeability of Free Space
τ_F	=	Fluorescence Lifetime
τ_T	=	Triplet Lifetime

λ	=	Wavelength

CHAPTER ONE

INTRODUCTION

1.1 NANOPARTICLES

Nanoparticles (NPs) have gained significant attention in diverse areas of research over the years and have found sundry applications in optical sensing, colorimetric detection, bioimaging, nonlinear optics, catalysis, drug delivery, photothermal and photodynamic therapies to mention a few **[1–17]**. NPs are particles with sizes that ranges from 1 to 100 nanometres (nm) **[18]**. Their large–surface–area–to–volume ratio combined with flexible surface chemistry makes them a suitable scaffold for the formation of dyad nano–platforms when linked or immobilized with other molecules. In this research work, NPs were combined with phthalocyanines (Pcs) for photodynamic therapy (PDT) and nonlinear optics (NLO) applications. The following NPs were considered in this work; silver (AgNPs), silver–gold (AgAuNPs), quantum dots (QDs), zinc oxide passivated with silica (ZnO/SiNPs) and silica (SiNPs). Their effects on the photophysicochemical, PDT and NLO activities of the Pcs will be discussed. The NPs were considered for reasons stated in the following subsections:

1.1.1 Silver (AgNPs) and silver–gold (AgAuNPs) NPs

Among the diverse noble metal–based NPs that have been exploited for biological applications, AuNPs and AgNPs **[19,20]** have proven to be highly efficient drug carriers with good chemical inertness, large–surface–area–to–volume ratios, minimal dark cytotoxicity, and ease of structural and surface modifications. These properties have afforded them placement in different biomedical applications such as in photodynamic therapy (PDT),

photothermal therapy (PTT) **[16,21–25]**, gene therapy, biological imaging and sensing **[23–25]**. Their anticancer activity is highly selective and specific when independently administered or in conjugates with other molecules by targeting the mitochondrial of the tumour cells before they induce tumour cell death **[26,27]**. Despite research reports which have shown the biomedical applications of AgNPs and AuNPs when independently administered **[19,20]**, limited research studies have been done on their phthalocyanines (Pcs) Pcs–NPs dyad forms for biomedical applications. It is pertinent to note that synergistic properties can be achieved when these two biologically active components (Pcs and AgNPs, Pcs and AgAuNPs) are combined in dyad forms for PDT application. Hence, the effects of AgNPs and AgAuNPs on the photophysicochemical behaviour and PDT activity of Pcs will be evaluated in this research work. The AgNPs and AgAuNPs were selected due to the heavy–atom effect of Ag and Au which is expected to foster improved triplet state population as well as enhance permeability and retention (EPR) effect which affords selective accumulation of their conjugates with Pcs in the tumour cells **[21,28–30]**. The administration of the conjugates of AgNPs or AgAuNPs with Pcs is expected to afford a more efficacious PDT activity in comparison to their independent forms. AgNPs **[31]** and AgAuNPs **[31]** were functionalised with NH_2 containing ligand for linkage with COOH substituted Pcs, **Figure 1.1**.

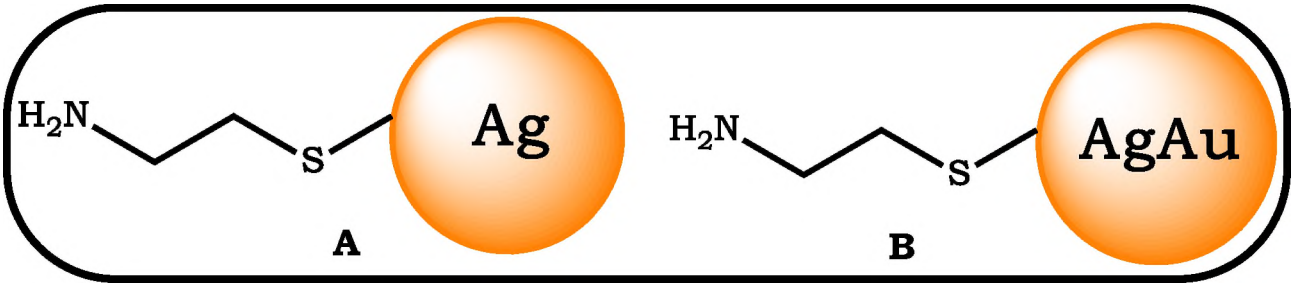

Figure 1.1: Representation of cysteamine (Cyst) capped AgNPs (A), and AgAuNPs (B) used in this work.

1.1.2 Semiconductor quantum dots

Semiconductor quantum dots (QDs) are zero–dimensional nanocrystals. They are often fabricated from elements in groups II–VI or III–V of the periodic table. Their properties originate from their physical size which ranges from 1 to 10 nm in diameter **[32–34]**. QDs are known to exhibit excellent physicochemical properties which include high molar absorptivity, broad absorption, symmetrical narrow emission, size tunability, multi–coloured light emission, good photo–stability and high photoluminescence (PL) **[35]**. The relatively small size and optoelectronic behaviour of QDs can be attributed to their quantum confinement **[36]**. QDs may consist of a core which is sometimes passivated with a "shell", or in some cases, two shells, collectively known as a double shell **[37,38]**. The presence of shells on QDs enhances their PL and stability by minimizing the surface defects **[39]**. In addition to PL and improvement in stability, shells also serve to minimize the extreme toxicity often associated with QDs by preventing the leaching of the Cd^{2+} ions from the QDs **[40,41]**. QDs can be designed to have good dispersibility in different media with minimal or

no aggregation and this is often achieved by choice of synthetic route or phase transfer process **[42]**. Several core, core/shell and core/shell/shell QDs such as CdTe **[39]**, CdSe **[43]**, CdSe/CdS **[43,44]**, CdTe/CdSe **[45]**, CdTe/CdS/ZnS **[46]** are known. *In vitro* and *in vivo* research studies have shown that QDs when passivated with shell are relatively innocuous to host cells **[40,41,47–50]**. QDs have also found applications in NLO **[12]**, bioimaging **[48]** and PDT **[51]**.

In this research work, the effects of QDs on the NLO and photophysicochemical properties of Pcs will be evaluated. Synergistic effect of Pcs–QDs in dyad forms is expected to improve the NLO and photophysicochemical properties. Finally, the *in vitro* dark cytotoxicity of the Pcs alone and their conjugates with QDs will be assessed. As earlier stated for AgNPs and AgAuNPs, the heavy–atom effect of QDs are expected to enhance the triplet state population. QDs utilised in this research work were functionalised with NH_2 or COOH containing ligands for ease of covalent linkage to Pcs substituted with COOH or OH moieties respectively. The representation of the NH_2 or COOH functionalised QDs is shown in **Figure 1.2.** The TOPO capped QDs were mixed with Pcs without chemical bond formation due to absence of suitable anchor moiety on the former.

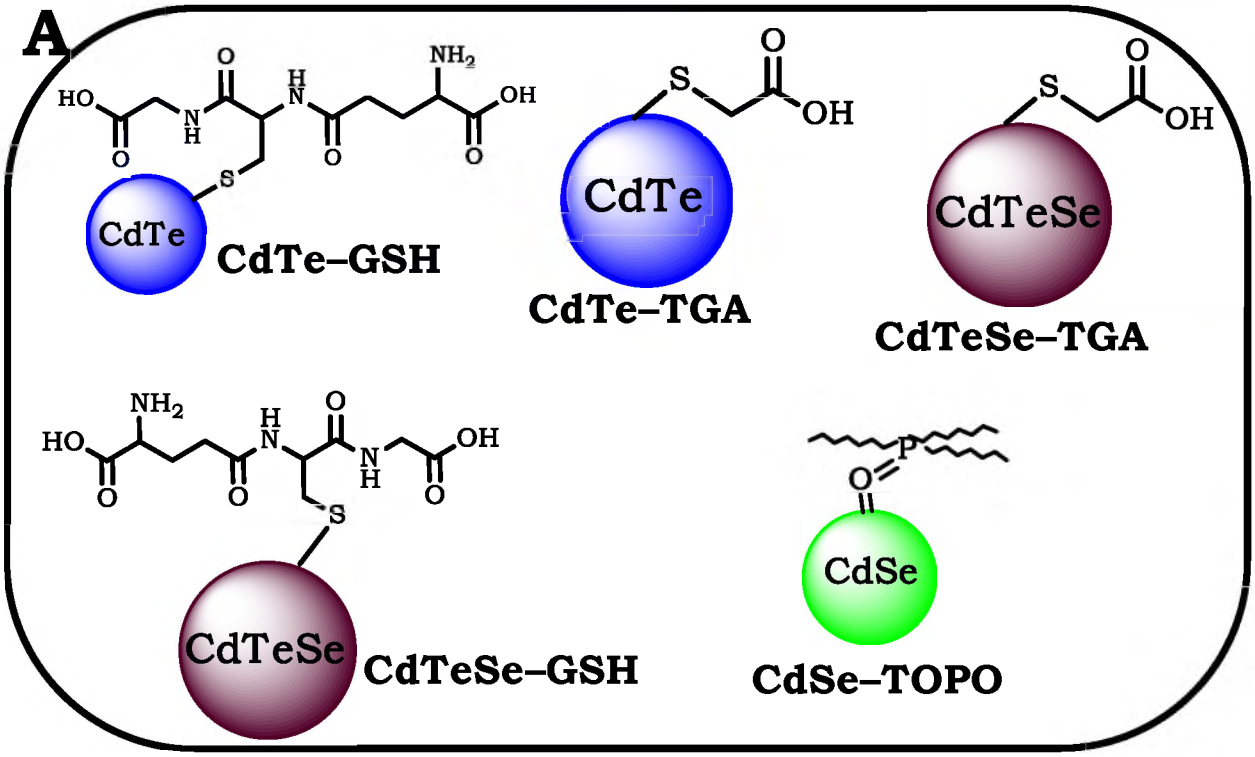
A
CdTe
CdTe–GSH
CdTe
CdTe–TGA
CdTeSe
CdTeSe–TGA
CdTeSe
CdTeSe–GSH
CdSe
CdSe–TOPO

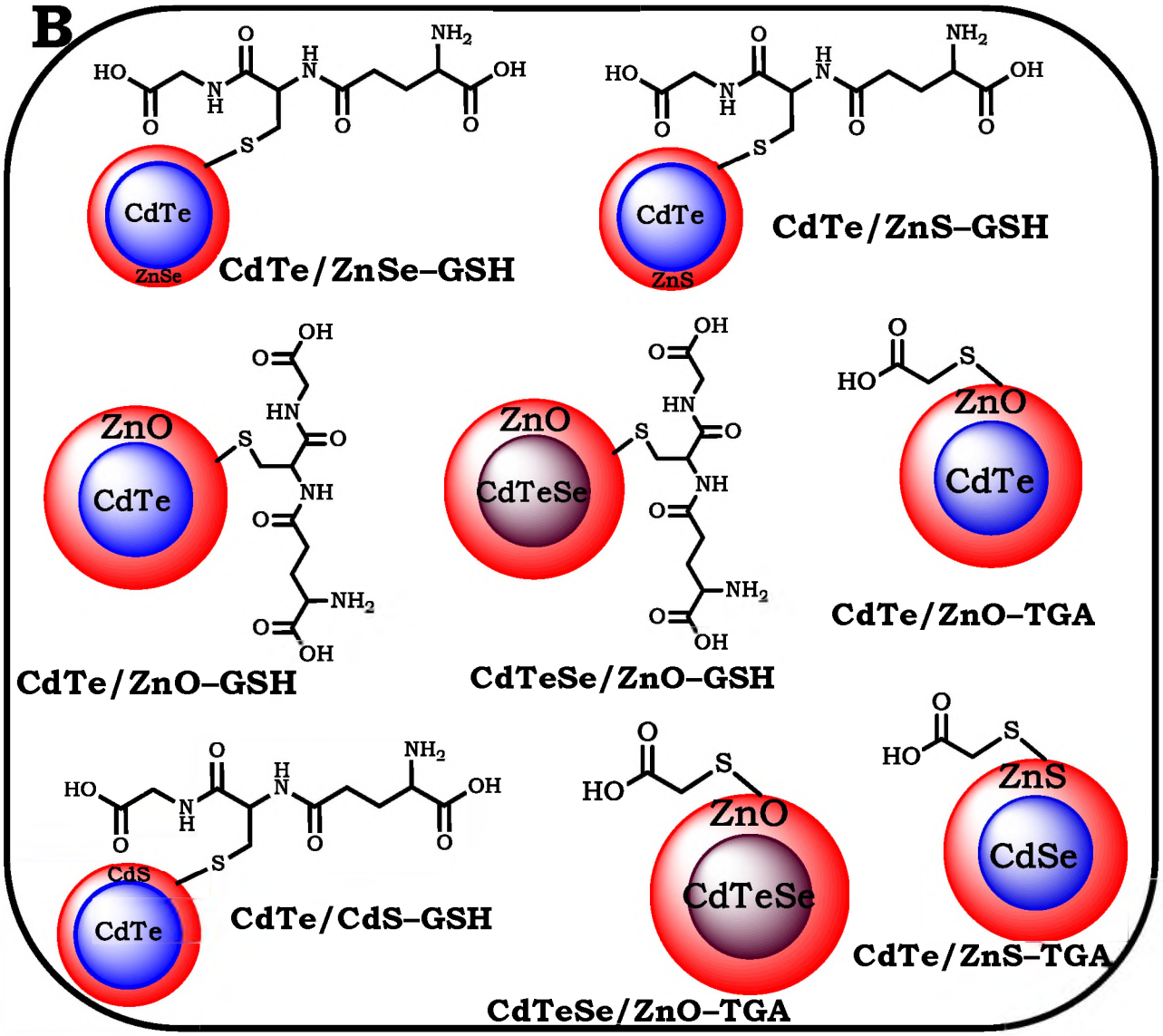
B
CdTe
ZnSe
CdTe/ZnSe–GSH
CdTe
ZnS
CdTe/ZnS–GSH
ZnO
CdTe
CdTe/ZnO–GSH
ZnO
CdTeSe
CdTeSe/ZnO–GSH
ZnO
CdTe
CdTe/ZnO–TGA
CdS
CdTe
CdTe/CdS–GSH
ZnO
CdTeSe
CdTeSe/ZnO–TGA
ZnS
CdSe
CdTe/ZnS–TGA

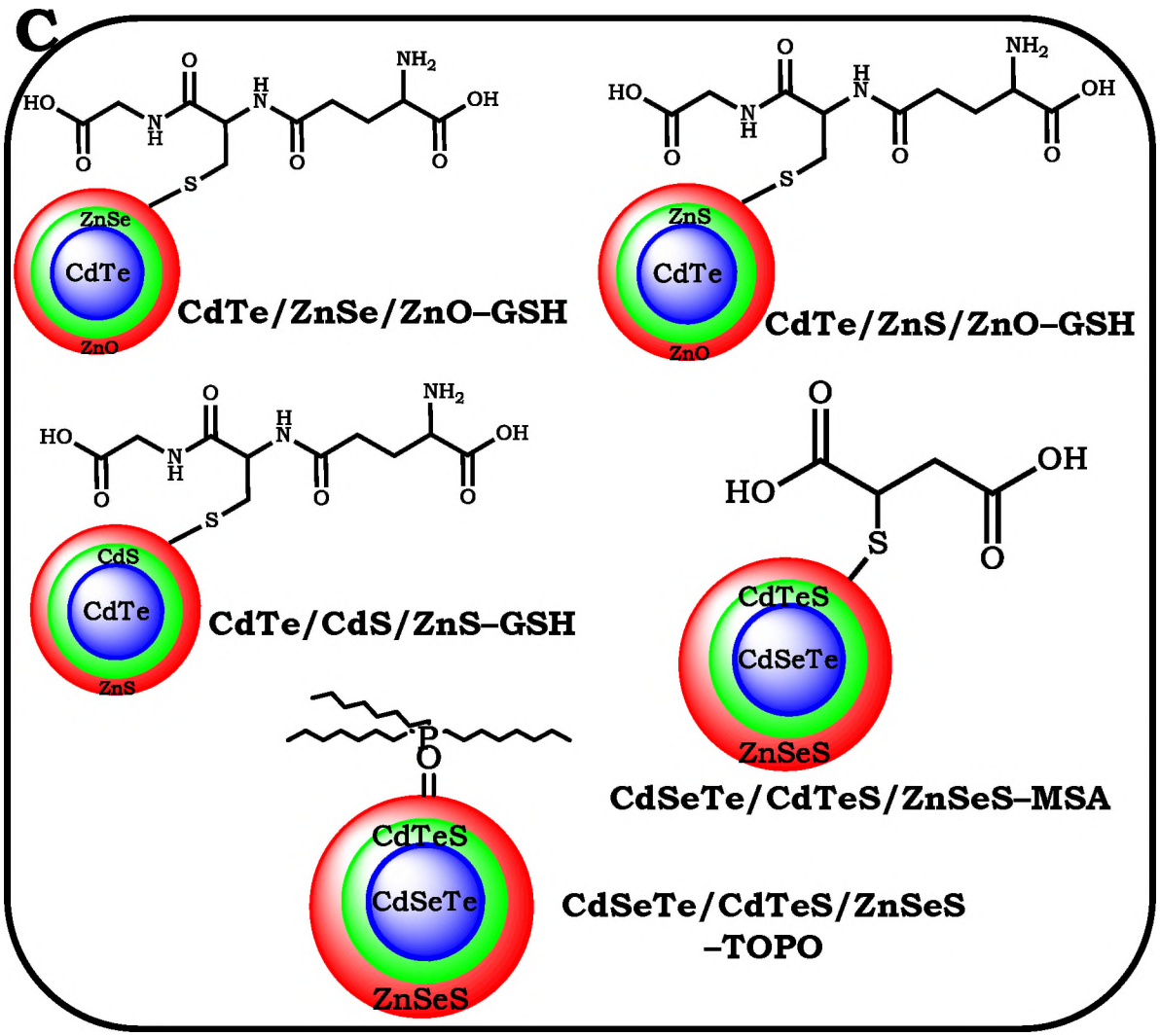

Figure 1.2: Representation of core (A), core/shell (B), and core/shell/shell (C) QDs employed in this work. **GSH = Glutathione, TOPO = Triocytylphospine oxide, MSA = Mercaptosuccinic acid. MSA, TOPO, and GSH capped QDs were studied when alone and in the presence of Pcs. TGA capped QDs were studied independently in the absence of Pcs.**

Table 1.1 shows the QDs used in this research work and the studies performed on them. The QDs ranges from core to core/shell/shell and ternary alloy QDs. The references **[39,43,46,52–54]** for the QDs syntheses are provided where applicable, **Table 1.1**. The TGA capped QDs were independently studied in the absence of Pcs due to lack of suitable anchor group (NH_2) on the latter.

Table 1.1: QDs synthesised in this research work.

QDs	Capping	Denoted as	Studies	Ref.
Core QDs				
CdTe	TGA	**CdTe–TGA**	Photophysics, cytotoxicity	**[39]**
CdTe	GSH	**CdTe–GSH**	Photophysics, cytotoxicity	**[39]**
CdSe	TOPO	**CdSe–TOPO**	Photophysics, NLO	**[43]**
CdTeSe	TGA	**CdTeSe–TGA**	Photophysics	**[52]**
CdTeSe	GSH	**CdTeSe–GSH**	Photophysics, cytotoxicity	New
Core/Shell QDs				
CdTe/ZnSe	GSH	**CdTe/ZnSe–GSH**	Photophysics	**[53]**
CdTe/ZnS	GSH	**CdTe/ZnS–GSH**	Photophysics, cytotoxicity	**[53]**
CdTe/ZnO	TGA	**CdTe/ZnO–TGA**	Photophysics, cytotoxicity	**[54]**
CdSe/ZnS	TGA	**CdSe/ZnS–TGA**	Photophysics	**[43]**
CdTe/CdS	GSH	**CdTe/CdS–GSH**	Photophysics,	**[53]**
CdTe/ZnO	GSH	**CdTe/ZnO–GSH**	Photophysics, cytotoxicity	New
CdTeSe/ZnO	TGA	**CdTeSe/ZnO–TGA**	Photophysics, cytotoxicity	New
CdTeSe/ZnO	GSH	**CdTeSe/ZnO–GSH**	Photophysics, cytotoxicity	New
Core/Shell/Shell QDs				
CdTe/CdS/ZnS	GSH	**CdTe/CdS/ZnS–GSH**	Photophysics	**[46]**
CdTe/ZnSe/ZnO	GSH	**CdTe/ZnSe/ZnO–GSH**	Photophysics	New

CdTe/ZnS/ZnO	GSH	**CdTe/ZnS/ZnO–GSH**	Photophysics, cytotoxicity	New
CdSeTe/CdTeS/ ZnSeS	TOPO, MSA	**CdSeTe/CdTeS/ ZnSeS–TOPO, CdSeTe/CdTeS/ ZnSeS–MSA**	Photophysics, NLO	New
The GSH and MSA capped QDs were covalently linked to Pcs with chemical bond formation. TOPO capped QDs were mixed with QDs without chemical bond formation. REF. = Synthesis References				

1.1.3 Zinc oxide NPs

Zinc oxide NPs (ZnONPs) are another type of semiconductor NPs that have found applications in solar cells **[55,56]**, electrical and optical devices **[57,58]**, electrostatic dissipative coating **[59]** and catalysis **[60,61]**. ZnONPs have also been reported to possess anticancer activity due to the fact that they generate reactive oxygen species upon excitation at a suitable wavelength **[62]**. Their wide range of applications could be attributed to their good optical and electrical properties, ease of synthesis, thermal and chemical stability **[63]**.

The ZnONPs employed in this work were passivated with SiNPs as reported in the literature **[64]** and functionalised with NH_2 containing ligand for linkage to COOH substituted Pcs, **Figure 1.3**. In this work, the effect of ZnO/SiNPs on the photophysicochemical behaviours and *in vitro* PDT of Pcs will be evaluated.

1.1.4 Silica–based NPs

Silica nanoparticles (SiNPs) have found extensive applications in different fields which include nonlinear optics, drug delivery, bioimaging and

sensing **[65–68]**. Their extensive use could be adduced to their good physicochemical properties which include low toxicity, tunable size, biocompatibility, porosity, large surface–area–to–volume ratio, thermal stability, ease of synthesis and surface modification **[69–82]**. Their interesting physicochemical properties have afforded them applications in PDT as drug delivery agents **[83,84]** and gene therapy as encapsulation agents for biomolecules (DNA) **[85]**. Furthermore, SiNPs have been found to sometimes improve the photophysicochemical behaviour of photosensitizers when they are immobilized or covalently linked to them **[86]**.

In this research work, the effects of functionalised SiNPs on the photophysicochemical behaviour and *in vitro* cytotoxicity of Pcs will be assessed. The SiNPs used in this work were capped with NH_2 containing ligand for linkage with COOH substituted Pcs, **[87,88] Figure 1.3**.

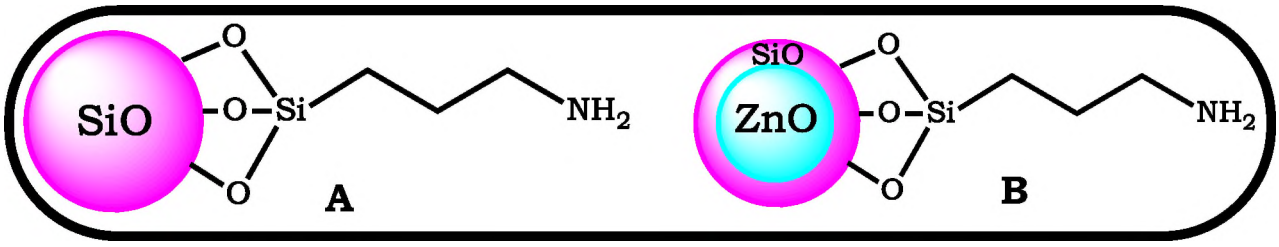

Figure 1.3: Representation of SiNPs–APTES (A), and ZnO/SiNPs–APTES (B) used in this work. **APTES = (3–aminopropyl)triethoxysilane.**

1.2 METALLOPHTHALOCYANINES (MPcs)

Phthalocyanines are planar aromatic macrocycles which are made up of 18 π–electron conjugated ring system with four isoindole units linked via nitrogen atoms, **Figure 1.4 [89–92]**. MPcs have found a diverse range of

applications due to their ease of structural modification, high molar absorptivity, absorption in the near infra–red region, good optical properties, chemical and thermal stability **[89–102]**. They have found applications in NLO, solar cells, photocatalysis, molecular electronics, optoelectronics, photonics, thermal writing displays, photocatalysis, electrocatalysis, gas sensing and PDT, to mention a few **[94–102]**. MPcs can be modified into multinuclear forms which include dimers, trimers and multi decker forms **[103–109]** which may result in enhancement of their activities in some of the mentioned applications. Both mononuclear and multinuclear Pcs were employed in this research work.

Substitution of MPcs macrocycles can be done at different positions which include the non–peripheral (α) and peripheral (β) positions **[89,90,110,111]** as shown in **Figure 1.4**. Positions 1, 4, 8, 11, 15, 18, 22 and 25 are the non-peripheral (α) positions, while positions 2, 3, 9, 10, 16, 17, 23 and 24 are the peripheral (β) position.

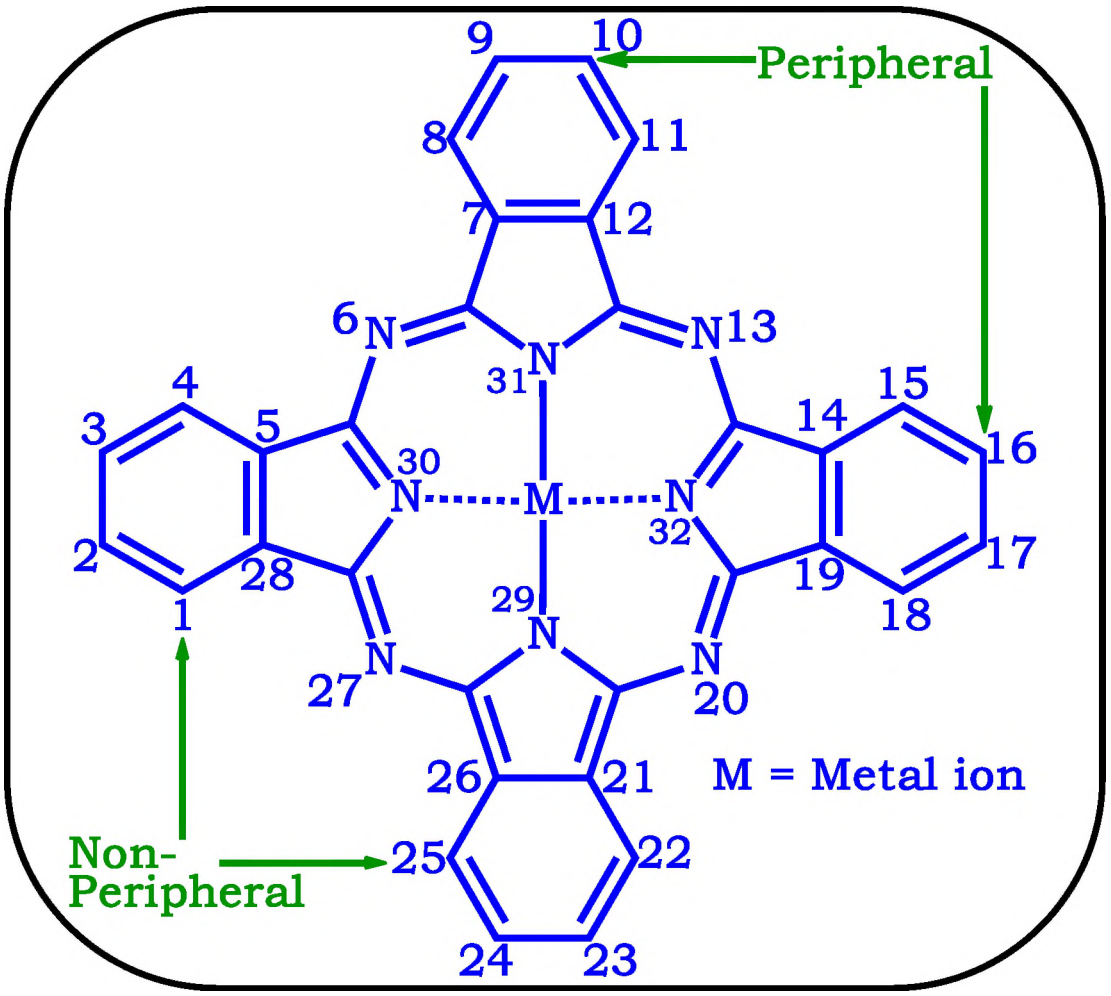

Figure 1.4: Molecular structure of mononuclear Pcs showing the non–peripheral (α) and peripheral (β) positions.

1.2.1 Synthesis of symmetrical and asymmetrical mononuclear Pcs

Symmetrical Pcs can be synthesized by cyclo–condensation of mono–substituted phthalonitriles as precursors to obtain tetra–substituted Pcs **[89,112,113]**, **Scheme 1.1**. The use of mono–substituted 3–nitrophthalonitrile precursor yields non–peripheral substitution while mono–substituted 4–nitrophthalonitrile yields peripheral substitution as shown in **Scheme 1.1**.

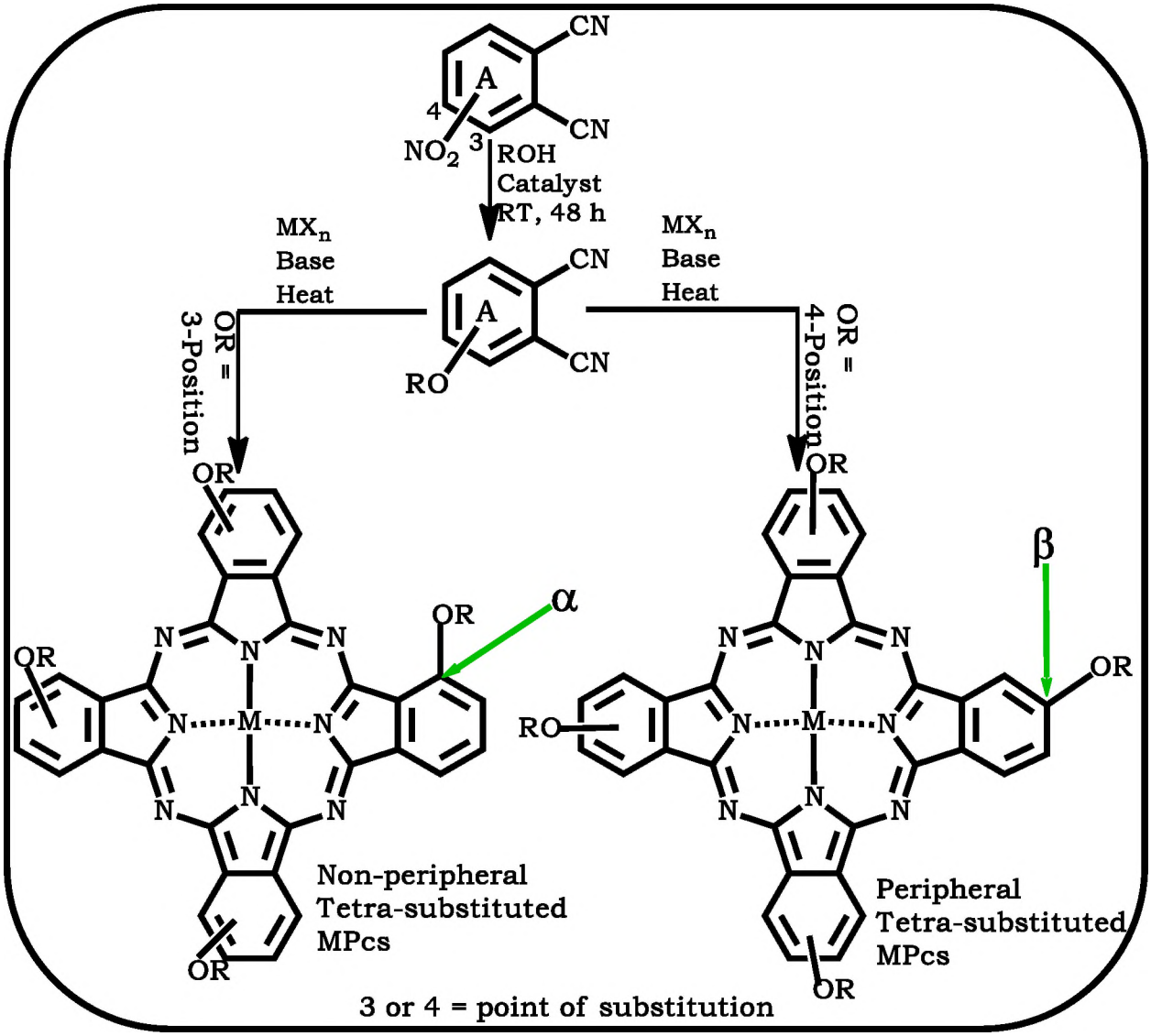

Scheme 1.1: Synthetic routes for non–peripheral (α) and peripheral (β) substituted MPcs

It is pertinent to note that the inherent uniformity of symmetrical Pcs sometimes limit their application where specific binding or coordination with other molecules are needed **[114]**.

Efforts have been made towards the design and synthesis of asymmetrical Pcs with single anchor moiety located at a specific position (**AAAB**), **Scheme 1.2**. Reports have shown that asymmetry (loss of symmetry)

improves the photophysical properties of Pc type compounds **[115]**. Similarly, lack of symmetry has been reported to enhance the NLO behaviour of Pc compounds **[116]**. Several methods have been reported on the synthesis of asymmetrical Pcs such as statistical mixed condensation route **[114,117,118]**, subphthalocyanine ring expansion route **[114,119,120]** and polymeric–support based route **[114,121,122]**. Among these routes, statistical mixed condensation has been the most utilized protocol for fabrication of asymmetrical Pcs with three identical and one non–identical isoindole subunits (A_3B) due to simplicity and satisfactory results which are usually obtained from this approach. The statistical mixed condensation route is known to be non–selective due to the reaction of two different substituted phthalonitrile or 1,3–diiminoisoindoline precursors **[114,117,118]**. Theoretically, six possible products could be obtained from this method as shown in **Scheme 1.2**. Chromatographic separation is required to isolate the target ligand (A_3B) from the statistical mixture of Pcs. The most widely used mole ratios for asymmetrical MPcs include 3:1 or 9:1 (A:B). Higher mole ratios could also be utilized depending on the reactivity of the different phthalonitrile precursors to be used **[114,117,118]**.

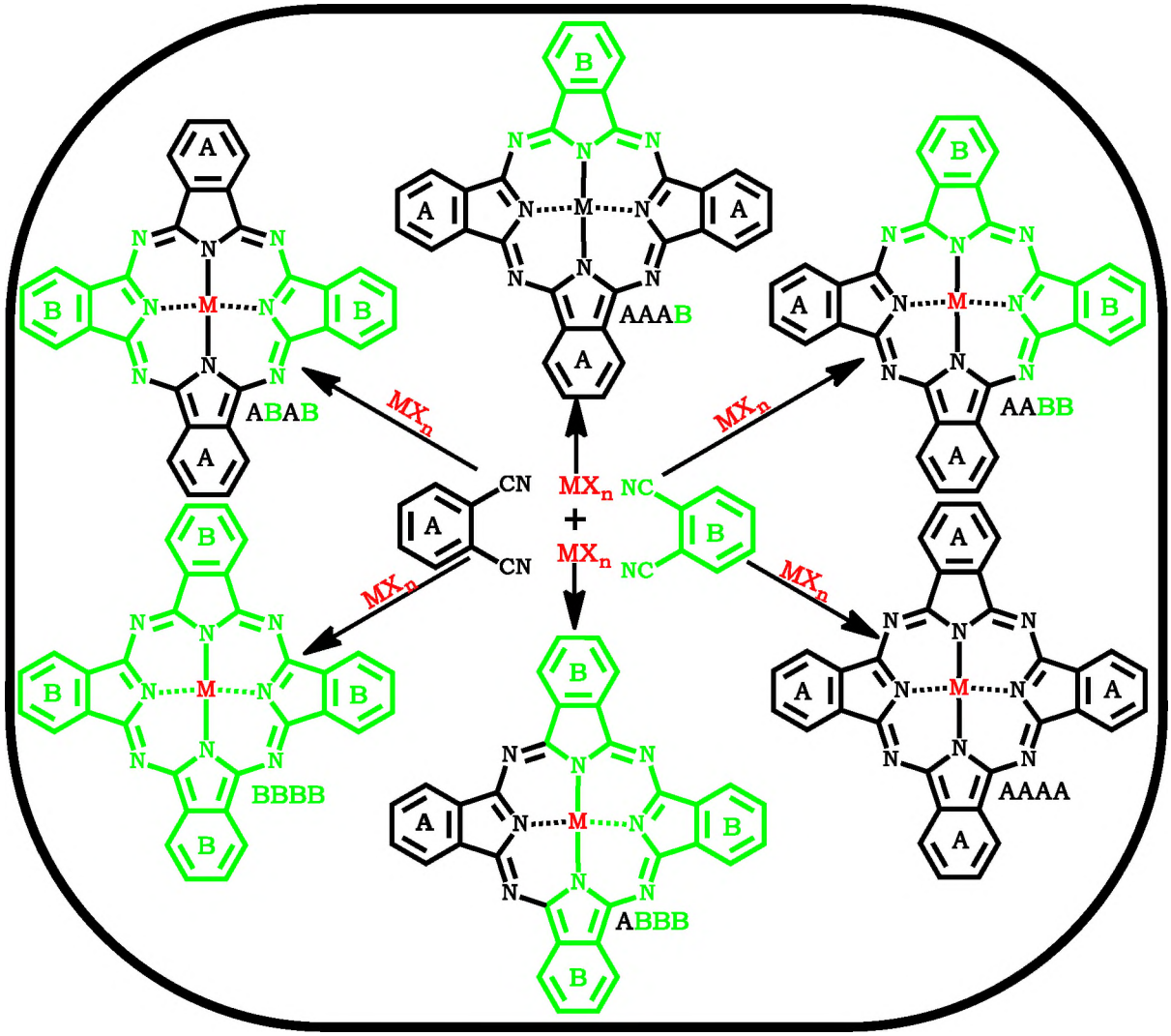

Scheme 1.2: Synthetic route for fabrication of asymmetrical Pcs via statistical mixed condensation approach.

1.2.2 Synthesis of symmetrical and asymmetrical multinuclear MPcs

The structural flexibility possessed by Pcs has led to the development of multinuclear MPcs. Of note is the use of lanthanide metals to obtain multinuclear Pcs due to their capacity to form coordination with more than one Pc macrocycles **[122–125]**.

Extensive work has been done on the synthesis of symmetrical multinuclear MPcs with limited studies on their asymmetrical analogues.

This could be due to the possibility of forming many products making it difficult to separate the target Pc compound due to similar solubility.

Two major synthetic routes are usually utilised in the synthesis of homoleptic multinuclear MPcs: (i) cyclo–condensation of phthalonitrile in the presence of organic base, lanthanide metal, solvent and heat **[126]** and (ii) the template synthesis which involve the use of unmetalated Pcs (H_2Pc) in the presence of lanthanide metal, organic base, high boiling point solvent and heat **[124,126]**, **Scheme 1.3**. The template synthesis can be used to obtain the asymmetrical homoleptic multinuclear MPcs by using the statistical mixed condensation as described in the previous section **(1.2.1.)**.

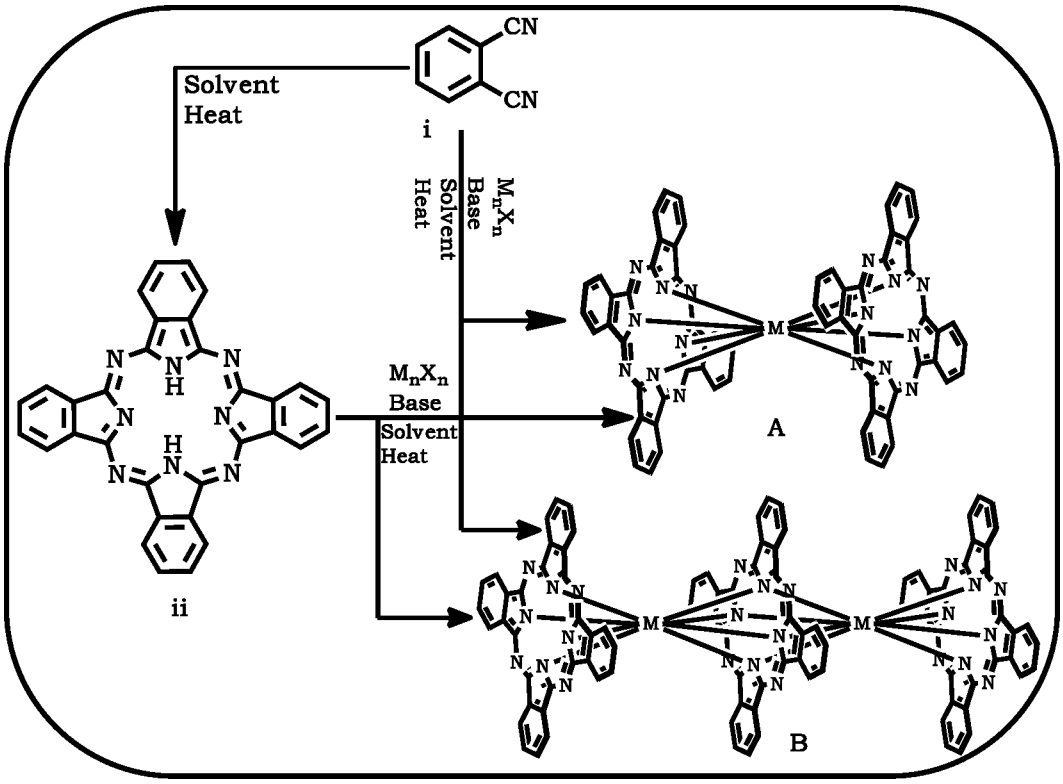

Scheme 1.3: Synthetic route for homoleptic multinuclear MPcs; i. Direct approach, and ii. Template approach: (A) Bis and Tris (B) MPcs

This work reports on the synthesis of asymmetrical $LnPc_2$ and Ln_2Pc_3 for NLO studies. **Table 1.2** shows some examples of symmetrical multinuclear MPcs which have been used for NLO but no homoleptic asymmetrical multinuclear MPcs were reported **[127–136]**. This work reports for the first time on the synthesis of Eu based asymmetrical multinuclear Pcs ($EuPc_2$ and Eu_2Pc_3) and their linkage to ternary alloy QDs. Their symmetrical analogues were mixed with ternary alloy QDs due to absence of a suitable coordination points on the two components (Pcs and TOPO–QDs). The NLO properties of the symmetrical and asymmetrical multinuclear MPcs as well as their conjugates were investigated for the first time in this work.

Table 1.2: Examples of multinuclear MPcs used as NLO absorbers

COMPOUNDS	REFERENCE
Eu_2Pc_3	127
$SmPc_2$	128
$LuPc_2$	129
$GdPc_2$	129
$Eu[Pc(OC_5H_{11})_8]_2$	130
$Eu[Pc(C_7H_{15})_8]_2$	130
$LuPc_2$	131
$LuPc_2$	132
$LuPc_2$	133
$YbPc_2$	134
Nd_2Pc_3	135
Lu_2Pc_3	136

1.2.3 Ground state electronic absorption

1.2.3.1 Mononuclear Pcs

MPcs are known to have two distinct ground state electronic absorption bands as shown in **Figure 1.5**. The characteristic absorption bands of MPcs include the B–band usually seen around 300–400 nm and Q–band at 670 nm depending on the structural properties of the Pcs.

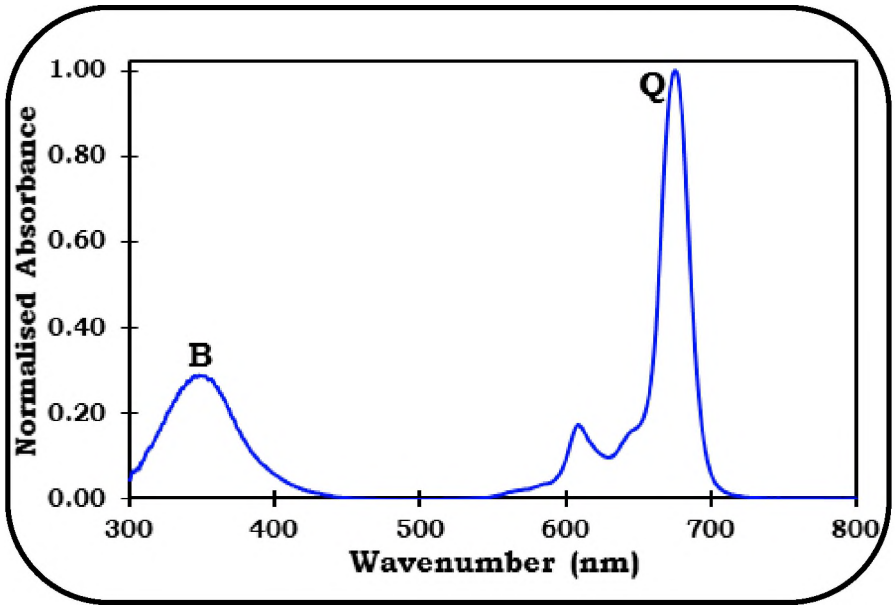

Figure 1.5: Representative ground state electronic absorption spectrum of MPcs [unpublished work].

The absorption spectra of MPcs are dependent on nature of the central metal, point of substitution, ring expansion, protonation, nature of substituents and solvents **[137–140]**. Unmetalated Pcs are known to have a split Q–band due to their reduced symmetry (D_{2h}), **Figure 1.6**. In H_2Pc, the split Q–bands, Q_1 and Q_2 result from the transitions from a_{1u} of the highest occupied molecular orbital (HOMO) to b_{2g} and b_{3g} of the lowest unoccupied molecular orbital (LUMO) respectively as shown in **Figure 1.6**.

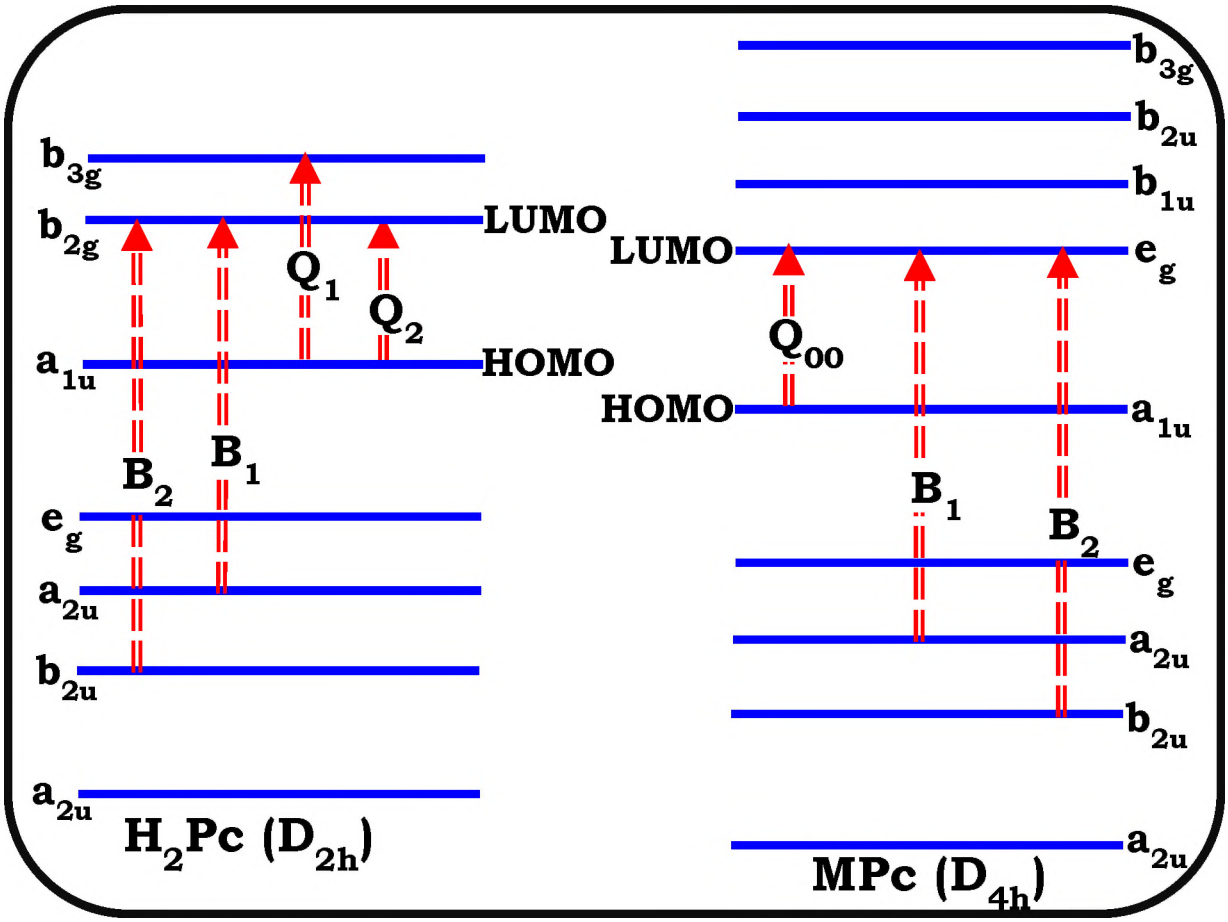

Figure 1.6: Ground state electronic transition of molecular orbital representation of mononuclear Pcs.

Metalated Pcs are often characterised by a symmetrical Q–band due to their D_{4h} symmetry which result from the transitions from a_{1u} of the HOMO to the degenerate e_g of the LUMO, **Figure 1.6**. MPcs are often characterized with two B bands, B_1 and B_2 which result from the transitions from a_{2u} and b_{2u} of the HOMO to e_g of the LUMO **[141–144]**, **Figure 1.6**.

1.2.3.2 Multinuclear Pcs

The multinuclear Pcs have more complex spectra compared to mononuclear Pcs **[144,145]**, **Figure 1.7**. The bis MPcs usually show five

distinct peaks corresponding to the B or soret band, blue valence (BV) band, Q–band, red valence (RV) band and near infrared (NIR) band, **Figure 1.7**. The intense split B band result from the allowed transition between $6e_1(\pi) \leftarrow 4a_1(\pi^*)$, **Figure 1.8**.

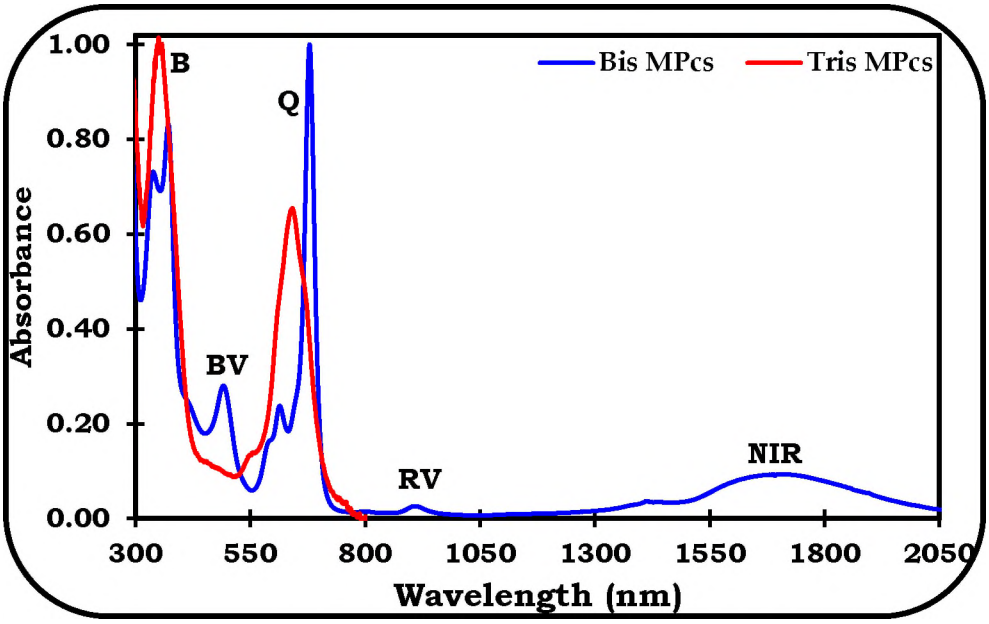

Figure 1.7: Representative ground state electronic absorption spectra of multinuclear Pcs [unpublished work].

The typical blue valence band of the bis MPc is observed around 500 nm which is due to the electronic transition between $2a_2(\pi^*) \leftarrow 5e_1(\pi)$ while the symmetrical narrow Q–band result from the allowed electronic transition between $6e_3(\pi^*) \leftarrow 2b_1(\pi)$ **[145–151]**. The slightly attenuated red valence band around 900 nm is often associated with the forbidden transition between $6e_1(\pi^*) \leftarrow 2a_2(\pi)$ involving the semi–occupied molecular orbital (SOMO) while the ring–to–ring charge transfer transition band in the near

infrared region is associated with the electronic transition between $2a_1 \leftarrow 2b_1$ as shown in **Figure 1.8**.

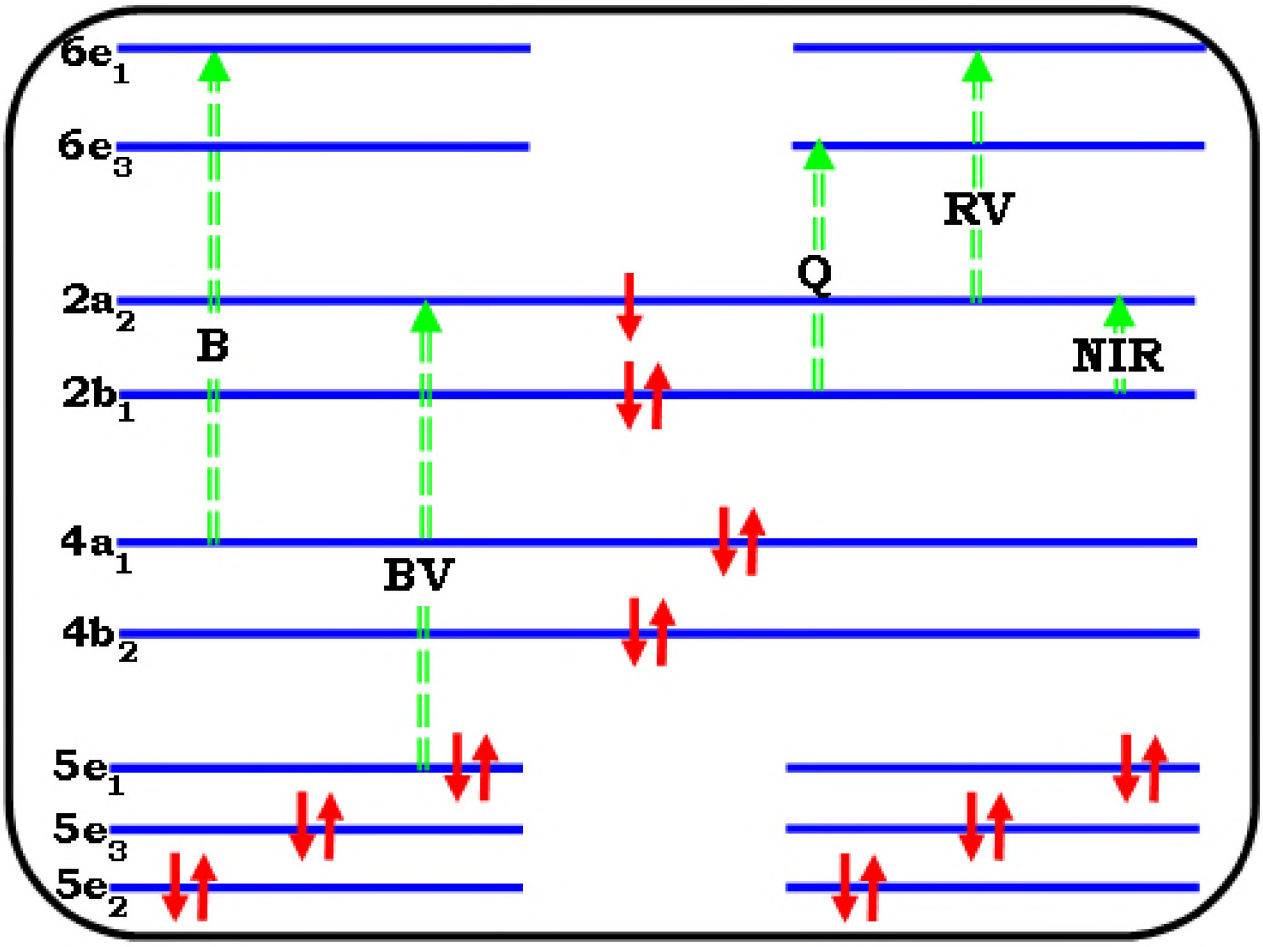

Figure 1.8: Ground state electronic transition molecular orbital representation of bis MPcs [145,151].

1.2.4 Metallophthalocyanines and conjugates synthesised in this research work

Table 1.3 shows some examples of Pcs which have been linked to various NPs in the literatures. Thus, the linkage of Zn, Al, and Ni mono–amino, COOH substituted Pc derivatives to QDs and SiNPs have been reported in the literatures **[67,86,152–182]**. This work reports for the first time on the covalent linkage of; (i) asymmetrical mononuclear Pcs with mono–

substituents (COOH, OH, SH) to QDs, SiNPs, ZnO/SiNPs, HSA and chitosan; and (ii) asymmetrical multinuclear Pcs ($LnPc_2$ and Ln_2Pc_3) to ternary alloy QDs. Subsequently, the NLO properties of the multinuclear Pcs and their conjugates were investigated for the first time in this work.

Table 1.3: Examples of Pcs and their conjugates with nanoparticles used for different applications

Pcs	NANOPARTICLES	STUDIES	REF.
MPcs–QDs			
Aluminum tetrasulfonated Pc	CdSe/CdS/ZnS–DHLA	PDT	**[152]**
In octa–carboxy Pc	CdSe/ZnS–GSH	Photophysical	**[153]**
Zn tetra–carboxy Pc	CdTe/ZnS–GSH	Photophysical	**[154]**
Zn mono–aminophenoxy Pc	CdTe–TGA	Photophysical	**[155]**
Zn tri–*tert*–butylimido Pc	CdTe–MPA	Photophysical	**[156]**
In tetra–diaminopyrimidin–2–ylthiol Pc	CdTe/ZnSe/ZnO–GSH	Photophysical	**[157]**
Zn tetra–amino Pc	CdTe–MPA	Photophysical	**[158]**
Zn tetra–mercapto Pc			**[159]**
Zn mono–amino Pc			**[160]**
Zn mono–aminophenoxy Pc	CdTe–TGA		**[160]**
In tetra–amino Pc			**[158]**
Zn mono–aminophenoxy Pc	CdTe–L–cysteine	Photophysical	**[155]**
Zn mono–carboxy Pc	CdTe/ZnS–CALNN	Photophysical	**[161]**
Ge mono–carboxy Pc	CdTe/ZnS–CALNN	Photophysical	**[161]**
Zn octa–carboxy Pc	CdTe/ZnS–GSH	Photophysical	**[162]**
Al mono–aminophenoxy Pc	CdSe/ZnS–GSH	Fluorescence Sensor	**[163]**
Co tetra–amino Pc	CdTe/ZnS–GSH		**[164]**
Al tetra–amino Pc	CdTe/ZnS–MPA		**[165]**
Ni mono–mercaptosuccinic Pc	CdTe/ZnS–GSH	Fluorescence Sensor	**[166]**
Zn tri–*tert*–butylaminoethoxy Pc	CdSe	Solar cell	**[167]**
Ni tetra–amino Pc	CdTe–TGA	Electrocatalysis	**[168]**
In tetra–aminophenoxy Pc	CdSe–MSA	NLO	**[169]**

In tetra–aminophexoxy Pc	CdSe/ZnS–MSA	NLO	**[170]**
Ga octa–*tert*–butylphenoxy Pc	CdTe–TGA	NLO	**[171]**
In tetra–*tert*–butylphenoxy Pc	CdTe–TGA	NLO	**[171]**
In tetra–phenoxy Pc	CdTe–TGA	NLO	**[171]**
MPcs–SiNPs			
Zn mono–carboxyphenoxy Pc	SiNPs–APTES	NLO	**[86]**
Zn tetra– *tert*–butyl Pc	SiNPs	PDT	**[172]**
Si siloxy–(dimethyl)–dimethylpropan–amine Pc	SiNPs	PDT	**[173]**
In tetra–aminophenoxy Pc	SiNPs–APTES	NLO	**[174]**
Zn tetra–amino Pc	SiNPs	Cytotoxicity	**[175]**
ClAl unsubstituted Pc	SiNPs	NLO	**[67]**
MPcs–AgNPs or AuNPs			
Zn tri–*tert*–butylaminoethoxy Pc	AuNPs	Photophysical	**[176]**
Metal free Pc	AuNPs or AgNPs	NLO	**[177]**
Zn tetra–hexanedithiol Pc	AuNPs	PDT	**[178]**
Zinc hexanedithiol Pc	AgNPs or AuNPs	PACT	**[179]**
Silicon hexanedithiol Pc	AgNPs or AuNPs	PACT	**[179]**
MPcs–other components			
Co tetra–sulfonated Pc	Chitosan microsphere	Water purification	**[180]**
Silicon (dimethylamino)-2-propoxy Pc	HSA	PDT	**[181]**

DHLA = Dihydrolipoic Acid, MPA = Mercaptopropionic Acid, TGA = Thioglycolic Acid, MSA = Mercaptosuccinic Acid, GSH = Glutathione, APTES = (3–aminopropyl)triethoxysilane, PACT = Photodynamic antibacterial chemotherapy, HSA = Human serum albumin, CALNN = Cysteine-Alanine-Leucine-Asparagine-Aspartate

Table 1.4 lists the Pcs used in this work with compounds numbers ranging from **1** to **14**. Symmetrical, asymmetrical mononuclear and multinuclear

phthalocyanines (Pcs) were synthesised in this research work. Compounds **2–4**, **6**, **7** and **9** were synthesised as reported in the literatures **[182–185]** while compounds **1**, **5**, **8**, **10–14** are reported in this research work for the first time. The Pcs are represented as follows: metal–free 2,3–bis[2'-(2"–mercaptoethoxy]–9,10,16,17,23,24–hexa–*n*–butoxy phthalocyanine (**1**), zinc(II) 2,3–mono–(4–carboxyphenoxy) Pc (**2a**), zinc(II) 2,3–mono–(3'–carboxyphenoxy) Pc (**2b**) **[182]**, zinc(II) 1,8(11),15(18),22(25)–tetra–(4'–*tert*–butylphenoxy) Pc (**3**) **[183]**, zinc(II) 2,9(10),16(17),23(24)–tetra–(4'–*tert*–butylphenoxy) Pc (**4**) **[184]**, aluminium(III) chloride 2,9(10),16(17),23(24)–tetra–(4'–*tert*–butylphenoxy) Pc (**5**), zinc(II) 2,9(10),16(17),23(24)–tetra–(4'–carboxyphenoxy) phthalocyanine (**6**) **[182]**, aluminium(III) chloride 2,9(10),16(17),23(24)–tetra–sulfonated Pc (**7**) **[185]**, indium(III) chloride 2,9(10),16(17),23(24)–tetra–(3'–carboxyphenoxy) Pc (**8**), aluminium(III) chloride octa–carboxy Pc (**9**) **[185]**, zinc(II) 2,3–mono–2–(4'–oxy)phenoxy)acetic acid Pc (**10**), europium(III) bis(2,3,9,10,16,17,23,24–octa–*n*–butoxy) Pc (**11**), dieuropium(III) tris(2,3,9,10,16,17,23,24–octa–*n*–butoxy) Pc (**12**), europium(III) bis{2,3–bis[2'–(2''–hydroxyethoxy)ethoxy]–9,10,16,17,23,24–hexa–*n*–butoxy Pc (**13**), dieuropium(III) tris{2,3–bis[2'–(2''–hydroxyethoxy)ethoxy]–9,10,16,17,23,24–hexa–*n*–butoxy Pc (**14**). The carboxylic acid moiety of compounds **2**, **6**, **8–10** were used for the covalent linkage of the compounds to the amino moiety of the nanoparticles, chitosan and HSA to form an amide bond, **Table 1.5**. The sulfonic acid moiety of compound **7** was activated using thionyl chloride to afford

covalent linkage with the amine moiety of the GSH–QDs to forming sulfonamide bond, **Table 1.5**. The carboxylic acid moiety of the MSA capped QDs was activated to afford coupling with compounds **13** and **14** which resulted in an ester bond formation for the dyad forms (**13**–CdSeTe/CdTeS/ZnSeS–MSA and **14**–CdSeTe/CdTeS/ZnSeS–MSA), **Table 1.5**. The thiol moiety of Pc **1** was linked to the surface of QDs to form sulfur–metal bond (**1**–CdSe–TOPO). Compound **11** and **12** were mixed with QDs to form composites without chemical bond formation. Compounds **3**–**6** were doped onto SiNPs via reverse microemulsion technique.

Zn and In were chosen as central metals for the MPcs due to their heavy–atom effect which promote intersystem crossing to the triplet state leading to enhanced triplet state, and singlet quantum yields as well as improved PDT activity. Al was chosen since AlPcSmix (containing a mixture of different sulfonated derivatives) is currently in clinical trials **[99]**. Eu was chosen due to its ability to form coordination with one or more Pc macrocycles which can afford multinuclear MPc compounds **[127]**.

The Pcs synthesised in this research work were chosen based on the following research focus:

i. The photophysicochemical properties of asymmetrical compound **2a** will be compared with their symmetrical analogue (**6**).
ii. The effects of central metal on the photophysicochemical properties of compounds **4** (Zn) and **5** (Al); **6** (Zn) and **8** (In) will be studied.

iii. The effects of point of substitution on the photophysicochemical properties of compounds **3** and **4** will be evaluated (peripheral vs non–peripheral.

iv. The effects of nature of substituents will be evaluated on the photophysicochemical properties of compounds **4** and **6** as well as **7** and **9**.

v. The comparative effects of oxo bridge spacing between COOH and MPc macrocycle of compounds **2a**, **2b** and **10** on the photophysicochemical properties and PDT activity will be evaluated.

vi. The NLO properties of symmetrical and asymmetrical compounds **1**, **11**, **12**, **13** and **14** will be evaluated.

Table 1.4: Synthesised Pcs for photophysicochemical properties and PDT or NLO applications

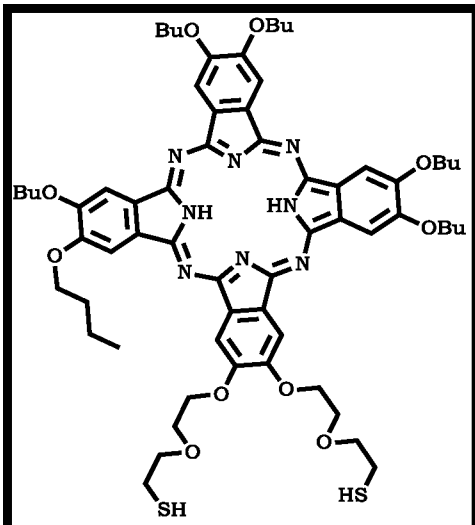 Pc **1** **NLO**	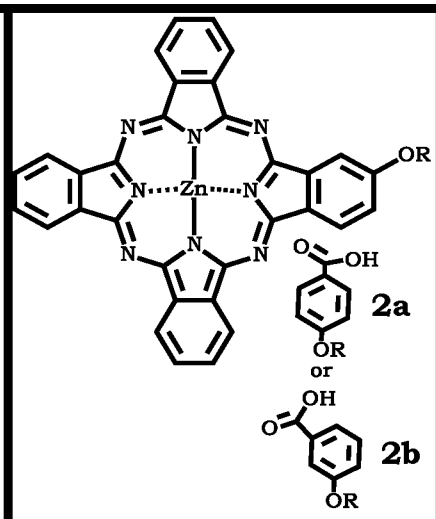 **2a** or **2b** **[182] Photophysicochemical, *In vitro* PDT**	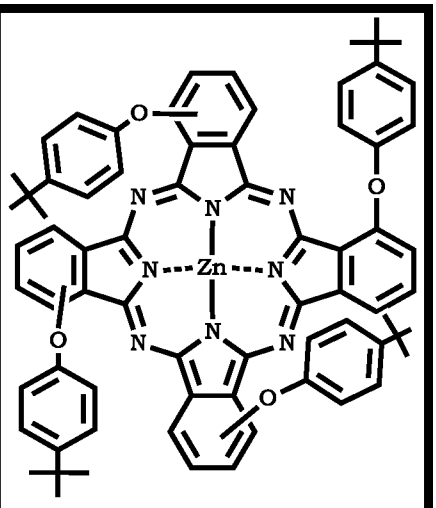 **3 [183] Photophysicochemical**
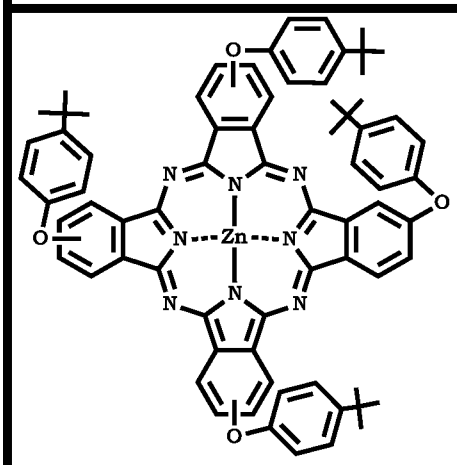 **4 [184] Photophysicochemical**	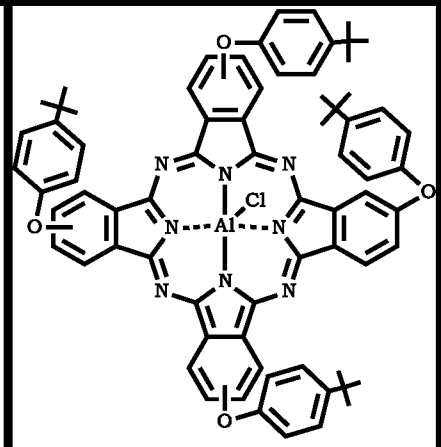 **5 Photophysicochemical**	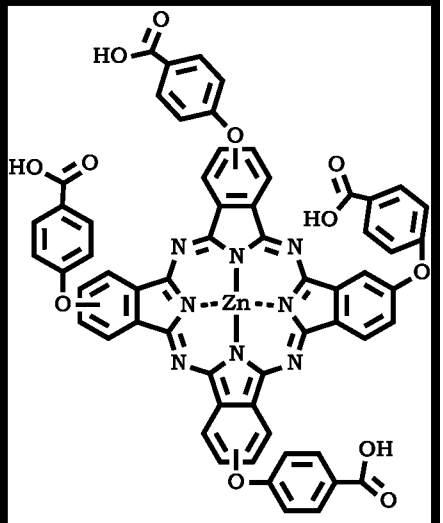 **6 [182] Photophysicochemical, *In vitro* Cytotoxicity**

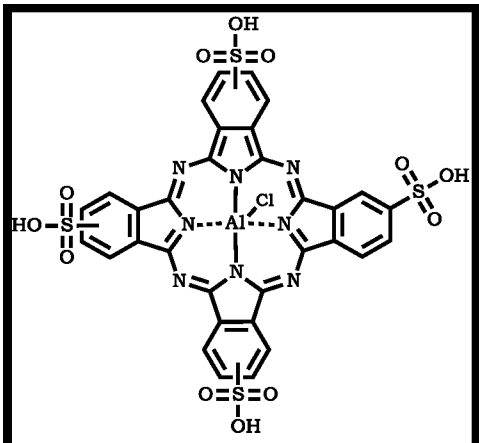

7 [185]
Photophysicochemical

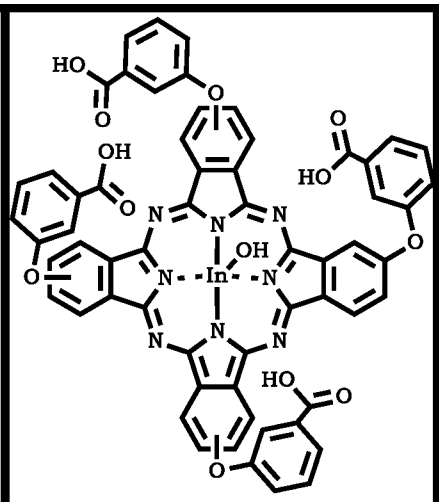

8
Photophysicochemical

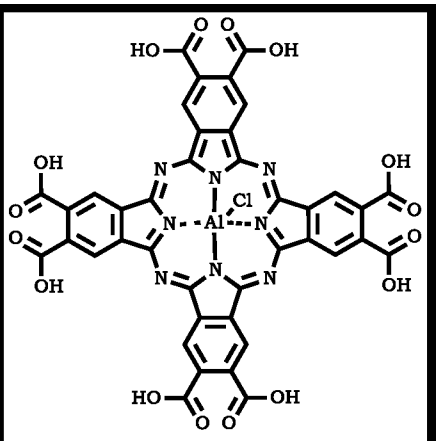

9 [185]
Photophysicochemical, *In vitro* Cytotoxicity

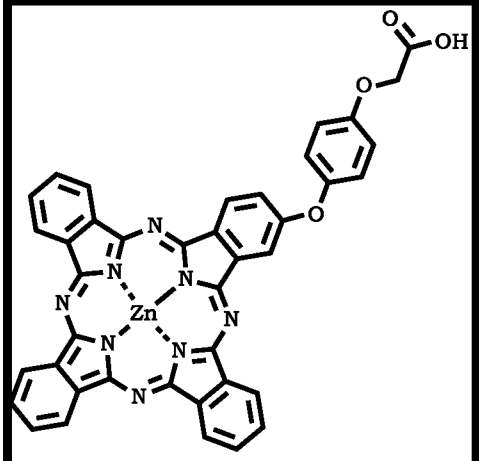

10
Photophysicochemical, *In vitro* PDT

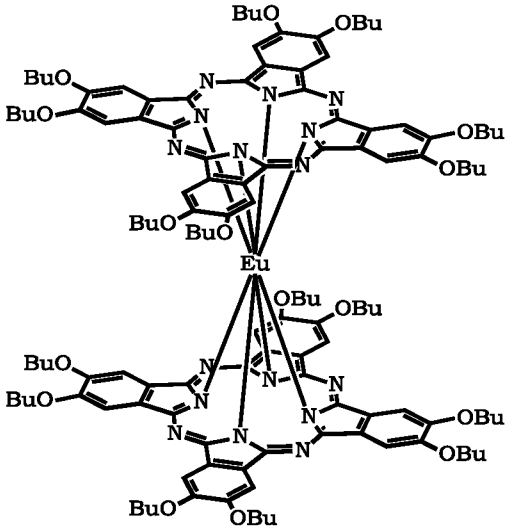

11 (NLO)

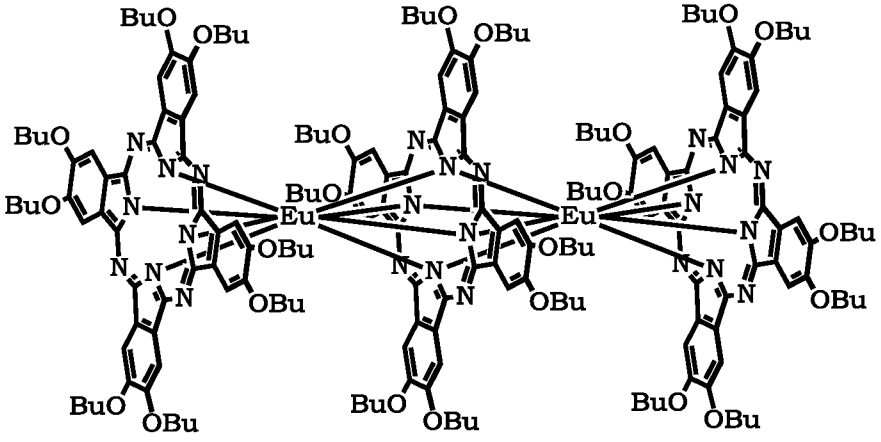

12 (NLO)

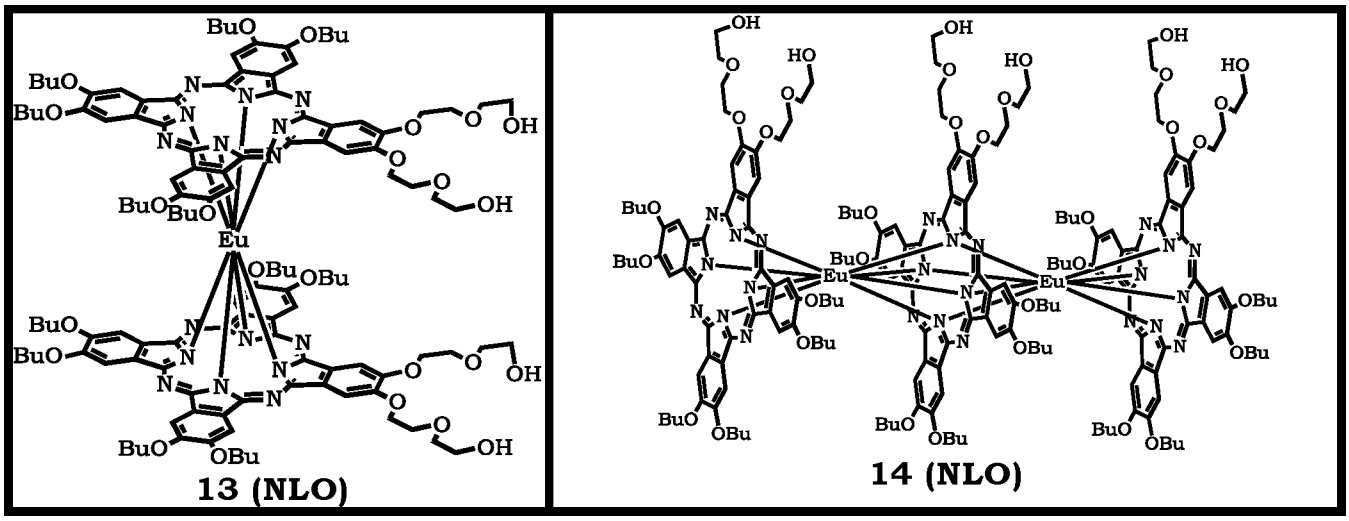

Table 1.5 shows the Pcs and their conjugates with NPs, chitosan, and HSA as well as their mode of coordination and studies performed on them in this work. The GSH, MSA and TOPO capped QDs were studied alone and in the presence of Pcs while the TGA capped ones were studied alone without Pcs.

Table 1.5: Synthesised Pcs and conjugates with NPs, chitosan, HSA for photophysicochemical properties and PDT or NLO applications

Pcs	Nanoparticles	Bond Formed	Applications
1	**CdSe–TOPO**	S–Metal	NLO
2a	**(CdTe, CdTe/CdS, CdTe/CdS/ZnS)–GSH**	Amide	Photophysicochemical
2b	**SiNPs–APTES**	Amide	Photophysicochemical, and *In vitro* cytotoxicity
2b	**ZnO/SiNPs–APTES**	Amide	Photophysicochemical, and *In vitro* PDT
3	**Uncapped SiNPs**	Doped	Photophysicochemical
4	**Uncapped SiNPs**	Doped	Photophysicochemical
5	**Uncapped SiNPs**	Doped	Photophysicochemical
6	**Uncapped SiNPs**	Doped	Photophysicochemical
6	**(CdTe, CdTeSe, CdTe/ZnO, CdTeSe/ZnO, CdTe/CdS, CdTe/CdS/ZnS)–GSH**	Amide	Photophysicochemical, and *In vitro* cytotoxicity
7	**CdTe/CdS/ZnS–GSH**	Sulfonamide	Photophysicochemical
8	**(CdTe, CdTe/ZnSe, CdTe/ZnSe/ZnO)–GSH**	Amide	Photophysicochemical
9	**(CdTe, CdTe/ZnS, CdTe/ZnS/ZnO)–GSH**	Amide	Photophysicochemical, and *In vitro* cytotoxicity
10	**AgNPs–Cyst**	Amide	Photophysicochemical, and *In vitro* PDT
10	**AgAuNPs–Cyst**	Amide	
11	**CdSeTe/CdTeS/ZnSeS –TOPO**	Mixture	NLO
12	**CdSeTe/CdTeS/ZnSeS –TOPO**	Mixture	NLO
13	**CdSeTe/CdTeS/ZnSeS –MSA**	Ester	NLO

14	**CdSeTe/CdTeS/ZnSeS –MSA**	Ester	NLO
	MPcs–other components		
2b	**HSA**	Amide	Photophysicochemical and *In vitro* PDT
2b	**Chitosan**		

1.3 NONLINEAR OPTICS (NLO)

Nonlinear optical (NLO) materials are important in protecting light sensitive materials from intense laser beams **[186–188]**. NLO materials are required to have important properties such as large nonlinear absorption (NLA) coefficient, fast response time and efficient optical limiting (OL) power **[188,189]**. OL is governed by a number of mechanisms **[190–192]** which include: NLA, nonlinear refraction and nonlinear scattering. OL for Pcs occurs via nonlinear absorption at 532 nm laser irradiation. The observed NLA mechanism could be attributed to the population of the excited states through multi–photon absorption resulting in reverse saturable absorption (RSA) **[193–196]**. Among the π-conjugated organic molecules that have been exploited for NLO application, Pcs have proven to be superior NLO absorbers due to their good thermal and chemical stability, ease of structural modification and synthesis **[197,198]**. The presence of the extensive π-electron conjugated system plays an indispensable role in the optical nonlinearities of Pcs. Furthermore, it has been suggested that the enhanced optical nonlinearities often depicted by lanthanide multinuclear Pcs ($LnPc_2$ or

Ln_2Pc_3) could be attributed to their highly expanded π-electron conjugated systems and heavy lanthanide central metals **[116,150,197–199]** which foster high population of the excited triplet state. Thus, multinuclear Pcs containing central metals such as La, Sm, Gd, Cd and Eu have been investigated for their NLO properties **[116,200–206]**.

QDs are also known to possess considerable NLO properties **[12]**. Despite the synergistic properties that can be exploited when the two are in dyad form (QDs and multinuclear MPcs), little or scanty studies have been done on them when the two are covalently linked or mixed. OL materials display a decreasing transmittance as a function of the incidence fluence as shown in **Figure 1.9**.

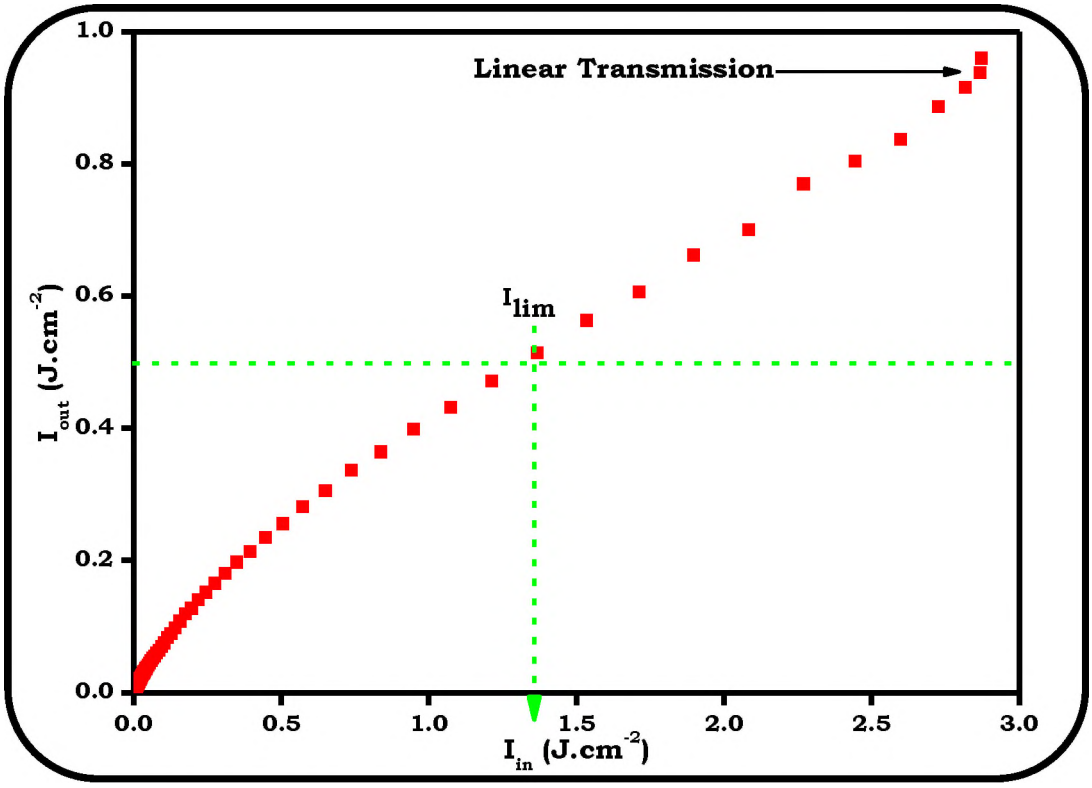

Figure 1.9: Typical input fluence versus output fluence [unpublished work]

At low incidence fluence, the material has a linear transmittance while at some critical fluence or threshold, the transmittance changes abruptly and leads to clamping of the output fluence at a constant value that would presumably be less than the amount required to damage the optical element **[193]**. This critical point is referred to as the threshold limit intensity or fluence, (I_{lim}) **[193]** as shown in **Figure 1.9**. The lower the I_{lim} values the better the material as an optical limiter.

In this study, open aperture Z–scan technique was employed to show the strength of the nonlinear absorption **[193]**. A sample is allowed to pass through from one point to the other along the path (*Z*) of a focused Gaussian beam and the transmittance is measured as a function of the sample's position relative to the focus, **Figure 1.10**.

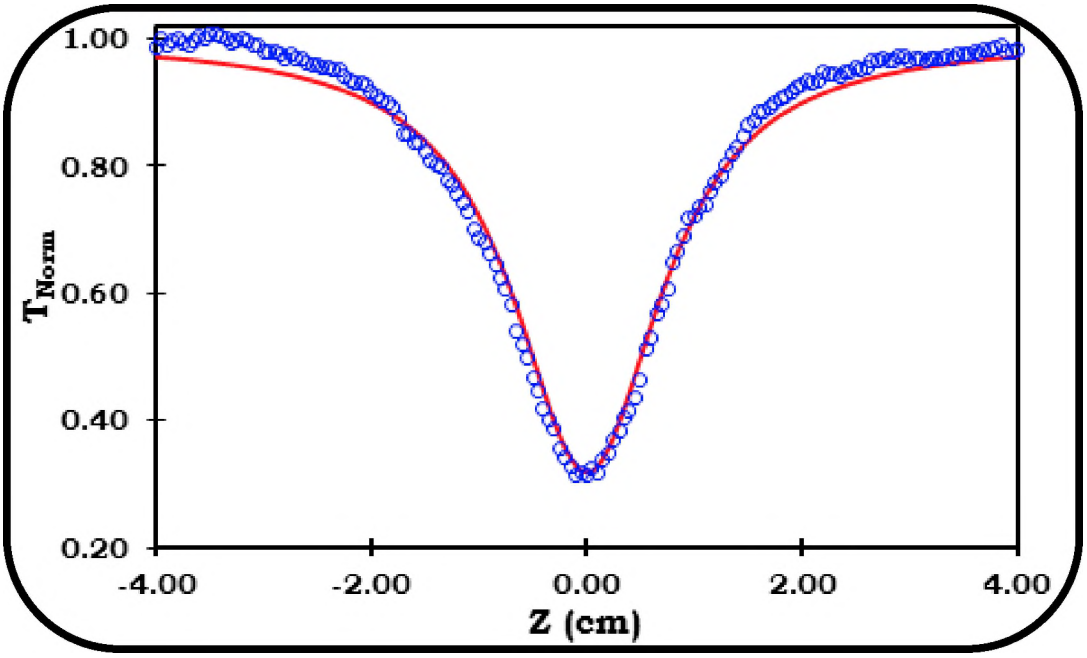

Figure 1.10: Typical open aperture Z-scan curves. Red curve fitting shows the theoretical fit, and the blue curve shows the experimental data [unpublished work].

For open aperture Z–scan, the nonlinear optical activity data may be fitted to equation 1.1 **[193]**:

$$T_{Norm}(z) = \frac{1}{[1 + \beta_{eff} L_{eff} (\frac{I_0}{1 + (\frac{z}{z_0})^2})]} \quad \textbf{(1.1)}$$

where β_{eff} and I_0 are the effective intensity dependent nonlinear absorption coefficient and the intensity of the beam at focus respectively. z and z_0 are sample positions with respect to the input intensity and Rayleigh length (defined by $\frac{\pi w_0^2}{\lambda}$; λ = wavelength of the laser beam and ω_0 = beam waist at the focus (z = 0)), respectively. L_{eff} is the effective thickness of the sample and is given by equation 1.2:

$$L_{eff} = \frac{1 - e^{-\alpha L}}{\alpha} \quad \textbf{(1.2)}$$

where α is the linear absorption coefficient and L is the thickness of the sample.

The imaginary component of the third order optical susceptibility (Im[$\chi^{(3)}$] in esu) is directly proportional to β_{eff} via equation 1.3 **[191]**:

$$\mathrm{Im}[\chi^{(3)}] = \frac{(n^2 \varepsilon_0 c \lambda \beta_{eff})}{(2\pi)} \quad \textbf{(1.3)}$$

In equation 1.3, c and n are the speed of light in vacuum and the linear refractive index respectively. ε_0 is the permittivity of free space and λ is the wavelength of the laser light.

By definition, limiting intensity (I_{lim}/J.cm^{-2}) is the input fluence at which the output fluence is 50% of the linear transmission, **Figure 1.9** **[193,207,208]**. As shown in **Table 1.3**, most of the Pcs used in the presence of NPs for NLO were symmetrical analogues. This work reports on asymmetrical Pcs linked to ternary alloy QDs for NLO. As previously mentioned, asymmetry is known to improve NLO behaviour of Pcs **[116]**.

1.4 PHOTODYNAMIC THERAPY (PDT)

Photodynamic therapy (PDT) is a minimally invasive cancer treatment modality which requires a suitable photosensitizer, laser light and molecular oxygen for selective destruction of cancer cells **[99,101,209–212]**.

Among the photosensitizers that have been tested for PDT, MPcs have been reported to show efficacious photosensitization and this marked phenomenon has placed them in different phases of PDT clinical trials **[99,101,213–219]**. The good photosensitization observed for MPcs could be attributed to their red to near-infrared absorption which allows for greater tissue penetration **[144,220]**. Phthalocyanines are seen as ideal photosensitizers since they often exhibit minimal dark cytotoxicity, have long triplet lifetimes, and high triplet and singlet quantum yields, depending on their central metal and ring substituents **[221]**.

The pharmacological response of PDT is often dependent on the singlet oxygen generation which could be produced via the type **I** or type **II**

mechanisms, **Scheme 1.4**. In type **I** mechanism, the excited triplet state of the MPcs react with substrates (biomolecules such as protein, lipids) leading to abstraction of hydrogen atom which initiate free radicals such as hydrogen peroxide and superoxide.

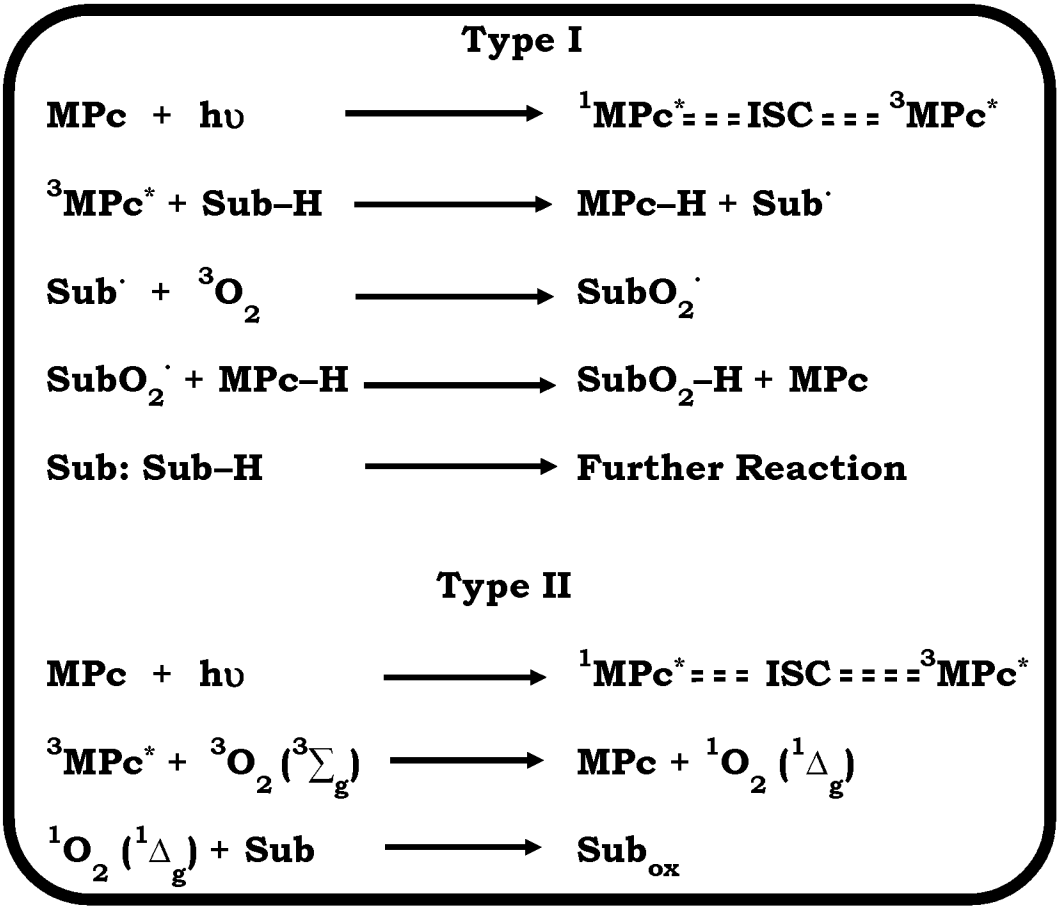

Scheme 1.4: Photoreaction mechanism of PDT. Sub = Substrate, ISC = intersystem crossing.

In the type **II** mechanism, the excited triplet state of the MPcs undergoes direct energy transfer to the ground state molecular oxygen to form singlet oxygen which is the reactive oxygen species responsible for the tumor cytocidal activity **[210]**. Despite the fascinating properties possessed by MPcs, limited selectivity and specificity remains a daunting challenge

towards their efficacy in PDT. In order to improve their selectivity and specificity, strides have been taken towards combination therapy which involves the incorporation of suitable drug–carriers like nanoparticles, HSA, and chitosan to improve their bioaccumulation and bioavailability. Some examples of MPcs that have been used for PDT clinical trials are shown in **Figure 1.11 [217,222–228]**.

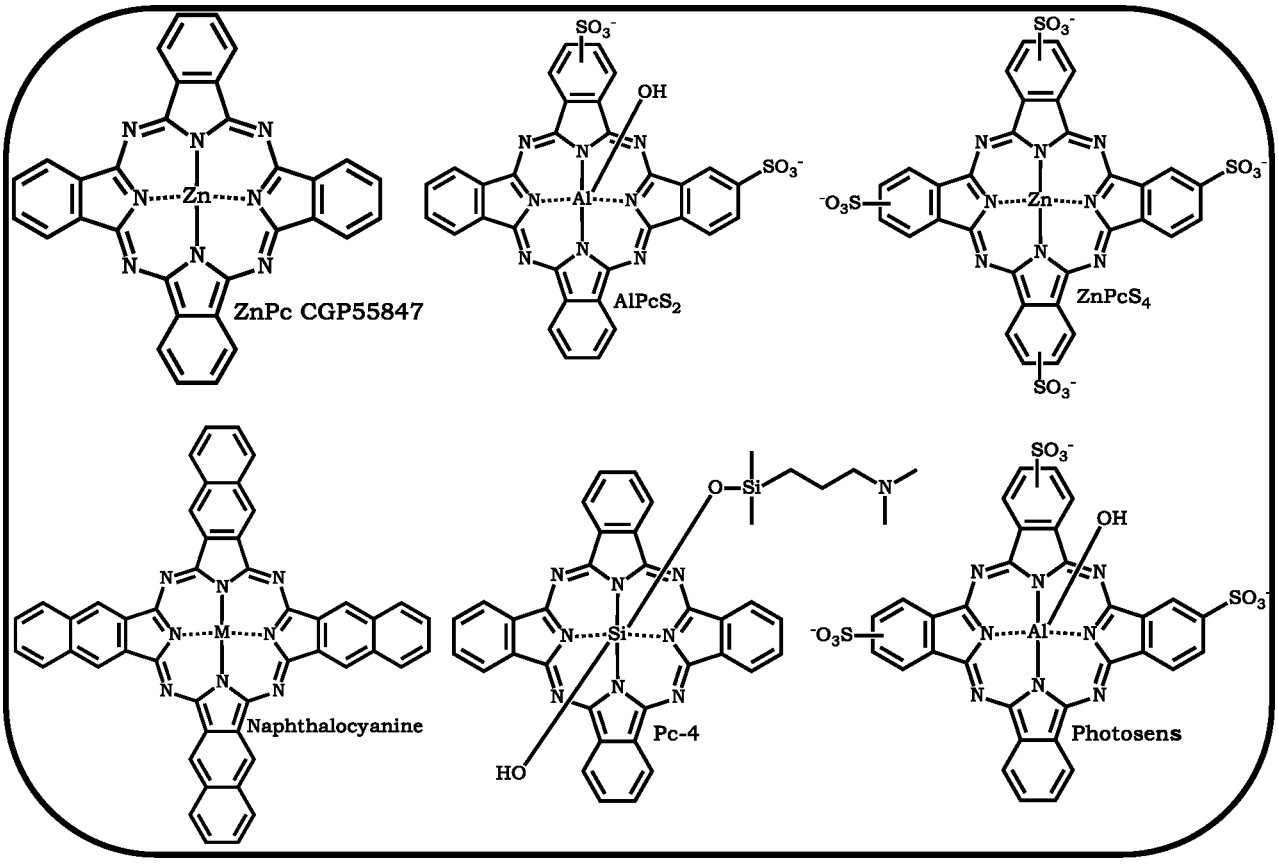

Figure 1.11: Molecular structure of some MPcs in clinical trials

1.5 PHOTOPHYSICS AND PHOTOCHEMISTRY

The Jablonski diagram, as shown in **Figure 1.12** can be used to highlight the photophysicochemical properties of MPcs which include the radiative processes such as the fluorescence (Flu), phosphorescence (Pho) and non–

radiative processes such as internal conversion (IC), vibrational relaxation (VR), intersystem crossing (ISC) and energy transfer (ET) **[229,230]**.

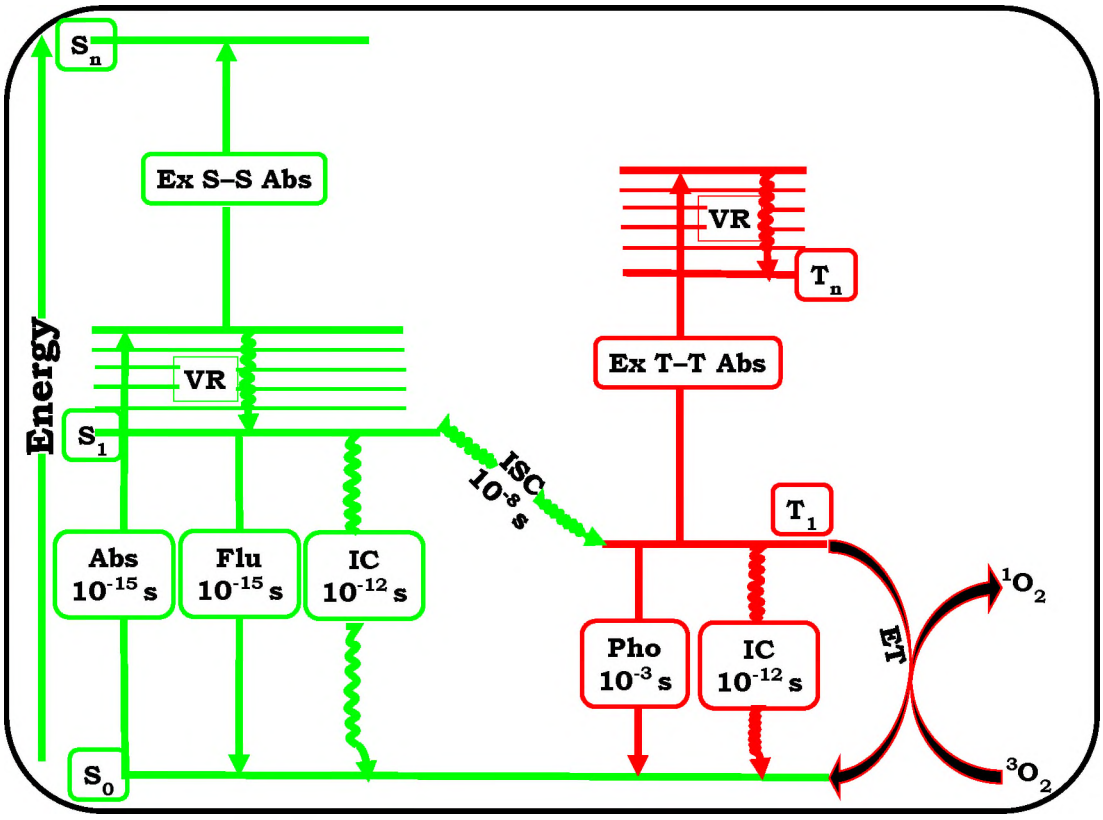

Figure 1.12: A modified Jablonski diagram illustrating the transition between the ground state singlet (S_0) and electronic excited (Ex) states (S_1 and T_1). Excited state singlet–singlet absorption (Ex S–S abs), Excited state triplet–triplet absorption (Ex T–T abs), fluorescence (Flu), phosphorescence (Pho), internal conversion (IC), vibrational relaxation (VR), intersystem crossing (ISC) and energy transfer (ET).

1.5.1 Fluorescence quantum yield (Φ_F)

Fluorescence quantum yield is the measure of the number of fluorescence photons emitted per excitation photon absorbed **[231]**. The fluorescence lifetime (τ_f) is the measure of the average time spent by the fluorophores in the excited singlet state. Several factors have been reported to influence Φ_F

of MPcs which include; the nature of solvent, pH, aggregation, temperature, nature of central metal, photo–induced energy transfer (PET) or Förster resonance energy transfer (FRET), concentration, nature of substituents and point of substitution. In this study, comparative approach was employed using equation 1.4 **[232]** for the determination of the Φ_F of Pcs or QDs and unsubstituted ZnPc was used as standard for the Pcs in DMSO (Φ_F = 0.2 **[233]**) and Rhodamine 6G for the QDs in ethanol (Φ_F = 0.94 **[231]**).

$$\Phi_F = \Phi_{F(std)} \frac{F.A_{std}.n}{F_{std}.A.n_{std}} \quad \textbf{(1.4)}$$

where $\Phi_{F(std)}$ is the fluorescence quantum yield of the standard, F and F_{StD} represent the areas under the fluorescence emission curves of the sample and standard, respectively, A and A_{std} are the absorbances of the sample and standard, respectively at the excitation wavelength, n and n_{std} are the refractive indices of the solvents used for the sample and standard, respectively. The absorbances of the MPcs and QDs were kept between ~0.05 and 0.1 to avoid self–quenching effects when emission spectra were measured **[231,234,235]**. The fluorescence quantum yields of the quantum dots in the nanoconjugates with MPcs can be calculated using equation 1.5:

$$\Phi_{F(QD)}^{Linked} = \Phi_{F(QD)} \frac{F_{QD}^{Linked}}{F_{QD}} \quad \textbf{(1.5)}$$

where $\Phi_{F(QD)}$ represents the fluorescence quantum yields of the quantum dots alone and were used as standards, F_{QD} is the fluorescence intensity of the quantum dots alone, $F_{(QD)}^{Linked}$ represents the fluorescence intensity of the quantum dots in the linked conjugates.

The fluorescence lifetime of all the MPcs, QDs and their conjugates can be determined using the time–correlated single–photon counting (TCSPC) set–up **[231,236]**.

1.5.2 Triplet quantum yield (Φ_T) and triplet lifetime

The triplet quantum yields (Φ_T) measure the fraction of absorbing MPcs that undergoes intersystem crossing (ISC) to populate the triplet state as shown in **Figure 1.12**. The lifetime of the triplet state is defined as the average time taken by MPcs in the excited triplet state (T_1). Equation 1.6 is often regarded as the triplet absorption method. The Φ_T values of the MPcs alone and in conjugates were calculated using a comparative method as reported in the literature, equation 1.6 **[237,238]**:

$$\Phi_T = \Phi_{T(std)} \frac{\Delta A_T . \varepsilon_T^{std}}{\Delta A_T^{StD} . \varepsilon_T} \qquad \textbf{(1.6)}$$

where $\Phi_{T(std)}$ is the triplet quantum yield of the unsubstituted ZnPc standard ($\Phi_{T(ZnPc)}$= 0.65 in DMSO **[237]**), ΔA_T and ΔA_T^{std} represent the changes in the triplet state absorption of the sample and standard, ε_T and ε_T^{std} denote the triplet state molar extinction coefficients of the sample and standard, respectively. ε_s and ε_s^{std} were determined from ground state molar extinction coefficient of the sample and standard, ε_T *and* ε_T^{std}

accounts for the change in the absorbance of the triplet state using Equation 1.7.

$$\varepsilon_T = \varepsilon_s \cdot \frac{\Delta A_T}{\Delta A_s} \quad \textbf{(1.7a)}$$

$$\varepsilon_T^{std} = \varepsilon_s^{std} \cdot \frac{\Delta A_T^{std}}{\Delta A_S^{std}} \quad \textbf{(1.7b)}$$

The lifetime of the transient photosensitizers may be obtained by fitting Equation 1.8 to triplet absorption data **(Figure 1.13)**, where $A(t)$ and A_o are the relative absorbances at time t = t and t = 0, respectively, K is the triplet absorption rate constant and τ_T is the excited triplet state lifetime.

$$A(t) = A_o e^{(-t/\tau_T)} + Kt \quad \textbf{(1.8)}$$

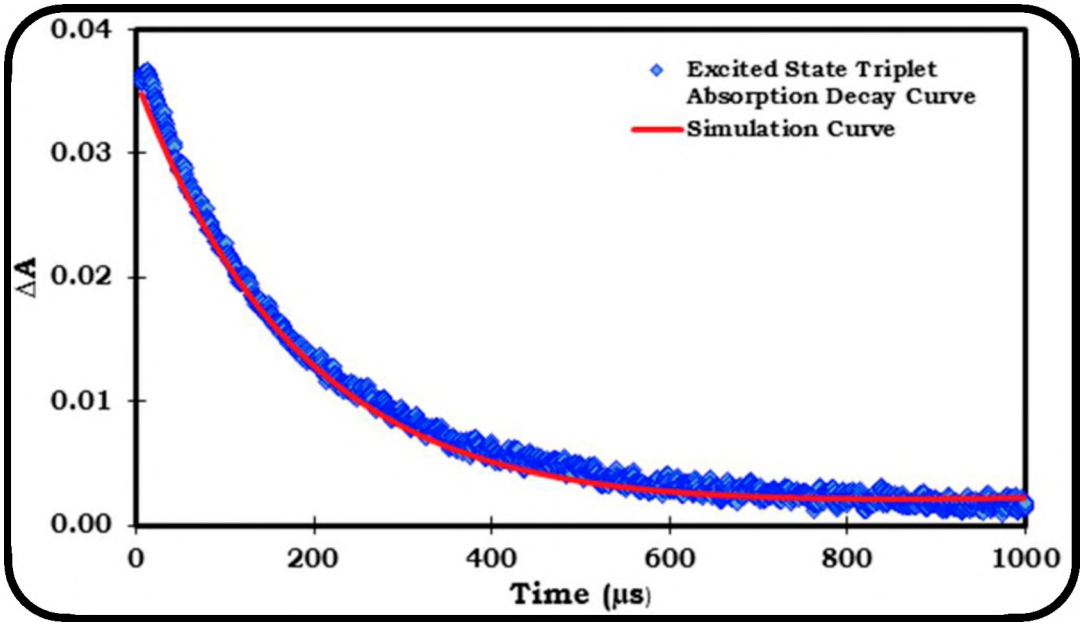

Figure 1.13: Fitted excited triplet state absorption decay curve of MPcs [unpublished work].

Alternatively, the triplet lifetime may be determined by fitting the triplet depletion absorption data obtained from the laser flash photolysis measurements to the appropriate exponential equation using OriginPro® 8 software.

It is assumed that three processes jointly deactivate the excited singlet state of MPcs which include: fluorescence, intersystem crossing and internal conversion. The quantum yields of the internal conversion (Φ_{IC}) of the MPcs and the conjugates were assessed using equation 1.9:

$$\Phi_{IC} = 1 - (\Phi_T + \Phi_F) \quad \textbf{(1.9)}$$

The intersystem crossing time (τ_{isc}) may be calculated **[182]** using equation 1.10:

$$\tau_{isc} = \frac{\tau_{avF}}{\Phi_T} \quad \textbf{(1.10)}$$

where τ_{avF} is the average excited singlet state lifetimes and Φ_T is the triplet quantum yield.

1.5.3 Singlet oxygen (Φ_Δ) and photodegradation quantum yield (Φ_{pd})

Singlet oxygen ($^1O_2$) is the chief cytotoxic species for PDT and it is usually generated by energy transfer process between excited triplet state (T_1) of MPc (^{3}MPc*) and ground state molecular oxygen ($^3O_2$) as shown in **Figure 1.12** and **Scheme 1.4**. Φ_Δ is the measure of the amount of $^1O_2$ generated per photon absorbed by the MPcs **[210,239,240]**. The Φ_Δ values of the MPcs and in conjugates can be determined using the optical or photochemical method. Both methods require a suitable singlet oxygen quencher such as 1,3-diphenylisobenzofuran (DPBF), sodium azide (NaN_3) 1,4-diazabicyclo-octane (DABCO) and tetrasodium α,α-(anthracene-9,10-diyl) dimethylmalonate (ADMA) **[241,242]**. The optical or luminescence

method involves the time–resolved phosphorescence decay of singlet oxygen at 1270 nm **[239,240]**. Sodium azide is often employed as singlet oxygen quencher for the optical method and it involves monitoring of the singlet oxygen using the dynamic course of $^1O_2$ concentration as reported in the literature **[243]** and equation 1.11 is employed **[239]**:

$$\boldsymbol{I(t) = B \cdot \frac{\tau_D}{\tau_T - \tau_D} \cdot [Exp^{-t/\tau_T} - Exp^{-t/\tau_D}]} \qquad \textbf{(1.11)}$$

where $I(t)$ is the phosphorescence signal intensity of $^1O_2$ at time t, τ_D is the lifetime of $^1O_2$, τ_T is the lifetime of MPc at triplet state, and B is a coefficient involved in sensitizer concentration and $^1O_2$ quantum yield.

The Φ_Δ values of the MPcs alone and in conjugates can then be determined using a comparative equation 1.12:

$$\Phi_\Delta = \Phi_\Delta^{std} \cdot \frac{B}{B^{std}} \qquad \textbf{(1.12)}$$

where Φ_Δ^{std} is the singlet oxygen quantum yield of unsubstituted ZnPc standard in DMSO (Φ_Δ= 0.67 **[242]**), $\boldsymbol{B}$ and $\boldsymbol{B^{std}}$ are the coefficients of the sample and standard, respectively.

Similarly, the photochemical method can also be used to quantify the Φ_Δ of the MPcs alone and in conjugates. This involves the illumination of the mixture of the samples and the singlet oxygen quencher at a fixed volume over predetermined time course. The time dependent absorption decay curve of the singlet oxygen quencher is spectroscopically monitored. The

Φ_Δ values of the MPcs alone and in the conjugates can then be calculated using equation 1.13:

$$\Phi_\Delta = \Phi_\Delta^{std} . \frac{R.I_{Abs}^{std}}{R^{std}.I_{Abs}} \quad \textbf{(1.13)}$$

where Φ_Δ^{std} is the singlet oxygen quantum yield of unsubstituted ZnPc standard in DMSO (Φ_Δ= 0.67 **[242]**), **R** and R^{std} are the singlet oxygen quenchers photo–bleaching rates in the presence of the samples, and the standard, I_{Abs} and I_{Abs}^{std} are the rates of light absorption by the samples, and standard, respectively and are defined by equation 1.14 and 1.15:

$$I_{Abs} = \frac{\propto.A.I}{N_A} \quad \textbf{(1.14)}$$

$$I_{Abs}^{std} = \frac{\propto.A.I}{N_A} \quad \textbf{(1.15)}$$

where $\alpha = 1\text{-}10^{-A(\lambda)}$, $A(\lambda)$ is the absorbance of the sensitizer at the illumination wavelength, A is the illuminated cell area (expressed in cm^2), I is the intensity of light (expressed in photons $cm^{-2}s^{-1}$) and N_A is the Avogadro's constant.

The Φ_Δ values of the MPcs are often dependent on the excited triplet state, triplet lifetime and the effectiveness of energy transfer process.

The efficiency of energy transfer between ground state molecular oxygen and excited triplet state of the MPcs or conjugates may be calculated using equation 1.16:

$$S_\Delta = \frac{\Phi_\Delta}{\Phi_T} \quad \textbf{(1.16)}$$

where $\mathbf{S_\Delta}$ is the efficiency of energy transfer, $\mathbf{\Phi_T}$ is the triplet quantum yield and Φ_Δ is the singlet quantum yield.

Photodegradation is a process that involves the oxidative decomposition of MPcs upon illumination. Phthalocyanines with low photostability usually show photodegradation quantum yield of 10^{-3} **[244]**. The main factors influencing the photodegradation rate include the nature of substituents, central metal, axial ligand attached to central metal, aggregation and temperature **[244]**. The photodegradation quantum yield (Φ_{pd}) can be determined using equation 1.17 **[244]**:

$$\Phi_{pd} = \frac{(C_0 - C_t).V}{I_{abs}.\ t} \qquad \textbf{(1.17)}$$

where C_0 and C_t in mol dm^{-3} are the concentrations of the sample before and after illumination, respectively, V is the solution volume, t is the illumination time per cycle while I_{abs} is defined above.

1.5.4 Förster Resonance Energy Transfer Parameters (FRET)

FRET is a radiationless energy transfer process which occurs between a suitable excited donor molecule (QDs) and an acceptor molecule (MPcs) in close proximity, **Figure 1.14**. Energy transfer from the donor to the acceptor molecule is often accompanied by loss or decrease in the fluorescence quantum yield and lifetime of the donor leading to enhancement in the fluorescence properties of the acceptor **[231]**. This process is often fostered by dipole–dipole interaction between donor and acceptor. The efficiency of FRET is dependent on the center to center

distance between donor and acceptor (r), the degree of spectral overlap of the donor's fluorescence emission spectrum and the acceptor's absorption spectrum (J) and the orientation of the donor and acceptor transition dipoles **[231]**.

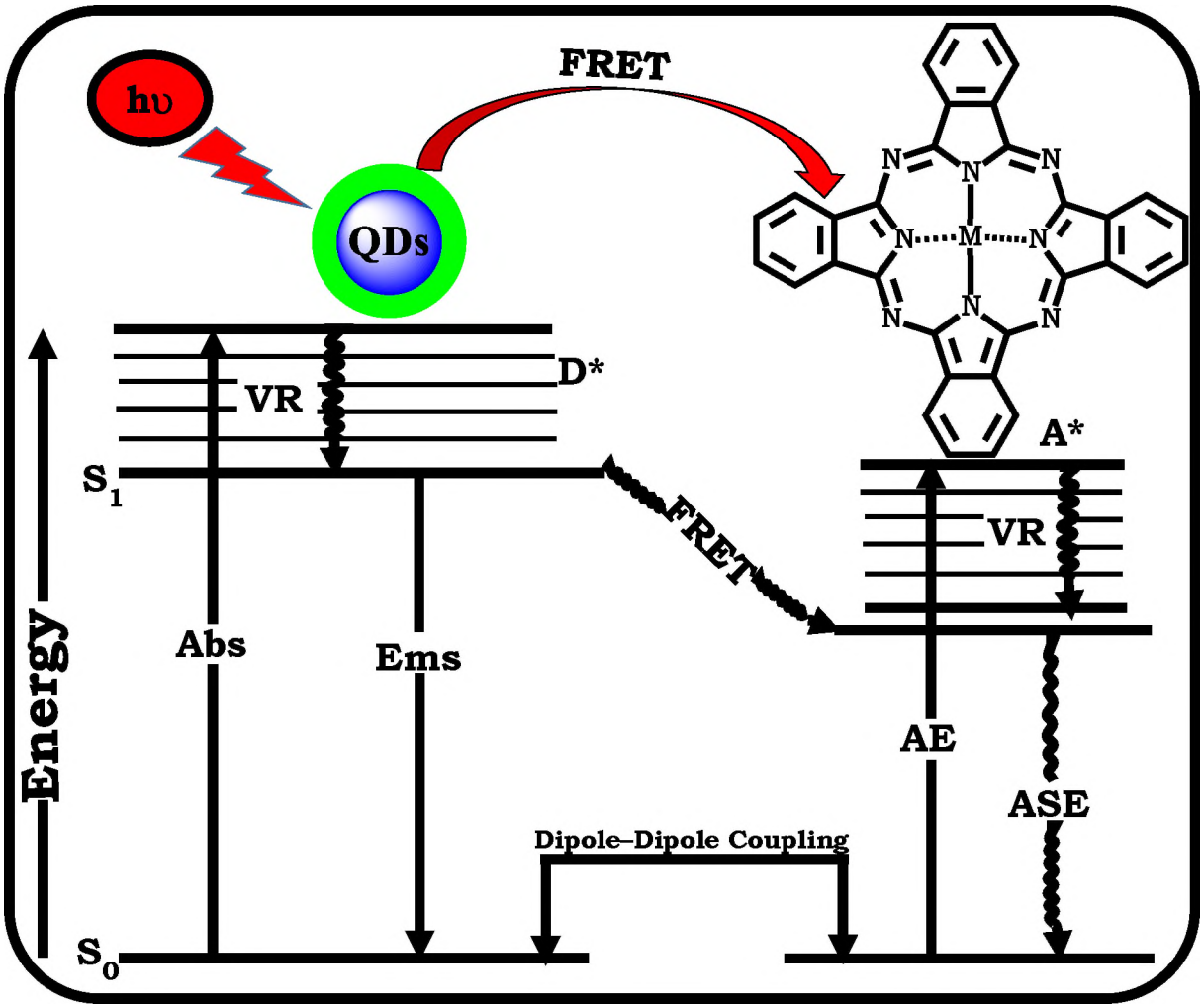

Figure 1.14: FRET diagram illustrating energy transfer from quantum dots QDs (Donor, D) to MPc (Acceptor, A): Abs = absorption, Ems = emission, AE = non radiative acceptor excitation, ASE = acceptor sensitized emission, S_0 = singlet ground state S_1 = singlet excited states, VR = vibrational relaxation.

The FRET efficiencies (*Eff.*) of the conjugates can be quantified using the photoluminescence lifetime measurements of the donor (QDs) in the

absence (τ_A) and presence (τ_P) of the acceptor (MPcs) equation 1.18 **[231, 245–247]**:

$$Eff = 1 - \frac{\tau_P}{\tau_A} \quad \textbf{(1.18)}$$

Alternatively, the fluorescence quantum yield of the donor in the presence ($\Phi_{F(QDs)}^{Conjugate}$) or absence ($\Phi_{F(QDs)}$) of the acceptor can be used to determine the value of the FRET *Eff.*, using equation 1.19.

$$Eff = 1 - \frac{\Phi_{F(QDs)}^{Conjugate}}{\Phi_{F(QDs)}} \quad \textbf{(1.19)}$$

The FRET efficiency is related to r (Å), the donor–acceptor distance according to equation 1.20 **[231,245–247]**:

$$Eff = \frac{R_0^{\,6}}{R_0^{\,6} + r^6} \quad \textbf{(1.20)}$$

where r is the center to center distance (Å) between donor and acceptor, R_0 (the Förster distance, Å) is the critical distance between the donor and the acceptor molecules at which the efficiency of energy transfer is 50%. R_0 depends on the quantum yield of the donor according to equation 1.21 **[231,245–247]**:

$$R_0^6 = 8.8 \times 10^{23} k^2 n^{-4} \Phi_{F(QDs)} J \quad \textbf{(1.21)}$$

where k is the dipole orientation factor (the value of k for the donor–acceptor pairs is assumed to be 2/3, this assumption is often made in donor–acceptor pairs in liquid media), n is the solvent's refractive index,

$\Phi_{F(QDs)}$ is the fluorescence quantum yield of the donor and $J\,(cm^6)$ is Förster overlap integral, given by equation 1.22:

$$J = \int F_{(QDs)}\,(\lambda)\varepsilon_{\mathrm{MPc}}(\lambda)\lambda^4\,\partial\lambda \qquad \textbf{(1.22)}$$

where $F_{(QDs)}$ is the normalized QDs emission spectrum. ε_{MPc} is the molar absorptivity of MPcs $(M^{-1}cm^{-1})$ and λ is the wavelength (nm) at the absorption maximum of the acceptor (Q-band). The FRET parameters were computed into the PhotochemCAD® software **[247]**.

1.6 SUMMARY OF AIMS OF THESIS

The aims of this thesis include:

1. Synthesis of functionalized nanoparticles.
2. Synthesis and characterization of symmetrical, asymmetrical, mononuclear and homoleptic multinuclear (bis and tris) phthalocyanines.
3. Covalent linkage of phthalocyanines with nanoparticles, chitosan and HSA.
4. Doping of phthalocyanines with silica nanoparticles using reverse microemulsion.
5. Comparative studies of the photophysicochemical properties of the phthalocyanine compounds and their conjugates in solution.
6. *In vitro* cytotoxicity and photodynamic therapy activities of phthalocyanines and conjugates with nanoparticles, chitosan and HSA.

7. Nonlinear optical behaviour of homoleptic multinuclear phthalocyanines and conjugates or mixture in solution.

CHAPTER TWO

EXPERIMENTAL

2.1 MATERIALS

2.1.1 General solvents

Ultra–pure water was obtained from a Milli–Q® Water System (Millipore Corp, Bedford, MA, USA). Dimethyl sulfoxide (DMSO, spectroscopy grade), 1–pentanol, thionyl chloride, deuterated (DMSO, chloroform) or chloroform, quinoline, nitrobenzene, 1–hexanol, cyclohexanol, and 25% ammonium hydroxide were obtained from Sigma Aldrich®. Absolute ethanol (EtOH), methanol (MeOH), dimethylformamide (DMF), cyclohexane, tetrahydrofuran (THF), nitric acid, hexane, sulfuric acid, n–hexane, n–octanol, ethyl acetate, acetone, diethyl ether and petroleum ether were obtained from SAARCHEM®. Dichloromethane (DCM) was purchased from BM® scientific.

2.1.2 Chemicals and reagents for nanoparticles (NPs) syntheses

Selenium grey powder (Riedel–de–Haen®), zinc acetate dihydrate, glutathione, thioglycolic acid, sodium borohydride, tellurium granules, cadmium chloride, cadmium oxide, Triton X 100, tetraethyl orthosilicate (TEOS), gold(III) chloride trihydrate, cysteamine (Cyst), silver acetate, (3–aminopropyl)–triethoxysilane (APTES), diphenyl ether (DPE), zinc metal powder, sulfur (S), sodium hydroxide, potassium hydroxide pellets, triocylphosphine oxide (TOPO), oleylamine (OLM), oleic acid (OA), 1–octadecene (ODE) and mercaptosuccinic acid (MSA) were obtained from Sigma Aldrich®. The synthesis of the following NPs have been reported

elsewhere **[39,43,46,52,53,87,88]**: SiNPs–APTES **[87,88]**, ZnO/SiNPs–APTES **[64]**, CdTe–TGA/GSH **[39]**, CdSe–TOPO **[43]**, CdTeSe–TGA **[52]**, CdTe/ZnS–TGA/GSH **[53]**, CdSe/ZnS–TGA **[43]**, CdTe/ZnSe–GSH **[53]**, CdTe/CdS/ZnS **[46]**.

2.1.3 Chemicals for phthalonitrile precursors, phthalocyanines syntheses and conjugation to NPs, chitosan and HSA

Zinc acetate dihydrate, europium(III) acetate tetrahydrate, *tert*–butyl phenol, 3,4–dihydro–2H–pyran, thiourea, triphenyphospine (PPh_3), trifluoroacetic acid (CF_3COOH), iodine, imidazole, *N,N'*-dicyclohexylcarbodiimide (DCC), *N'N'*–dimethylpyridin–4–amine (DMAP), (4–hydroxyphenoxy)acetic acid, 1,8–diazabicyclo[5.4.0]undec–7–ene (DBU), 1,2–dicyanobenzene (DCB), silica gel, neutral alumina, indium(III) chloride, aluminium(III) chloride, 3–hydroxyl benzoic acid, 4–hydroxyl benzoic acid, catechol, n–bromosuccinimide (NBS), chitosan, human serum albumin (HSA), zinc cyanide, 1–ethyl–3–(3–dimethylaminoproplyl) carbodiimide hydrochloride (EDC), 9,10–N–hydroxysuccinimide (NHS), potassium carbonate, sodium sulfite ($NaSO_3$), toluene sulfonic acid (TSoH), 2–(2–chloroethoxy)ethanol, urea, phthalimide, benzene–1,2,4–tricarboxylic anhydride, ammonium molybdate, ammonium chloride and chitosan were obtained from Sigma Aldrich®. The synthesis of the following phthalonitriles were done as reported in the literatures **[182,248]**: 4–(3'–carboxyphenoxy) phthalonitrile **[182]**, 4–nitrophthalonitrile **[248]**, 3–(4'–

tert–butylphenoxy) phthalonitrile **[248]**, and 4–(4'–*tert*–butylphenoxy) phthalonitrile **[248]**.

2.1.4 Chemicals and reagents for photophysicochemical studies

Aluminium sulfonated phthalocyanine (AlPcSmix) was synthesised as reported in the literature **[249]**, sodium azide, unsubstituted zinc phthalocyanine (ZnPc), rhodamine 6G, 1,3-diphenylisobenzofuran (DPBF), and anthracene–9,10–bis–methylmalonate (ADMA) were obtained from Sigma Aldrich®.

2.1.5 Chemicals and reagents for cell studies

Cultures of human breast adenocarcinoma cells (MCF–7 cells) were obtained from Cellonex®. Dulbecco's phosphate–buffered saline (DPBS), trypan blue, Dulbecco's modified Eagle's medium (DMEM), 10% (v/v) heat–inactivated fetal calf serum (FCS), 100 unit/mL penicillin-100 µg/mL streptomycin–amphotericin B were obtained from Lonza® (Biowest®). Milliwell® plates and WST–1 cell proliferation neutral red reagent were obtained from Roche®.

2.2 INSTRUMENTATION

1. Ground state electronic absorption spectra were recorded on a Shimadzu® UV–2550 spectrometer or Perkin–Elmer® UV/Vis/NIR spectrometer at the range of 250 nm to 2500 nm.

2. FT–IR spectra were acquired on a Bruker® ALPHA FT–IR or Perkin Elmer® spectrometer with universal attenuated total reflectance (ATR) sampling accessory.
3. Mass spectra data of Pcs were acquired on a Bruker® AutoFLEX III Smartbeam TOF/TOF mass spectrometer operated in positive ion mode using alphacyano benzoic acid matrix with 354 nm nitrogen laser as ionizing source.
4. Proton nuclear magnetic resonance (^{1}H NMR) spectra of Pcs were recorded on a Bruker® AMX 400 MHz or AMX 600 MHz.
5. The morphologies of the NPs and their conjugates with Pcs were recorded on a ZEISS® LIBRA model 120 transmission electron microscope (TEM) operated at 90 kV.
6. The elemental compositions of the NPs and their conjugates with Pcs were qualitatively measured on a INCA® PENTA FET coupled with VAGA TESCAM® energy dispersive x-ray (EDX) spectrometer operated at 20 kV.
7. The elemental composition data of Pcs (carbon, hydrogen, nitrogen, sulfur) were acquired on a Vario-Elementar® Microcube ELIII Series elemental analyser (CHNS).
8. X–ray diffraction patterns were recorded on a Bruker® D8 Discover X-ray powder diffractometer (XRD) equipped with a LynxEye® detector (proportional counter), using Cu Kα radiation (l = 1.5405 A°, nickel

filter). XRD data were obtained at a scanning rate of 1° min^{-1} with a filter time–constant of 2.5 s per step and a slit width of 6.0 mm. Samples were placed on a zero background silicon wafer slide. The XRD data were processed using EVA® (evaluation curve fitting) software. Baseline corrections were performed on each diffraction patterns.

9. A Metrohm Swiss® 827 pH meter was used for pH measurements.

10. Fluorescence excitation and emission spectra were measured on a Varian Eclipse® spectrofluorometer using 360 nm to 1100 nm filter. Excitation spectra were recorded at the wavelength of the emission maxima.

11. Fluorescence lifetimes were measured on a FluoTime 300, Picoquant® GmbH time correlated single photon counting setup (TCSPC) with a diode laser (LDH–P–485 and LDH–P–670, Picoquant® GmbH, 20 MHz repetition rate, 44 ps pulse width). LDH–P–485 was used for the QDs and LDH–P–670 was used for the Pcs. Fluorescence was detected under the magic angle with a peltier cooled photomultiplier tube (PMT) (PMA-C 192–N–M, Picoquant®) and integrated electronics (PicoHarp® 300E, Picoquant® GmbH). A monochromator with a spectral width of about 8 nm was used to select the required emission wavelength. The response function of the system, which was measured with a scattering Ludox solution (DuPont®), had a full width at half-maximum (FWHM) of about 300 ps. The ratio of stop to start pulses was kept low (~0.05) to ensure

good statistics. All luminescence decay curves were measured at the wavelength of emission maxima. The data were analysed with the FluoFit software (Picoquant®). The support plane approach was used to estimate the errors of the decay times **[231]**. The layout of the TCSPC is shown in **Figure 2.1**.

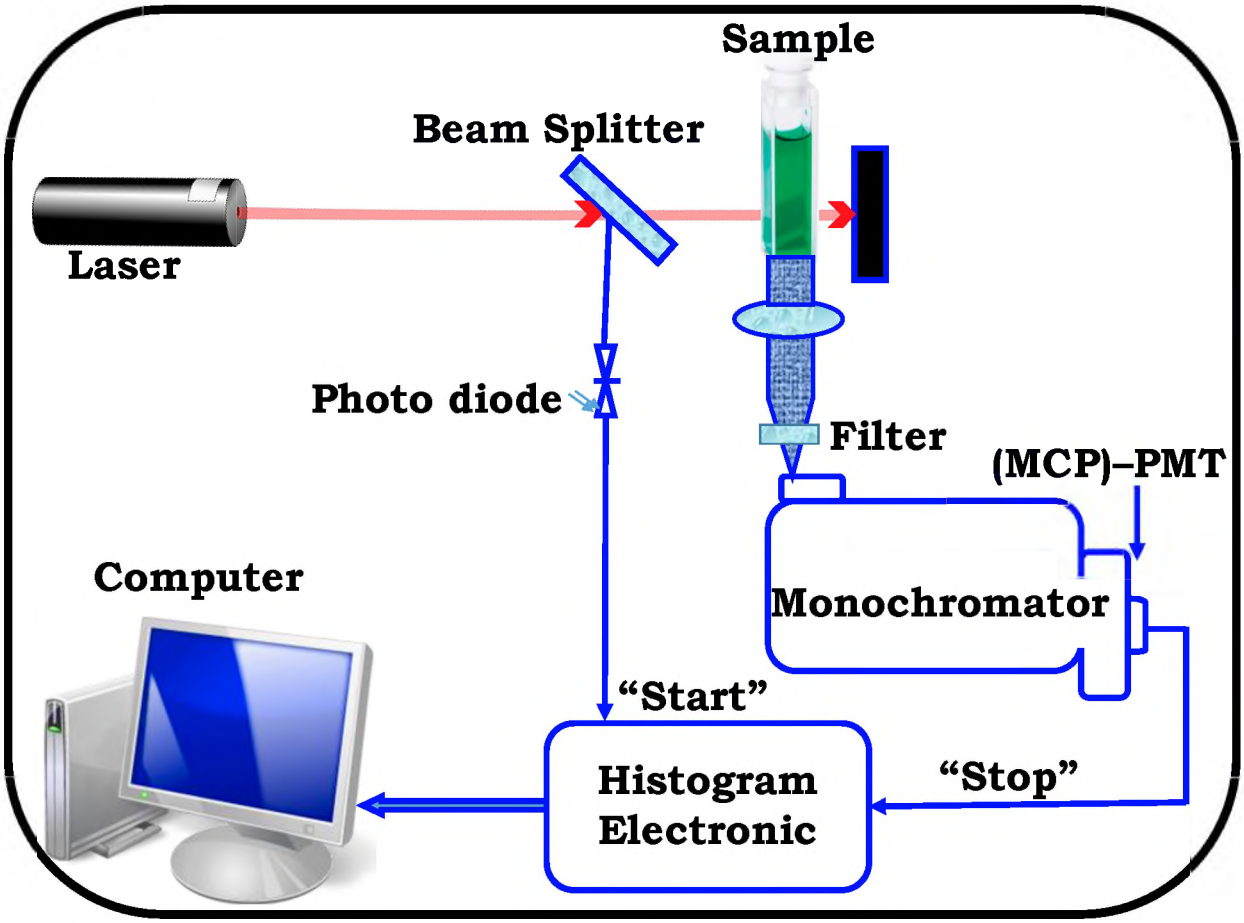

Figure 2.1: Schematic representation of time correlated single photon counting (TCSPC) set–up. (MCP)–PMT = Monochromator Photomultiplier Tube.

12. Triplet quantum yields data of the Pcs and conjugates were acquired using a laser flash photolysis system. The excitation pulses were produced using a tunable laser system consisting of an Nd:YAG laser

(355 nm, 135 mJ/4–6 ns) pumping an optical parametric oscillator (OPO, 30 mJ/3–5 ns) with a wavelength range of 420–2300 nm (NT–342B, Ekspla®) as described elsewhere **[250]**. The detailed procedure of the flash photolysis experiment is as follows: The absorbance of sample solution and the standard were ~1.5 at Q–band. The solution was introduced into a 1 cm path length UV–Visible spectrophotometric cell and deaerated using argon for 15 min. Thereafter the solution was sealed and illuminated using an appropriate excitation wavelength source (the crossover wavelength of the sample and the standard is utilized as the laser excitation source wavelength). The maximum triplet absorption detection wavelength was determined from the transient curve. The triplet lifetimes were determined by exponential fitting of the kinetic curves using OriginPro® 8 software. The laser flash photolysis set–up is shown in **Figure 2.2**.

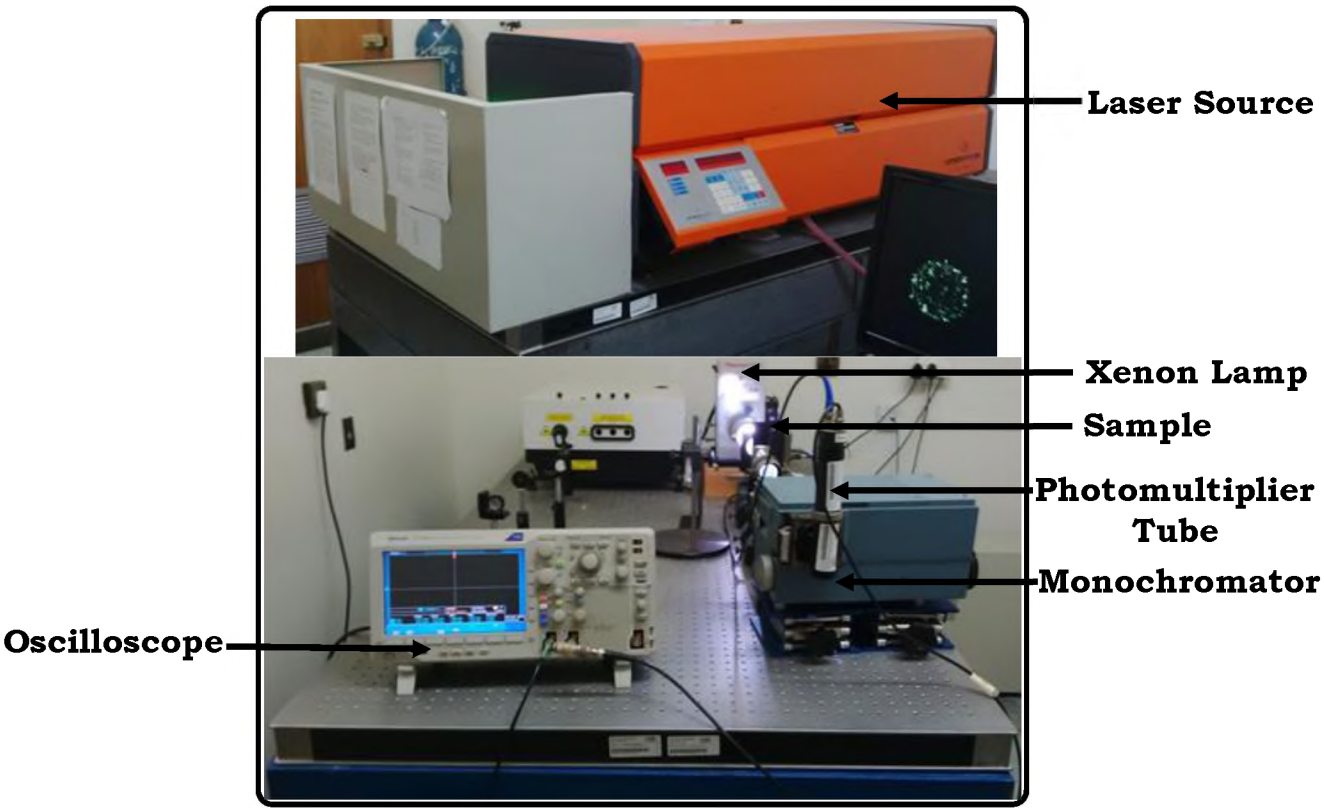

Figure 2.2: Laser flash photolysis set–up.

13. The X-ray photoelectron spectroscopy (XPS) data were obtained using a Kratos® Axis Ultra DLD, with an Al (monochromatic) anode, equipped with charge neutralizer and the operating pressure was kept below 5 $x10^{-9}$ torr. The resolution was 10 eV pass energy in the slot mode. For the XPS wide scan, the following parameters were used: emission current was kept at 12.5 mA and the anode (HT) voltage at 15 kV. The resolution was maintained at 160 eV pass energy using a hybrid lens in the slot mode. For the high resolution scans, the resolution was changed to 40 eV pass energy in the slot mode.

14. Illuminations for photodegradation (Φ_{Pd}), singlet oxygen quantum yields (Φ_{Δ}), and some cell studies were performed using a general electric quartz lamp (300 W). A 600 nm (± 3 nm) cut-off glass filter (Schott®) for ultra violet radiation and a water filter for infrared radiation. An interference filter, 700 nm with a band of 40 nm was additionally employed before the sample chamber. Light intensities were measured with a POWER MAX 5100 (Molelectron® detector incorporated) power meter and were found to be 4.3×10^{15} photons cm^{-2} s^{-1} for Φ_{Pd}, Φ_{Δ}, and cell studies. The layout of the photochemical set–up is shown in **Figure 2.3**.

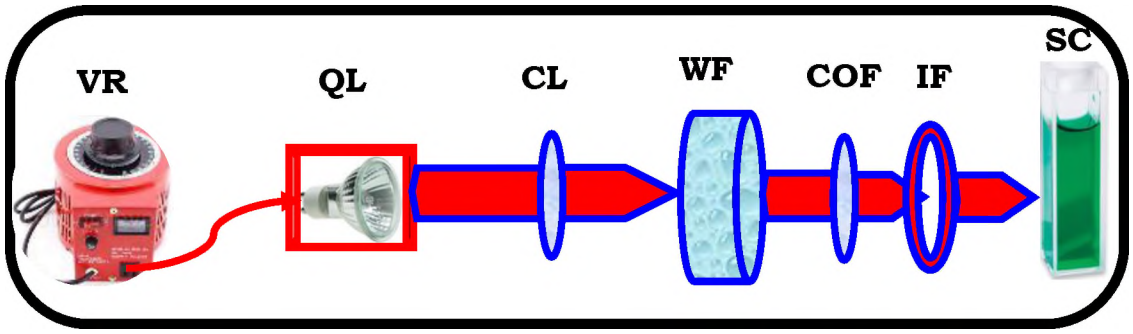

Figure 2.3: Schematic illustration of photochemical set–up. VR = Voltage regulator, QL = Quartz lamp, CL = Collimating lens, WF = Water filter, COF = Cut–off filter, IF = Interference filter, SC = Sample cell.

15. The nonlinear optical data of the Pcs and their conjugates with QDs were acquired on Z-scan equipment made at University of Stellenbosch, South Africa. The open aperture Z-scan measurements in this research work were done using a frequency-doubled Nd:YAG laser (Quanta-Ray, 1.5 J/10 ns fwhm pulse duration) as the excitation source. The laser was operated in a near Gaussian transverse mode at 532 nm (second

harmonic), with a pulse repetition rate of 10 Hz and energy range of 0.1 µJ to 0.1 mJ, limited by the energy detectors (Coherent J5–09). The low repetition rate of the laser prevents cumulative thermal nonlinearities. The beam was spatially filtered to remove the higher order modes and tightly focused with a 15 cm focal length lens. The Z–scan system size (l × w × h) was 600 mm × 300 mm × 350 mm (excluding the computer, energy meter, translation stage driver and laser system). The liquid samples were placed in a quartz cuvette (internal dimensions: 2 mm × 10 mm × 55 mm, 0.7 mL) and a path length of 2 mm (Starna® 21–G–2) **[169]**. The layout of the Z–scan is shown in **Figure 2.4**.

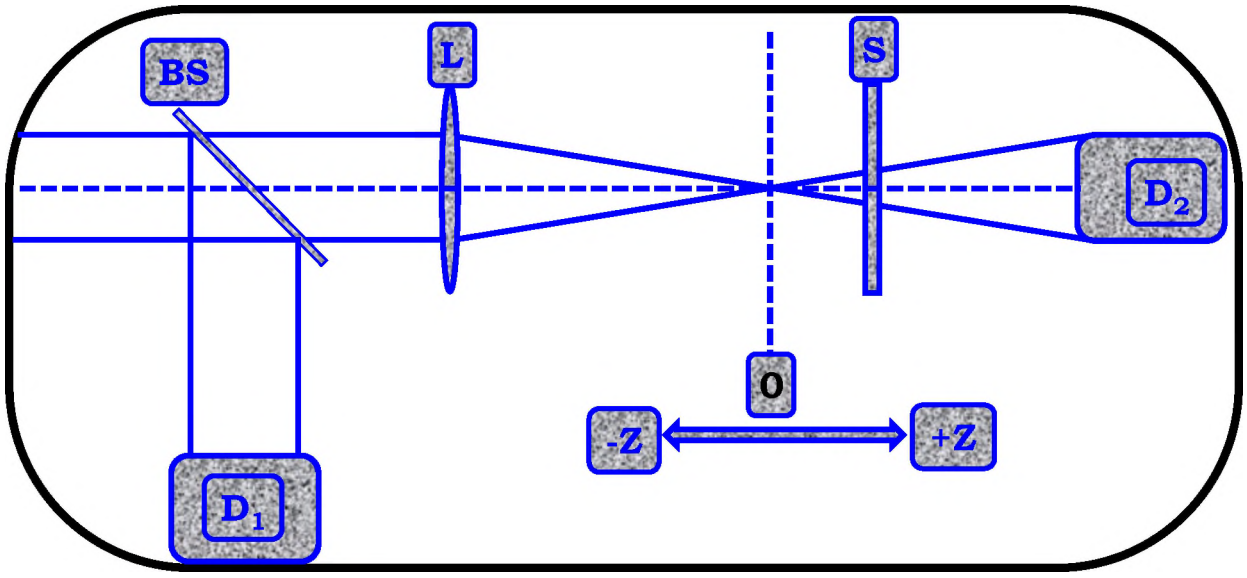

Figure 2.4: Schematic illustration of open aperture Z–scan set–up. BS = Beam splitter, L = Lens, D1 and D2 = Photodetectors, S = Sample.

16. Illumination for PDT studies of Pcs and conjugates were performed using a Modulight® Medical Laser system (ML) 7710–680 channel Turnkey laser system coupled with 2 X 3W channels at 680 nm,

cylindrical output channels, aiming beam, integrated calibration module, foot/hand switch pedal, fibre sensors (subminiature version A) connectors and safety interlocks. Illumination kit for *in vitro* PDT studies with capacity to hold 127.76 x 85.48 mm 96 well tissue culture plate. The photo of 96–well tissue culture plates and Modulight medical laser system is shown in **Figure 2.5**.

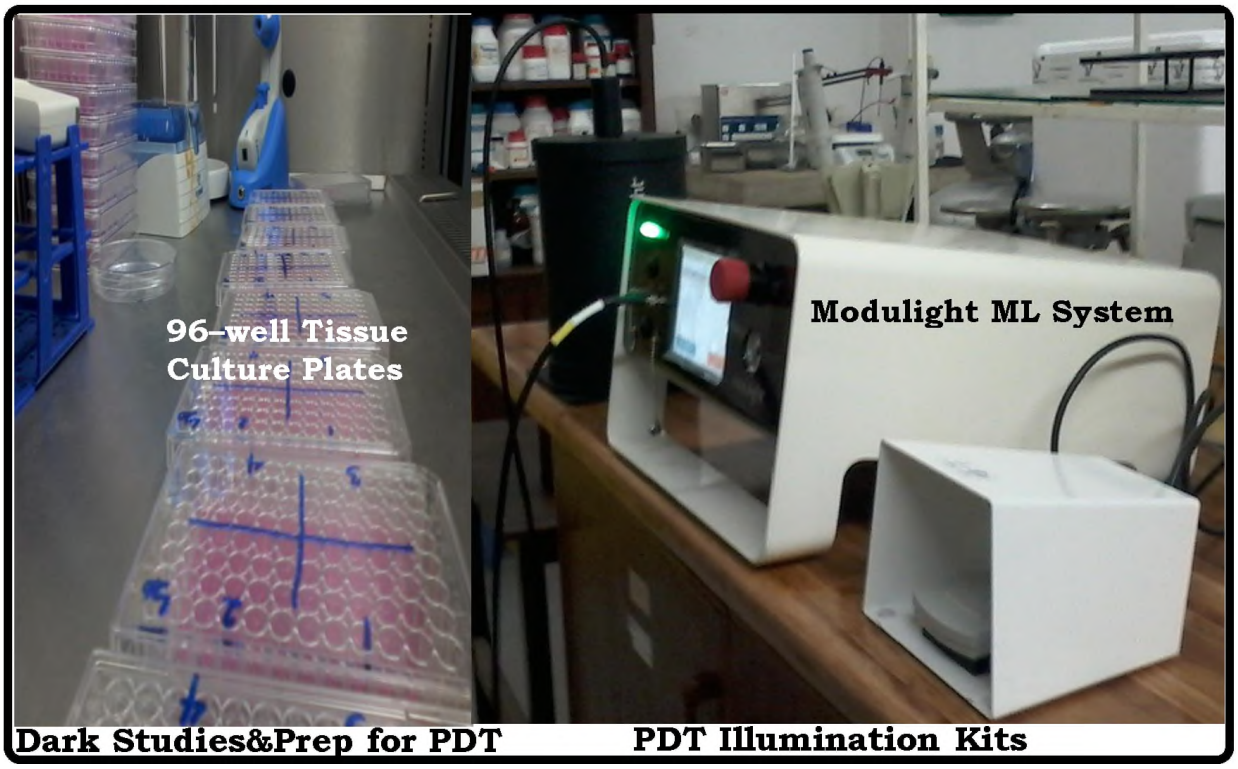

Figure 2.5: Experimental set up for dark cytotoxicity and PDT studies. ML = Medical Laser.

17. Sterilization of PDT disposables were done using an Autoclave RAU®–530D.

18. Cells were cultured in humidified atmosphere incubator with ~5% CO_2 and physiological temperature at 37 ˚C (HealForce®).

19. The cells were viewed under phase contrast using a Zeiss® AxioVert.A1 Fluorescence LED (FL–LED) inverted microscope.

20. The cell viability was measured using a WST–1 cell proliferation neutral red reagent (Roche®) with a Synergy 2 multi–mode microplate reader (BioTek®).

21. The surface areas and pore sizes of the SiNPs–APTES and ZnO/SiNPs–APTES were obtained from the nitrogen adsorption/desorption isotherms using a surface and porosity analyser operated at 77K (Micrometrics ASAP® 2020).

22. Thermogravimetric analysis (TGA) of the Pcs, NPs and conjugates were performed on a Perkin Elmer® TGA 4000 analyzer operated at temperature range of 30 to 900 ^{o}C, heating rate of 10 ^{o}C min^{-1}, maintained under a steady N_2 flow rate of 20 mL min^{-1}.

23. The time resolved phosphorescence decay of singlet oxygen generation was monitored at 1270 nm using an ultrasensitive germanium detector (Edinburgh® Instruments, EI–P) combined with a 1000 nm long pass filter (Omega®, 3RD 1000 CP) and a 1270 nm band pass filter (Omega®, C1275, BP50). The layout of the luminescence method set–up is shown in **Figure 2.6**. Signals were recorded with a digital real–time oscilloscope (Tektronix TDS® 360). The singlet oxygen phosphorescence signal of standard and samples in the presence and absence of sodium azide were compared to obtain the coefficient **[251]**.

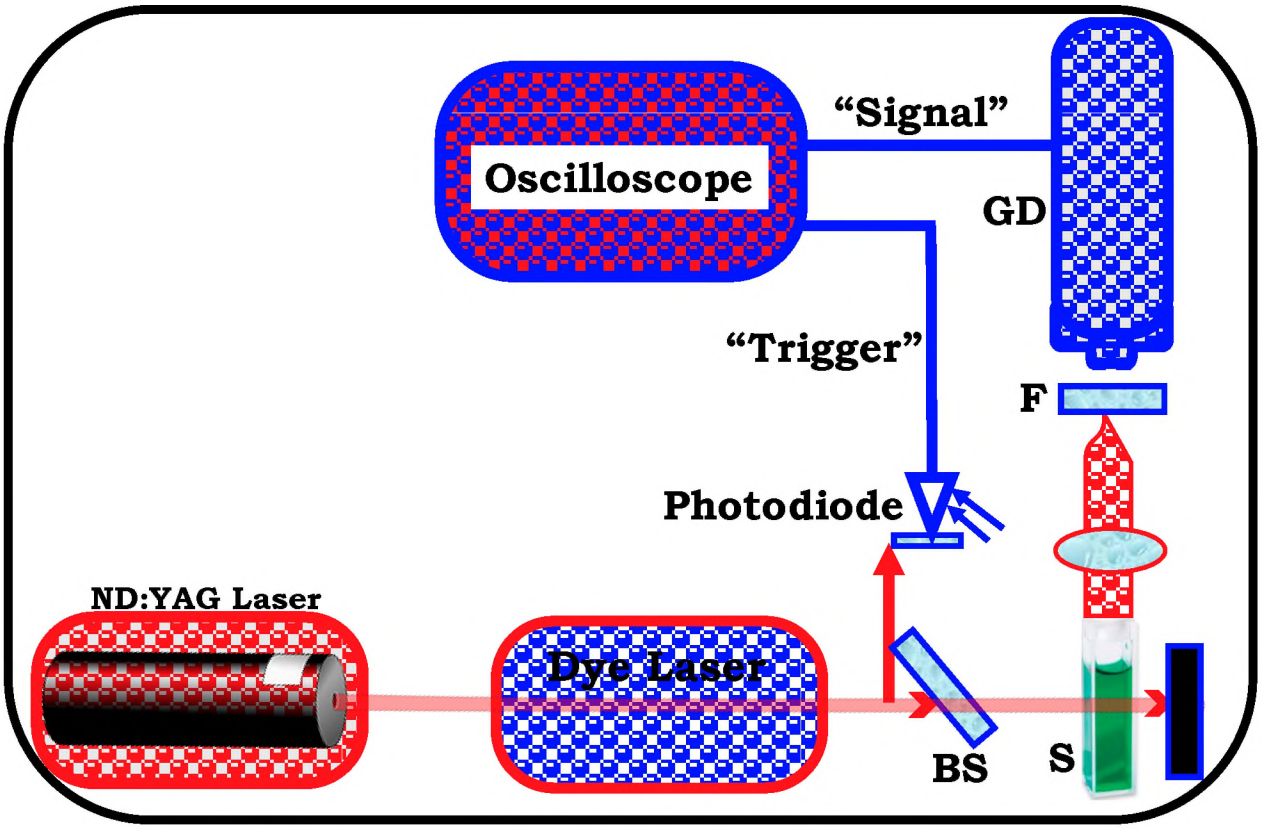

Figure 2.6: Schematic diagram for singlet oxygen detection using luminescence method. GD = Germanium Detector, F = Filter, S = Sample, BS = Beam Splitter.

2.3 SYNTHESES OF NANOPARTICLES (NPs)

The synthetic pathways for the NPs are shown in **Schemes 3.1–3.3**.

2.3.1 Cysteamine (Cyst) capped AgNPs and AgAuNPs, Scheme 3.1

The cysteamine capped AgNPs (AgNPs–Cyst) were synthesized as reported in the literature **[31]** with modifications as follows: diphenyl ether (20.0 g, 118 mmol) and silver acetate (0.25 g, 1.50 mmol) were weighed into a round bottom flask, followed by addition of oleylamine (10 mL) and oleic acid (5 mL). The reaction mixture was heated to reflux at 160 °C with constant stirring and maintained under argon flow for 5 h. Afterwards,

cysteamine (0.015 g, 0.19 mmol) was added to the formed AgNPs and the reaction mixture was allowed to stir for further 2 h at reduced temperature (100 ^{o}C). The reaction mixture was cooled to ambient temperature. The AgNPs–Cyst were precipitated out of solution with ethanol under centrifugation. The obtained AgNPs–Cyst were purified with ethanol and the solid precipitate was air dried in enclosed fume hood.

The AgAuNPs–Cyst were synthesized as outlined above for AgNPs–Cyst **[31]** except for the addition of silver acetate (0.19 g, 1.13 mmol) and gold(III) chloride trihydrate (0.15 g, 0.37 mmol). All the other reaction conditions as well as the isolation of the AgNPs–Cyst were the same as for AgNPs–Cyst synthesis.

2.3.2 Syntheses of semiconductor QDs

2.3.2.1 GSH capped CdTeSe and CdTeSe/ZnO, Scheme 3.2

Sodium hydrogen telluride (NaHTe) precursor was prepared as follows: tellurium granules (0.85 g, 6.66 mmol) and $NaBH_4$ (0.53 g, 14.01 mmol) were weighed into 50 mL round bottom flask, and millipore water (20 mL) was added. The reaction mixture was maintained under ice bath with argon bubbling for 10 h. Afterwards, a pink colouration was observed which indicated the successful formation of the precursor. The same mole ratio was applied to the formation of the NaHSe precursor using selenium powder instead of tellurium granules.

$CdCl_2$ (1.2 g, 6.55 mmol) was weighed into a 3–neck round bottom flask, TGA or GSH (0.95 mL, 0.013 M) and millipore water (200 mL) were added. The pH of the reaction mixture was adjusted under continuous stirring to 11 using 1 M NaOH, followed by deaeration for 30 min with argon flow. Firstly, inert NaHTe precursor (3 mL) was injected into the reaction mixture followed by refluxing at 100 °C for 40 min, after which deaerated NaHSe precursor (3 mL) was added. The reaction mixture was maintained under argon flow for 3 h. The QDs formed at this stage are the CdTeSe–GSH or CdTeSe–TGA QDs. For the addition of the ZnO shell, zinc acetate dihydrate (0.44 g, 2.00 mmol) was dissolved in 40 mL ultrapure millipore water (adjusted to pH 8 with 1 M NaOH solution) and was added to the formed ternary core QDs (CdTeSe–GSH or CdTeSe–TGA). The reaction mixture was refluxed in open air to form the CdTeSe/ZnO–GSH or CdTeSe/ZnO–TGA QDs. The fluorescence and absorption profiles were used to monitor the growth of the QDs at predetermined time course. Upon observation of the target absorption and emission maxima, the reactions were stopped and cooled to ambient temperature. The QDs were isolated out of solution using absolute ethanol under centrifugation. The obtained QDs were successively purified with methanol, acetone and water. The solid samples were oven or vacuum dried for 24 h and stored in the dark for further characterization. The longer the heating time, the larger the size of the QDs (Oswald ripening). Hence, different sizes of QDs were obtained by varying the heating time.

2.3.2.2 CdTe/ZnO–GSH, Scheme 3.3A

The GSH capped CdTe/ZnO QDs were synthesised by first synthesizing the TGA capped CdTe/ZnO QDs as reported in the literature **[53]** with modifications as follows. Then, GSH ligand (0.18 g, 0.60 mmol) was introduced into the growing TGA quantum dot core to foster a ligand exchange **[53]**. It is important to note that residual TGA might be present in the formed binary core QDs (CdTe–GSH). To form a ZnO shell on the CdTe–GSH (CdTe/ZnO–GSH), the crude CdTe–GSH solution was heated at 100 °C under atmospheric air condition. Zinc acetate dihydrate (0.13 g, 0.61 mmol) in water (8 mL) was added to the solution at a rate of 0.50 mL/2 min. QDs growth monitoring, isolation, purification and storage are the same as described in the previous section. The CdTe/ZnO–GSH QDs were dried under vacuum for 24 h. Different sizes of QDs were obtained by varying the heating time.

2.3.2.3 CdTe/ZnSe/ZnO–GSH, Scheme 3.3B

CdTe/ZnSe/ZnO–GSH QDs were synthesized using a similar protocol reported for other core/shell/shell **[46]** as follows: $CdCl_2$ (1.00 g, 5.46 mmol) was weighed into a round bottom flask, TGA (0.92 mL, 0.013 M) and millipore water (200 mL) were added. The pH of the reaction mixture was adjusted under stirring to 11 using 1 M NaOH, followed by deaeration for 30 min under argon flow. Inert NaHTe precursor (3 mL, prepared in **2.3.2.1**) was injected into the reaction mixture, followed by refluxing at 100 °C for 40 min, after which 40 mL solution containing GSH at pH 8

(1.23 g, 4.00 mmol) was introduced to facilitate ligand exchange **[53]** and the solution was left stirring for 30 min. Thereafter, 10 mL solution containing zinc acetate dihydrate (0.44 g, 2.00 mmol) was injected into the growing CdTe–GSH core, followed by addition of inert NaHSe precursor (3 mL, prepared in **2.3.2.1**) to form the core/shell (CdTe/ZnSe–GSH). The reaction mixture was then maintained under argon flow for 4 h. The QDs at this stage are CdTe/ZnSe–GSH. Upon formation of the CdTe/ZnSe–GSH (4.1): the reaction was stopped and cooled to ambient temperature. For the formation of the ZnO shell, zinc acetate dihydrate (0.44 g, 2.00 mmol) in 40 mL ultrapure millipore water (adjusted to pH 8 with 1.00 M NaOH solution) was added to the formed core/shell QDs, followed by refluxing under atmospheric air. QDs growth monitoring, isolation, purification and storage are the same as described in **2.3.2.1**. Different sizes of QDs were obtained by varying the heating time.

2.3.2.4 CdTe/ZnS/ZnO–GSH, Scheme 3.3C

The synthesis of CdTe/ZnS/ZnO–GSH is the same as reported in the previous sections **(2.3.2.3)** except for the replacement of the Se with S which was done using the same mole ratio. The S source was obtained from GSH. Different sizes of QDs were obtained by varying the heating time.

2.3.2.5 CdSeTe/CdTeS/ZnSeS–TOPO/MSA, Scheme 3.3D

TOPOTe and TOPOSe precursors were prepared as reported in the literature **[252]**. Zn (in OA) and S (in ODE) precursors were also prepared as reported in the literature **[252]**. Cd precursor was prepared as follows: CdO (0.80 g, 6.23 mmol) was weighed into a 3–necked round bottom flask, OA (15 mL) and ODE (25 mL) were added. The reaction mixture was heated for 30 min under reflux.

For the synthesis of TOPO capped CdSeTe/CdTeS/ZnSeS QDs, CdO (1.55 g, 12.07 mmol) was weighed into a 3–necked flask, then OA (40 mL) and ODE (60 mL) were added. The reaction mixture was heated to ~320 °C under reflux and was maintained under argon flow for 20 min until a yellow solution was seen. The temperature was reduced to 260 °C. Then the TOPOSe precursor (20 mL) was added to the flask. On addition of the TOPOSe precursor, the colour of the solution changed to reddish–brown which indicate successful formation of the binary core QDs (CdSe–TOPO). Following this, TOPOTe (20 mL) precursor was injected into the binary core QDs to form the ternary core alloy QDs (CdSeTe–TOPO). The ternary core QDs were allowed to grow for 30 min, followed by simultaneous injection of Cd (40 mL), TOPOTe (15 mL), and sulfur (10 mL) precursors leading to formation of the inner shell (CdTeS). The ternary core/shell QDs were allowed to grow for 20 min. Furthermore, Zn (25 mL), TOPOSe (15 mL) and S (10 mL) precursors were simultaneously injected into the growing ternary core/shell QDs and the QDs were allowed to grow for further 60 min

leading to formation of the outer shell (ZnSeS). The reaction progress and crystal growth were monitored by measuring the absorption and fluorescence at predetermined time course. On formation of the target size, the QDs were isolated out of solution using ethanol. Finally, the QDs were successively purified with diethyl ether, ethanol and dried. The formed CdSeTe/CdTeS/ZnSeS–TOPO QDs were transferred into a round bottom flask containing chloroform (10 mL) and MSA (2.50 g, 16.65 mmol) dissolved in 50 mL methanolic solution containing KOH (3.00 g, 53.57 mmol) was added to the QDs mixture. The reaction mixture was allowed to stir for 2 h to afford the phase transfer from hydrophobic QDs to hydrophilic QDs. The formed hydrophilic MSA capped CdSeTe/CdTeS/ZnSeS QDs were precipitated out of solution using ethanol and purified with methanol, dried in air for characterization and further studies.

2.4 SYNTHESES OF PHTHALONITRILE AND PHTHALOCYANINES

The synthetic pathways for the phthalonitriles and phthalocyanines are shown in **Schemes 3.4–3.10**. Only one new phthalonitrile was synthesized in this work, **Scheme 3.7A**.

2.4.1 2-(4-(3,4-dicyanophenoxy)phenoxy)acetic acid, Scheme 3.7A

The synthesis of 2–(4–(3,4–dicyanophenoxy)phenoxy)acetic acid is as follows: 4–nitrophthalonitrile (2.00 g, 0.012 mmol) and (4–hydroxyphenoxy)acetic acid (1.94 g, 0.012 mol) were weighed into a round

bottom flask and dry DMF (50 mL) was added. The reaction mixture was placed under argon flow with continuous stirring at ambient temperature. Then, K_2CO_3 (3.00 g, 22.0 mol) was added to the reaction mixture. After 24 h, more K_2CO_3 (2.00 g, 14.0 mol) was added. The reaction mixture was left stirring for further 24 h to afford 2–(4–(3,4–dicyanophenoxy)phenoxy)acetic acid. The product was transferred into a beaker containing ice and a few drops of HCl were added to allow for effective precipitation from solution. The solid product was successively purified with water and finally recrystallised in methanol.

Yield: 59% (w/w); IR [(KBr) υ_{max}/cm^{-1}]: 3458 (OH), 3084, 2923 (C-H), 2229 (C≡N), 1712 (C=O), 1580, 1504, 1437 (C-C), 1241 (C–O–C), 1081, 924, 811 (C-N); ^{1}HNMR ($CDCl_3$): δ, ppm 13.04 (H, OH-H), 7.78–7.01 (7H, Ar-H), 4.68 (2H, CH_2-H).

2.4.2 Synthesis of metal–free 2,3–bis[2'-(2''–mercaptoethoxy]–9,10,16,17,23,24–hexa–*n*–butoxy phthalocyanine (1), Scheme 3.4

Prior to synthesis of Pc **1**, metal–free 2,3–bis[2'–(2"–hydroxyethoxy)ethoxy]–9,10,16,17,23,24–hexa–*n*–butoxyphthalocyanine (**15**) was synthesised as reported in the literature **[253]**. The iodination reaction was performed as reported in the literature **[254]** with modification as follows: I_2 (0.1055g, 0.42 mmol) was weighed into a round bottom flask and DCM (5 mL) was added. The reaction mixture was stirred at ambient temperature for 10 min, followed by addition of PPh_3 (0.1134 g, 0.43 mmol) and the reaction mixture was allowed to stir for further 30 min. Imidazole (0.0565 g, 0.75 mmol) was added into the reaction mixture which was allowed to stir for 10 min. Then, Pc **15** (0.1000 g, 0.087 mmol) was added and the reaction

mixture was allowed to stay overnight with constant stirring at ambient temperature. The progress of the reaction was monitored using a thin layer chromatography (TLC). Upon completion evidenced by TLC, 1 mL saturated $Na_2SO_{3(aq)}$ solution (0.05 g, 0.40 mmol) was added to the reaction mixture, followed by stirring for 15 min at ambient temperature. The neutralized reaction mixture was evaporated to dryness, and subsequently purified using a silica packed column with isocratic elution and solvent mixture of chloroform and hexane (90:10) to obtain the pure isolate. The obtained pure isolate (**16**) in **Scheme 3.4** was evaporated to dryness for further studies.

Yield: 84%, ^{1}H NMR ($CDCl_3$–d_6): δ, ppm 8.35 – 8.15 (8H, Pc-H), 4.61–1.86 (52H, CH_2), 1.25 (18H, CH_3-H), -3.05 (2H, NH-H).

The thionation reaction was done as previously reported elsewhere **[255]** with modification. Iodo substituted H_2Pc, **Scheme 3.4** (**16**, 0.07 g, 0.051 mmol) and thiourea (0.04 g, 0.526 mmol) were weighed into a round bottom flask and a mixture of THF/EtOH (10 mL/3 mL) was added. The reaction mixture was degassed for 5 min and refluxed at 80 °C under argon flow for 5 h to form the thiouronium salt form of the H_2Pc. The thiouronium salt form of the H_2Pc was hydrolysed with 2 mL of 20% saturated $NaOH_{(aq)}$ solution for 2 h to form Pc **1**. The obtained product (**1**) was neutralized with glacial acetic acid (0.63 mL) and transferred into separatory funnel containing 25 mL of H_2O and 10 mL of $CHCl_3$. The organic phase containing the compound of interest was further purified twice and

evaporated. The purified product was separated using a silica packed column with 20% hexane in $CHCl_3$, and $CHCl_3$:MeOH.

Yield: 39% (w/w); UV/vis (DCM): λ_{max}/nm (log Ɛ): 347 (4.56), 419 (4.14), 643 (4.46), 663 (4.57), 700 (4.51). IR [(KBr) υ_{max}/cm^{-1}]: 3288 (OH), 2929, 2865 (C-H), 2556 (SH), 1603, 1451 (C-C), 1380 (C–N), 1270 (C–O–C), 1195, 1096, 1019 (C-N); calculated for $C_{64}H_{82}N_8O_{10}S_2$; (C 64.73, H 6.96, N 9.44, S 5.40)% Found: (C 64.32, H 6.98, N 8.78, S 4.95)%; ^1H NMR ($CDCl_3$–d_6): δ, ppm 8.38–8.26 (8H, Pc-H), 4.68–1.88 (52H, CH_2), 1.54 (2H, SH-H), 1.25 (18H, m, methyl-H), -2.96 (2H, NH-H). MS (MALDI–TOF) (m/z): Calcd. for $C_{64}H_{82}N_8O_{10}S_2$: 1188, Found: 1189 $[M + H]^+$.

2.4.3 Zinc(II) 1,8(11),15(18),22(25)–tetra–(4'–*tert*–butylphenoxy) phthalocyanine (3), Scheme 3.5A

The compound was synthesised as follows: 3–(4'–*tert*–butylphenoxy) phthalonitrile (2.20 g, 7.97 mmol), urea (0.66 g, 11.00 mmol), zinc acetate dihydrate (0.50 g, 2.27 mmol) and ammonium molybdate (0.015 g, 0.012 mmol) were weighed into a round bottom flask. Nitrobenzene (10 mL) was added into the flask under deaerated condition using argon flow. The reaction mixture was heated to 240 °C for 1 h with constant stirring. Afterwards, the temperature was lowered to 200 °C and the heating continued for a further 4 h. The obtained product (**3**) was precipitated out of solution with excess hexane and diethyl ether. The obtained product was purified using a silica packed column and solvent mixture of petroleum ether and ethyl acetate as eluent.

Yield: 21% (w/w); UV/vis (DMSO): λ_{max}/nm (log Ɛ): 345 (4.52), 629 (4.48), 697 (5.23). IR [(KBr) υ_{max}/cm^{-1}]: 3036, 2954 (aromatic C-H_{str}), 1607 (C=C), 1581, 1506, 1480 (C-C), 1333 (C-N), 1292, 1239, 1174 (C-O-C), 1111, 1089 (C-O), 1047, 1013, 1003 (C–H), 964, 932, 881, 824, 799, 761, 740 (C=C-H); calculated for $C_{72}H_{64}ZnN_8O_4$; C 73.87, H 5.51, N 9.57. Found: (C 74.69, H 5.65, N 9.06)%; ^1H NMR (DMSO-d_6, 400 MHz): δ, ppm 9.14–8.11

(12H, m, Pc-H), 7.86–7.49 (16H, m, phenyl-H), 1.40–1.17 (36H, d, *t*bu-H), MS (MALDI–TOF) (m/z): Calcd. for $C_{72}H_{64}ZnN_8O_4$: 1169, Found: 1174 $[M + 5H]^+$.

2.4.4 Aluminum(III) chloride 2,9(10),16(17),23(24)–tetra–(4'–*tert*–butylphenoxy)phthalocyanine (5), Scheme 3.5B

The compound was synthesised as follows: 4–(4'–*tert*–butylphenoxy) phthalonitrile (0.80 g, 2.90 mmol) was weighed into a round bottom flask containing deaerated $AlCl_3$ (0.60 g, 4.51 mmol), urea (0.40 g, 6.67 mmol) and quinoline (5 mL). The reaction mixture was heated to 240 °C for 1 h with constant stirring. Afterwards, the temperature was lowered to 200 °C and the heating continued for a further 5 h. The obtained product was precipitated out of solution with 50% saturated aqueous methanol and purified with 1 M HCl to remove excess $AlCl_3$ and urea. Water was finally used to remove residual aluminum species and HCl. The obtained product (**5**) was further purified with a silica packed column chromatography using 20% hexane in chloroform and gradient eluents of methanol and chloroform.

Yield: 48% (w/w); UV/vis (DMSO): λmax/nm (log Ɛ): 364 (4.77), 620 (4.47), 684 (5.20). IR [(KBr) υmax/cm^{-1}]: 3038, 2959 (aromatic C-H_{str}), 1600 (C=C), 1506, 1470 (C-C), 1344 (C-N), 1268, 1233, 1166 (C-O-C), 1108 (C-O), 1074, 1052, 1013 (C–H), 952, 874, 827, 754, 728 (C=C-H); calculated for $C_{72}H_{64}AlClN_8O_4$; C 74.05, H 5.52, N 9.60. Found: C 73.96, H 5.79, N 9.24 %; ^{1}H NMR (DMSO-d_6, 400 Hz): δ, ppm 8.90–8.22 (12H, m, MPc-H), 7.39–6.96 (16H, m, phenyl-H), 0.70–0.62 (36H, d, *t*bu-H). MS (MALDI–TOF) m/z: Calcd. for $C_{72}H_{64}AlClN_8O_4$: 1168, Found: 1135 $[M - Cl]^-$

2.4.5 Indium(III) chloride 2,9(10),16(17),23(24)–tetra–(3'–carboxyphenoxy) phthalocyanine (8), Scheme 3.6

The compound was synthesised as follows: 4–(3–carboxyphenoxy) phthalonitrile (0.50 g, 0.00189 mmol) was weighed into a round bottom

flask containing $InCl_3$ (0.40 g, 0.0018 mmol) and 1–pentanol (3 mL) were introduced into the flask under a nitrogen atmosphere, followed by introduction of DBU (0.10 mL, 0.64 mmol). The reaction mixture was heated to 200 °C for 8 h with constant stirring. The product was precipitated out of solution with excess methanol and exhaustively purified with ethanol, 1 M HCl and finally with water until a clear supernatant was observed. The product (**8**) was re–dissolved in DMF and re–precipitated with methanol. Methanol, 1 M HCl and water were used in the final purification. The product was oven dried at 100 °C.

Yield: 25% (w/w); UV/vis (DMSO): λmax/nm (log Ɛ): 363 (4.31), 624 (4.80), 691 (4.95). IR [(KBr) υmax/cm^{-1}]: 3063 (OH), 2929 (C-H), 2650 (OH), 1716 (C=O), 1582 (C=C), 1474 (C=N), 1391 (C–O), 1268 (C–O–C), 1080, 1043 (C–H); calculated for $C_{60}H_{33}InN_8O_{13}$; C 60.62, H 2.80, N 9.43. Found–(C 60.78, H 3.51, N 7.53)%; ^1H NMR (DMSO-d_6): δ, ppm 12.07 (4H, s, COOH), 8.13–7.55 (12H, m, Pc-H), 7.43–6.89 (16H, m, Phenyl-H), 2.17 (H, s, axial OH). MS (MALDI–TOF) (m/z): Calcd. for $C_{60}H_{33}InN_8O_{13}$: 1188; Found: 1184 $[M–4H]^-$.

2.4.6 Zinc(II) 2(3)–mono–2–(4–oxy)phenoxy)acetic acid phthalocyanine (10), Scheme 3.7B

The compound was synthesised as follows: 2–(4–(3,4–dicyanophenoxy)phenoxy)acetic acid (0.50 g, 7.97 mmol), 1,2–dicyanobenzene (0.65 g, 2.89 mmol) and zinc acetate dihydrate (0.40 g, 2.27 mmol) were weighed into a round bottom flask. Then, DBU (0.50 mL, 11.0 mmol) and 1–pentanol (5 mL) were added. The reaction mixture was heated to 240 °C for 1 h with stirring under argon flow. Afterwards, the temperature was lowered to 200 °C and the heating continued for further

5 h. The obtained product was precipitated out of solution with methanol, purified with 1 M HCl and finally with water. The obtained product (**10**) was oven dried at 100 °C. The purification and isolation of the A_3B target ligand was achieved using a silica packed column with gradient eluents of tetrahydrofuran and methanol.

Yield: 9% (w/w); UV/vis (DMSO): λ_{max}/nm (log Ɛ): 352 (4.33), 610 (4.23), 676 (5.02). [(KBr) υ_{max}/cm^{-1}]: 3290 (OH), 2917 (C-H), 1718 (C=O), 1602 (C=C), 1485 (C-C), 1328 (C-N), 1204 (C–O–C), 1075 (C-0); calculated for $C_{40}H_{22}N_8O_4Zn$; (C 64.57, H 2.98, N 15.06)% Found: (C 64.93, H 3.22, N 14.37), ^{1}HNMR (DMSO): δ, ppm 9.38 (1H, acetic-H), 9.37–8.26 (15 H, MPc macrocycle-H), 8.25 – 7.83 (4H, phenyl–H), 2.89–2.73 (2H, CH_2-H); MS (MALDI–TOF) (m/z): Calcd. for $C_{40}H_{22}N_8O_4Zn$: 744.07, Found: 745.96 $[M + 2H]^+$.

2.4.7 Europium(III) bis(2,3,9,10,16,17,23,24–octa–*n*–butoxy) phthalocyanine (11), Scheme 3.8

Prior to synthesis of compound **11**, metal free (2,3,9,10,16,17,23,24–octa–*n*–butoxy)phthalocyanine (**17**, **Scheme 3.8**) was synthesised as reported in the literature **[253]**. Compound **17** (0.02 g, 0.018 mmol) and europium(III) acetate tetrahydrate (0.019 g, 0.048 mmol) were weighed into a flask. Then, DBU (0.027 mL, 0.017 mmol) and *n*–octanol (1 mL) were added. The reaction mixture was refluxed at 200 °C under argon flow for 12 h. The reaction completion was evidenced by TLC, and UV–Vis spectra. The obtained dark–green sticky product (**11**) was evaporated and separated using a silica packed column with gradient eluents of MeOH:$CHCl_3$. The product was further purified with a gel permeation column chromatography using a sephadex sorbent with 2.5% of MeOH in $CHCl_3$. The final pure isolate was air dried in enclosed fume hood.

Yield: 0.015 g (70%), UV/vis (DCM): λ_{max}/nm (log Ɛ): 294 (4.99), 344 (4.97), 366 (4.98), 367 (4.40), 646 (4.62), 676 (5.01); calculated for $C_{128}H_{160}EuN_{16}O_{16}$; (C 65.96, H 6.92, N 9.62)% Found–(C 65.89, H 6.87, N 8.43) %; IR [(KBr) υ_{max}/cm^{-1}]: 3337 (OH), 2929, 2865 (C-H), 1598 (C-C), 1447 (C-C), 1371 (C–N), 1317 (Pc$^{\bullet-}$), 1264 (C–O–C), 1188, 1072, 1033 (C-N); ^{1}H NMR ($CDCl_3$–d_6): δ, ppm 6.71 (16H, Pc-H), 2.27 – 5.69 (96H, CH_2-H), 1.44 (48H, CH_3-H); MS (MALDI–TOF) (m/z): Calcd. for $C_{128}H_{161}EuN_{16}O_{16}$ [M + H]$^+$: 2331.2, Found: 2331.8.

2.4.8 Dieuropium(III) tris(2,3,9,10,16,17,23,24–octa–*n*–butoxy) phthalocyanine (12), Scheme 3.8

Compound **12** was synthesized and purified as described above for compound **11** but without DBU.

Yield: 0.015 (72%); UV/vis (DCM): λ_{max}/nm (log Ɛ): 293 (5.30), 353 (5.30), 642 (5.06); calculated for $C_{192}H_{240}Eu_2N24O_{25}$; (C 64.70, H 6.86, N 9.19) % Found: (C 64.50, H 7.16, N 9.07) %; IR [(KBr) υ_{max}/cm^{-1}]: 3348 (OH), 2937, 2866 (C-H), 1600 (C-C), 1457 (C-C), 1370 (C–N), 1266 (C–O–C), 1190, 1171 (C-N); ^{1}H NMR ($CDCl_3$–d_6): δ, ppm 12.07–9.16 (24H, Pc-H), 6.38–2.16 (168H, CH_3 or CH_2-H), 1.50 (48H, CH_3-H); MS (MALDI–TOF) (m/z): Calcd. for $C_{192}H_{241}Eu_2N_{24}O_{24}$ [M + H]$^+$: 3572.7, Found: 3573.6.

2.4.9 Europium(III) bis{2,3–bis[2'–(2''–hydroxyethoxy)ethoxy]–9,10,16,17,23,24–hexa–*n*–butoxyphthalocyanine (13) and dieuropium(III) tris{2,3–bis[2'–(2''–hydroxyethoxy)ethoxy]–9,10,16,17,23,24–hexa–*n*–butoxyphthalocyanine (14), Scheme 3.9

2.4.9.1 Protection of metal–free 2,3-bis[2'–(2''–hydroxyethoxy)ethoxy]-9,10,16,17,23,24–hexa–n–butoxyphthalocyanine, Scheme 3.9

Compound **18** was synthesized in accordance with the literature **[253]**. The hydroxyl end of the diethylene glycol (DEG) substituents of compound **18** were protected with tetrahydropyran (THP) as follows: compound **18** (0.04 g 0.035 mmol) and *p*-toluene sulfonic acid (TsOH), (0.01 g, 0.058 mmol) were weighed into a round bottom flask. Chloroform (15 mL) and excess 3,4–dihydro–2H–pyran (0.11 g, 1.29 mmol) were added to the flask.

The reaction mixture was stirred at ambient temperature for 30 min. The reaction progress was monitored with TLC: upon completion evidenced by TLC and UV–Vis spectroscopy, it was neutralized with saturated solution of $K_2CO_{3(aq)}$ (0.03 g, 0.22 mmol) and stirred further for 30 min. The product (**19**) was purified using a silica packed chromatography with gradient eluents of 20% hexane in chloroform and MeOH/$CHCl_3$.

Yield: 0.043 g (89%); ^{1}H NMR ($CDCl_3$–d_6): δ, ppm 8.41–8.34 (8H, Pc–H), 4.75–1.51 (70H, BuO/ethoxy/THP–H), 1.26–1.23 (18H, CH_3–H), –2.46 (2H, NH–H); MALDI–TOF MS: m/z calculated for $C_{74}H_{98}N_8O_{14}$: 1323.7, Found: 1323.9 $[M]^+$.

2.4.9.2 Europium(III) bis{2,3–bis[2'–(2''–hydroxyethoxy)ethoxy]–9,10,16,17,23,24–hexa–*n*–butoxyphthalocyanine (13), Scheme 3.9

Compound **19** (0.038 g, 0.029 mmol), and europium(III) acetate tetrahydrate (0.029 g, 0.0.072 mmol) were weighed into a flask. Then, DBU (0.043 mL, 0.28 mmol) and *n*–octanol (1 mL) were added. The reaction mixture was refluxed at 200 °C under argon flow for 12 h. The reaction completion was evidenced by TLC, and UV–Vis spectroscopy. The obtained dark–green sticky product was evaporated and separated using a silica packed column with gradient eluents of methanol and chloroform to afford THP protected **13a**. For deprotection, compound **13a** (0.025 g, 0.058 mmol) was dissolved in 5 mL of methanol in the presence of TsOH (0.01g, 0.058). The reaction mixture was stirred at ambient temperature for 5 h. Reaction progress was monitored by MALDI–TOF MS and TLC. Upon completion of deprotection process, TsOH was neutralized by saturated $Na_2CO_{3(aq)}$ solution. The obtained target compound (**13**) was evaporated

and separated using a biobead packed column with 2.5% of MeOH in $CHCl_3$. Finally, it was purified with sephadex column, the pure isolate was air dried in enclosed fume hood.

Yield: 0.022 (95%). UV/vis (DCM): λ_{max}/nm (log Ɛ): 290 (4.83), 340 (4.81), 370 (4.86), 492 (4.36), 611 (4.29), 675 (4.94); calculated for $C_{128}H_{160}EuN_{16}O_{24}$; (C 62.53, H 6.56, N 9.11) % Found-(C 62.13, H 7.67, N 9.39)%; IR [(KBr) υ_{max}/cm^{-1}]: 3355 (OH), 2923, 2865 (C-H), 1596(C-C), 1493 (C-C), 1371 (C–N), 1315 ($Pc^{\bullet-}$), 1265 (C–O–C), 1036 (C-N); ^1H NMR ($CDCl_3$–d_6): δ, ppm 6.94–6.72 (16H, Pc-H), 4.49 (4H, OH-H) 6.24–2.26 (104H, CH_2-H), 1.45 (36H, CH_3-H); MS (MALDI–TOF) (m/z): Calcd. for $C_{128}H_{161}EuN_{16}O_{24}$ $[M + H]^+$: 2459.5, Found: 2459.1.

2.4.9.3 Dieuropium(III) tris{2,3–bis[2'–(2''–hydroxyethoxy)ethoxy]–9,10,16,17,23,24–hexa–*n*–butoxyphthalocyanine (14), Scheme 3.9

Compound **14** was synthesized and purified as described above for compound **13,** but in the absence of DBU.

Yield: 0.02 g (90%). UV/vis (DCM): λ_{max}/nm (log Ɛ): 290 (5.28), 354 (5.30), 641 (5.12); calculated for $C_{192}H_{240}Eu_2N_{24}O_{36}$; (C 61.27, H 6.43, N 8.93) % Found–(C 60.49, H 6.85, N 8.42)%; IR [(KBr) υ_{max}/cm^{-1}]: 3367 (OH), 2925, 2864 (C-H), 1601 (C-C), 1456 (C-C), 1372 (C–N), 1269 (C–O–C), 1193, 1130, 1069 (C-N); ^1H NMR ($CDCl_3$–d_6): δ, ppm 12.14–9.11 (24H, Pc-H), 6.60–2.15 (156H, CH_2–H) 4.49 (6H, OH-H), 1.71 – 6.93 (156H, methylene-H), 2.15–1.47 (54H, CH_3–H). MS (MALDI–TOF) (m/z): Calcd. for $C_{192}H_{241}Eu_2N_{24}O_{36}$ $[M+H]^+$: 3765.6, Found: 3765.9.

2.5 Pcs–NPs Conjugation Procedures

The synthetic pathways for the formation of the Pc–NPs conjugates are shown in **Schemes 3.10–3.16**. Coupling agents were chosen based on the solubility of the Pc compounds. For the hydrophilic compounds, EDC was employed and for the lipophilic ones, DCC was used.

2.5.1 Sulfur–metal bond for Pc 1 with CdSe–TOPO (3.8) QDs, Scheme 3.10

CdSe–TOPO (25 mg) was weighed into a flask, followed by addition of 2 mL solution of 6 mg/mL Pc **1** in dichloromethane. The reaction mixture was stirred for 18 h to form sulfur–metal bond (S–M). Afterwards, the reaction mixture was evaporated to dryness. The conjugate is represented as **1**–CdSe–TOPO.

2.5.2 Amide bond formation for compounds 2a, 6, 8, and 9 with QDs

The covalent linkages were performed as reported in the literature **[156]** with modifications as follows, **Scheme 3.11** (Using **2a** and **6** with QDs as examples):

Compounds **2a**, **6** and **9**, 0.01 g (corresponding to 1.4×10^{-2} mmol, 8.9×10^{-3} mmol, and 1.1×10^{-2} mmol, respectively), were weighed into a separate round bottom flask and dry DMF (3 mL) was added. EDC (0.019 g, 0.1 mmol) and NHS (0.012 g, 0.1 mmol) were added to the reaction mixture to activate the carboxylic acid moiety of the Pcs. The reaction mixture was left stirring at ambient temperature for 24 h, after which 3 mL of a solution containing 0.02 g of QDs (See **Table 1.5** for QDs used for each compound) were added and the mixture was left stirring for further 24 h leading to the formation of amide linked Pc–QDs.

For compound **8**, DCC/DMAP were employed as coupling agents due to their good solubility in organic solvents as well as the Pc compound which allows for efficient activation of the COOH ring substituents of **8**. The conjugation protocol is as follows: Compound **8** (0.01 g, 8.4×10^{-3} mmol)

was weighed into a 20 mL round bottom flask and dry DMF (2 mL), DCC (0.01 g, 5×10^{-2} mmol) and DMAP (0.005 g, 5×10^{-2} mmol) were added into the reaction mixture to activate the carboxylic acid moiety of the MPc. The reaction mixture was left stirring at ambient temperature for 28 h, after which 3 mL of a solution containing 0.05 g of QDs were added respectively and the reaction mixture was left stirring for a further 52 h leading to the formation of an amide linked MPc–QDs.

The nanohybrids were isolated out of solution with ethanol and were exhaustively purified with ethanol and methanol. The nanohybrids were dried in fume hood to obtain a powder form. Different sizes of the QDs were obtained by varying the heating time. The conjugates are represented as follows. Values in the bracket represent the QDs sizes obtained by XRD.

2a–CdTe–GSH (2.4), **2a**–CdTe/CdS–GSH (3.1), **2a**–CdTe/CdS/ZnS–GSH (4.2), **2a**–CdTe/CdS/ZnS–GSH (5.1), and **2a**–CdTe/CdS/ZnS–GSH (6.7).

6–CdTe–GSH (2.4), **6**–CdTe/CdS–GSH (3.1), **6**–CdTe/CdS/ZnS–GSH (4.2), **6**–CdTe/CdS/ZnS–GSH (5.1), and **6**–CdTe/CdS/ZnS–GSH (6.7).
6–CdTe–GSH (2.9), **6**–CdTe/ZnO–GSH (4.6), **6**–CdTeSe–GSH (3.6), **6**–CdTeSe/ZnO–GSH (5.1), and **6**–CdTeSe/ZnO–GSH (6.5).

8–CdTe–GSH (3.2), **8**–CdTe/ZnSe–GSH (4.1), **8**–CdTe/ZnSe/ZnO–GSH (4.5), **8**–CdTe/ZnSe/ZnO–GSH (6.2), and **8**–CdTe/ZnSe/ZnO–GSH (7.6).

9–CdTe–GSH (2.7), **9**–CdTe/ZnS–GSH (4.1), **9**–CdTe/ZnS/ZnO–GSH (4.8), **9**–CdTe/ZnS/ZnO–GSH (5.8), and **9**–CdTe/ZnS/ZnO–GSH (8.9).

2.5.3 Conjugation of compound 2b to SiNPs–APTES (20) and ZnO/SiNPs–APTES (13), Scheme 3.12A

Compound **2b** (0.02 g, 2.80×10^{-2} mmol) was dissolved in two separate vials containing 2 mL dry DMF each and the carboxylic acid moiety of the MPc was activated using DCC (0.015 g, 7.27×10^{-5} mol). The solution was

placed on constant stirring for 48 h at ambient temperature. Then, DMAP (0.0075 g, 6.14 × 10^{-5} mol) and 1 mL solution of 0.05 g of SiNPs–APTES (20) and ZnO/SiNPs–APTES (13) were added respectively. The reaction mixture was left stirring for 48 h to obtain the amide linked MPc–NPs. The nanoconjugates were precipitated out of solution using ethanol and successively purified with ethanol and methanol. The nanoconjugates were vacuum dried. The conjugates are represented as follows: **2b**–SiNPs–APTES (20), and **2b**–ZnO/SiNPs–APTES (13).

2.5.4 Conjugation of compound 2b to HSA, Scheme 3.12B

Compound **2b** (0.21 g, 2.94 × 10^{-4} mol) was dissolved in dry DMF (3 mL). DCC (0.061 g, 2.96 × 10^{-4} mol) was added to the solution to activate the carboxylic acid moiety of compound **2b**. The reaction mixture was left stirring at ambient temperature for 24 h. Thereafter, NHS (0.03g, 2.61 × 10^{-4} mol) and 1 mL saturated solution of $HSA_{(aq)}$ (0.08 g) were added. The reaction mixture was left stirring for further 48 h leading to the formation of amide linked **2b**–HSA. The conjugate was precipitated out of solution with ethanol and was exhaustively purified with methanol and ethanol. The conjugate was dried under vacuum to obtain a powder which was further purified using a size exclusion chromatography. The conjugate is represented as **2b**–HSA.

2.5.5 Conjugation of compound 2b to chitosan, Scheme 3.12B

Prior to the conjugation, bulk chitosan (0.01 g) was dissolved in 2 mL of 2% glacial acetic acid. Compound **2b** (0.02 g, 2.80 × 10^{-5} mol) was dissolved

in dry DMF (2 mL), then DCC (0.015 g, 7.27 × 10^{-5} mol) was added to activate the carboxylic acid moiety of the MPc. The reaction mixture was placed on constant stirring for 24 h at ambient temperature. NHS (0.007 g, 6.09 × 10^{-5} mol) and chitosan solution prepared above were added. The reaction mixture was allowed to stir for further 48 h to form amide linked **2b**–chitosan. The conjugate was precipitated out of solution using ethanol and successively purified with ethanol and methanol. The conjugate was vacuum dried. The conjugate is represented as **2b**–chitosan.

2.5.6 Sulfonamide bond formation for compound 7 with QDs, Scheme 3.13

The covalent linkage was done as reported in the literature **[256]** with modifications. Compound **7** (0.02 g, 2.2 × 10^{-2} mmol) was weighed into a round bottom flask, dry DMF (5 mL) was added and the reaction mixture was stirred in ice bath for 20 min. Equimolar amount of thionyl chloride was introduced into the reaction gently to activate the sulfonic acid moiety of the Pc. The reaction mixture was left stirring at ambient temperature for 2 h, after which 5 mL solution containing 0.02 g of QDs were added and the reaction mixture was left stirring for further 24 h leading to the formation of a sulfonamide linked Pc-QDs. The nanocomposites were precipitated out of solution with acetone and were successively purified with ethanol to remove unreacted QDs and Pc because the QDs and Pc alone are sparingly soluble in ethanol while the conjugate is not soluble in

ethanol at all. The nanocomposites were oven dried at 100 ^{o}C to obtain a powder form. The nanocomposites are represented as follows:

7–CdTe/CdS/ZnS–GSH (5.2), and **7**–CdTe/CdS/ZnS–GSH (6.3)

2.5.7 Conjugation of compound 10 with AgNPs–Cyst (11.3) and AgAuNPs–Cyst (11.6), Scheme 3.14

The conjugation of compound **10** to AgNPs–Cyst (11.3) and AgAuNPs–Cyst (11.6) was done by activation of the carboxylic moiety of compound **10** with DCC/DMAP, followed by addition of the NPs as follows: compound **10** (0.020 g, 0.027 mmol) was weighed into two flasks, then 2 mL of DMF and DCC (0.017 g, 0.082 mmol) were added to each flask. The reaction mixtures were allowed to stir for 48 h at ambient temperature. This was followed by addition of DMAP (0.010 g, 0.082 mmol) and AgNPs–Cyst (11.3) or AgAuNPs–Cyst (11.6) (0.008 g) to each reaction mixture which were allowed to stir for further 48 h at ambient temperature resulting in the formation of amide bond between compound **10** and Cyst capped NPs. The formed nanoconjugates were precipitated out of solution with methanol and successively purified with ethanol. The purified nanoconjugates were air dried in enclosed fume hood. The obtained conjugates are represented as follows: **10**–AgNPs–Cyst (11.3) and **10**–AgAuNPs–Cyst (11.6).

2.5.8 Mixing of compounds 11 and 12 with TOPO–QDs

Compounds **11** and **12** were mixed with TOPO QDs as follows: 25 mg (25 mg/mL) of CdSeTe/CdTeS/ZnSeS–TOPO (6.6) was weighed into a flask, 1 mL of DCM was added, followed by addition of 2 mL solution of compounds **11** and **12** (2.5 mg/mL) respectively. The reaction mixture was placed on

constant stirring for 24 h, followed by the evaporation of the products (**11**–CdSeTe/CdTeS/ZnSeS–TOPO (6.6) and **12**–CdSeTe/CdTeS/ZnSeS–TOPO (6.6)) to dryness.

2.5.9 Conjugation of compounds 13 and 14 to MSA–QDs, Scheme 3.15

Compounds **13** and **14** were covalently linked to MSA QDs as follows: 0.025 g of CdSeTe/CdTeS/ZnSeS–MSA was weighed into a flask, 2 mL of deionized water and EDC (0.015 g, 0.08 M) were added. The reaction mixture containing the MSA–QDs was placed on constant stirring for 2 h to activate the carboxylic acid moiety of the MSA–QDs. Afterwards, 1 mL chloroform solution of compound **13** and **14** (0.005 g/mL), were added into the activated MSA–QDs solution. The reaction mixture was left stirring for 24 h leading to the formation of ester linked **13**–CdSeTe/CdTeS/ZnSeS–MSA (7.3) and **14**–CdSeTe/CdTeS/ZnSeS–MSA (7.3). The conjugates were purified using a sephadex packed column and tetrahydrofuran as eluent.

2.5.10 Doping of compounds 3 to 6 onto silica nanoparticles (SiNPs) using reverse microemulsion method, Scheme 3.16

The doping of the MPcs onto SiNPs was done as reported in the literature **[88]** with modifications as follows: Triton X–100 (1.80 mL), 1–hexanol (1.80 mL) and cyclohexane (7.50 mL) were introduced into 50 mL round bottom flask. The reaction mixture was allowed to stir for 20 min. Afterwards, 1 mL of 0.051 mM each of the compounds (**3** to **6**) in DMF, was added. The reaction mixture was further stirred for 10 min, followed by the introduction of TEOS (0.15 mL, 0.77 mmol), dropwise addition of H_2O (0.40

mL) for 10 min and the introduction of 25% NH_3OH solution (0.06 mL) for 1 h. The solution was left stirring for 24 h for the formation of the MPcs doped SiNPs. The products were collected with ethanol under centrifugation. The products were purified with ethanol and water to remove unreacted materials. Finally, the purified products were vacuum dried. The same protocol was applied for SiNPs without MPcs. The MPcs doped SiNPs are represented as follows:

3–SiNPs (60), **4**–SiNPs (34), **5**–SiNPs (40), and **6**–SiNPs (39).

2.6 CELL STUDIES

The *in vitro* dark cytotoxicity studies were performed on the following: compound **2b** and its conjugates (**2b**–ZnO/SiNPs–APTES (13), **2b**–HSA, **2b**–SiNPs–APTES (20), and **2b**–chitosan); compound **6** and its conjugates (**6**–CdTe–GSH (2.9), **6**–CdTeSe/ZnO–GSH (5.1), and **6**–CdTeSe/ZnO–GSH (6.5)); compound **9** and its conjugates (**9**–CdTe/ZnS–GSH (4.7) and **9**–CdTe/ZnS/ZnO–GSH (5.8)); compound **10** and its conjugates (**10**–AgNPs–Cyst (11.3) and **10**–AgAuNPs–Cyst (11.6)). PDT activity was investigated on compound **2b** and its conjugates (**2b**–ZnO/SiNPs–APTES (13), **2b**–HSA, and **2b**–chitosan); and compound **10** and its conjugates (**10**–AgNPs–Cyst (11.3) and **10**–AgAuNPs–Cyst (11.6)). For both *in vitro* cytotoxicity and PDT studies, human adenocarcinoma cells (MCF–7 cells) was employed.

2.6.1 *In vitro* dark cytotoxicity studies

Prior to the *in vitro* photodynamic therapy studies of the drugs, the *in vitro* cytotoxicity studies in the dark against human breast adenocarcinoma

cells (MCF–7 cells) were performed. The MCF–7 cells were cultured using Dulbecco's modified Eagle's medium (DMEM) containing 4.5 g/L glucose with L-glutamine and phenol red, supplemented with 10% (v/v) heat-inactivated fetal calf serum (FCS) and 100 unit/mL penicillin–100 μg/mL streptomycin–amphotericin B. The cells were grown in 75 cm^2 vented flasks (Porvair®) and incubated at 37 °C and 5% CO_2 with humidified atmosphere and routinely subcultured by standard trypsinisation.

The viable trypsinised cells were counted via trypan blue dye exclusion assay (0.40% trypan blue solution) using a hemocytometer. The cells were seeded at a cell density of 10,000 cells/well in supplemented DMEM containing phenol red in 96–well tissue culture plates (Porvair®). Afterwards, the cells were incubated at 37 °C and 5% CO_2 for 24 h to foster cell attachment to the wells. The attached cells were rinsed with 100 μL phosphate buffer saline (PBS) once, followed by administration of 100 μL supplemented DMEM containing gradient doses of the respective drugs. The stock drug concentrations were prepared in DMSO or PBS and made up to marked volume with supplemented DMEM. The effect of DMSO or PBS on the cells were investigated by incubation of the cells for 24 h with 1.6% (v/v) DMSO or PBS in supplemented DMEM which represents the highest percentage of DMSO or PBS in the drug gradient solutions. Placebo cells were incubated with or without DMSO and PBS in supplemented DMEM with phenol red.

The 96–well plates containing the cells and drugs were incubated at 37 °C and 5% CO_2 in the dark for 24 h. After 24 h treatment, the wells were rinsed with 100 μL DPBS once, supplemented DMEM with phenol red was added and the plates re-incubated for 24 h. Cell survival was expressed as percentage of placebo cells (cells without drugs containing supplemented DMEM with phenol red). After 24 h re–incubation with supplemented DMEM with phenol red, cell proliferation neutral red reagent (WST–1 assay) was used to quantify the surviving cells.

2.6.2 *In vitro* photodynamic therapy studies

Photodynamic therapy studies of the drugs were assessed by incubation of attached cells seeded as earlier described in the previous section **(2.6.1)**. Gradient doses of each drug were administered in 96-well plate containing the attached cells with density of 10,000 cells/well in a supplemented DMEM (100 μL). The plate was incubated at 37 °C in 5% CO_2 in the dark for 24 h, and were rinsed with 100 μL PBS and the supplemented phenol red DMEM was replaced with supplemented phenol red free DMEM. The plates were subsequently illuminated with fixed light dosimetry of 170 J/cm^2. Modulight® ML7200 series Illumination set–up or lamp was used as illumination source. After illumination, the supplemented phenol red free DMEM was replaced with supplemented DMEM with phenol red; each experiments were done in their entirety in three independent triplicate (n=3). Cell survival was expressed as percentage of placebo cells (cells

without drugs). Surviving cells were quantified after re–incubation with culture media with the use of WST–1 assay after 24 h.

2.6.3 WST–1 toxicity and cell proliferation

The WST–1 assay was used to assess the toxicity and cell proliferation in the monolayer of the cells treated with the drugs and the placebo cells, respectively. This was performed as specified in the manufacturer's instruction and a Synergy 2 multi–mode microplate reader (BioTek®) at a 450 nm was used to quantify the stained viable cells.

The percent cell viability was determined using equation 2.1:

$$\% \text{ cell viability} = \frac{\text{Absorbance sample at 450 nm}}{\text{Absorbance control at 450 nm}} \times 100 \qquad \textbf{(2.1)}$$

where the absorbance of sample is the cells containing drugs while absorbance of control is the placebo cells containing only supplemented DMEM with phenol red.

2.6.4 Statistical analysis

The data obtained from the experiments were statistically analysed using Microsoft Excel worksheet 2010 (Microsoft®) and Graphpad Prism6 (Graphpad®). Each experiment was repeated in its entirety at least three times each with triplicate replicates (n=3). One–way analysis of variance (ANOVA) for the *in vitro* dark cytotoxicity and PDT data of the drugs against MCF–7 cell was evaluated. A p–value < 0.05 was considered to be statistically significant.

The results discussed in the subsequent chapters have been published or submitted for publication in peer–reviewed journals.

1. David O. Oluwole, Tebello Nyokong, Physicochemical behavior of nanohybrids of mono and tetra substituted carboxyphenoxy phthalocyanine covalently linked to CdTe/CdS/ZnS–GSH. ***Polyhedron***, 87 (2015) 8–16.

2. David O. Oluwole, Jonathan Britton, Philani Mashazi, Tebello Nyokong, Photophysical behavior of nanocomposites of aluminum tetrasulfonated phthalocyanine with glutathione capped CdTe/CdS/ZnS quantum dots. ***Syn. Met.***, 205 (2015) 212–221.

3. David O. Oluwole, Tebello Nyokong, Comparative photophysicochemical behaviour of nanoconjugates of indium tetracarboxyphenoxy phthalocyanines covalently linked to CdTe/ZnSe/ZnO–GSH. ***J. Photochem. Photobiol. A***, 312 (2015) 34–44.

4. David O. Oluwole, Chelsea M. Tilbury, Earl Prinsloo, Janice Limson, Tebello Nyokong, Photophysicochemical properties and *in vitro* cytotoxicity of zinc tetracarboxyphenoxy phthalocyanine–quantum dot nanocomposites. ***Polyhedron***, 106 (2016) 92–100.

5. David O. Oluwole, Imran Uddin, Earl Prinsloo, Tebello Nyokong, The effects of silica based nanoparticles on the photophysicochemical properties and dark *in vitro* cytotoxicity study of zinc monocarboxyphenoxy phthalocyanine. ***J. Photochem. Photobiol. A***, 329 (2016) 221–231.

6. David O. Oluwole, Tebello Nyokong, Photophysicochemical behaviour of metallophthalocyanines when doped onto silica nanoparticles. ***Dyes Pigm.***, 136 (2017) 262–272.

7. David O. Oluwole, Earl Prinsloo, Tebello Nyokong, Photophysicochemical properties and *in vitro* photodynamic therapy study of zinc monocarboxyphenoxy phthalocyanine conjugate with human serum albumin and chitosan. ***Spectrochim Acta Part A***, 173 (2017) 292–300.

8. David O. Oluwole, Earl Prinsloo, Tebello Nyokong, Photophysicochemical properties and *in vitro* photodynamic therapy activity of nanoconjugates of zinc(II) mono 2-(4-oxy)phenoxy)acetic acid phthalocyanine with cysteamine capped Ag and AgAu nanoparticles. ***Polyhedron***, 119 (2016) 434–444.

9. David O. Oluwole, Alexey V. Yagodin, Nhlakanipho C. Mhkize, Kutloano E. Sekhosana, Alexander G. Martynov, Yulia G. Gorbunova, Aslan Yu. Tsivadze, Tebello Nyokong, Nanoconjugates of bis- and tris- sandwich phthalocyanines with quantum dots: first example of synthesis and investigation of nonlinear

optical behaviour. ***Chem. Eur. J***, 23 (2017) 1.

10. David O. Oluwole, Earl Prinsloo, Tebello Nyokong, Photophysicochemical and *in vitro* cytotoxicity of nanoconjugates of GSH–CdTe/ZnS/ZnO covalently linked to aluminum octacarboxy phthalocyanine. ***Spectrochim Acta Part A***–Submitted 30–12–2015.

11. David O. Oluwole, J. Britton, Alexander G. Martynov, Yulia G. Gorbunova, Aslan Yu. Tsivadze, Tebello Nyokong, Synthesis and optical limiting properties of nanocomposites of bis[2'-(2"-mercaptoethoxy] hexabutoxy phthalocyanine with quantum dots. ***In preparation***.

Side Publications:

12. Jonathan Britton, Alexander Martynov, David O. Oluwole, Yulia Gorbunova, Aslan Yu. Tsivadze, Tebello Nyokong, Improvement of nonlinear optical properties of phthalocyanine bearing diethyleneglycole chains: influence of symmetry lowering vs. heavy atom effect. ***J. Porphyr. Phthalocy.***, 20 (2016) 1296.

13. Njemuwa Nwaji, David Oluwole, John Mack, Samson Khene, Jonathan Britton, Njemuwa Nwaji, Marcel Louzanda, Improved nonlinear optical behaviour of indium ball type phthalocyanine linked to glutathione capped nanoparticles. ***Dyes Pigm.***, 140 (2017) 417.

14. Gonzalo Ramírez-García, David O. Oluwole, Siphesihle R. Nxele, Fanny d'Orlye, Tebello Nyokong, Fethi Bedioui, Anne Varenne, Characterization of phthalocyanine functionalized quantum dots by dynamic light scattering, laser Doppler and capillary electrophoresis, ***Analy. Bioanal. Chem.*** (2016) 1.

CHAPTER THREE

SYNTHESES AND CHARACTERIZATIONS

3.1 NANOPARTICLES (NPs)

For the surface functionalization of the NPs, priority was given to bifunctional ligands containing thiol, amine or carboxylic acid moieties for ease of linkage to Pcs.

Table 1.1 lists the QDs employed in this work, and **Table 3.2** lists the NPs which were linked or mixed to Pcs. Only the synthesis of the new NPs will be discussed in the following subsection:

3.1.1 Syntheses of NPs

3.1.1.1 Synthesis of AgNPs–Cyst (11.3) and AgAuNPs–Cyst (11.6)

The organometallic synthetic route was employed in this work as described by Liu *et al.* **[31]** with modifications. The oleylamine stabilized AgNPs and AgAuNPs were first synthesised followed by simultaneous phase transfer with cysteamine as shown in **Scheme 3.1**. The functionalization of the AgNPs and AgAuNPs with cysteamine was performed to foster their subsequent covalent attachment to COOH substituted MPc.

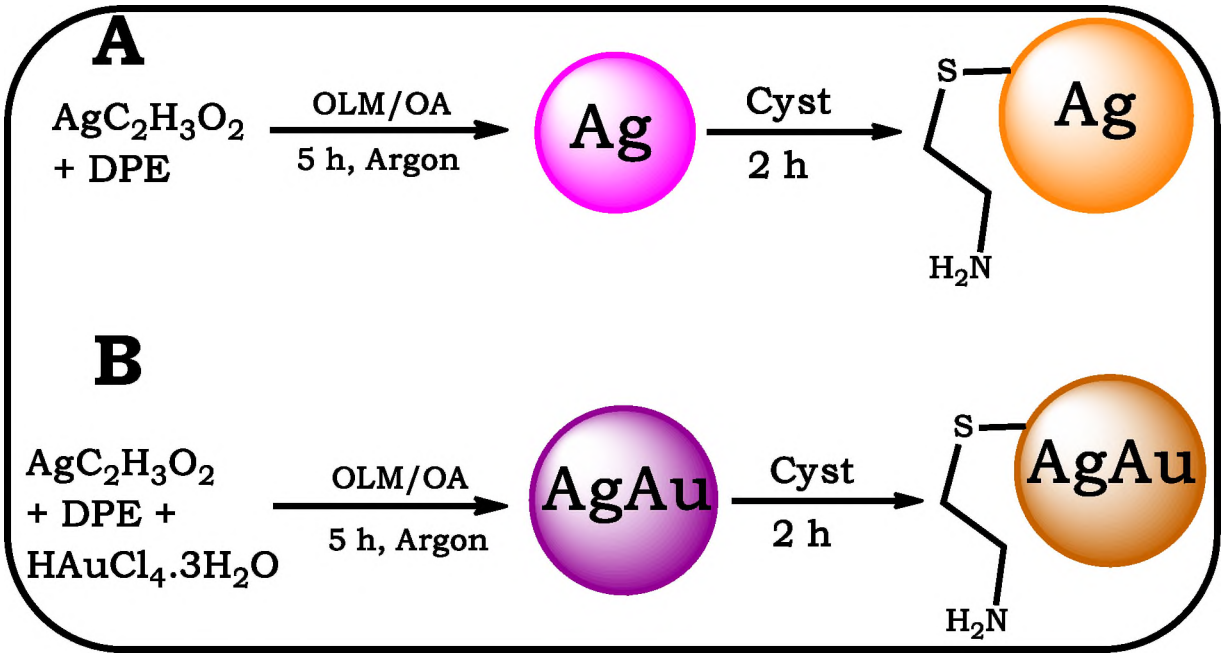

Scheme 3.1: Synthetic route for cysteamine (Cyst) capped silver (11.3) (A), and silver–gold nanoalloy (11.6) (B) from organometallic route. OLM = Oleylamine; OA = Oleic acid, DPE = Diphenyl ether.

3.1.1.2 Synthesis of semiconductor QDs

Hydrothermal and organometallic synthetic routes were employed in the syntheses of the QDs. The hydrothermal synthetic routes were mainly used for the syntheses of the glutathione (GSH) and thioglycolic acid (TGA) functionalised QDs namely: CdTe/ZnO, CdTe/ZnSe/ZnO, CdTe/ZnS/ZnO, CdTeSe, CdTeSe/ZnO; **Schemes 3.2** and **3.3**. The NaHTe or NaHSe QDs precursors were prepared by mixing appropriate mole ratios of sodium borohydride, tellurium or selenium in a known volume of water and the reaction mixtures were vigorously bubbled with argon or nitrogen flow for 12 h until the appearance of pale pink for NaHTe or pale brown for NaHSe indicating successful formation of the respective precursors. Prior to the injection of the precursors into the flask containing appropriate mole

ratios of $CdCl_2$ and stabilizers (TGA or GSH), the pH of the reaction mixture was adjusted to pH 11 with NaOH, followed by deaeration and maintenance of the reaction under refluxing with argon flow to form the QDs, **Schemes 3.2** and **3.3**. The absorption and fluorescence spectra were used to monitor the crystal growths of the QDs at a predetermined time. The QDs growth follows the Oswald ripening process due to varied reaction time (longer heating time afforded large sized QDs, hence, different sizes of QDs were collected at different reaction time). CdSeTe/CdTeS/ZnSeS QDs were synthesised via the organometallic route and the hydrophobic forms of the TOPO capped CdSeTe/CdTeS/ZnSeS QDs were treated with MSA to form hydrophilic CdSeTe/CdTeS/ZnSeS–MSA QDs as shown in **Scheme 3.3D**.

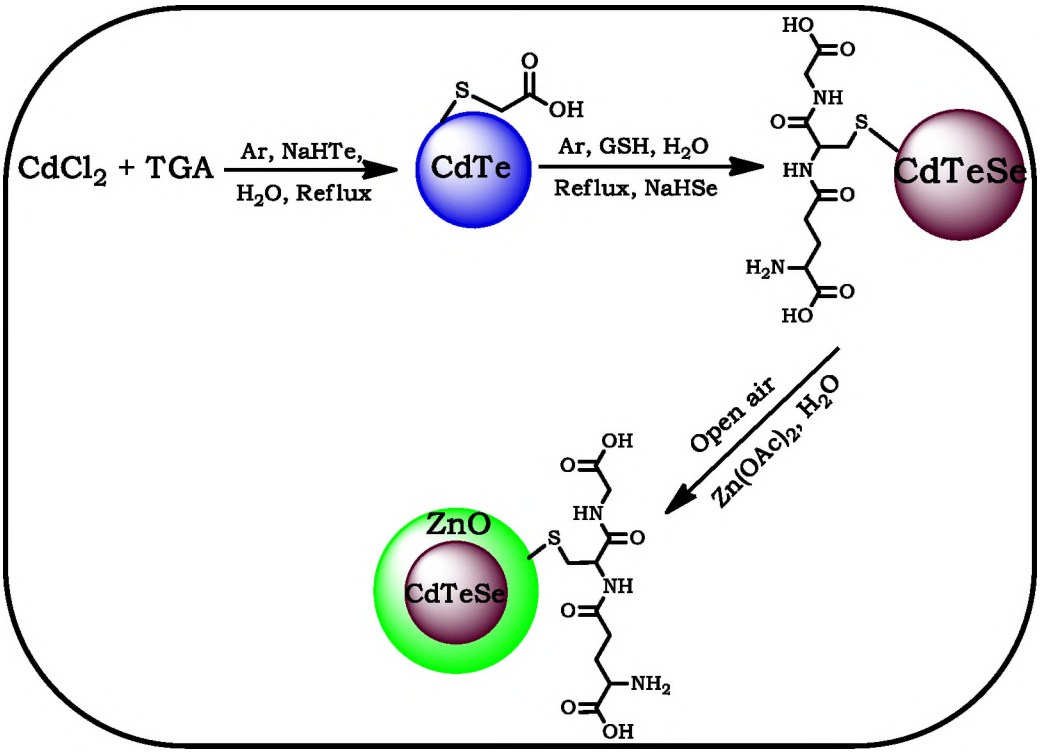

Scheme 3.2: Synthetic route for CdTeSe/ZnO–GSH

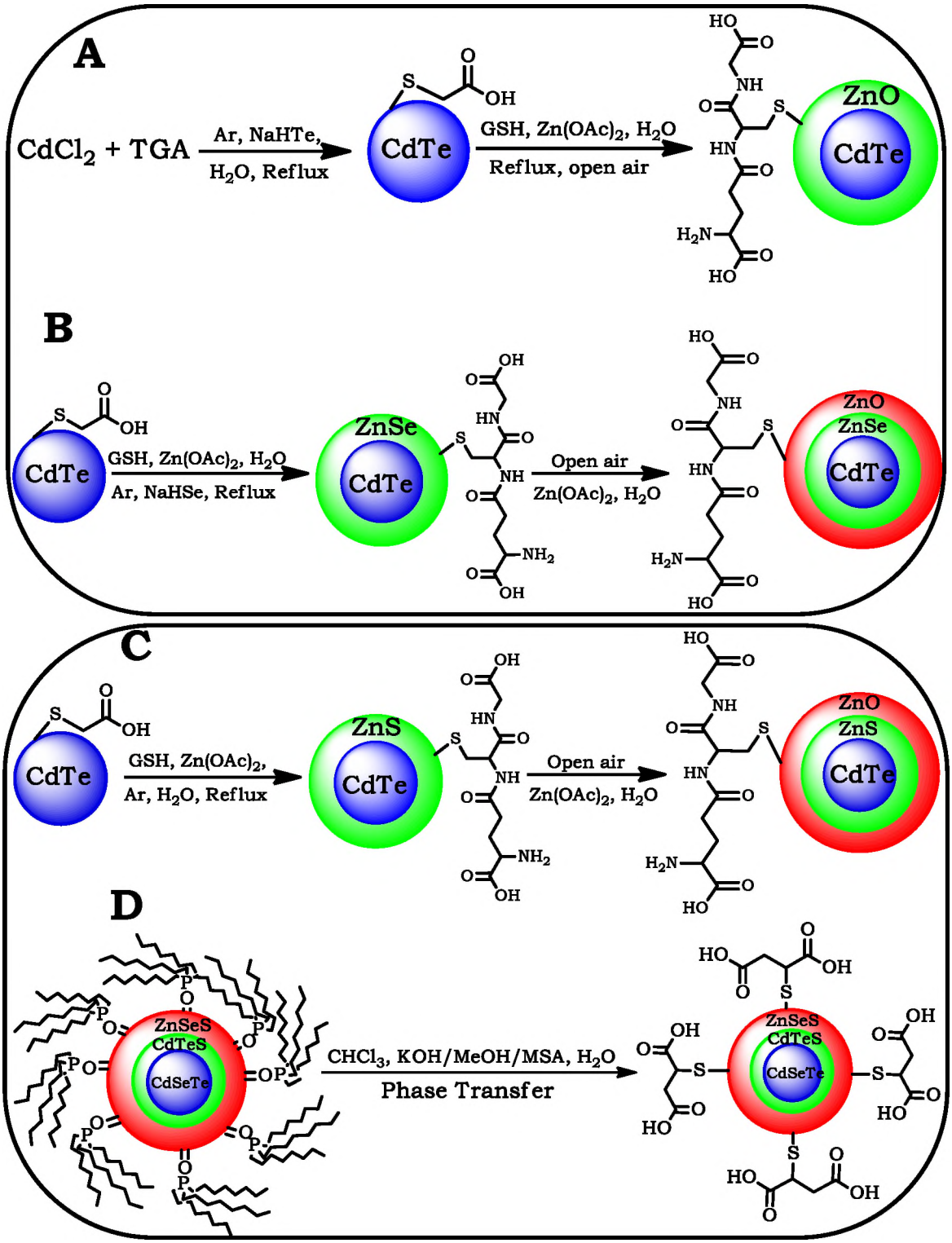

Scheme 3.3: Synthetic route for (A) CdTe/ZnO–GSH, (B) CdTe/ZnSe/ZnO–GSH, (C) CdTe/ZnS/ZnO–GSH, and (D) CdSeTe/CdTeS/ZnSeS–TOPO or CdSeTe/CdTeS/ZnSeS–MSA. GSH = Glutathione, TOPO = Trioctylphosphine oxide and MSA = Mercaptosuccinic acid

3.1.2 Characterization of the NPs

3.1.2.1 Absorption and Fluorescence Spectra

The absorption spectra of the cysteamine capped AgNPs (11.3) and AgAuNPs (11.6) showed their typical surface plasmon resonance (SPR) peaks at 420 nm and 418 nm with a broad band around 540 nm, for the latter which could be adduced to the presence of Au in the nanoalloy (AgAuNPs), **Figure 3.1**, **Table 3.1**.

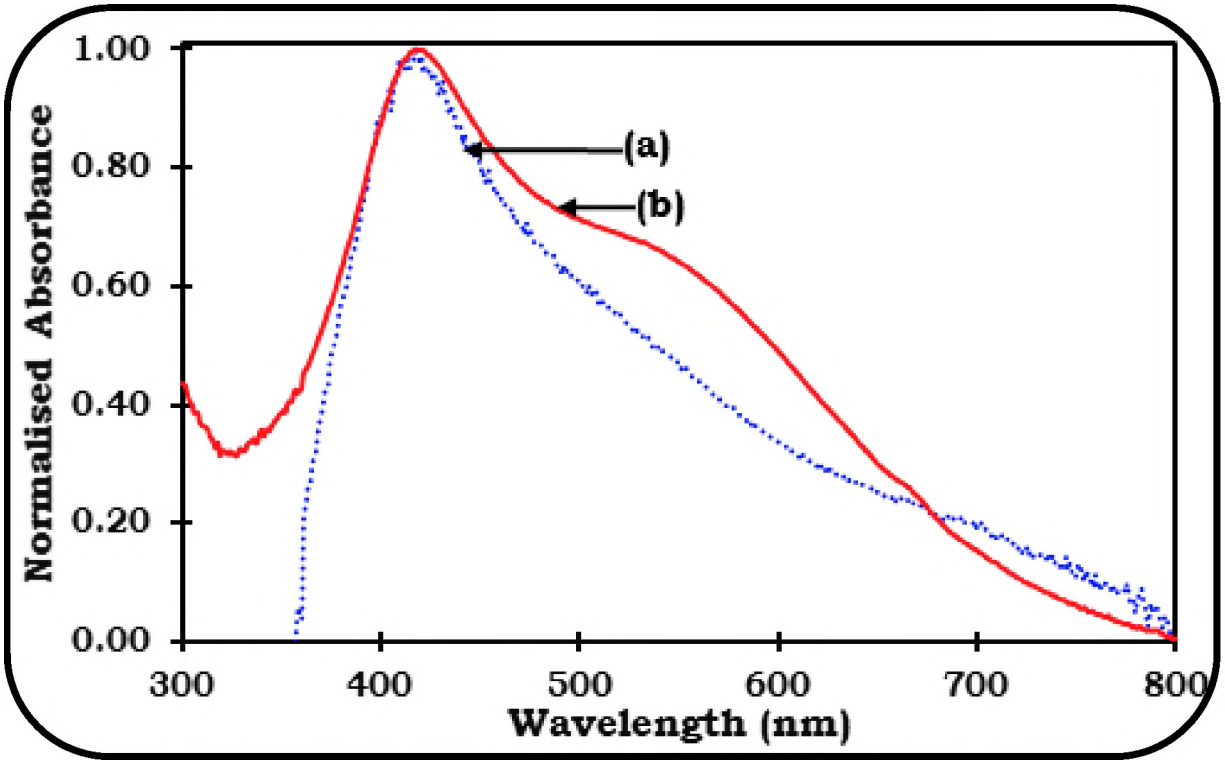

Figure 3.1: Absorption spectra of AgNPs–Cyst (11.3) (a), and AgAuNPs–Cyst (11.6) (b) in THF.

The semiconductor QDs showed their typical size dependent broad absorption and symmetrical narrow emission peaks, **Figure 3.2** (using CdTe–GSH (2.7), CdTe/ZnS–GSH (4.1), CdTe/ZnS/ZnO–GSH (4.7), CdTe/ZnS/ZnO–GSH (5.8) and CdTe/ZnS/ZnO–GSH (8.9) in water as

examples). A well–ordered bathochromic shift was observed in the absorption and emission wavelengths of the QDs as the heating time increases with increment in the particle sizes, **Table 3.1**. It is noteworthy that the addition of shells often reduces the surface defects on the core or core shell QDs resulting in bathochromic shift and enhanced photophysical properties **[257]**. In general, the bathochromic shifts in the absorption and emission wavelengths of the QDs follows this trend: core/shell/shell > core/shell > core, **Figure 3.2**. The red shifting in the absorption and emission wavelength of the core/shell/shell QDs in comparison to the core or core/shell could be adduced to the presence of more passivation on their core or core/shell.

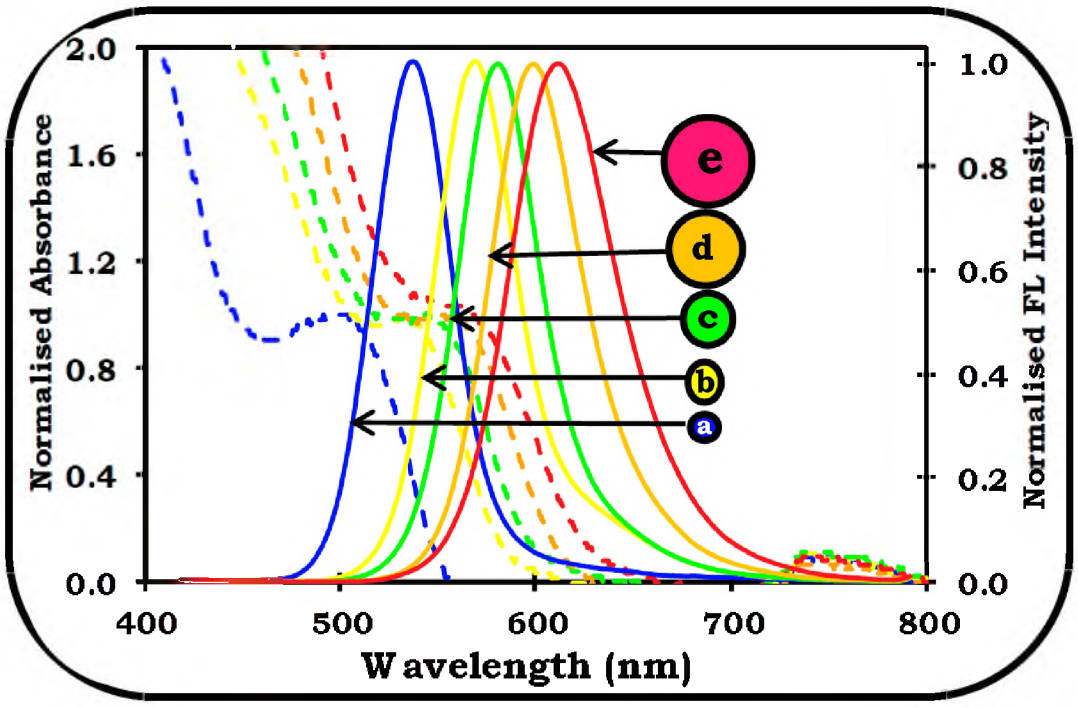

Figure 3.2: Normalized absorption (dotted line) and emission (solid line) spectra of (a) CdTe–GSH (2.7), (b) CdTe/ZnS–GSH (4.1), (c) CdTe/ZnS/ZnO–GSH (4.7), (d) CdTe/ZnS/ZnO–GSH (5.8), and (e) CdTe/ZnS/ZnO–GSH (8.9) in water at $\lambda_{exc.}$ = 400 nm.

Table 3.1: Absorption and emission data of nanoparticles employed in this work

Nanoparticles	Media	λ_{abs} (nm)	λ_{ems} (nm)
AgNPs–Cyst (11.3)	**THF**	**420**	
AgAuNPs–Cyst (11.6)	**THF**	**418, 540**	
Core QDs			
CdTe–TGA (2.8)	**Water**	539	581
CdTe–GSH (3.2)	**Water**	504	537
CdTe–GSH (3.8)	**Water**	512	542
CdTe–GSH (2.7)	**Water**	516	544
CdSe–TOPO (3.8)	**Chloroform**	551	568
CdTeSe–TGA (3.4)	**Water**	503	562
CdTeSe–GSH (3.6)	**Water**	500	594
Core/Shell QDs			
CdSe/ZnS–TGA (4.0)	**Water**	568	597
CdTe/CdS–GSH (3.1)	**Water**	515	547
CdTe/ZnSe–GSH (4.1)	**Water**	535	569
CdTe/ZnS–GSH (4.1)	**Water**	527	553
CdTe/ZnO–TGA (4.0)	**Water**	589	628
CdTe/ZnO–GSH (4.6)	**Water**	479	527
CdTeSe/ZnO–TGA (4.7)	**Water**	493	586
CdTeSe/ZnO–TGA (6.6)	**Water**	499	608
CdTeSe/ZnO–GSH (5.1)	**Water**	491	582
CdTeSe/ZnO–GSH (6.5)	**Water**	511	612

Core/Shell/Shell			
CdTe/CdS/ZnS–GSH (3.2)	**Water**	520	547
CdTe/CdS/ZnS–GSH (4.5)	**Water**	538	578
CdTe/CdS/ZnS–GSH (4.7)	**Water**	546	588
CdTe/CdS/ZnS–GSH (5.1)	**Water**	560	598
CdTe/CdS/ZnS–GSH (5.2)	**Water**	548	599
CdTe/CdS/ZnS–GSH (6.3)	**Water**	580	626
CdTe/ZnSe/ZnO–GSH (4.5)	**Water**	546	581
CdTe/ZnSe/ZnO–GSH (6.2)	**Water**	556	599
CdTe/ZnSe/ZnO–GSH (7.6)	**Water**	569	612
CdTe/ZnS/ZnO–GSH (4.7)	**Water**	547	582
CdTe/ZnS/ZnO–GSH (5.8)	**Water**	555	600
CdTe/ZnS/ZnO–GSH (8.9)	**Water**	576	625
CdSeTe/CdTeS/ZnSeS–TOPO (6.6)	**Chloroform**	612	625
CdSeTe/CdTeS/ ZnSeS–MSA (7.3)	**Water**	617	ND
SiNPs–APTES (20)*	–	–	–
ZnO/SiNPs–APTES (13)*	–	–	–

λ_{abs} = Absorption maxima, λ_{ems} = Emission maxima; Values in brackets represent the size of the NPs obtained from XRD. The asterisk represent values obtained from TEM

3.1.2.2 XRD Diffractograms

The cysteamine capped AgNPs showed five diffraction patterns which is typical of AgNPs (11.3) with peaks at 2θ values of 38.47°, 44.67°, 64.70°, 77.65°, 81.77°. The diffraction pattern of the AgAuNPs–Cyst (11.6) depicts pattern at 2θ values of 38.71°, 44.90°, 65.17°, 78.16° and 82.25°, **Figure 3.3**. The slight shift in the

2θ values of the AgAuNPs–Cyst (11.6) in comparison to AgNPs–Cyst (11.3) could be attributed to the presence of the Au in the latter (AgAuNPs–Cyst (11.6)).

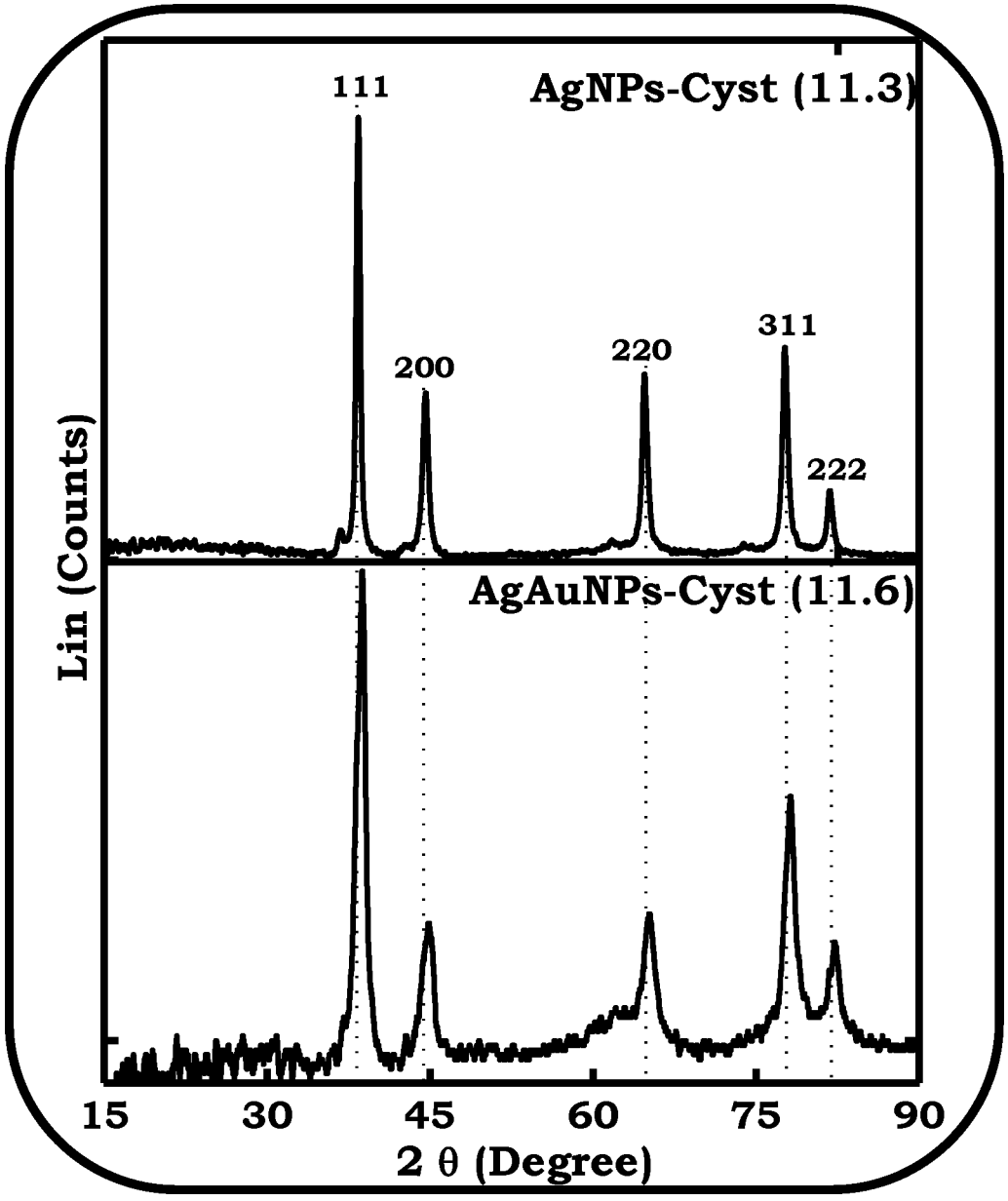

Figure 3.3: XRD diffractograms of AgNPs–Cyst (11.3) and AgAuNPs–Cyst (11.6)

The five diffraction patterns observed in the diffractograms of the AgNPs–Cyst (11.3) and AgAuNPs–Cyst (11.6) correspond to the crystalline planes of the faced–centred cubic structure of metallic silver with planes at 111, 200, 220, 311, 222

(JCPDS file No. 00-004-0783). The sizes of the NPs were determined based on the Debye-Scherrer equation (3.1) **[258]**:

$$d = \frac{k\lambda}{\beta Cos\theta} \qquad \textbf{(3.1)}$$

where λ is the wavelength of the X-ray source (1.5405 Å), k is an empirical constant equal to 0.9, β is the full width at half maximum of the diffraction peak and θ is the angular position. The diameters are 11.3 nm for AgNPs–Cyst and 11.6 nm for AgAuNPs–Cyst, **Table 3.1** (sizes in brackets after the name).

The XRD diffractogram of glutathione (GSH) showed a very broad peak at 2θ = 27° to 48° indicating the highly amorphous nature. The GSH capped QDs depicted three well resolved diffraction patterns with 2θ values which are consistent with the zinc blend crystal and cubic structure at planes 111, 220 and 311, **Figure 3.4**. The diffraction patterns of the core/shells or core/shells/shells QDs were similar to that of the core with slight shifts. In addition to the shift in 2θ values, there is broadening for the core/shell or core/shell/shell diffraction patterns, **Figure 3.4**. The three distinct diffraction patterns depicted by the GSH–QDs are listed as follows: CdTe–GSH (3.2) 2θ = 26.3°, 43.8°, 51.9°; CdTe/ZnSe–GSH (4.1) = 26.4°; and CdTe/ZnSe/ZnO–GSH (4.5) = 26.8°, 44.6°, 52.8°. The MSA capped CdSeTe/CdTeS/ZnSeS (7.3) QDs also showed similar patterns to the zinc blend crystal and cubic structure except for the appearance of an additional diffraction peak at 2θ = 38° which could be due to its ternary alloy crystal lattice form, **Figure 3.4**. The QDs sizes were

calculated based on the Debye–Scherrer equation 3.1 as defined above **[258]**, and are shown in brackets, **Table 3.1**.

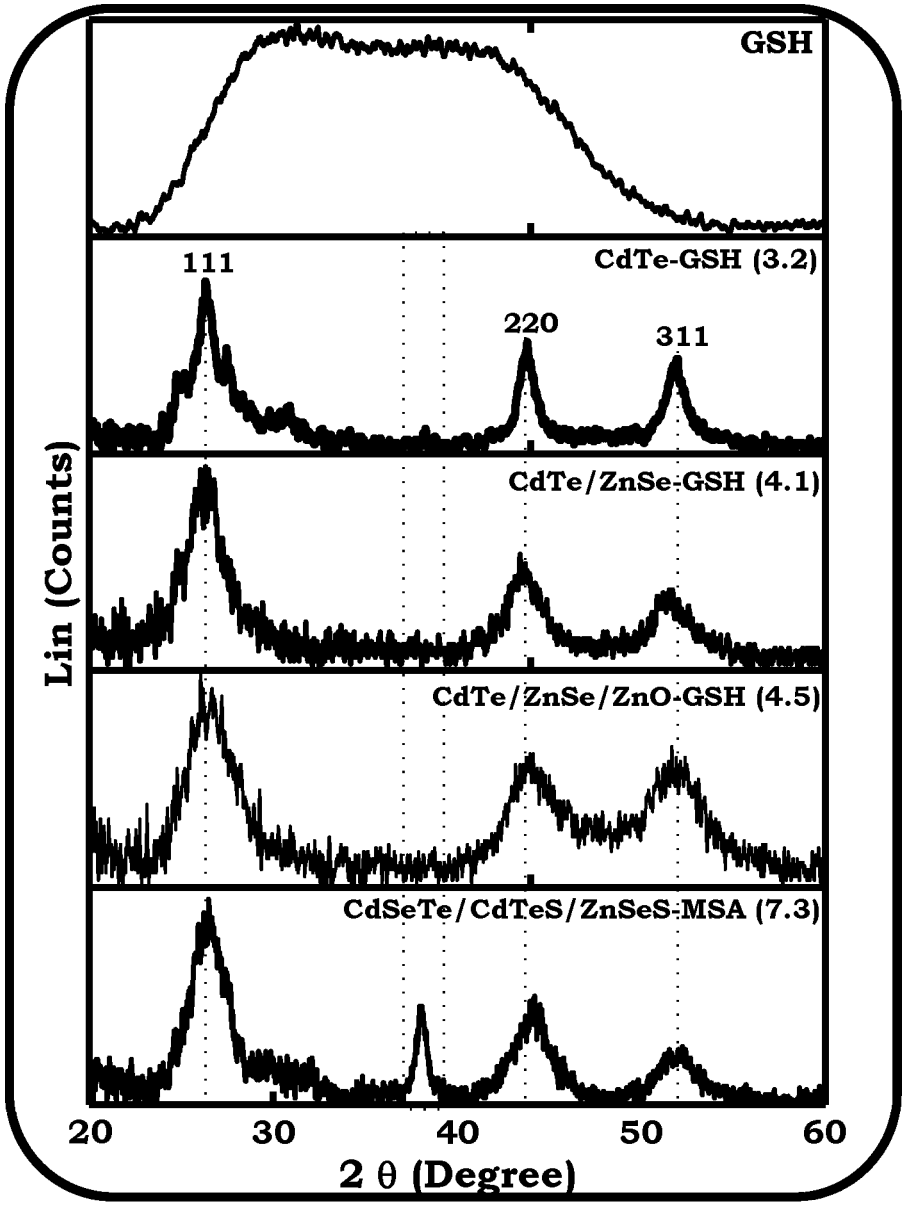

Figure 3.4: XRD diffractograms of CdTe–GSH (3.2), CdTe/ZnSe–GSH (4.1), CdTe/ZnSe/ZnO–GSH (4.5), and CdSeTe/CdTeS/ZnSeS–MSA (7.3).

3.1.2.3 TEM Micrographs

The TEM micrographs of AgNPs–Cyst and AgAuNPs–Cyst showed spherical shapes with estimated mean sizes of 14.2 nm and 20.9 nm, **Figure 3.5**.

These values are larger than obtained from XRD, this could be due to the sample preparation for TEM which involves evaporation of a solvent, which could lead to agglomeration.

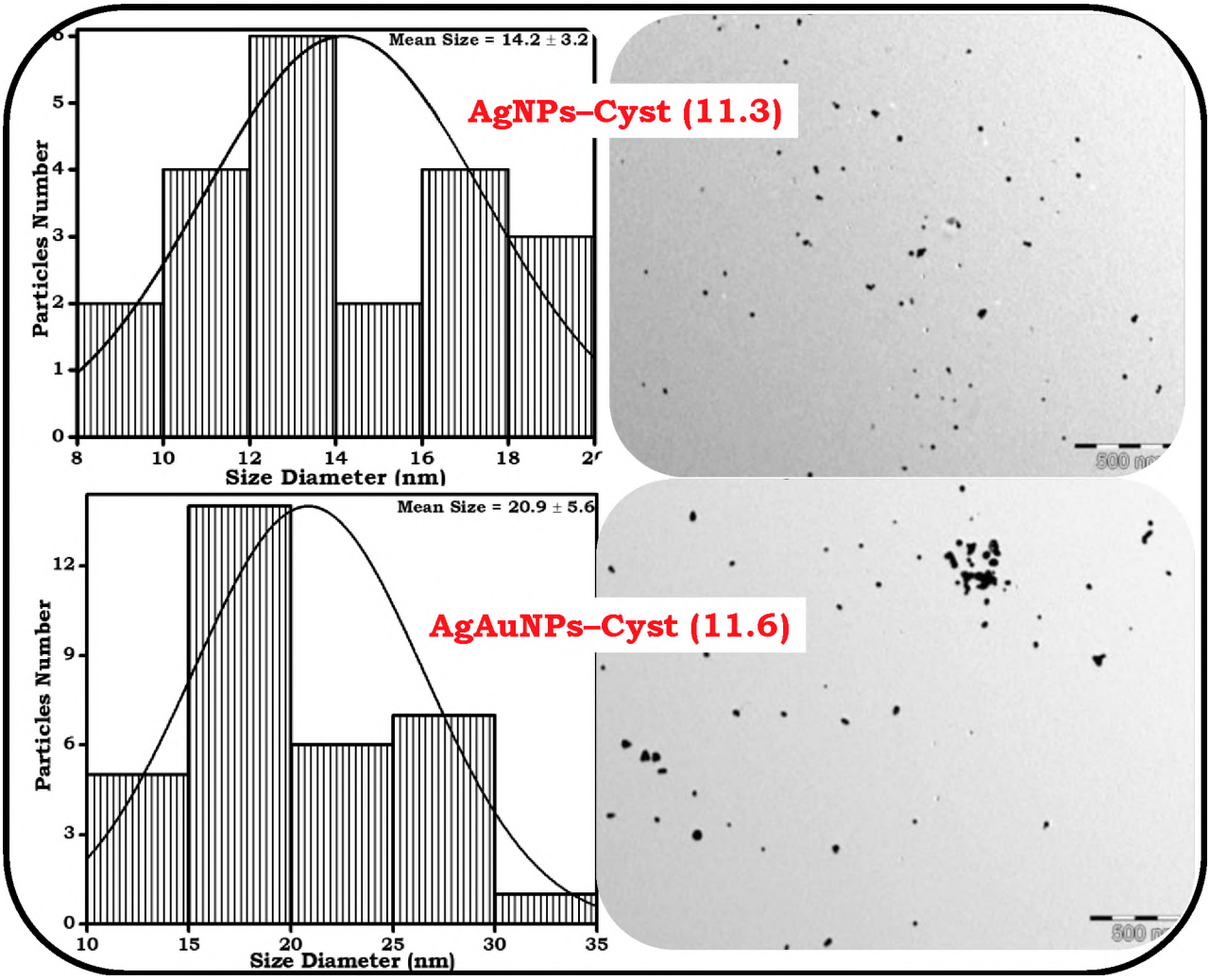

Figure: 3.5: Histograms and TEM micrographs of AgNPs–Cyst (11.3) and AgAuNPs–Cyst (11.6)

The morphologies and size distributions of the QDs (using CdSe–TOPO (4.2) and CdSeTe/CdTeS/ZnSeS–TOPO (6.6) as examples, **Figure 3.6**) were determined using a TEM. All the QDs were spherical with mean diameter of 4.2 ± 0.8 nm and 6.6 ± 0.8 nm for CdSe–TOPO (4.2) and

CdSeTe/CdTeS/ZnSeS–TOPO (6.6), respectively. The particles were mainly monodispersed with some polydispersity in some cases. The diameter of the QDs, as determined by TEM, are relatively the same as obtained by XRD.

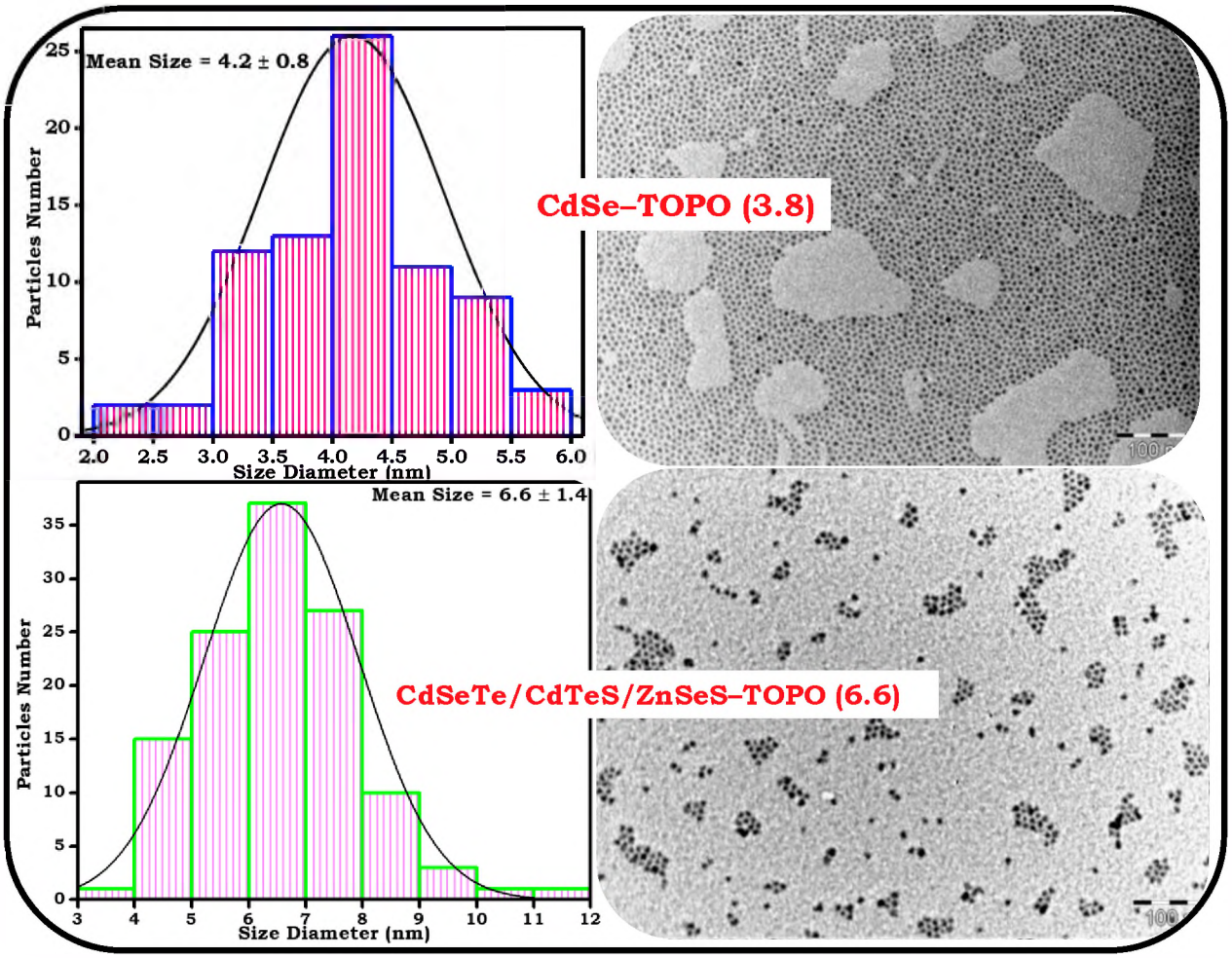

Figure 3.6: Histograms and TEM micrographs of CdSe–TOPO (3.8) and CdSeTe/CdTeS/ZnSeS–TOPO (6.6)

The mean sizes for SiNPs–APTES (20 nm) and ZnO/SiNPs–APTES (13 nm) were determined from TEM, **Table 3.1.**

3.1.2.4 EDX Spectra

The obtained elemental compositions using EDX were consistent with the expected compositions, **Figure 3.7** (using AgAuNPs–Cyst (11.6), SiNPs–APTES (20), **5**–SiNPs (40), and CdSeTe/CdTeS/ZnSeS–MSA (7.3) as examples).

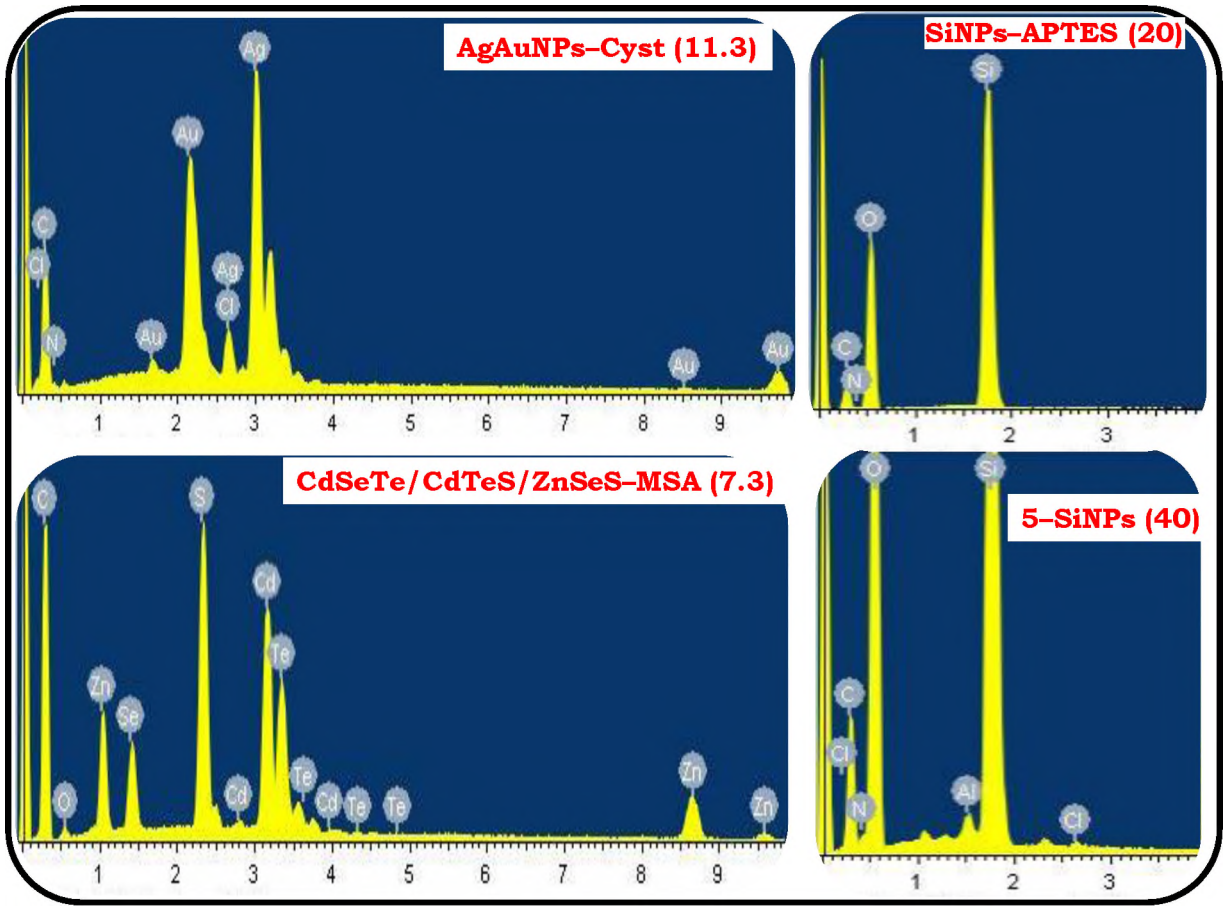

Figure 3.7: EDX spectra of AgAuNPs–Cyst (11.6), CdSeTe/CdTeS/ZnSeS–MSA (7.3), SiNPs–APTES (20), and 5–SiNPs (40)

3.1.2.5 FT–IR Spectra

The bifunctional ligands on the surface of the NPs were assessed to determine their organic functional moieties. For the cysteamine capped AgNPs (11.3) and AgAuNPs (11.6) (using AgAuNPs–Cyst (11.6) as an

example); C–N vibration at 1308 cm^{-1}, C–C vibration at 1457 cm^{-1}, C=C or NH vibration at 1641 cm^{-1}, C–H vibration at 2854 cm^{-1}, 2914 cm^{-1} were observed, **Figure 3.8**.

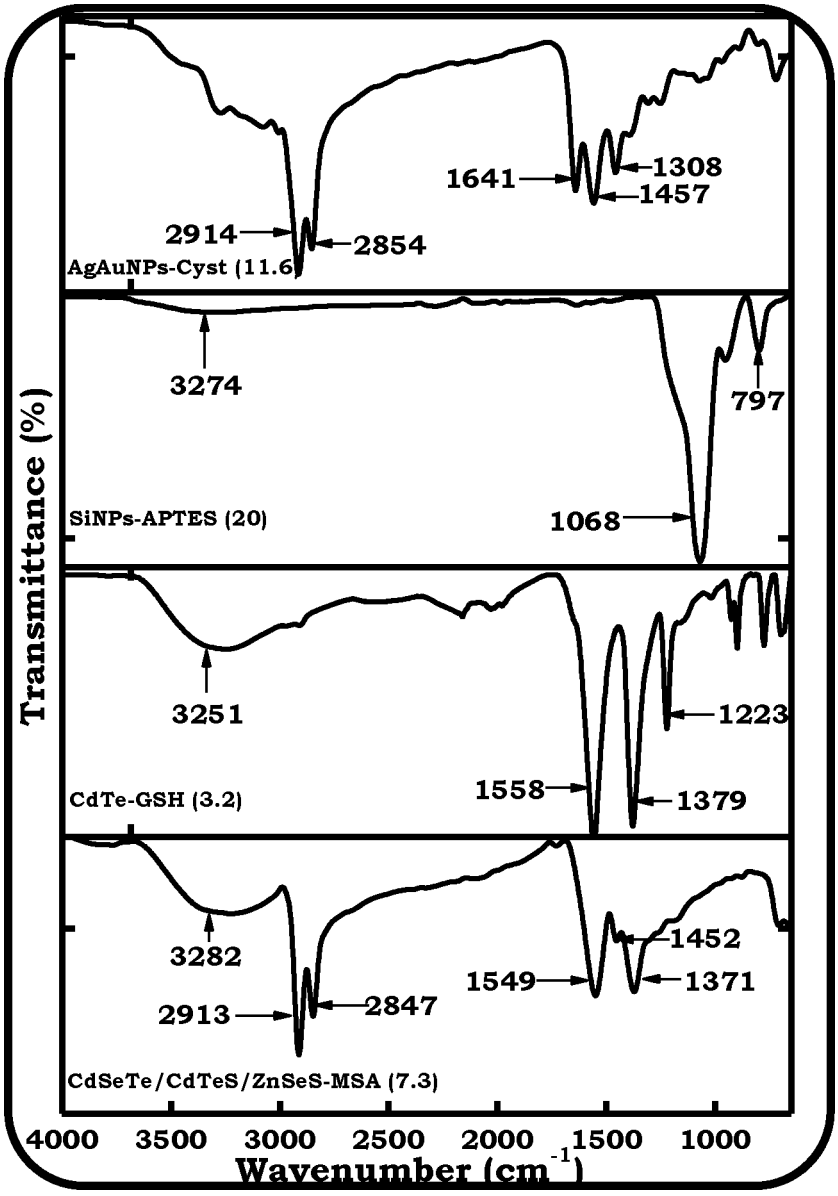

Figure 3.8: FT–IR spectra of AgAuNPs–APTES (11.6), SiNPs–APTES (20), CdTe–GSH (3.2), and CdSeTe/CdTeS/ZnSeS–MSA (7.3).

The APTES functionalised SiNPs (20) and ZnO/SiNPs (13), **Figure 3.8** (using SiNPs–APTES (20) as an example) depicted three distinct vibrational

bands at 3274 cm^{-1} corresponding to primary amine band from the capping ligand and 797 cm^{-1} and 1068 cm^{-1} corresponding to Si–O and siloxane bands respectively. The GSH capped QDs, **Figure 3.8** (using CdTe–GSH (3.2) as an example) depicted NH_2 vibrational band between 3251 cm^{-1}, a well resolved asymmetrical $–COO^-$ and symmetrical $–COO^-$ at 1558 cm^{-1} and 1379 cm^{-1} respectively, and C–N at 1223 cm^{-1}. The MSA capped QDs, **Figure 3.8** (using CdSeTe/CdTeS/ZnSeS–MSA (7.3) as an example) showed C–N vibration at 1371 cm^{-1}, C–C vibration at 1452 cm^{-1}, $–COO^-$ vibration at 1549 cm^{-1}, C–H vibration at 2847 cm^{-1}, 2913 cm^{-1} and OH vibrations between 3282 cm^{-1}. It is pertinent to note that the thiol vibrational bands of the MSA, Cyst and GSH disappeared due to the linkage with the NPs surfaces, **Figure 3.8**.

3.1.2.6 Surface Areas and Pore Sizes Analysis

The surface areas and pore sizes of the SiNPs–APTES (20) and ZnO/SiNPs–APTES (13) were obtained from the nitrogen adsorption/desorption isotherms using the Brunauer-Emmette-Teller (BET) and Barret-Joyner-Halenda methods.

Prior to the analysis of the SiNPs–APTES (20) and ZnO/SiNPs–APTES (13), the NPs were degassed for 24 h using a Micrometrics ASAP® 2020 surface area and porosity analyzer operated at 77 K. The nitrogen adsorption–desorption isotherms of SiNPs–APTES (20) **(Figure 3.9A)** and ZnO/SiNPs–APTES (13) **(Figure 3.9B)** shows type IV adsorption isotherms.

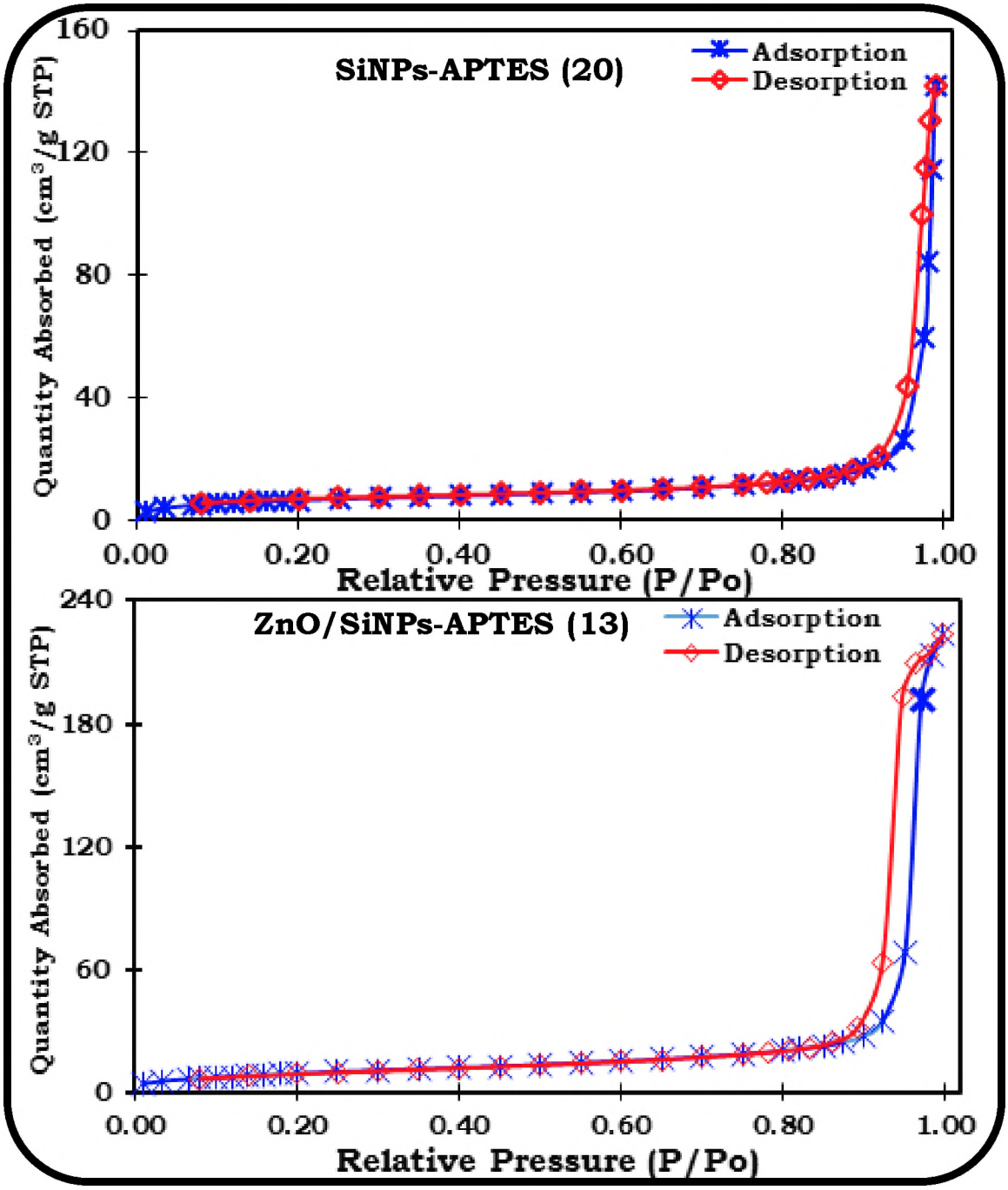

Figure 3.9: Nitrogen adsorption–desorption isotherms of SiNPs–APTES (20), and ZnO/SiNPs–APTES (13).

Type IV isotherms occur for porous adsorbent and this infer that at a low pressure, a monolayer is formed, after which a multilayer is formed at higher pressure indicating increased uptake of adsorbates with filled

pores. The surface areas of 23 m^2/g (35 m^2/g) and pore sizes of 306 Å (397 Å) for SiNPs–APTES (20) (ZnO/SiNPs–APTES (13) in brackets) were obtained. The surface areas and pore sizes of the ZnO/SiNPs–APTES were larger than that of the SiNPs–APTES. Thus, the smaller ZnO/SiNPs–APTES (13 nm) have a larger surface area than the larger SiNPs–APTES (20 nm), **Table 3.1**.

3.2 PHTHALOCYANINES (Pcs)

The synthesis of compounds **2**, **4**, **6**, **7**, **9** have been reported elsewhere and will not be discussed in the following subsections. The new compounds **3**, **5**, **8**, **10**–**14** synthesized in this work will be discussed in detail in the following subsections, **Schemes 3.4–3.9**.

3.2.1 Metal–free 2,3–bis[2'-(2''–mercaptoethoxy]–9,10,16,17,23,24–hexa–*n*–butoxy phthalocyanine (1), Scheme 3.4

Scheme 3.4 depicts the synthetic route for Pc **1**. Pc **15** was synthesized as reported in the literature **[253]**. Iodination of Pc **15** was done to obtain Pc **16**. Finally, thionation of **16** was performed to obtain Pc **1**. The Pcs were characterized with emphasis on Pc **1** using FT–IR, ^{1}H NMR, spectroscopies and MALDI–TOF mass spectrometry, and elemental analyses. The obtained data were consistent with the predicted structures. The compound showed good solubility in most organic solvents.

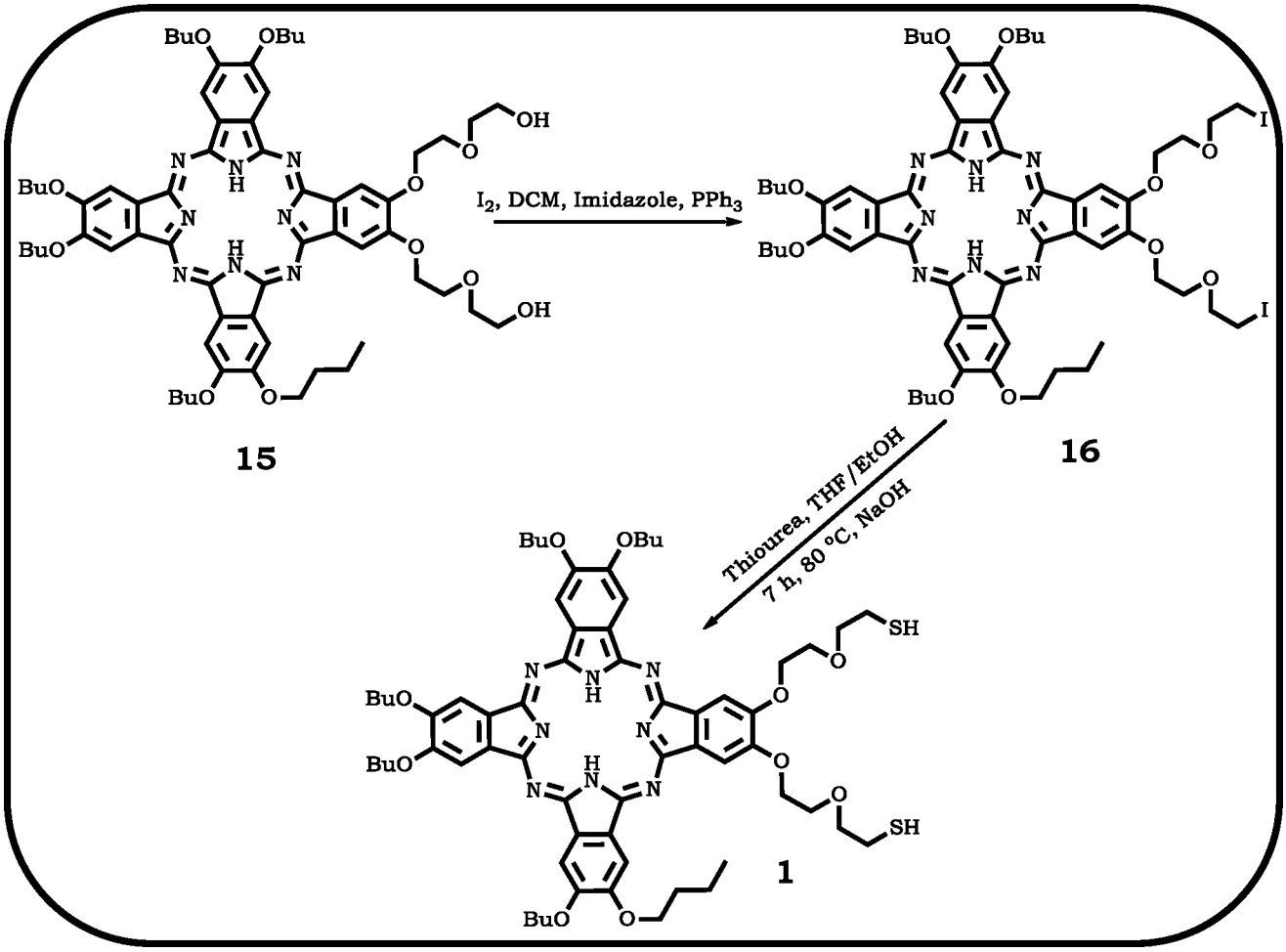

Scheme 3.4: Synthetic route for Pc 1.

The FT–IR spectrum of Pc **1** confirmed the presence C–H vibration at 2930 cm^{-1}, 2865 cm^{-1}, S–H vibration at 2556 cm^{-1}, C–C vibration at 1603 cm^{-1}, 1451 cm^{-1}, C–N vibration at 1380 cm^{-1}, C–O–C at 1270 cm^{-1}, C–O vibration at 1096 cm^{-1}, and 1019 cm^{-1}, **Figure 3.10**.

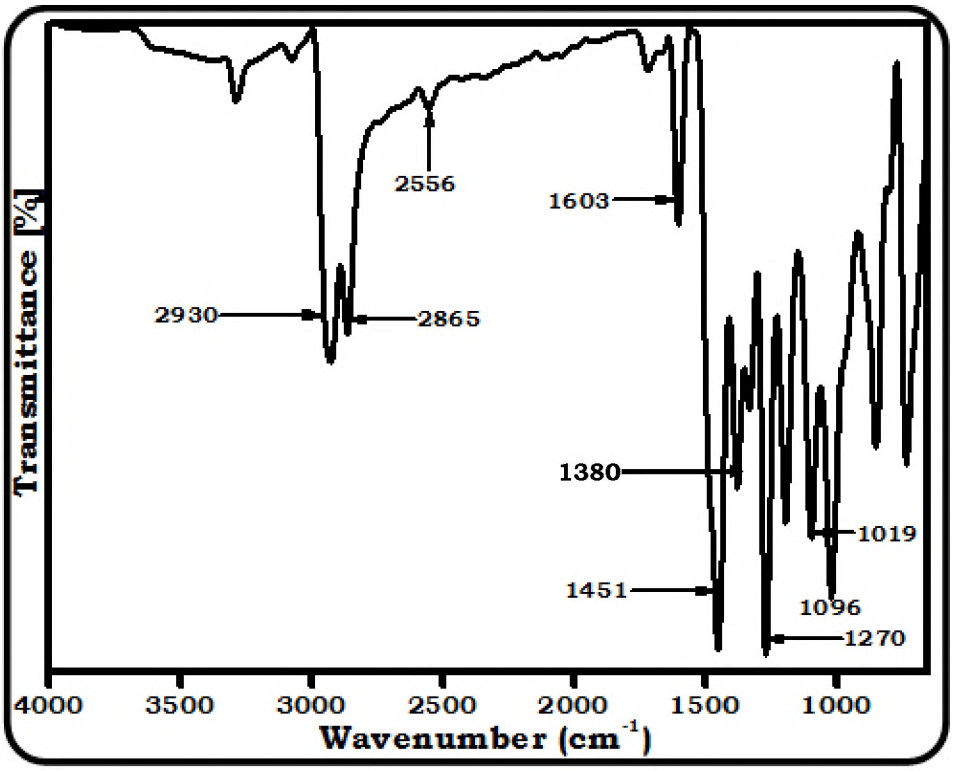

Figure 3.10: FT–IR spectrum of Pc 1

The ^{1}H NMR spectrum of Pc **1** depicted multiplet resonating at 8.38–8.26 ppm accounting for the aromatic protons of the Pc ring which gave 8 upon integration while the CH_2 protons occurred as multiplet resonating at 4.68–1.88 ppm and integrated for 52. The thiol resonance signal gave 2 protons upon integration at 1.54 ppm. The NH in the cavity of the Pc ring accounted for 2 protons at -2.96 ppm and the CH_3 substituents gave 18 protons at 1.25 ppm.

For Pc **1**, mass to charge ratio of 1188 m/z was expected and 1189 m/z was obtained. The ground state electronic absorption spectrum of Pc **1** in DCM is shown in **Figure 3.11**. The components of the split Q–band of the compound were observed at 663 nm and 700 nm, **Table 3.2**. The split Q–

band is associated with the absence of central metal in the Pc macrocycle. The UV–Vis spectrum of Pc **1** did not show any sign of aggregation at concentrations ranging from 8.42 x 10^{-7} to 5.90 x 10^{-6} mol/L in DCM. The Beer-Lambert law was obeyed at the studied concentrations.

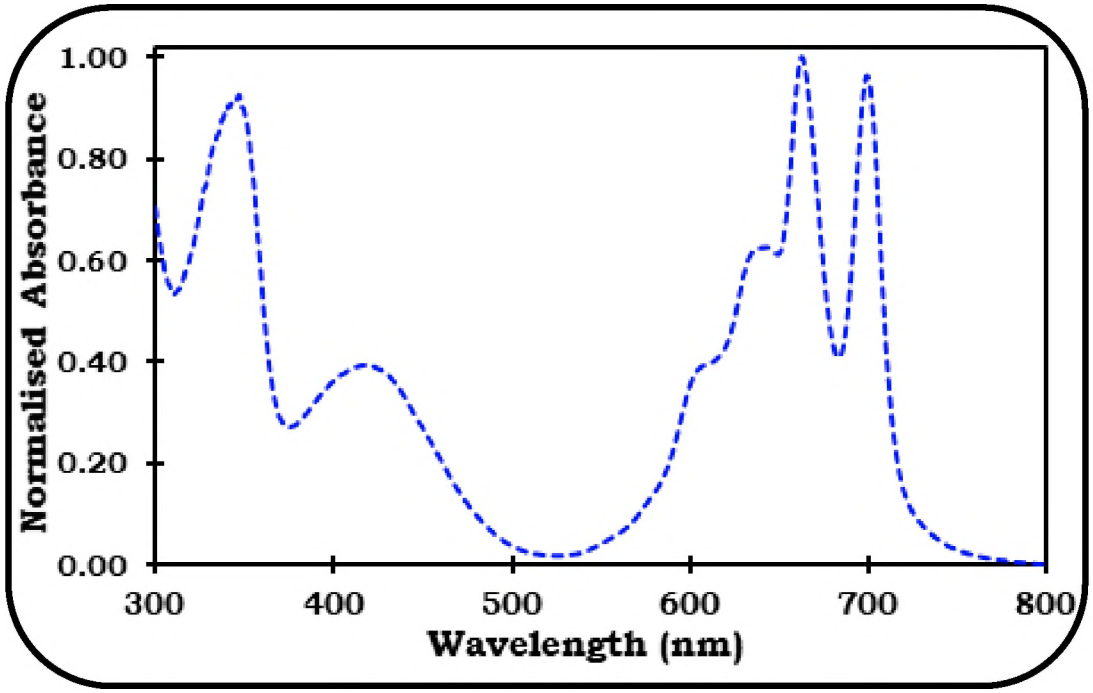

Figure 3.11: Absorption spectrum of Pc 1 in DCM at 5.90 x 10^{-6} M.

Table 3.2: Q–band of the respective compounds and their corresponding conjugates synthesised in this research work.

Compounds	Media	Q–band λ_{abs} (nm)
1	DCM	663, 700
1–CdSe–TOPO (3.8)	DCM	659, 706
2a	DMSO	674
2a–CdTe–GSH (2.4)	DMSO	673
2a–CdTe/CdS–GSH (3.1)	DMSO	674
2a–CdTe/CdS/ZnS–GSH (4.2)	DMSO	673
2a–CdTe/CdS/ZnS–GSH (5.1)	DMSO	673
2a–CdTe/CdS/ZnS–GSH (6.7)	DMSO	675
2b	DMSO	674
2b–HSA	DMSO	674
2b–Chitosan	DMSO	675
2b–SiNPs–APTES (20)*	DMSO	675
2b–ZnO/SiNPs–APTES (13)*	DMSO	675
3	DMSO	697
3–SiNPs(60)* [Doped]	DMSO	699
4	DMSO	681
4–SiNPs(34)* [Doped]	DMSO	681
5	DMSO	684
5–SiNPs(40)* [Doped]	DMSO	687

6	DMSO	678
6–SiNPs (39)* [Doped]	DMSO	680
6–CdTe–GSH (2.4)	DMSO	681
6–CdTe/CdS–GSH (3.1)	DMSO	682
6–CdTe/CdS/ZnS–GSH (4.2)	DMSO	680
6–CdTe/CdS/ZnS–GSH (5.1)	DMSO	681
6–CdTe/CdS/ZnS–GSH (6.7)	DMSO	681
6–CdTe–GSH (2.9)	DMSO	680
6–CdTe/ZnO–GSH (4.6)	DMSO	680
6–CdTeSe–GSH (3.6)	DMSO	680
6–CdTeSe/ZnO–GSH (5.1)	DMSO	680
6–CdTeSe/ZnO–GSH (6.5)	DMSO	680
7	PBS	680
7–CdTe/CdS/ZnS–GSH (5.2)	PBS	675
7–CdTe/CdS/ZnS–GSH (6.3)	PBS	674
8	DMSO	691
8–CdTe–GSH(3.2)	DMSO	688
8–CdTe/ZnSe–GSH (4.1)	DMSO	689
8–CdTe/ZnSe/ZnO–GSH (4.5)	DMSO	689
8–CdTe/ZnSe/ZnO–GSH (6.2)	DMSO	689
8–CdTe/ZnSe/ZnO–GSH (7.6)	DMSO	689

9	PBS	689
9–CdTe–GSH (2.7)	PBS	685
9–CdTe/ZnS–GSH (4.1)	PBS	685
9–CdTe/ZnS/ZnO–GSH (4.8)	PBS	685
9–CdTe/ZnS/ZnO–GSH (5.8)	PBS	685
9–CdTe/ZnS/ZnO–GSH (8.9)	PBS	685
10	DMSO	676
10–AgNPs–Cyst (11.3)	DMSO	675
10–AgAuNPs–Cyst (11.6)	DMSO	675
11	DCM	676
11–CdSeTe/CdTeS/ZnSeS–TOPO (6.6)	DCM	675
12	DCM	643
12–CdSeTe/CdTeS/ZnSeS–TOPO (6.6)	DCM	663
13	DCM	676
13–CdSeTe/CdTeS/ZnSeS–MSA (7.3)	DCM	676
14	DCM	642
14–CdSeTe/CdTeS/ZnSeS–MSA (7.3)	DCM	645

Values in brackets represent the size of the NPs alone obtained from XRD and the asterisk represent values obtained from TEM

3.2.2 Zinc(II) 1,8(11),15(18),22(25)–tetra–(4'–*tert*–butylphenoxy) phthalocyanine (3) and aluminum(III) chloride 2,9(10),16(17),23(24)–tetra–(4'–*tert*–butylphenoxy)phthalocyanine (5)

Scheme 3.5 illustrates the synthetic routes for **3** (**Scheme 3.5A**) and **5** (**Scheme 3.5B**). Compound **3** was obtained by cyclotetramerization of 4

moles equivalent of 3–(4'–*tert*–butylphenoxy) phthalonitrile in the presence of zinc salt, nitrobenzene, ammonium molybdate and urea, followed by refluxing under inert atmosphere. Compound **5** was obtained by cyclocondensation of 4–(4–*tert'*–butylphenoxy) phthalonitrile in the presence of aluminium(III) chloride, quinoline and urea, followed by refluxing under inert atmosphere. The compounds were characterized by ^{1}H NMR, MALDI–TOF mass spectroscopies and elemental analyses. The obtained data were consistent with the predicted structures. The compounds showed good solubility in organic solvents.

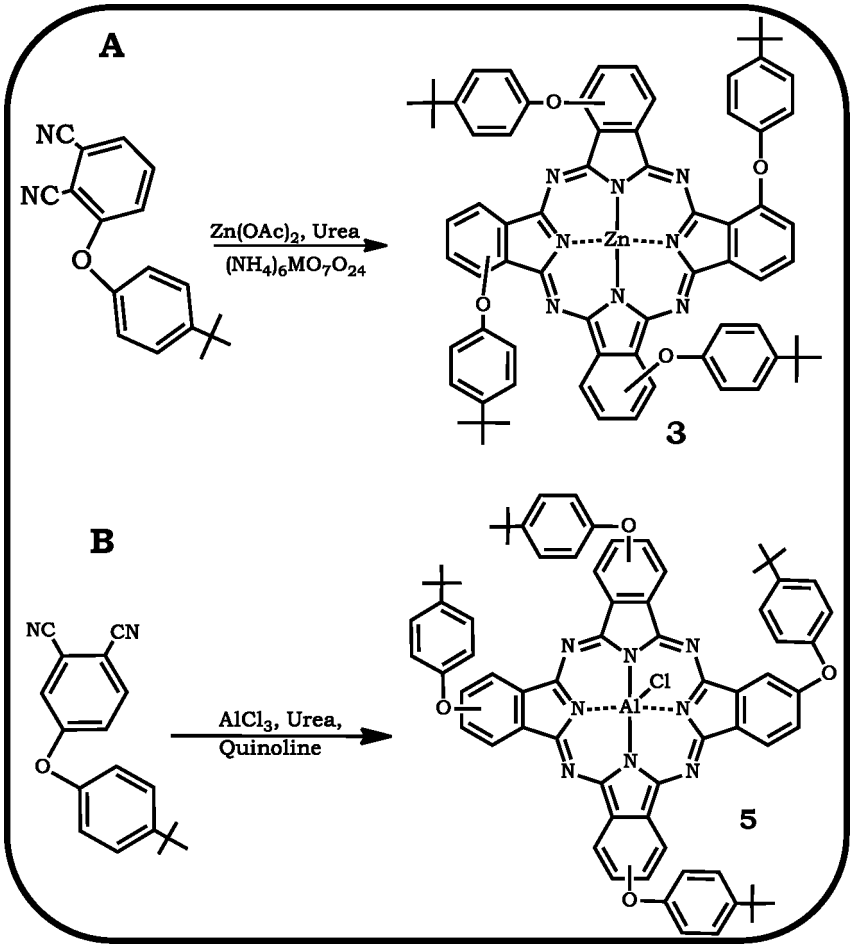

Scheme 3.5: Synthetic routes for compounds 3 (A) and 5 (B)

The ^{1}H NMR of compound **3** showed multiplet with resonance signals at 9.14–8.11 ppm which accounted for 12 protons corresponding to the Pc aromatic ring and the phenyl ring depicted multiplet which accounted for 16 protons with resonance signals at 7.86–7.49 ppm. *tert*–Butyl substituents resonating at 1.40–1.17 ppm as multiplet accounted for 36 protons upon integration. For compound **5,** the Pc aromatic ring gave 12 protons with resonance signal at 8.90–8.22 ppm while the resonance signals of the phenyl ring were observed as multiplet at 7.39–6.96 ppm and integrated to give 16 protons. *tert*–Butyl substituents resonating at 0.70–0.62 ppm as multiplet which accounted for 36 protons. *tert*–Butyl protons were seen as multiplet due to the tetra substituted nature of the obtained phthalocyanines which could be a mixture of four possible structural isomers. The different isomers showed similar NMR signals, hence no effort was made to separate them. A similar trend has previously been reported **[259]**.

For **3**, mass to charge ratio of 1169 m/z was expected and 1174 m/z was obtained. It has been reported that Pc molecular ion peaks can exist as $[M]^{+}$, $[M + nH]^{+}$, or $[M - nH]^{-}$ **[260]**, hence the observed mass spectrum pattern for compound **3**. For compound **5**, mass to charge ratio of 1168 m/z was calculated and 1135 m/z was found. This could be due to the removal of the chloride which has been reported before **[259]**.

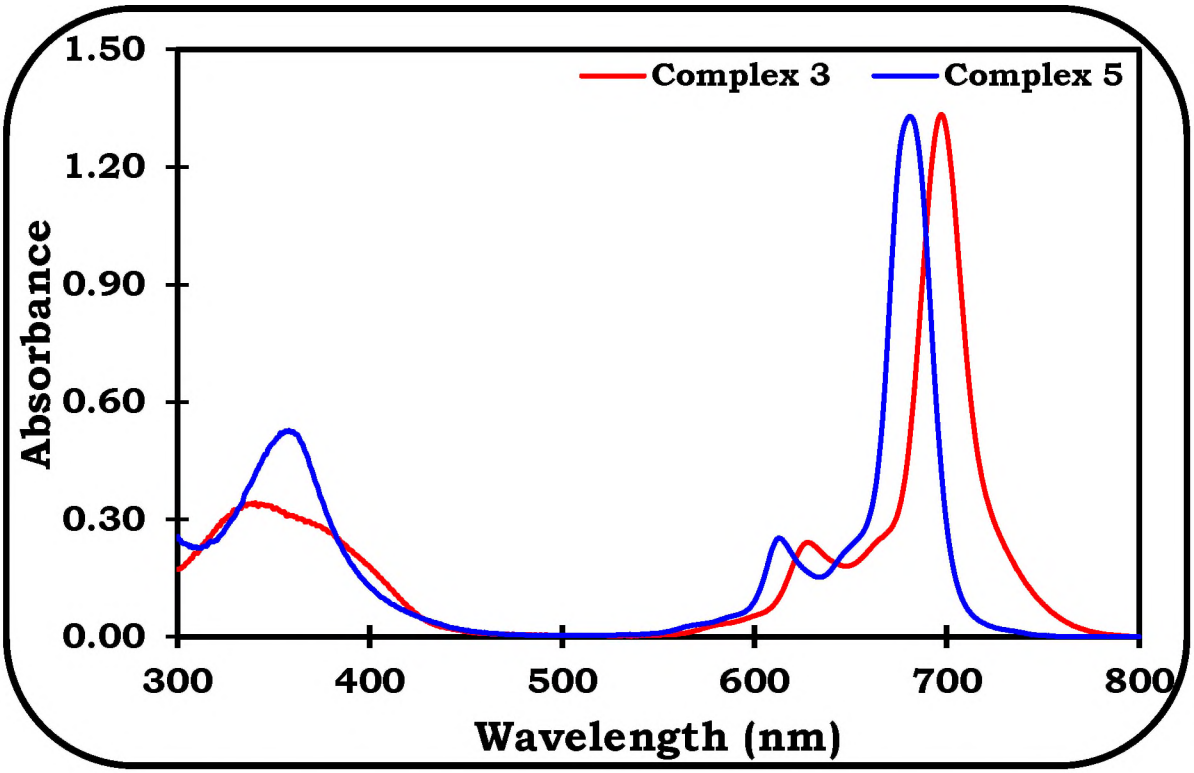

Figure 3.12: Absorption spectra of compounds 3 and 5 in DMSO (~8 × 10^{-6} M)

The UV–Vis spectra of compounds **3** and **5** were recorded at the concentrations used for the determination of triplet state parameters, ~ 8 × 10^{-6} M**, Figure 3.12**. Both compounds **3** and **5** did not show any sign of aggregation at concentrations ranging from ~ 1 x 10^{-6} to 1 x 10^{-5} mol/L in DMSO when independently measured. The Beer–Lambert law was obeyed at the studied concentrations. The Q–band of **3** was more red shifted compared to that of **4** (**Table 3.2**) due to non–peripheral substitution in the former, which is known to result in bathochromic shift **[261]**. *tert*–Butyl containing substituents are known to result in the distortion of the Pc ring due to their bulkiness **[262]**. Distortion and nature of substituents of Pcs often results in red shifting of the Q–band **[263]**, hence the observation of

the red shifting of the Q–band for **4** at 681 nm (containing *tert*–butyl substituents) compared to **6** (containing carboxyphenoxy substituents) at 678 nm, **Table 3.2**. Compound **5** was blue shifted compared to **3** and this could be attributed to the effect of relatively light metal in the former, heavy central metals are known to result in bathochromic shift in the absorption and emission wavelengths of Pcs **[138]**. For compounds **3** and **5** at concentrations less than 10^{-7} M, absorption and excitation spectra were similar and mirror images of the emission spectrum (**Figure 3.13**, using compound **3** as an example).

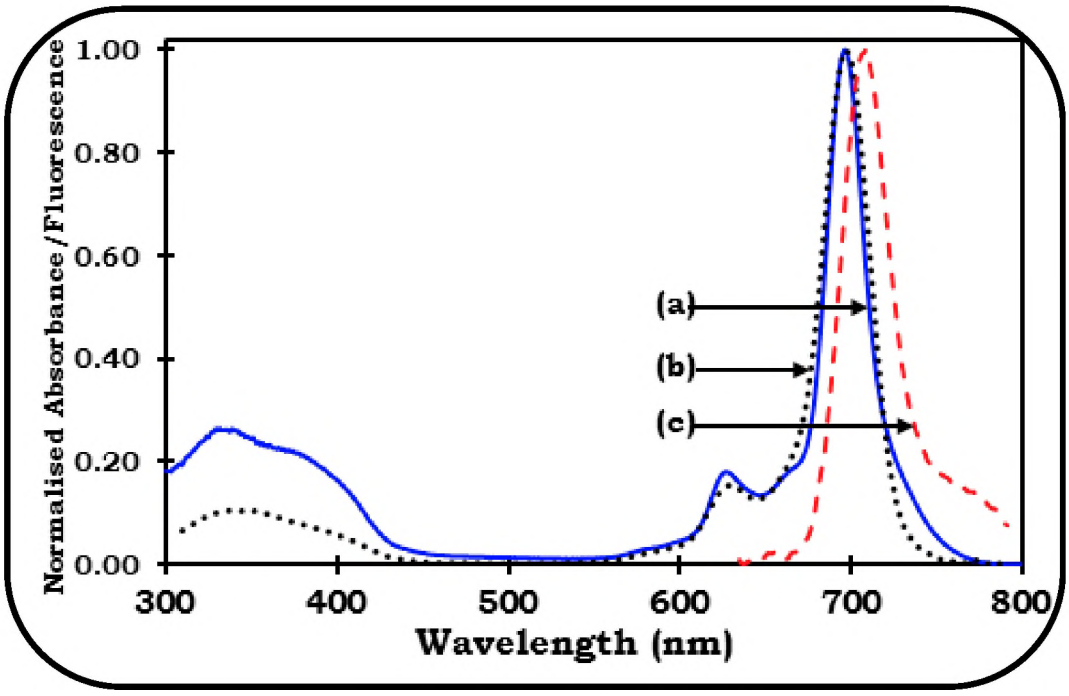

Figure 3.13: Absorption (a), excitation (b), and emission (c), spectra of compound 3 in DMSO at λ_{exc} = 616 nm.

Comparing compounds **7** and **9** having same central metal but different ring substituents, the latter showed red shifted Q–band due to more electron withdrawing groups **[139,144,264]**, **Table 3.2**.

3.2.3 Indium(III) chloride 2,9(10),16(17),23(24)–tetra–(3'–carboxyphenoxy) phthalocyanine (8)

Scheme 3.6 depicts the synthetic route for compound **8**. The cyclotetramerization of 4–(3'–carboxyphenoxy) phthalonitrile in the presence of $InCl_3$ in 1–pentanol catalyzed by DBU under nitrogen environment resulted in the formation of compound **8**.

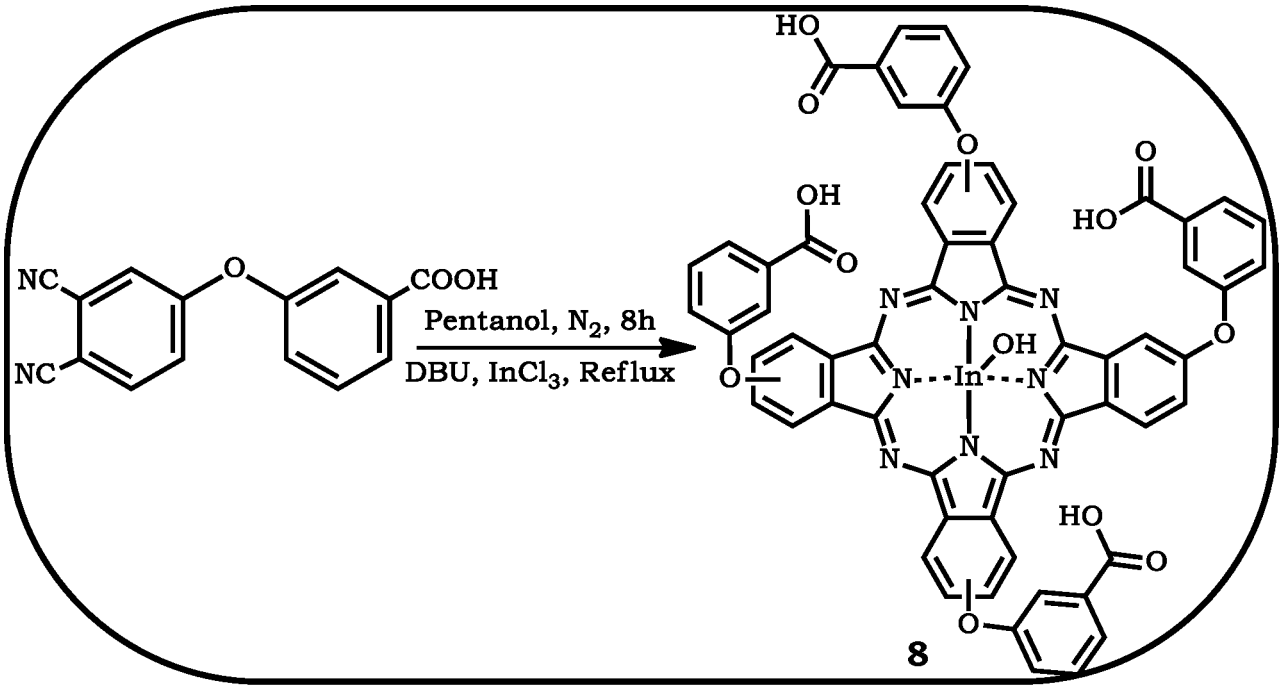

Scheme 3.6: Synthetic route for compound 8.

The compound was characterized by FT–IR, ^1H NMR, and MALDI–TOF mass spectroscopies as well as elemental analyses. The obtained data were consistent with the predicted structure.

FT–IR spectrum confirmed the presence of C=O vibration at 1716 cm^{-1} and OH vibrations between 2650 cm^{-1} and 3063 cm^{-1}.

The ^{1}H NMR spectrum of compound **8** showed the Pc aromatic ring as multiplet accounting for 12 protons with resonance signal at 8.13–7.55. The resonance signals of the phenyl ring were seen as multiplet at 7.43–6.89 ppm and integrated to give 16 protons. The COOH substituents were observed at 12.07 as a singlet, integrating for 4 protons. Resonance signal at 2.17 ppm was due to proton of the axial OH attached to the indium central metal. Note that the axial ligand was determined to be OH^- (instead of Cl^- in $InCl_3$). This is a result of the purification procedure which resulted in the replacement of Cl^- with OH.

The mass spectrum gave expected value of the synthesized molecule at m/z: 1184 $[M-4H]^-$, the loss of 4 proton ions could be due to the ionisation of the hydrogen present with 4 carboxylic moieties on the MPc ring. As earlier stated, it has been reported that Pc molecular ion peaks can exist as $[M]^+$, $[M + nH]^+$, or $[M - nH]^-$ **[260]**, hence the observed mass spectrum pattern for **8**. Elemental analysis of the compound was in good agreement with calculated value. The synthesized compound showed good solubility in most organic solvents.

The Q–band of **8** was observed at 691 nm in DMSO, **Figure 3.14A**, **Table 3.2**. The UV–Vis spectrum of the compound showed no sign of aggregation at concentrations ranging from 4×10^{-7} to 2.33×10^{-5} M in DMSO. The Beer-Lambert law was obeyed at the studied concentrations. **Figure 3.14B** depicts the normalised absorption, emission, and excitation spectra of **8**. The emission maximum of **8** was observed at 704 nm and the excitation

maximum was seen at 695 nm, which is slightly different from the absorption spectrum maximum at 691 nm in DMSO.

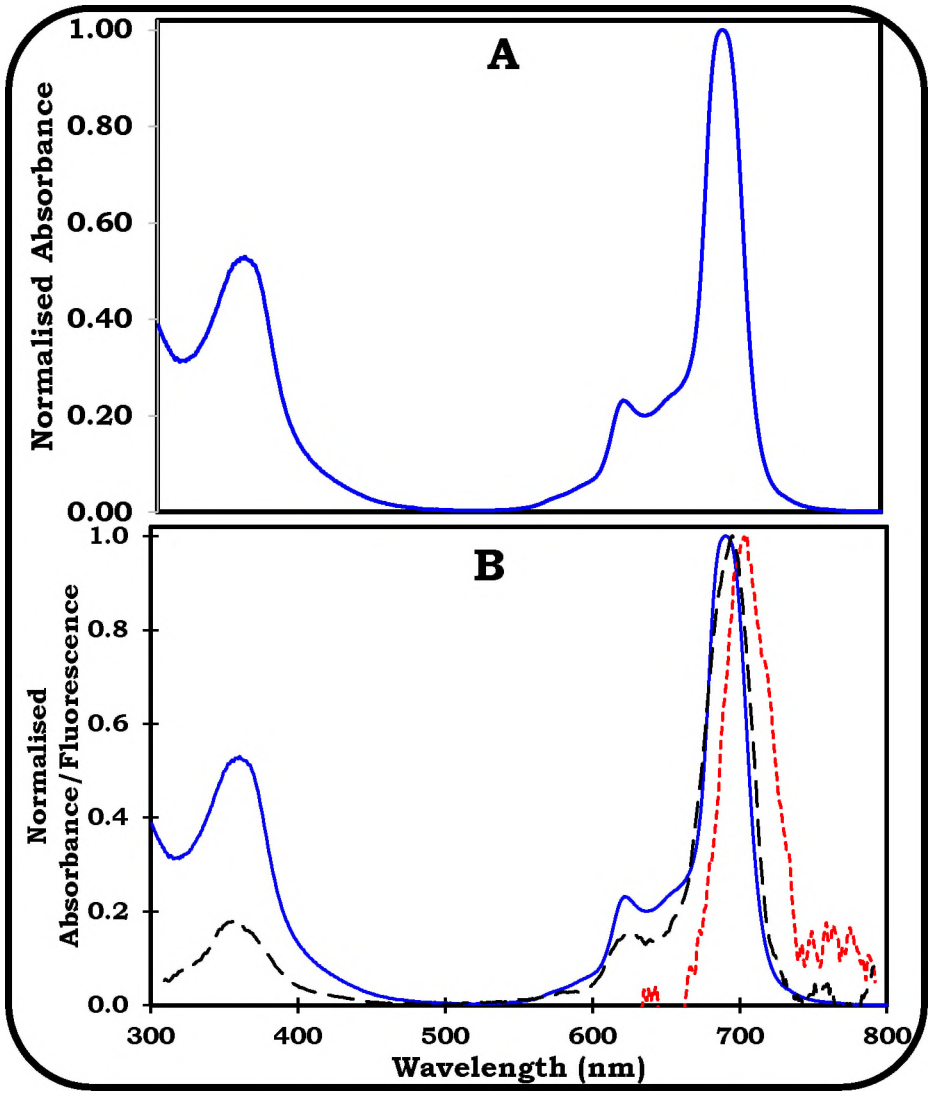

Figure 3.14: (A) Absorption spectrum (2.33 x 10^{-5} M); and (B) Absorption (a), excitation (b), and emission (c), spectra of compound 8 in DMSO at λ_{exc} = 612 nm.

The small differences in the wavelength between excitation and absorption could be due to different equipment used. The excitation spectrum was found to be a mirror image of the emission spectrum. Comparing **6** and **8** having same ring substituents but different central metals, **8** accounted

for more red shifted absorption and emission wavelengths compared to **6** due the presence of heavier metal (In) **[138]**.

3.2.4 Zinc(II) 2(3)–mono–2–(4–oxy)phenoxy)acetic acid phthalocyanine (10)

Scheme 3.7 depicts the synthetic route for 2–(4–(3,4–dicyanophenoxy)phenoxy)acetic acid and compound **10**. 2–(4–(3,4–dicyanophenoxy)phenoxy)acetic acid was synthesized by nucleophilic substitution of 4–nitrophthalonitrile with 4–hydroxyphenoxy acetic acid in DMF and argon flow at ambient temperature, **Scheme 3.7A**.

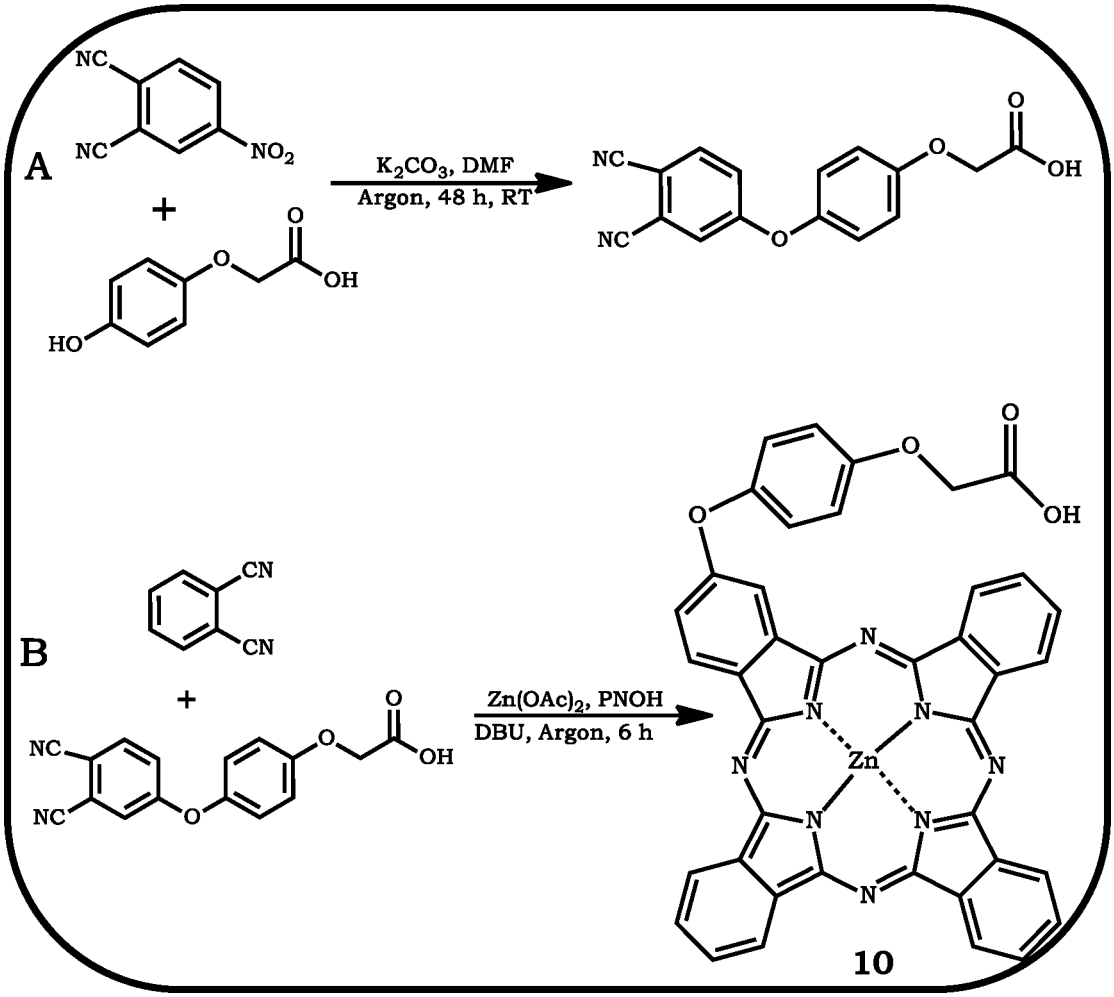

Scheme 3.7: Synthetic route for 2–(4–(3,4–dicyanophenoxy)phenoxy)acetic acid (A), and compound 10 (B).

The obtained results for the phthalonitrile was consistent with predicted structure. Compound **10** was obtained by statistical mixed condensation of 2–(4–(3,4–dicyanophenoxy)phenoxy)acetic acid and 1,2–dicyanobenzene in the presence of zinc acetate dihydrate in 1–pentanol catalyzed by DBU under argon atmosphere, **Scheme 3.7B**. The compound was characterized using FT–IR, ^{1}H NMR, MALDI–TOF mass spectroscopies and elemental analyses. The obtained data were consistent with the predicted structures. The compound showed good solubility in most organic solvents.

The FT–IR spectrum of compound **10** confirmed the presence of OH vibration at 3290 cm^{-1}, C–H vibration at 2917 cm^{-1}, C=O vibration at 1718 cm^{-1}, C=C vibration at 1602 cm^{-1}, C-C vibration at 1485 cm^{-1}, C-N vibration at 1328 cm^{-1}, C-O-C at 1204 cm^{-1}, C-O vibration at 1075 cm^{-1}.

The ^{1}H NMR spectrum of compound **10** showed a singlet at 9.38 ppm which could be attributed to the OH proton of the acetic acid. The Pc aromatic ring showed its resonance signal as multiplet at 9.37–8.26 ppm which gave 15 protons upon integration, the resonance signals of the phenyl depicted quartet at 8.25–7.83 ppm accounting for 4 protons and the CH_2 moiety of the acetic acid accounted for 2 protons as doublet at 2.89–2.73 ppm.

For compound **10**, mass to charge ratio of 744.07 m/z was calculated and 745.96 m/z was obtained.

The ground state electronic absorption spectrum of compound **10** in DMSO is shown in **Figure 3.15A**. The Q–band of compound **10** was observed at 676 nm, **Table 3.2**. The UV–Vis spectrum of compound **10** did not show any sign of

aggregation at concentrations ranging from 4.09 x 10^{-7} to 1.16 x 10^{-6} M. The Beer–Lambert law was obeyed at the studied concentrations.

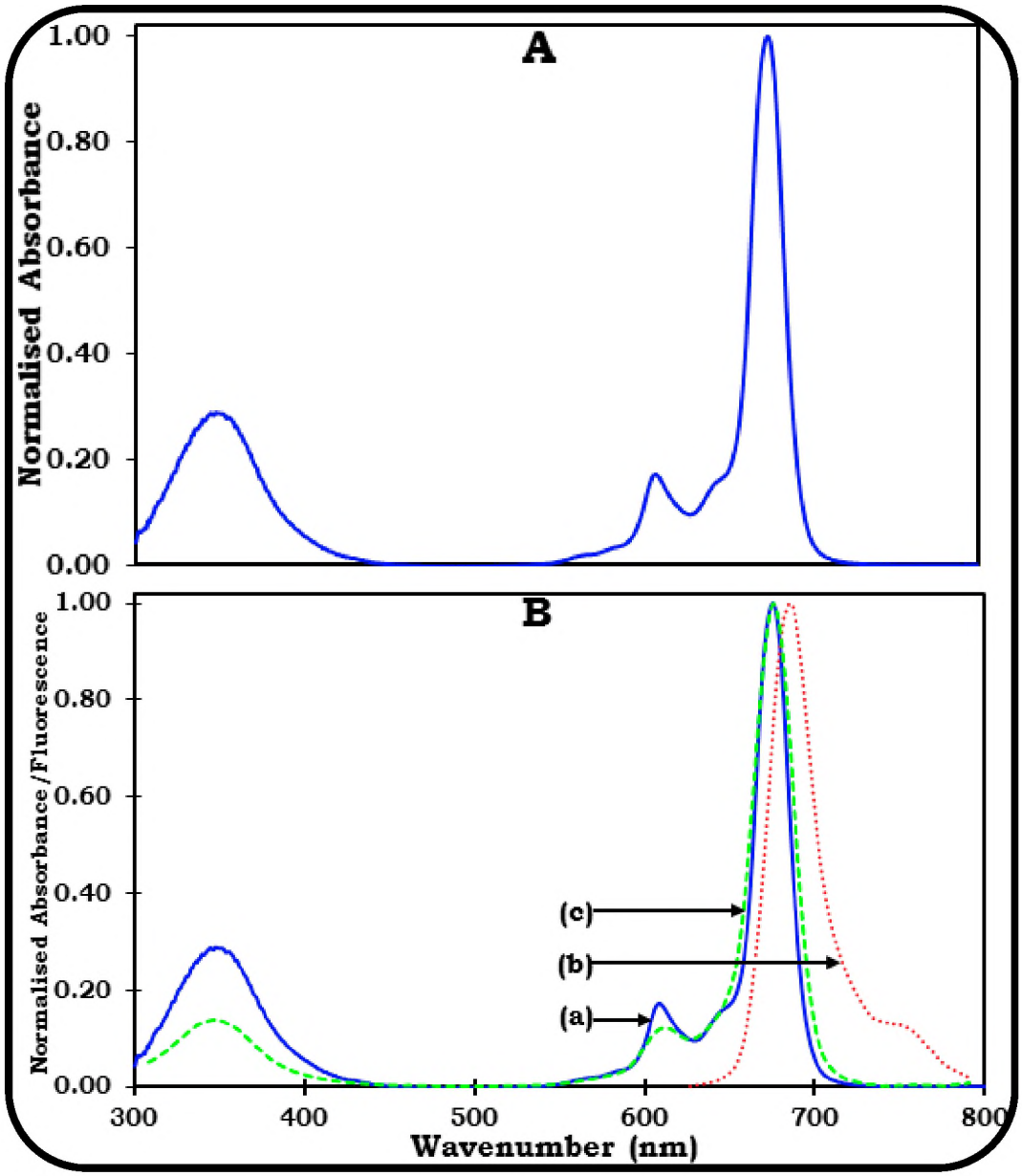

Figure 3.15: (A) Absorption spectrum (1.16 x 10^{-6} M); and (B) Absorption (a), excitation (b), and emission (c) spectra, of compound 10 in DMSO at λ_{exc} = 608 nm.

Figure 3.15B shows the normalised absorption, emission and excitation spectra of compound **10** in DMSO at excitation wavelength of 608 nm. The

ground state electronic absorption and excitation spectra of the compound were similar while the absorption and excitation spectra were mirror image of the emission spectrum. The observed similarity in the ground state electronic absorption and excitation spectra of the compound could be attributed to the similar molecular geometry possessed by the compound. Comparing compounds **6** and **10** with same central metal but different numbers and nature of ring substituents, the Q–band was relatively unchanged. Similar trend was observed in compounds **2a**, **2b** and **10, Table 3.2**.

3.2.5 Compounds 11 to 14

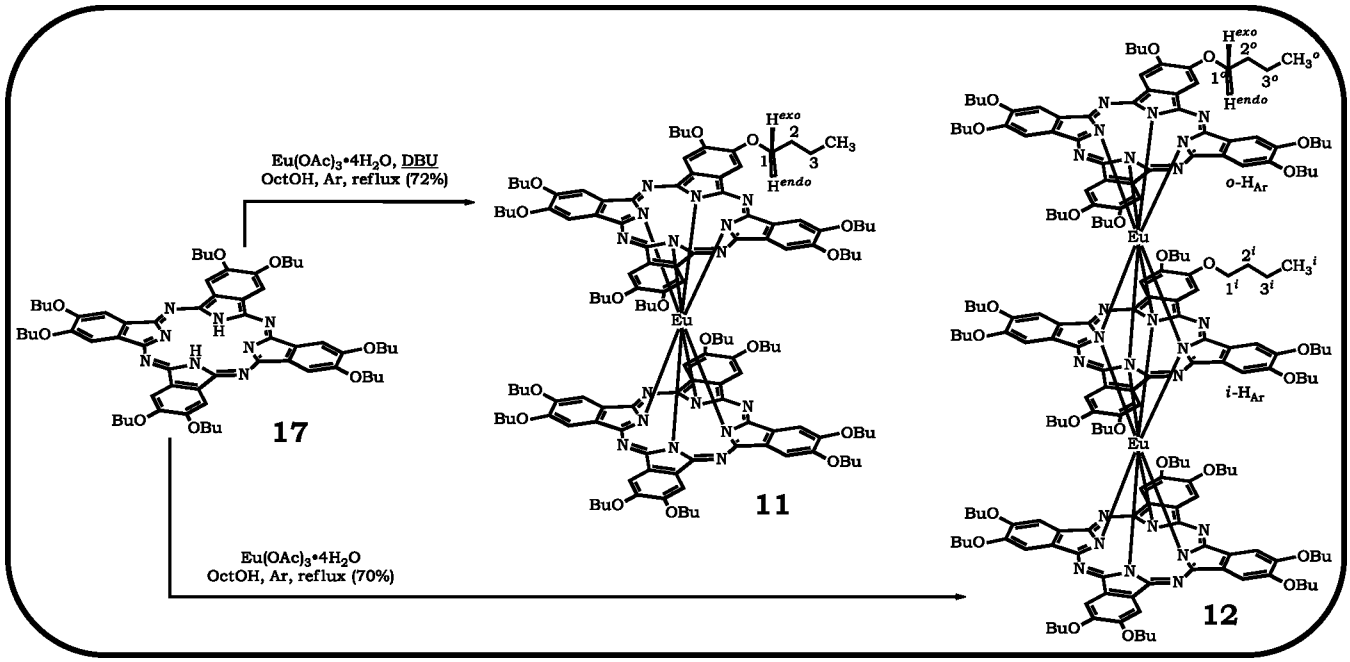

Scheme 3.8: **Synthetic route for sandwich compounds 11, and 12.**

Analogous protocol was utilized to synthesize compounds **11** and **12** using symmetrical mononuclear octa–*n*–butoxy–phthalocyanine (**17**) **[253]** as the

precursor to the symmetrical multinuclear MPcs formation. Bisphthalocyanine **11** was obtained upon reaction of **17** with $Eu(OAc)_3$ in refluxing octanol in the presence of DBU and the trisphthalocyanine **12** was obtained as the main product in the absence of DBU, **Scheme 3.8**.

For the synthesis of asymmetrical **13** and **14**, the direct applicability of the *statistical* mixed condensation approach is limited due to possible formation of 21 various $\mathbf{A_{8-n}B_n}$ products in the case of the double decker compounds, whose separation is obviously a nontrivial task. Taking starting phthalonitriles at ratios over **A**/**B**=20/1 can favour formation of $\mathbf{A_7B}$ double decker product in the mixture with $\mathbf{A_8}$ sandwich **[265]**, however in the case of triple decker compounds this approach is no longer applicable. Therefore, direct metalation of pre-synthesized low-symmetry Pcs with lanthanide salts proved to be the only *viable* approach for the synthesis of sandwich compounds with required arrangement of functional groups **[266–268]**.

Previously, various experimental protocols were reported, affording selective formation of double decker and triple decker compounds from Pc ligands and lanthanide salts **[269,270]**. Typically, these are reactions between H_2Pcs with corresponding acetates (OAc) or acetylacetonates (acac) in high boiling chlorinated aromatic solvents or alcohols either in the presence or in the absence of a base (DBU). However, neither prolonged refluxing of metal free hexa–*n*–butoxy–bis–[2'–(2"–hydroxyethoxy)ethoxy] Pc (**18**) with $Eu(OAc)_3$ or $Eu(acac)_3$ in various solvents, nor addition of DBU afforded the formation of the compounds, **Scheme 3.9** and the UV–Vis spectra of the reaction mixture only showed

characteristic split Q–bands of the unmetalated ligand (**18**). At the same time, Pcs which do not contain free OH–groups, successfully formed the sandwich Pcs (**Scheme 3.8**) under these conditions **[271–278]**.

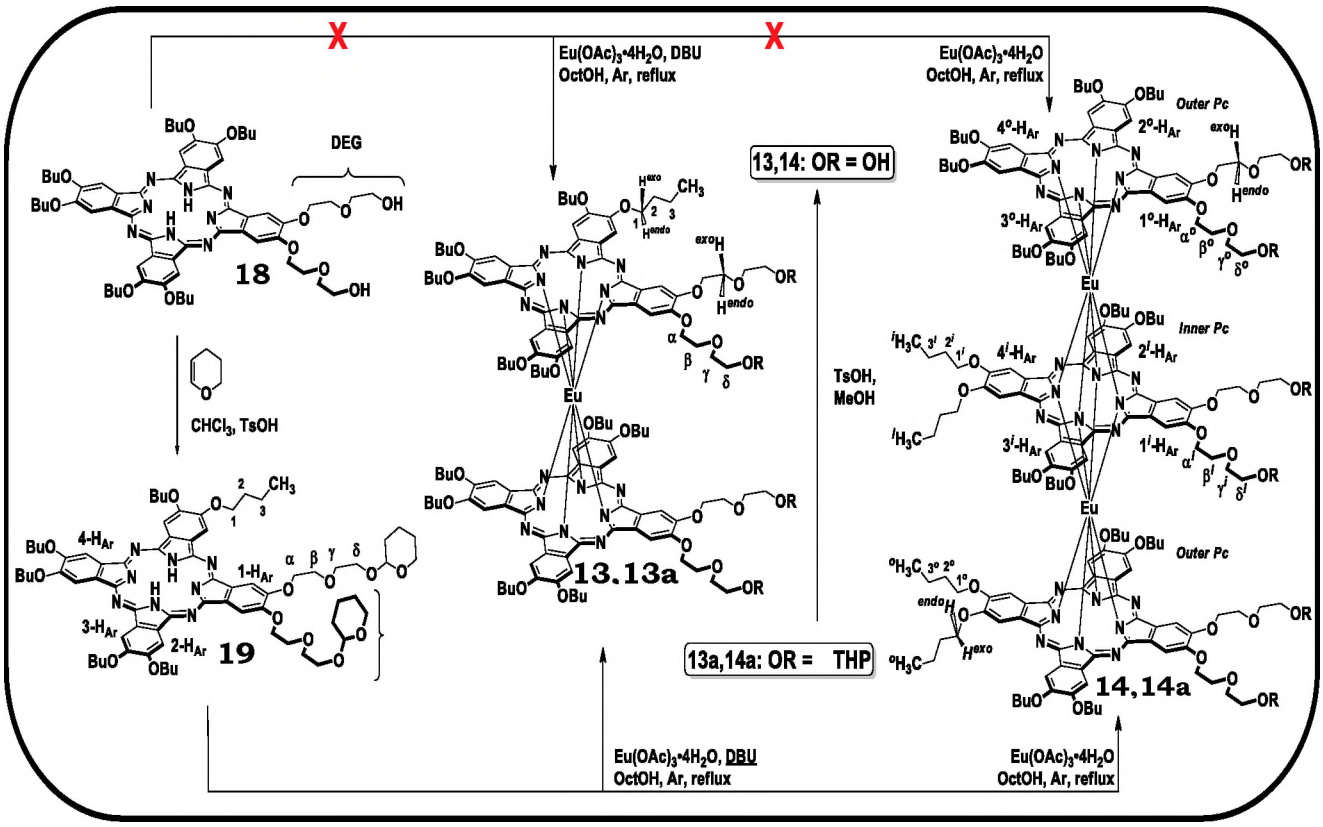

Scheme 3.9: Synthesis of sandwich compounds 13 and 14 bearing OH-terminated diethyleneglycol anchoring groups. Yields: iia – 89%; 13a – 73%; 13 – 95%; 14a – 72%; 14 – 90%.

Therefore, it can be tentatively explained that the specific reactivity of **18** by the presence of the two diethylene glycol (DEG) fragments with terminal OH–groups prevented the formation of the multinuclear MPcs by forming the podand–like chelating system which reacts with Eu^{3+} ions thereby preventing compound formation. Similar behaviour has previously been reported for tetra–(*meso*–benzo–15–crown–5)porphyrin when it failed to react with $Ce(acac)_3$ to form

double decker compound due to possible interference of crown–ether macrocycles with porphyrin cavity **[278]**. With the aim to suppress the undesired side reactions of metal free hexa–*n*–butoxy–bis–[2'–(2"–hydroxyethoxy)ethoxy] Pc, compound **18** was treated with excess 3,4–dihydro–2*H*–pyran (THP) in the presence of TsOH in dry chloroform, resulting in the formation of metal free hexa–*n*–butoxy–bis–[2'–(2"–tetrahydropyranyloxyethoxy)ethoxy] Pc **19**, **Scheme 3.9**. To synthesize the THP–protected double decker **13a**, Pc **19** was metalated with 1.5 equivalent of $Eu(OAc)_3$ in refluxing octanol under the previously reported conditions **[275]** targeted to form bisphthalocyanines. However, the reaction was not selective and the formation of a mixture of THP protected double decker (**13a**) and triple decker (**14a**) compounds were observed. Increasing the ratio of $Eu(OAc)_3$/**19** to 2.5 **[276,277]** resulted in formation of THP protected triple–decker **14a** as a sole sandwich product.

The modification of the reaction conditions by addition of DBU **[272]** resulted in formation of target bisphthalocyanine THP protected compound **13a** with traces of **14a** which was separated by size–exclusion chromatography. The newly optimized method afforded efficient, selective and viable approach towards synthesis of asymmetrical multinuclear phthalocyanines, containing $\mathbf{A_3B}$-type ligands.

Deprotection of THP–protected compounds **13a** and **14a** with TsOH in methanol afforded sandwich compounds **13** and **14** in efficient quantitative yields. The process of deprotection was monitored by thin layer chromatography (TLC) and MALDI–TOF mass spectrometry and removal of the THP groups was also

confirmed by the appearance of OH stretching bands in the FT–IR spectra (3355 cm^{-1} for **13** and 3367 cm^{-1} for **14**).

Purity of all the compounds were confirmed by MALDI–TOF mass spectrometry, elemental analysis, NMR, FT–IR and UV–Vis spectroscopies. The obtained data were consistent with the predicted structures. The compounds showed good solubility in most organic solvents, revealing UV–Vis spectra typical of double– and triple– decker phthalocyanines **(Figure 3.16)**. The mass spectra of the compounds are shown as **appendix 1**.

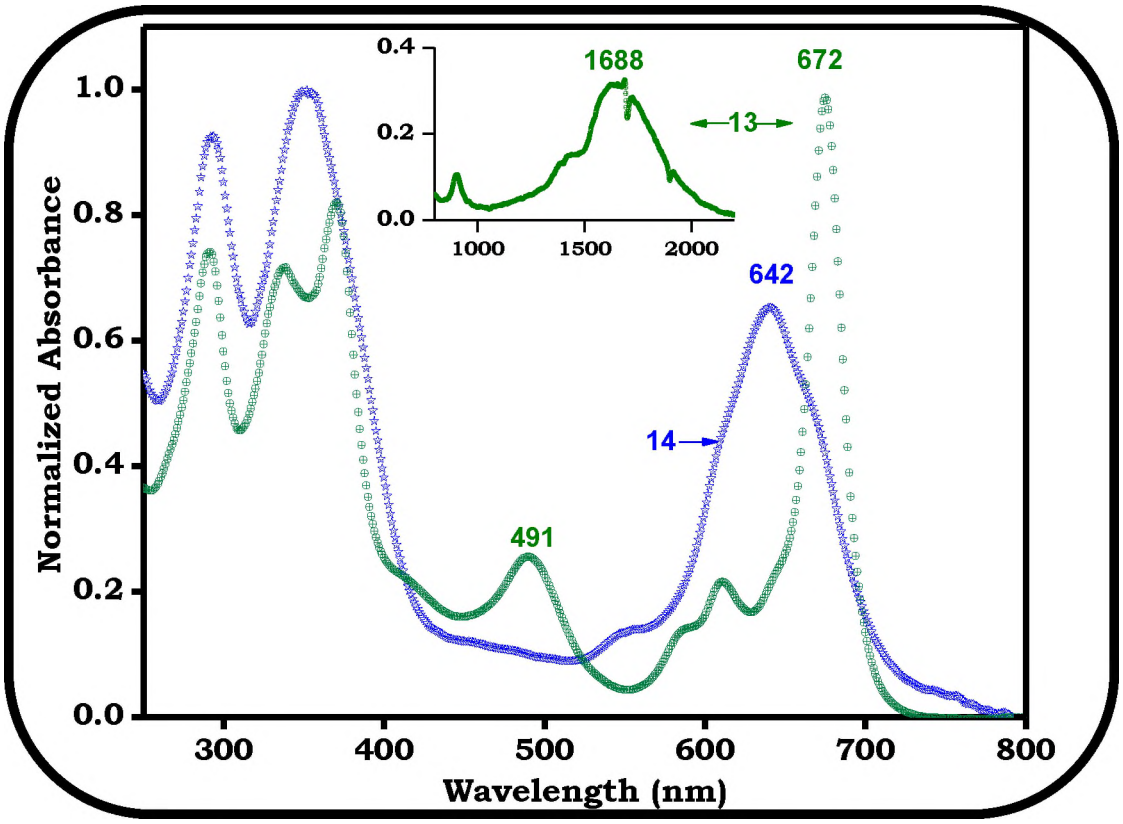

Figure 3.16: UV–Vis spectra of compounds 13, and 14 in DCM. The inset shows the NIR absorbance of compound 13 (~ 2.4×10^{-5} M).

Compounds **13** and **14** did not show any sign of aggregation at concentrations ranging from 3.7×10^{-6} to 2.4×10^{-5} M in DCM. The Beer-Lambert law was obeyed

within the studied concentration ranges. The appearance of $Pc^{\bullet-}$ structural benchmarks for double deckers **[271,279,280]**, namely bands in UV–Vis spectra at ~490 and ~1690 nm, **(Figure 3.16)** as well as near infrared–band at 1317 cm^{-1} for **11** and 1315 cm^{-1} for **13** confirms the presence of the unpaired electron delocalized on the molecular orbitals of the Pc ligands. Such an unpaired electron is absent in triple decker compounds **12** and **14**, where the charges of the ligands and metal ions compensated each other, therefore no near infrared (NIR) absorbance was observed in their UV–Vis spectra. Excitonic interaction between Pc^{2-} ligands resulted in broadening of the triple decker Q–band and its blue shifting to ~640 nm in comparison to the double decker compounds and appearance of a shoulder at ~685 nm **[281,282]**.

^1H NMR spectra of the synthesized double decker and triple decker compounds are also consistent with the proposed structure. In the case of bisphthalocyanines **11** and **13**, the resonance signals of the aromatic protons cannot be observed and the rest of the signals are broadened due to the presence of unpaired electron on Pc molecular orbitals. Moreover, the presence of paramagnetic Eu^{3+} ion resulted in significant down–field shift of the resonance signals in comparison with their chemical shifts in spectra of diamagnetic Pcs, **Figure 3.17**. In the case of triple deckers **12** and **14**, this down–field shifting is even more pronounced due to the presence of two paramagnetic nuclei (Eu^{3+}) **[283–286]**. The non–equivalence of inner and outer Pc rings, as well as diastereotopicity of geminal protons in CH_2–groups of outer substituted ligands afforded numerous resonance signals, which were assigned by means of ^1H-^1H

COSY NMR spectra, **Figures 3.18**. Mass spectra of compounds **11–14** are shown in **Appendix 1**.

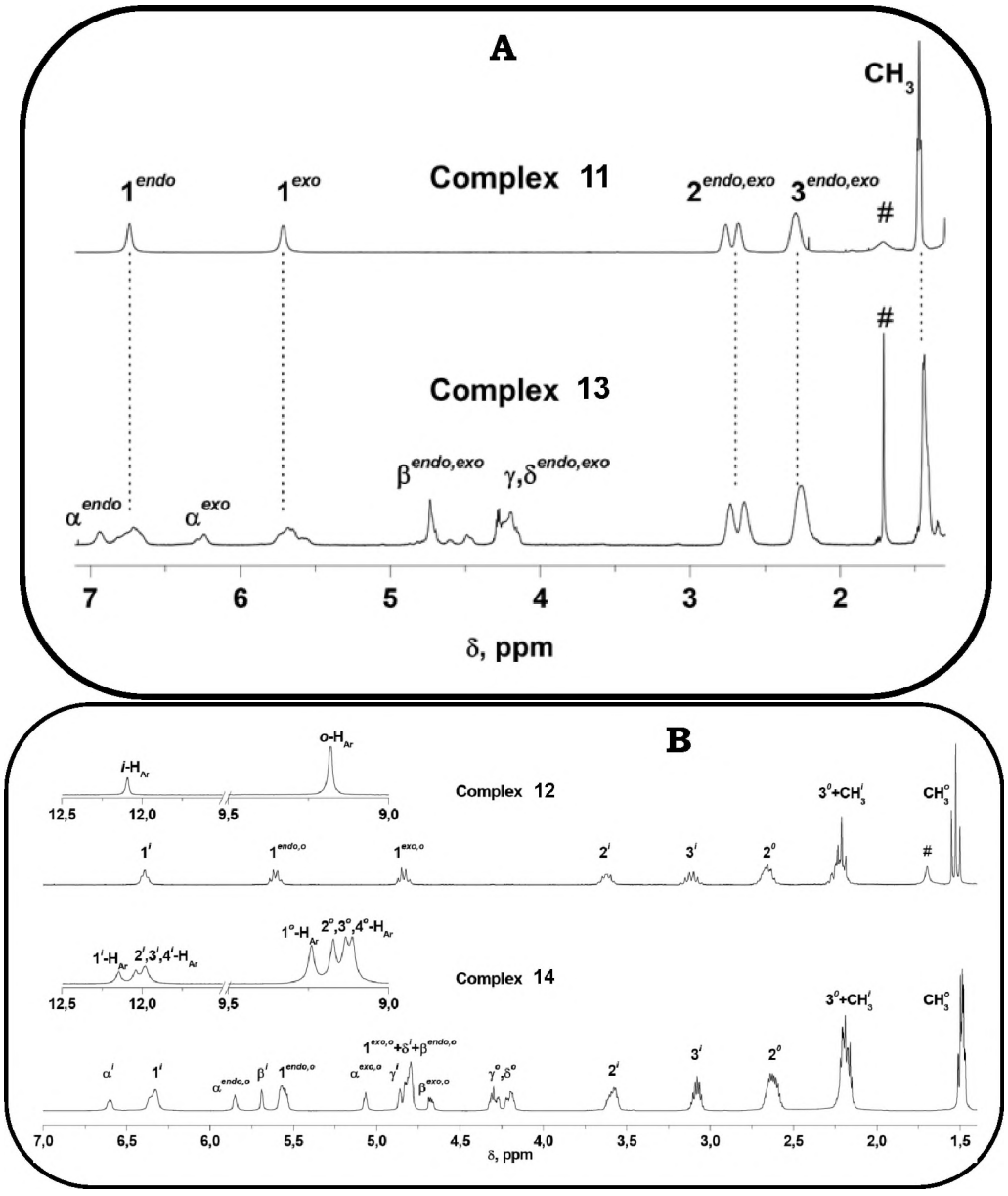

Figure 3.17: Assignment of ^{1}H-NMR spectra of compounds 11 and 13 (A) and 12 and 14 (B) in $CDCl_3$. Insets show zoomed areas of resonance signals of Pc aromatic protons. Numbering of protons is given in schemes 3.8 and 3.9. The residual water signal is marked with "#".

In the symmetrical compound **12**, the aromatic protons of one inner and two outer Pc rings depicted two resonance signals at 12.07 and 9.16 ppm with the

ratio of integral intensities 1:2 respectively. To the contrast, in the NMR spectrum of low–symmetry compound **14**, the resonance signals of aromatic protons showed notable splitting over the range of 12.14–9.11 ppm. The most down–field shifted signals in the multiplet correspond to the protons of benzene rings, containing DEG substituents. Therefore, such spectral behaviour is evidence of the electronic density polarization in the compounds, caused by the introduction of two DEG substituents, which slightly depicted more electronegative effect in comparison with butoxy–groups. Previously, this polarization was found to be responsible for the enhancement of NLO properties of low–symmetry Pcs in comparison with their symmetrical counterparts **[253]**.

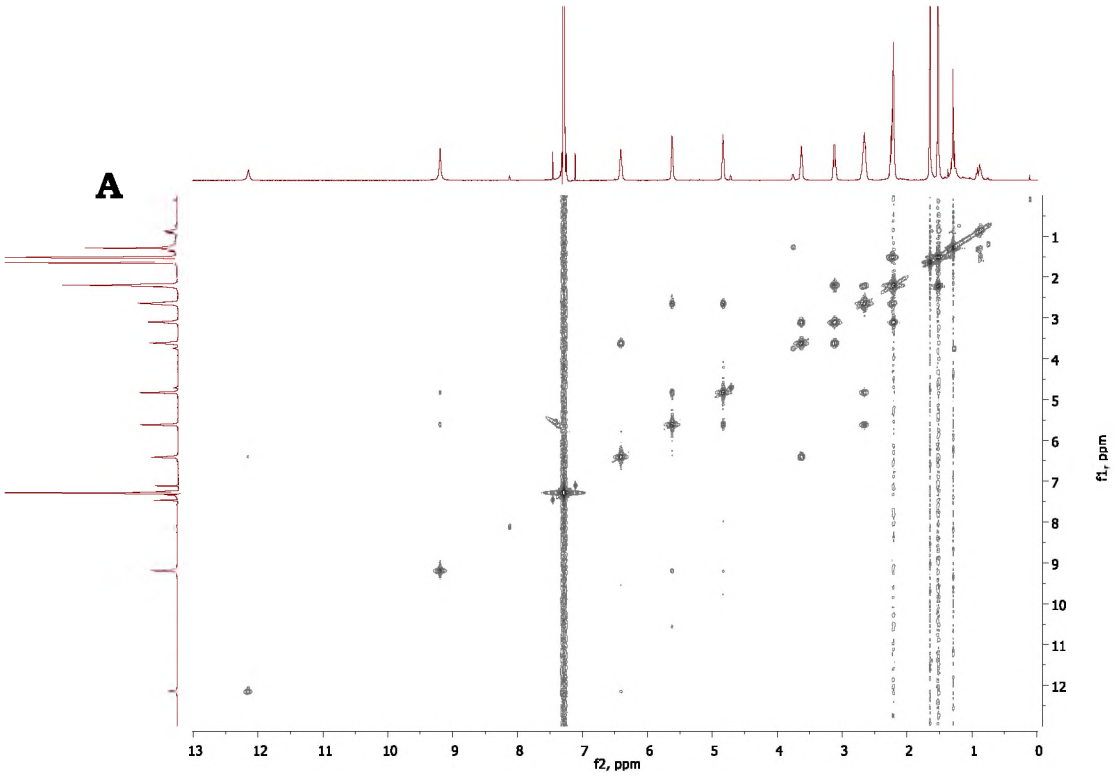

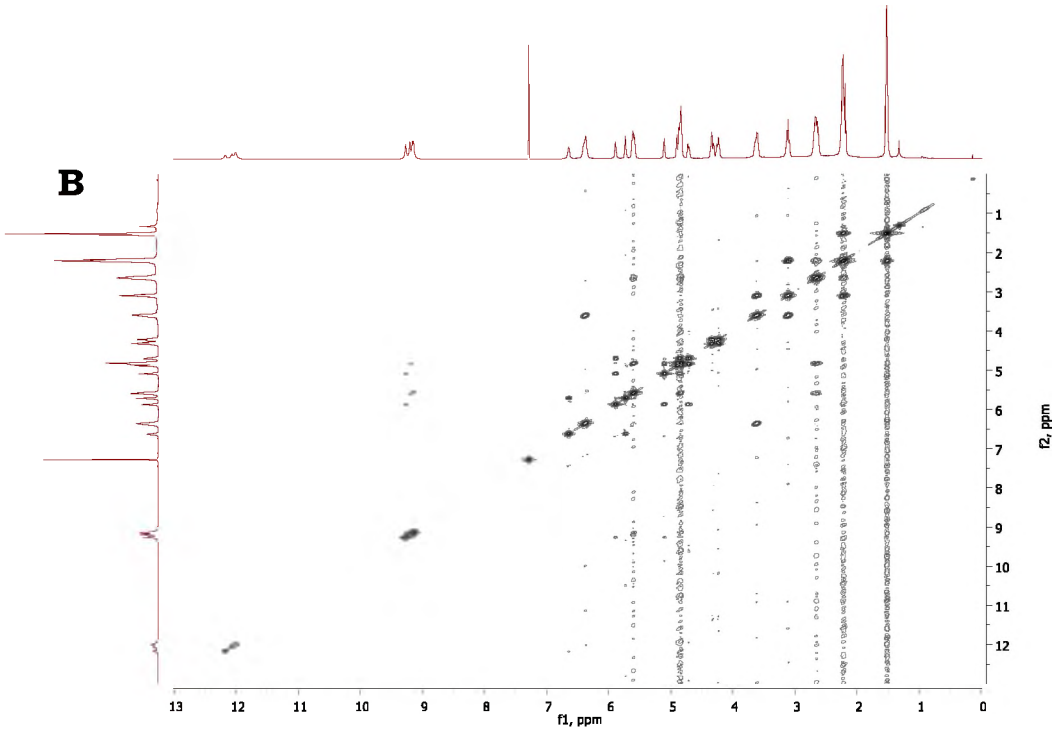

Figure 3.18: ^{1}H-^{1}H-COSY spectra of TD compounds 12 and 14.

3.3 METALLOPHTHALOCYANINES–NANOPARTICLES CONJUGATES

3.3.1 Synthesis of MPcs–NPs, –HSA and –Chitosan conjugates, Schemes 3.10–3.16

The formation of the MPcs–NPs conjugates was facilitated by the activation of the carboxylic acid moieties of the MPcs using suitable coupling agents, followed by the addition of amine functionalized NPs resulting in an amide bond between the MPcs and the NPs, **Schemes 3.11**, **3.12** and **3.14** (using **2a** and **6** with QDs; **2b** with SiNPs–APTES (20), and ZnO/SiNPs–APTES (13); and **10** with AgNPs–Cyst (11.3), and AgAuNPs–Cyst (11.6), as examples). Similarly, an amide bond was formed between **2b** and HSA or chitosan, **Scheme 3.12**. For the sulfonamide bond formation, the sulfonic acid moiety of the MPc (**7**) was activated using thionyl chloride, followed by

the introduction of amine functionalized CdTe/CdS/ZnS and this resulted in the formation of **7**–CdTe/CdS/ZnS–GSH, **Scheme 3.13**. Finally, the carboxylic acid moiety of the MSA capped QDs was activated using EDC, followed by administration of diethylene glycol substituted MPcs (**13** and **14**) to forming ester bond between the MPcs and QDs, **Scheme 3.15**. Compound **1** was linked to QDs by sulfur to metal bond, **Scheme 3.10**. The amide, and ester linked conjugates were performed at ambient temperature except for the sulfonamide linked conjugates which were done at 0 °C for the activation of the SO_3H substituents on the Pc due to high reactivity of thionyl chloride at elevated temperature. **Scheme 3.16** depicts the doping of MPcs (**3**–**6**) onto SiNPs. The formation of the MPcs doped SiNPs were obtained by successive mixing of TEOS with a solution of 1–hexanol, cyclohexane, Triton X 100 and the MPcs. Water was used to foster the hydrolysis of the TEOS around the MPcs leading to the formation of silicic acid having four silanol moieties. Ammonium hydroxide catalyses the doping of the MPcs onto SiNPs. Afterwards, the reaction mixture was slowly stirred for 24 h to promote the nucleation and particle growth of the MPcs doped SiNPs. The obtained MPcs doped SiNPs were collected using ethanol under centrifugation. The products were purified with ethanol and water.

The NPs were selected for linkage with Pcs due to the following reasons, **Table 3.2**:

1. Compounds **2a**, **6**, **8** and **9** were linked to core, core/shell, and core/shell/shell QDs to evaluate the effects of core, core/shell and core/shell/shell on the photophysicochemical properties of the Pc compounds. In addition, the effect of the QDs on the cytotoxicity of compound **6** was evaluated.
2. Compound **2b** was linked to SiNPs–APTES (20) and ZnO/SiNPs–APTES (13), to investigate the effects of SiNPs–APTES (20) and ZnO/SiNPs–APTES (13) on the photophysicochemical properties and *in vitro* PDT activity of the Pc compound.
3. Compounds **3** to **6** were doped onto unmodified SiNPs to assess the effects of central metal (comparing **3** and **5**), nature of substituents (comparing **4** and **6**), and asymmetry (comparing **2** and **6**) on the photophysicochemical properties of the Pc compounds.
4. Compound **7** was linked to CdTe/CdS/ZnS–GSH. The sulfonamide linked conjugates (**7**–CdTe/CdS/ZnS–GSH) and amide linked conjugates (**6**–CdTe/CdS/ZnS–GSH) were compared.
5. Compound **6** was linked to ternary core (CdTeSe–GSH) and core/shell (CdTeSe/ZnO–GSH) QDs to investigate the effects of ternary QDs on the photophysicochemical properties and *in vitro* cytotoxicity activity of the Pc compound.
6. Compound **10** was linked to AgNPs–Cyst (11.3), and AgAuNPs–Cyst (11.6) respectively, the effects of AgNPs–Cyst (11.3), and AgAuNPs–Cyst (11.6) on

the photophysicochemical properties and *in vitro* PDT activity of the Pc compound was evaluated.

7. Symmetrical compounds **11** and **12** were mixed with TOPO capped ternary multi–shell QDs for comparison with asymmetrical compounds **13** and **14** linked to MSA capped ternary multi–shell QDs. The effects of the ternary multi–shell QDs on the NLO properties of the Pc compounds were studied.
8. Pc **1** was linked to TOPO capped binary core QDs. The effects of the binary core QDs on the NLO properties of the Pc compound was studied.
9. Compound **2b** was linked to chitosan and HSA respectively, to compare the effects of HSA and chitosan on the photophysicochemical properties and *in vitro* PDT activity of the Pc compound.

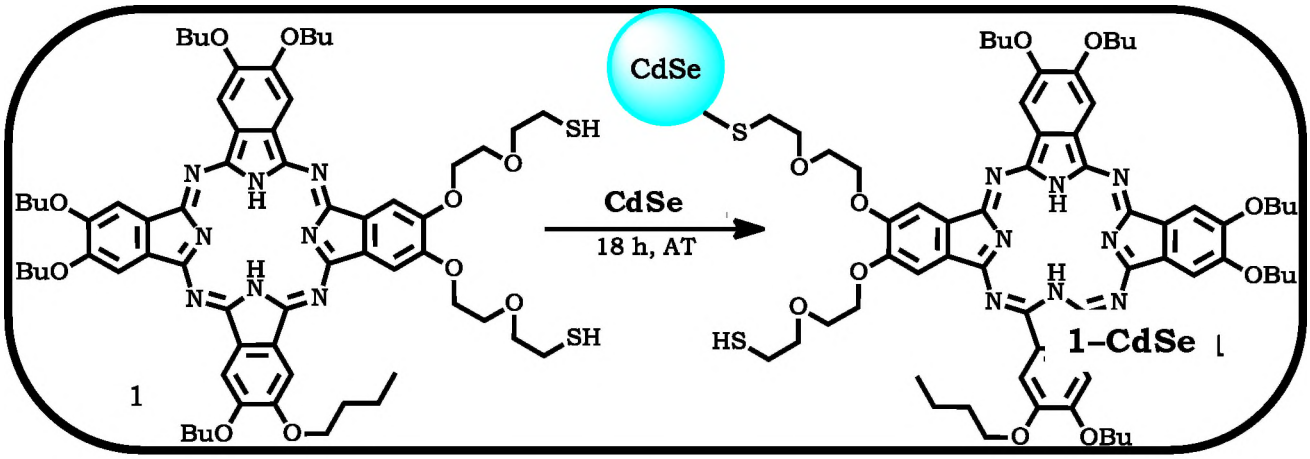

Scheme 3.10: Synthetic route for linkage of 1–CdSe–TOPO (3.8).

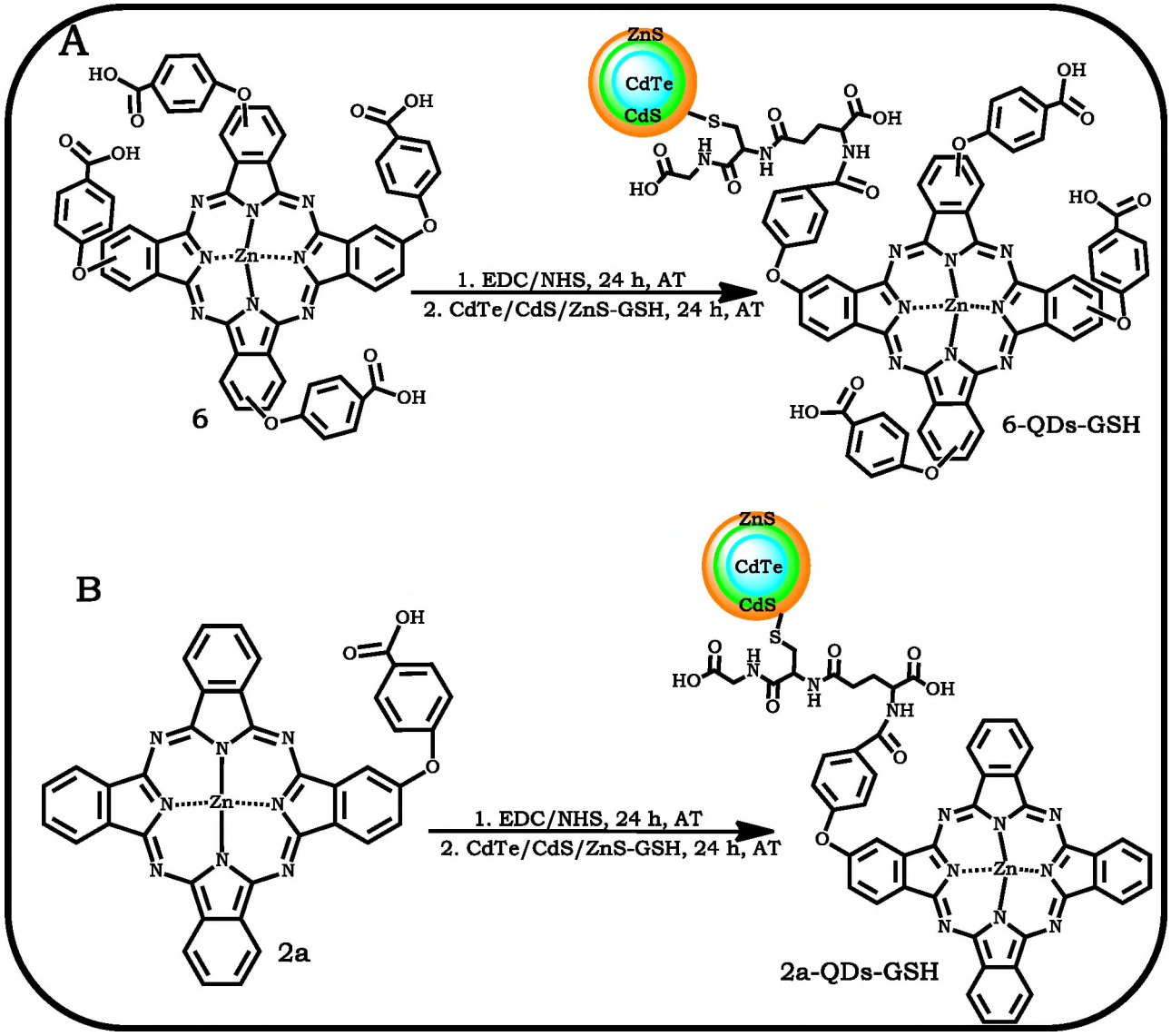

Scheme 3.11: Synthetic route for linkage of 2a–CdTe/CdS/ZnS–GSH (A) and 6–CdTe/CdS/ZnS–GSH (B).

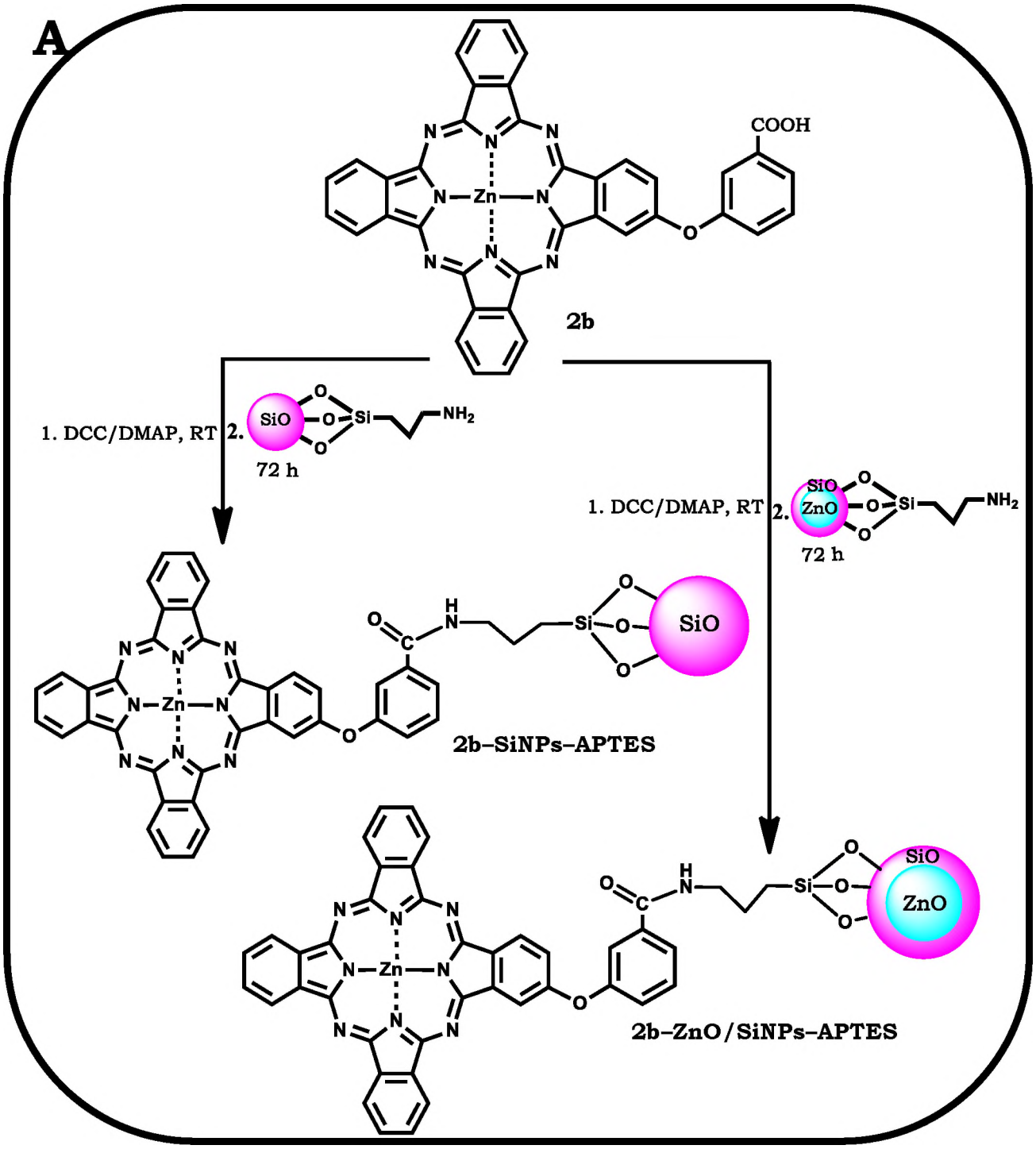
A
COOH
2b
1. DCC/DMAP, RT 2.
72 h
1. DCC/DMAP, RT 2.
72 h
2b–SiNPs–APTES
2b–ZnO/SiNPs–APTES

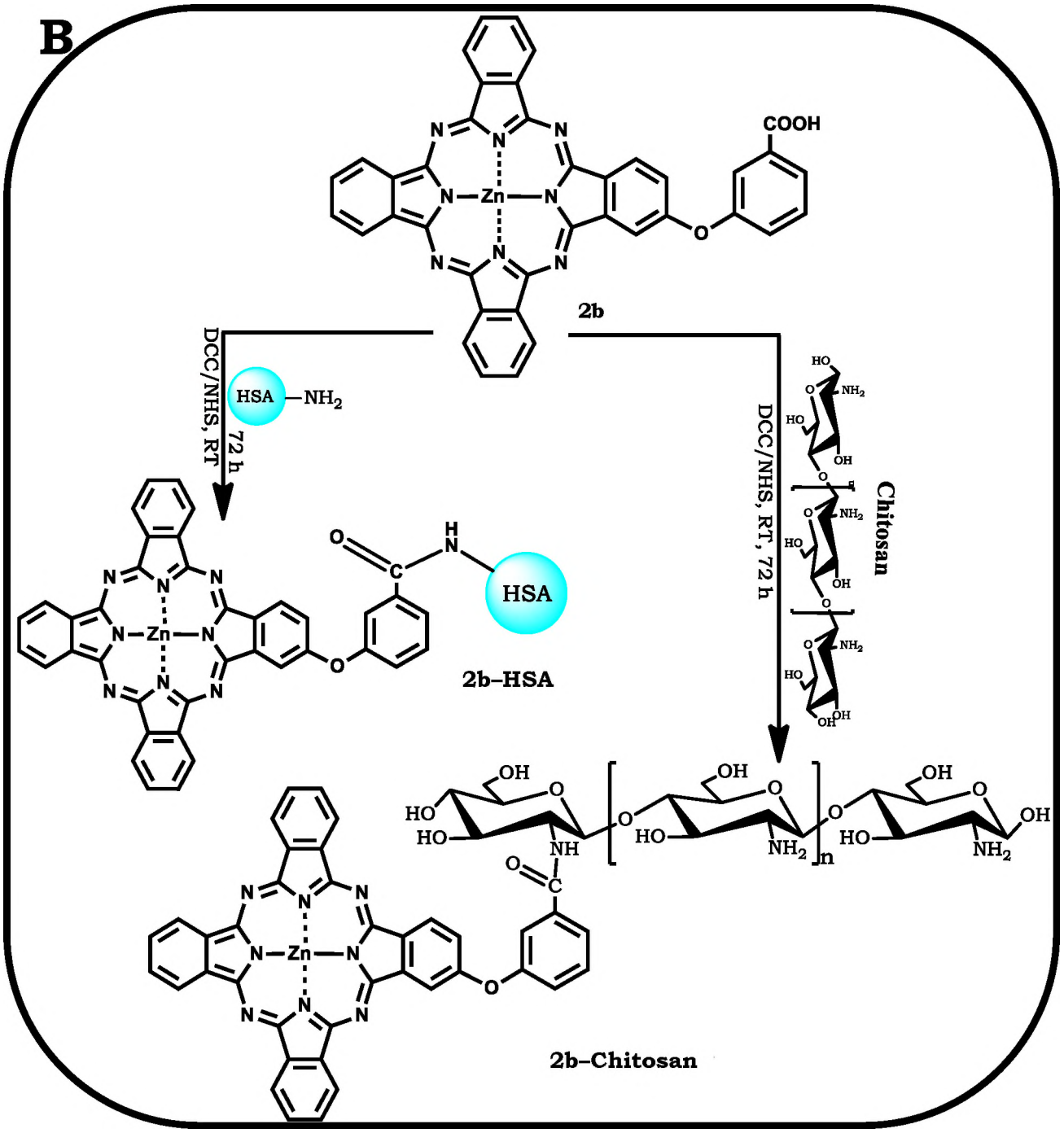

Scheme 3.12: Synthetic route for linkage of 2b–SiNPs–APTES (20) and 2b–ZnO/SiNPs–APTES (13) (A); and 2b–HSA, and 2b–Chitosan (B).

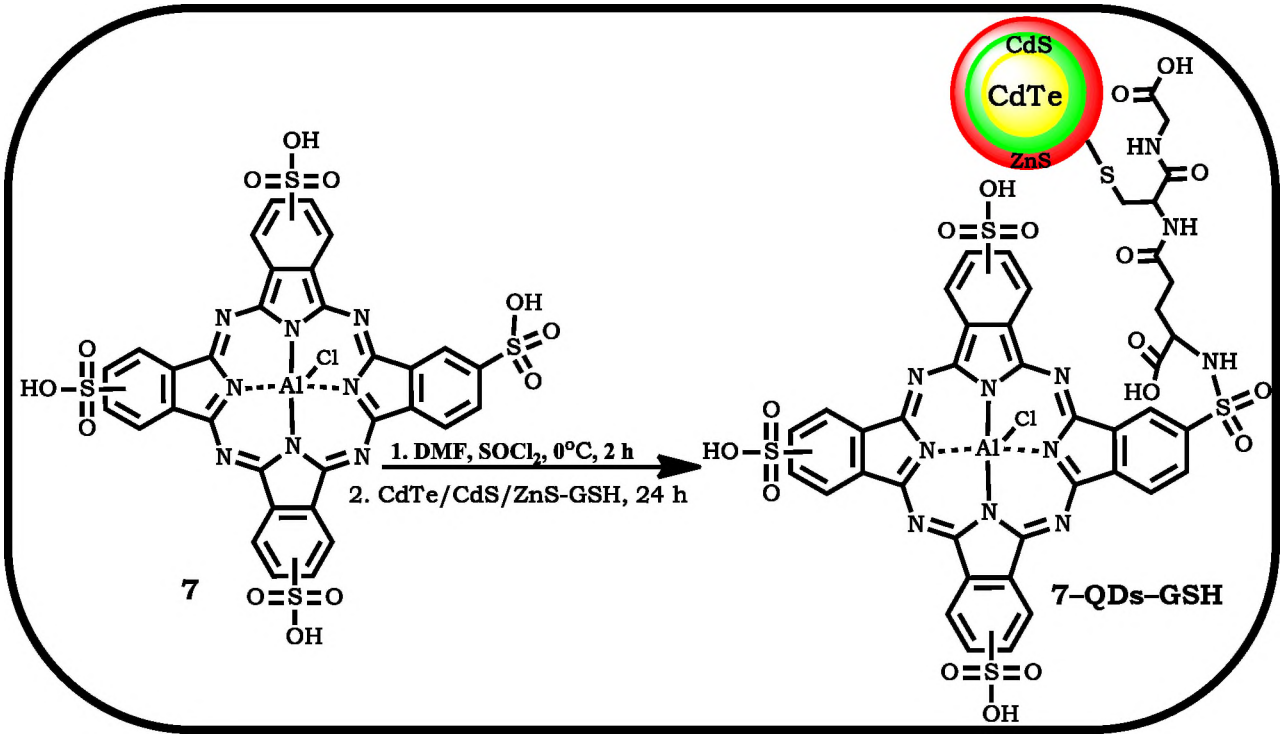

Scheme 3.13: Synthetic route for linkage of 7–CdTe/CdS/ZnS–GSH.

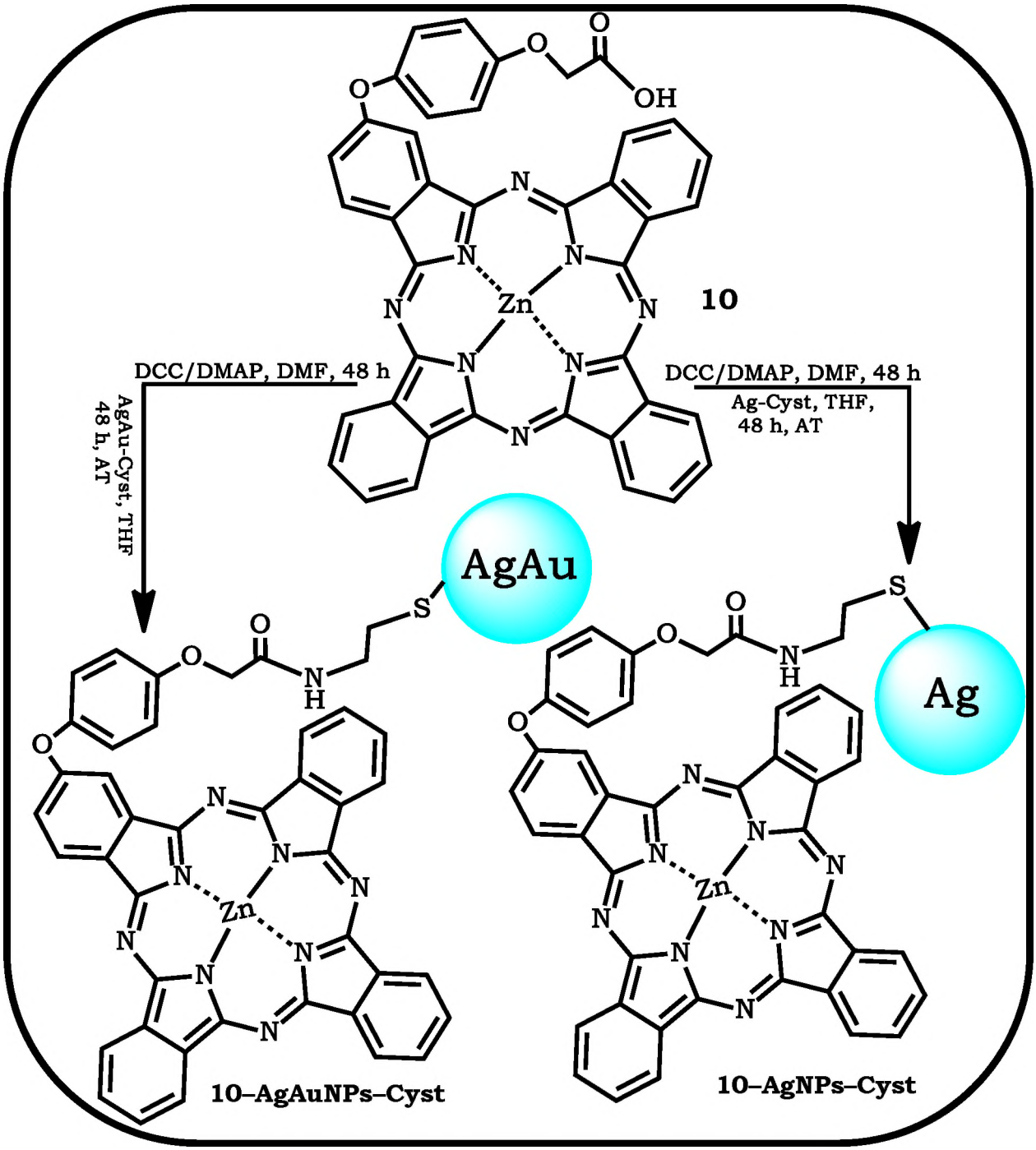

Scheme 3.14: Synthetic route for linkage of 10–AgNPs–Cyst (11.3) and 10–AgAuNPs–Cyst (11.6).

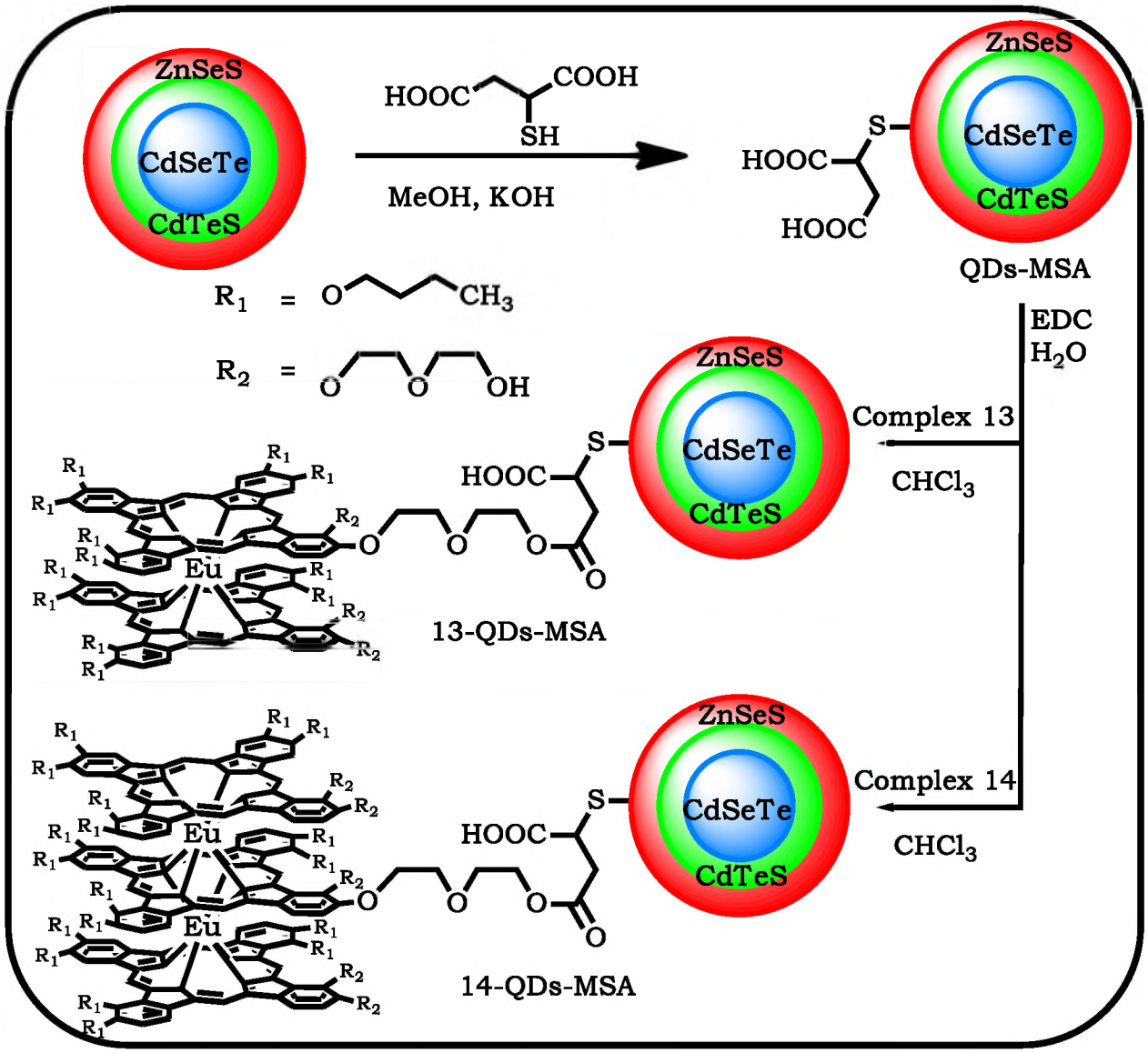

Scheme 3.15: Principle conjugation pathway for linkage of 13–CdSeTe/CdTeS/ZnSeS–MSA (7.3), and 14–CdSeTe/CdTeS/ZnSeS–MSA (7.3).

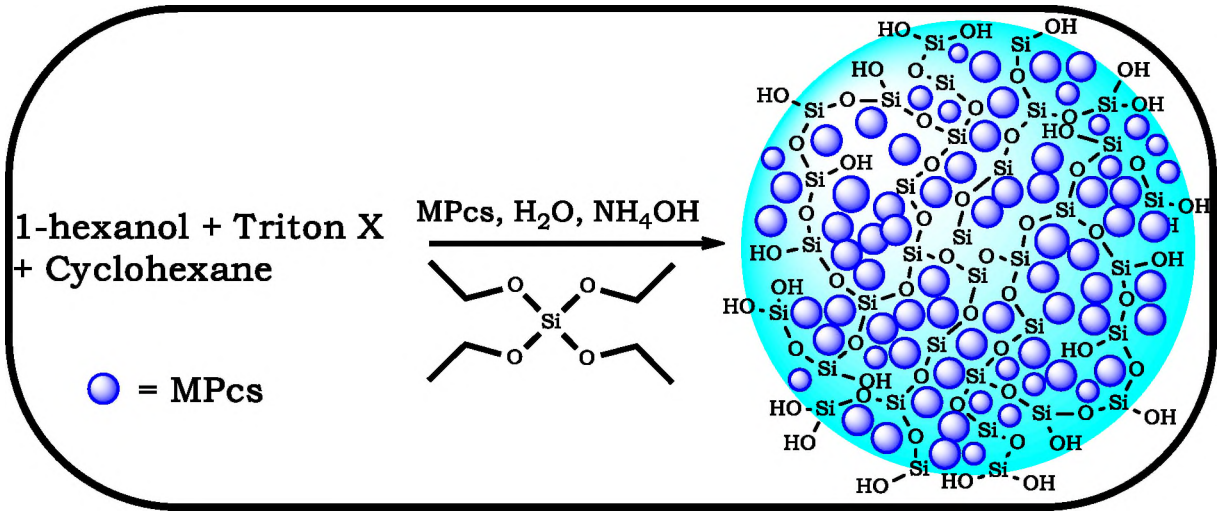

Scheme 3.16: Synthetic route for doping of compounds 3 to 6 onto SiNPs.

3.3.2 FT–IR Spectra

Confirmation of the bonds formation for the respective Pcs–NPs conjugates were performed using FT–IR spectroscopy. The FT–IR spectra of the respective compounds, NPs and their corresponding conjugates were compared.

For the sulfonamide linkage, **Figure 3.19A**; CdTe/CdS/ZnS–GSH (6.3), compound **7** and conjugate (**7**–CdTe/CdS/ZnS–GSH (6.3)) were used as examples. For the CdTe/CdS/ZnS–GSH (6.3): the IR vibration bands were at 3262 cm^{-1}, 1569 cm^{-1} (C=O), 1387 cm^{-1} (N-H) and 1223 cm^{-1} (C-N). In compound **7**: the bands are 3000 cm^{-1} (O–H), 1635 cm^{-1} (C=C), 1156 cm^{-1} (O=S=O), 1026 cm^{-1} (S=O). In **7**–GSH–CdTe/CdS/ZnS (6.3): the bands are 3384 cm^{-1} (O–H/NH_2), 1578 cm^{-1} (O=S-NH), 1159 cm^{-1} (O=S-NH) and 1028 cm^{-1} (S=O), **Figure 3.19A**. The appearance of sulfonamide bands at 1578 cm^{-1} and 1159 cm^{-1}, the attenuation of the OH or NH_2 band at 3384 cm^{-1}, relative shift in the S=O vibrational band from 1026 cm^{-1} to 1028 cm^{-1} indicate successful formation of the sulfonamide bond for the nanoconjugates (**7**–CdTe/CdS/ZnS–GSH (6.3)).

For the amide linkages (**Figure 3:19B**); SiNPs–APTES (20), compound **2b** and conjugate (**2b**–SiNPs–APTES (20)) were used as representatives. In the SiNPs–APTES (20): three distinct bands were observed at 3274 cm^{-1} corresponding to primary amine (NH_2) from the capping ligand, 1068 cm^{-1} corresponding to siloxane band (Si-O-Si) and 797 cm^{-1} corresponding to Si–O band (**Figure 3.19B**). **2b**–SiNPs–APTES (20) also showed three distinct vibrational bands at 3282 cm^{-1} corresponding to primary amine (NH_2) from the capping ligand, 1072 cm^{-1} corresponding to siloxane band (Si–O–Si) and 797 cm^{-1} corresponding to Si–O band. In addition, a partially split band at 1640 cm^{-1} and 1527 cm^{-1} corresponding to amide (HN–C=O) vibrational band which was not present in either compound **2b** nor the SiNPs–APTES (20) alone (**Figure 3.19B**) is observed.

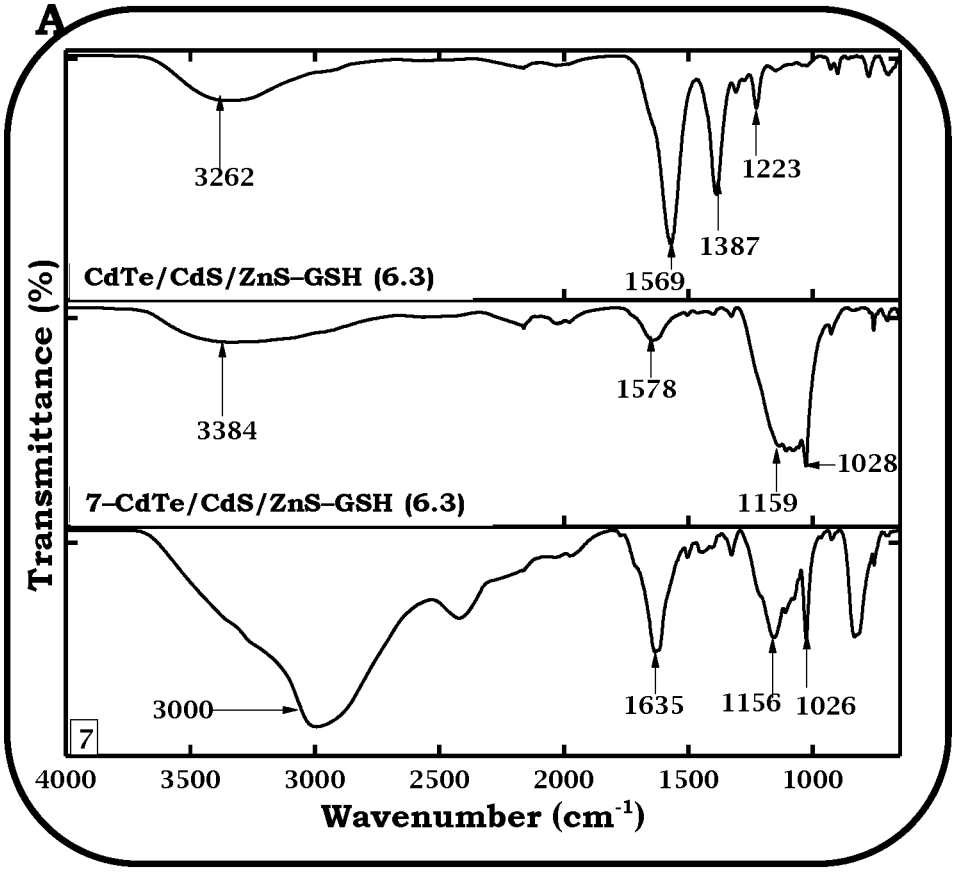

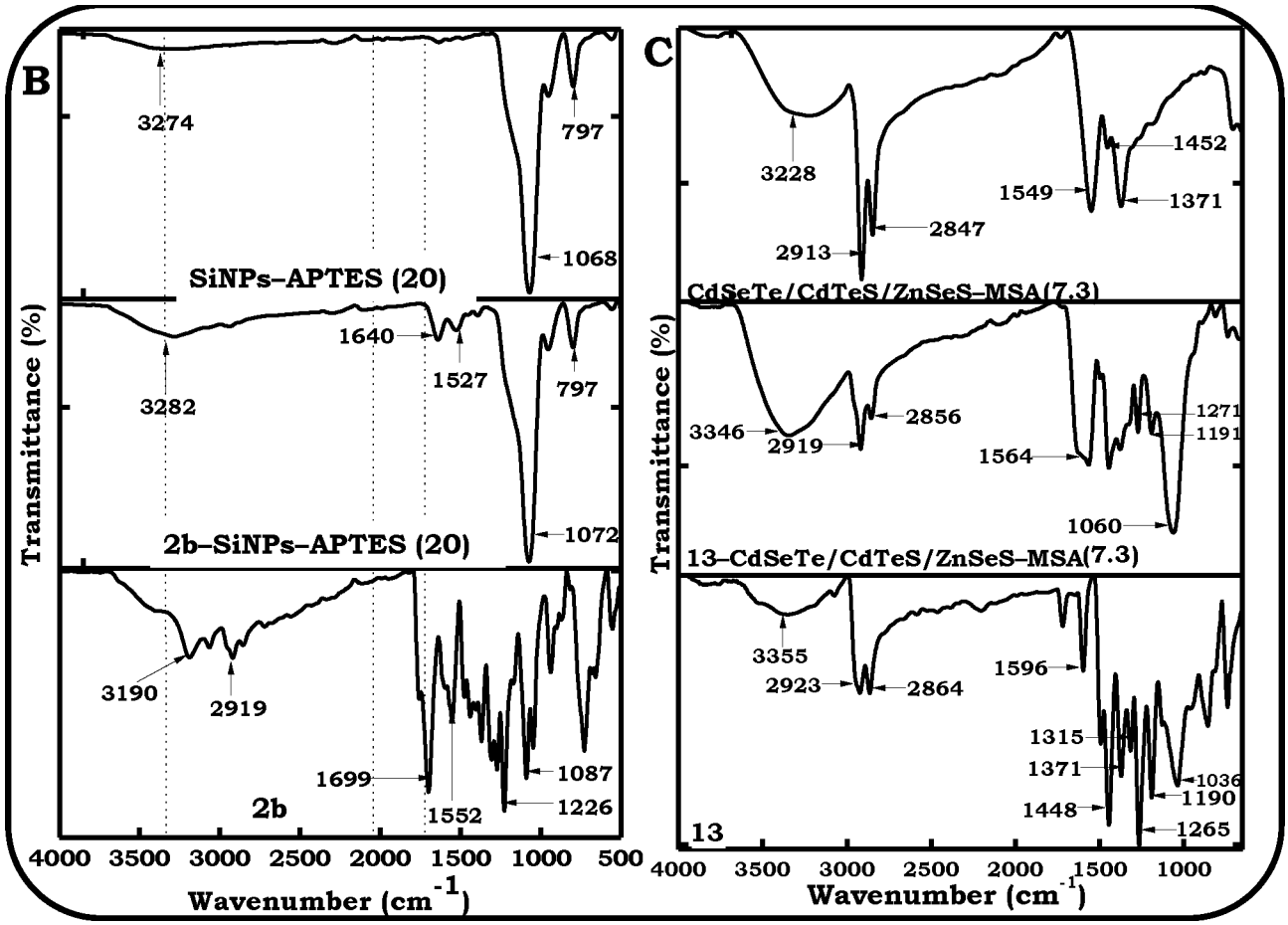

Figure 3.19: FT–IR spectra of (A) compound 7 and conjugate (sulfonamide bond); (B) 2b and conjugate (amide bond); and (C) 13 and conjugate (ester bond)

The presence of NH_2 vibration in **2b**–SiNPs–APTES (20) confirms that not all of the amino groups (located on NPs) are used for binding to compound **2b**. The presence of the amide vibrational bands confirms the amide bond formation. The IR spectrum for **2b**–SiNPs–APTES (20) was dominated by the siloxane band due to the smaller amount of MPc compared to the NPs. The same FT-IR spectra pattern was observed for the nanoconjugates of **2b**–ZnO/SiNPs–APTES (13). To further confirm the amide bond formation, XPS was employed below.

For the ester linkage using CdSeTe/CdTeS/ZnSeS–MSA (7.3), compound **13** and conjugate (**13**–MSA–CdSeTe/CdTeS/ZnSeS (7.3)) were used as examples, **Figure 3.19C**. For the CdSeTe/CdTeS/ZnSeS–MSA (7.3) QDs; the bands are 1371 cm^{-1} (C–N), 1452 cm^{-1} (C–C), 1549 cm^{-1} (C=O), 2847 cm^{-1}, 2913 cm^{-1} (C–H) and 3228 cm^{-1} (O–H). For **13**: the IR bands are 1036 cm^{-1}, 1371 cm^{-1} (C–N), 1265 cm^{-1} (C–O–C), 1315 ($Pc^{\cdot-}$ IR marker), 1448 cm^{-1}, 1596 cm^{-1} (C-C), 2923 cm^{-1}, 2864 cm^{-1} (C-H) and 3355 cm^{-1} (O–H). **13**–CdSeTe/CdTeS/ZnSeS–MSA (7.3) showed bands at 1060 cm^{-1} (C–O) and 1564 cm^{-1} (C=O). The appearance of the ester bond at 1060 cm^{-1} which is not present in either the CdSeTe/CdTeS/ZnSeS–MSA (7.3) nor **13** gives an indication on the successful formation of the ester bond.

3.3.3 XPS Analysis

To further establish the respective amide bonds formation and successful doping of the MPcs onto SiNPs, XPS was employed. ZnO/SiNPs–APTES (13), compound **2b** and conjugate (**2b**–ZnO/SiNPs–APTES (13)) were used as representatives. The wide scan depicted all the expected elemental compositions of the ZnO/SiNPs–APTES (13) as follows: Zn 2p (1021 eV and 1045 eV), Zn 2p Auger peak (499 eV), Zn 3s (139 eV), O 1s (531 eV), N 1s (399 eV), C 1s (285 eV and 290 eV), Si 2s (153 eV), Si 1s (102 eV), **Figure 3.20A(a)**. Compound **2b** gave the following peaks: Zn 2P (1021 eV and 1044 eV), O 1s (532 eV), N 1s (399 eV), C 1s (285 eV), **Figure 3.20A(b)**. Thus, the peaks present in compound **2b** are also present in the ZnO/SiNPs–APTES (13). **2b**–ZnO/SiNPs–APTES (13) showed peaks similar to those of ZnO/SiNPs–APTES (13) and **2b** alone. The atomic concentrations of the samples are listed in **Table 3.3**. **2b**–ZnO/SiNPs–APTES (13) shows an increase

in C and N when compared to individual components, since both have C and N. There is a decrease in O for **2b**–ZnO/SiNPs–APTES (13) compared to ZnO/SiNPs–APTES (13) but an increase compared to compound **2b** alone. It is possible that the intensity of the peaks is affected by the orientations of the Pcs onto the NPs surfaces.

A

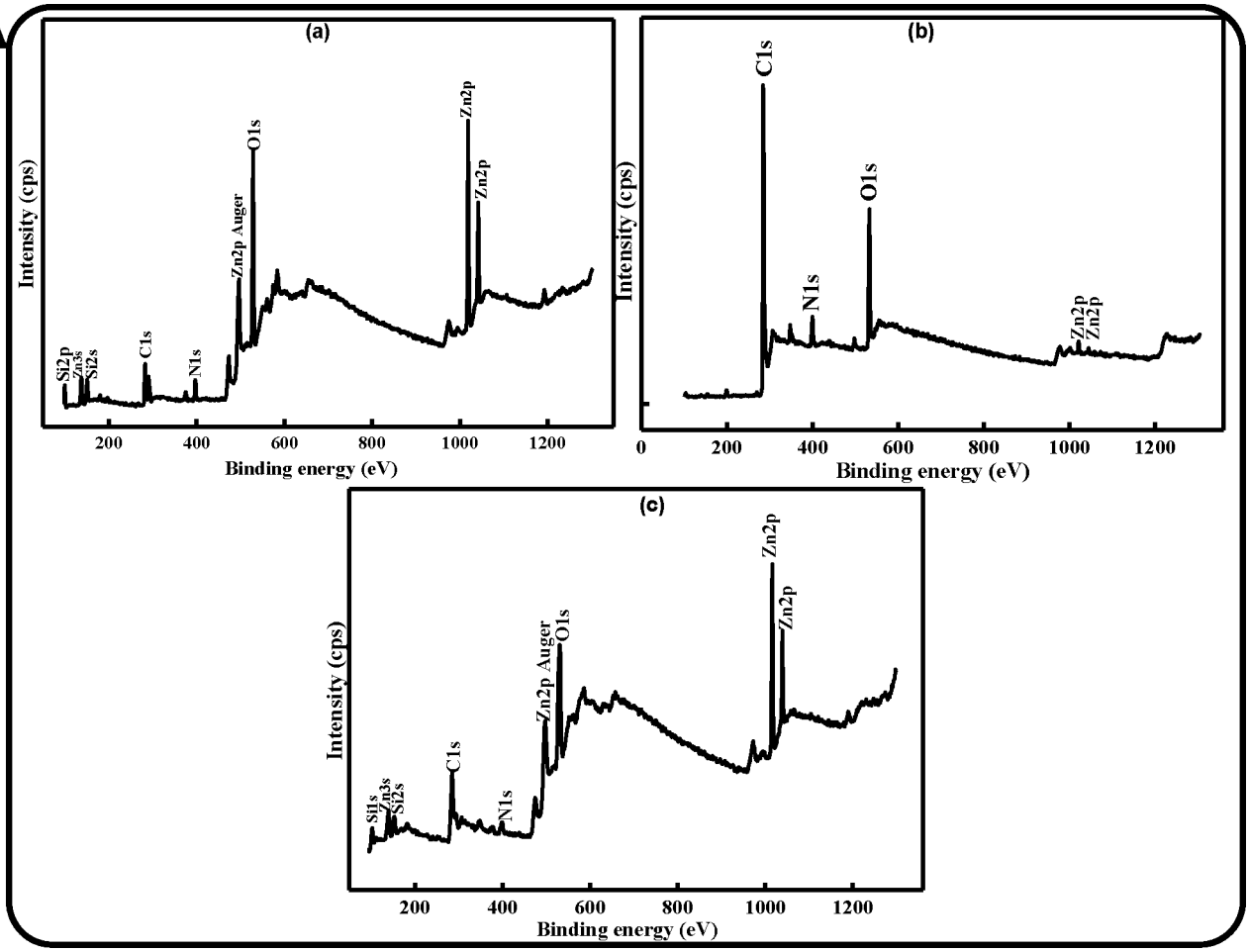

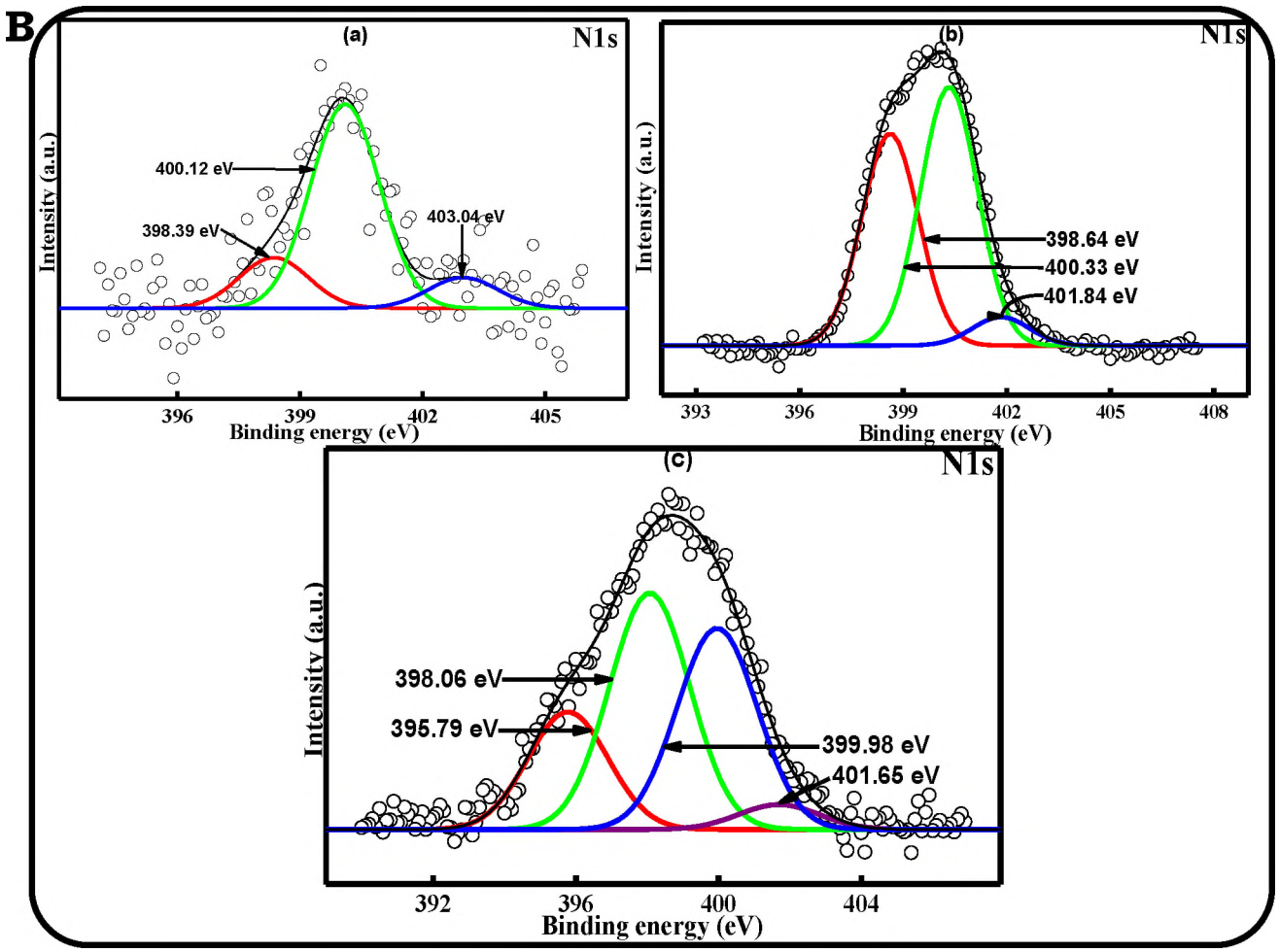

Figure 3.20: (A) Survey spectra of ZnO/SiNPs–APTES (13) (a), 2b (b), and 2b–ZnO/SiNPs–APTES (13) (c); and (B) High resolution spectra N 1s of ZnO/SiNPs–APTES (13) (a), 2b (b), and 2b–ZnO/SiNPs–APTES (13) (c).

The N 1s spectra of ZnO/SiNPs–APTES (13) exhibited three distinct sub peaks at 398.39 eV (N–H), 400.12 eV (N–C), 403.04 eV (C–C–N), **Figure 3.20B(a)** while **2b** depicted three sub peaks at 398.64 eV (–C=N), 400.33 eV (N), 401.84 eV (N–C), **Figure 3.20B(b)** and **2b**–ZnO/SiNPs–APTES (13) showed four distinct sub peaks at 395.79 eV (N–C), 398.06 eV (C=N), 399.98 eV (C–NH–C) and 401.65 eV (O=C–NH), **Figure 3.20B(c)**.

The latter is an additional peak that resulted from the linkage of the primary amine of APTES functionalized NPs with activated carboxylic acid moiety of the MPc to form amide (O=C–NH) bond, **Figure 3.20B(c)**, **[287,288].**

Table 3.3: XPS apparent surface compositions of Pc compound, NPs and their nanoconjugates

Samples	Atomic Concentrations (%)				
	C 1s	O 1s	N 1s	Si 2P	Zn 2P
ZnO/SiNPs–APTES (13)[a]	20.02	42.61	5.69	31.62	0.06
2b	12.01	10.93	4.91	N/A	0.36
2b–ZnO/SiNPs–APTES (13)[a]	50.96	31.47	7.31	5.03	5.22
SiNPs	41.37	27.03	0.00	15.50	0.00
4–SiNPs (34)[b]	43.28	27.58	0.02	14.11	N/A
5–SiNPs (40)[b]	41.75	27.58	0.85	14.29	N/A

(a) Amide linked conjugates and (b) Doped conjugates. Values in brackets represent the sizes obtained from TEM for the NPs alone. N/A = Not applicable

For the MPcs doped SiNPs, **Figure 3.21**; unmodified SiNPs, **3**–SiNPs (60), **4**–SiNPs (34), and **5**–SiNPs (40) were used as examples. The XPS wide scan showed all the expected elemental compositions of the unmodified SiNPs (33) at their respective binding energies with Si 2p (103 eV), Si 2s (154 eV), C 1s (285 eV), O 1s (532 eV) while the MPcs doped SiNPs showed similar pattern as the unmodified SiNPs (33) alone with increase in atomic concentrations of C and O upon doping, **Table 3.3** (using **4**–SiNPs (34) and **5**–SiNPs (40) as examples). In addition, N peak was obtained in the MPcs doped SiNPs which was absent in the unmodified SiNPs (33) alone, **Figure 3.21A**. The increase in the atomic concentrations of the MPcs doped SiNPs compared to the unmodified SiNPs (33) alone could be adduced to the presence of the MPcs doped onto SiNPs.

Since both the unmodified SiNPs (33) and the MPcs (using **3**–SiNPs (60) as an example) have O 1s in common but in different chemical environment, the high resolution O 1s peak were deconvoluted. Upon deconvolution of O 1s of the unmodified SiNPs, only one peak was obtained at 533.14 eV corresponding to siloxane peak, **Figure 3.21B** while the O 1s of the MPcs doped SiNPs showed two sub peaks with binding energies at 533.25 eV and 534.66 eV corresponding to Si–O–Si and C–O–C respectively as shown in **Figure 3.21B** (using **3**–SiNPs (60) as an example). The observed C–O–C sub peak in the conjugates could be attributed to the presence of MPcs which have oxo bridge spacing between their macrocycles and the ring substituents. It is pertinent to note that the increase in the atomic concentrations, the appearance of N and the presence of an extra peak (C–O–C) are due to the presence of the MPc compounds in the conjugates. The observed changes could serve as a possible indication of successful doping of the MPcs onto SINPs.

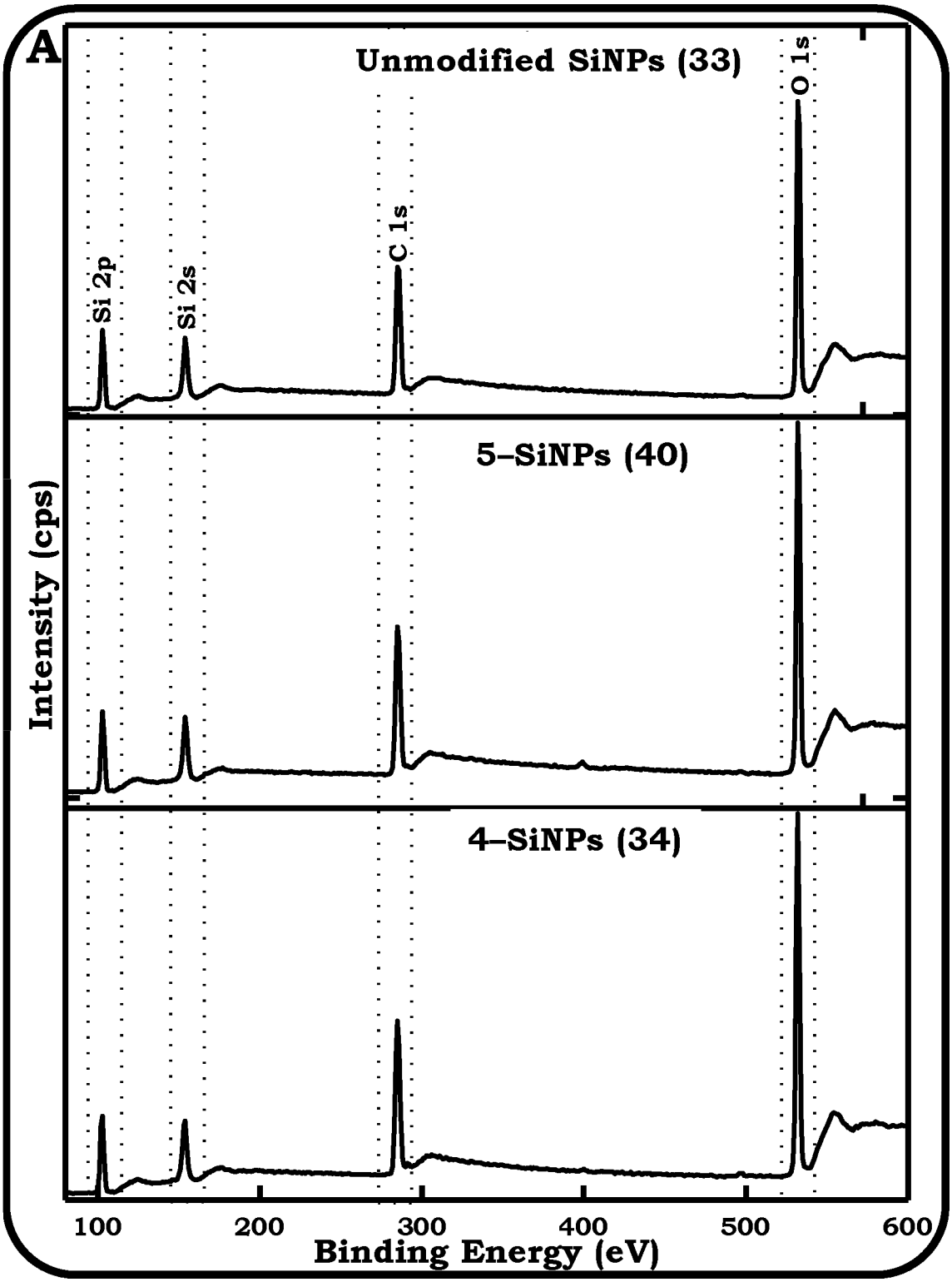
A
Unmodified SiNPs (33)
5–SiNPs (40)
4–SiNPs (34)
Si 2p
Si 2s
C 1s
O 1s
Intensity (cps)
100
200
300
400
500
600
Binding Energy (eV)

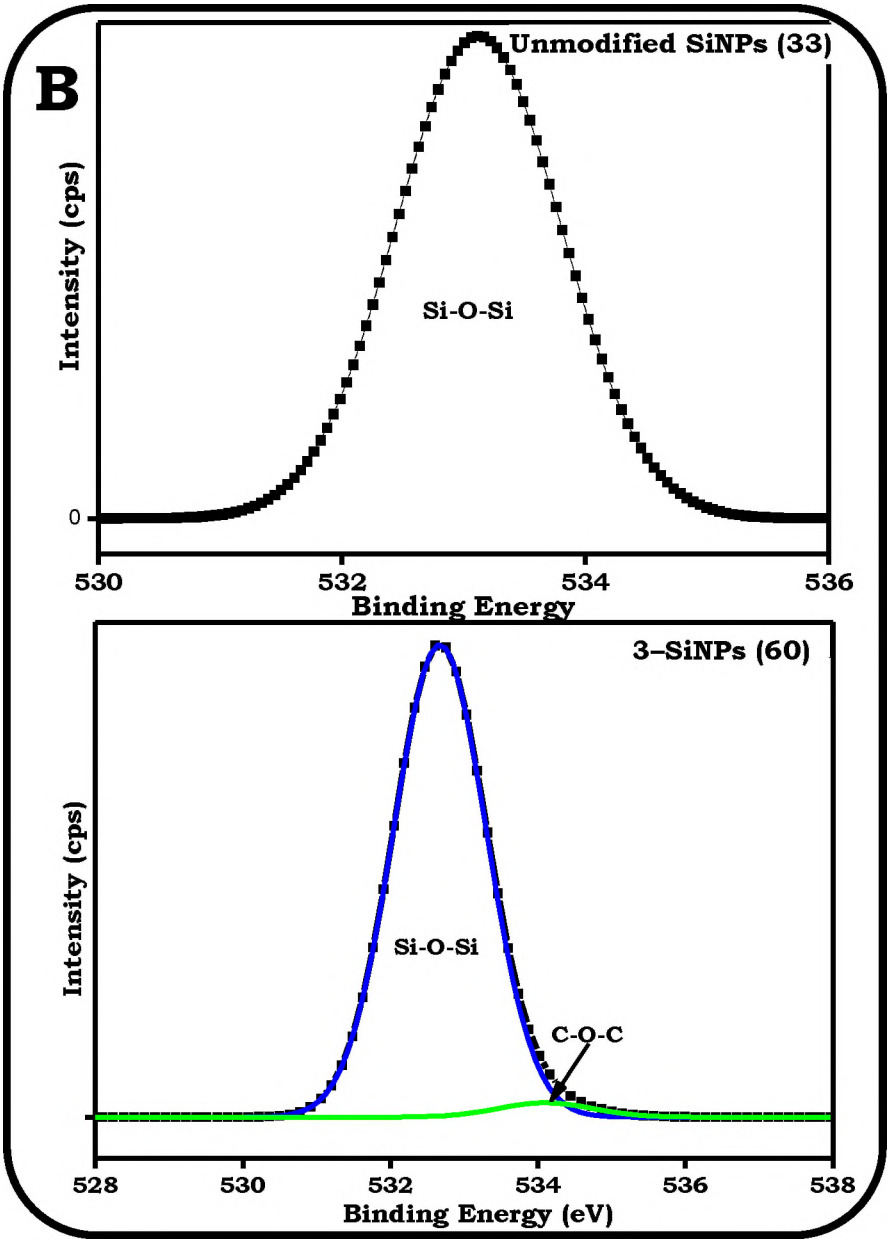

Figure 3.21: (A) Survey spectra of unmodified SiNPs (33), 5–SiNPs (40), and 4–SiNPs (34); and (B) High resolution spectra O 1s of unmodified SiNPs (33), and 3–SiNPs (60).

3.3.4 EDX Spectra

The EDX spectra of the NPs, Pcs and their conjugates were measured. SiNPs–APTES (20) and **2b**–SiNPs–APTES (20) were used as examples (**Figure 3.22**), SiNPs–APTES (20) showed carbon in addition to silicon, oxygen, and nitrogen

peaks, this is expected based on the composition of SiNPs which has (3–aminopropyl)triethoxysilane as it capping ligand, **Figure 3.22A(a)**. The conjugates (**2b**–SiNPs–APTES (20)) showed similar pattern but with the presence of zinc from **2b**, **Figure 3.22A(b)**. Compound **5** showed the presence of Al, Cl, C, O, and N while its doped analogue with unmodified SiNPs (33) showed all the elemental compositions in **5** with the addition of Si resulting from the SiNPs, **Figure 3.22B**

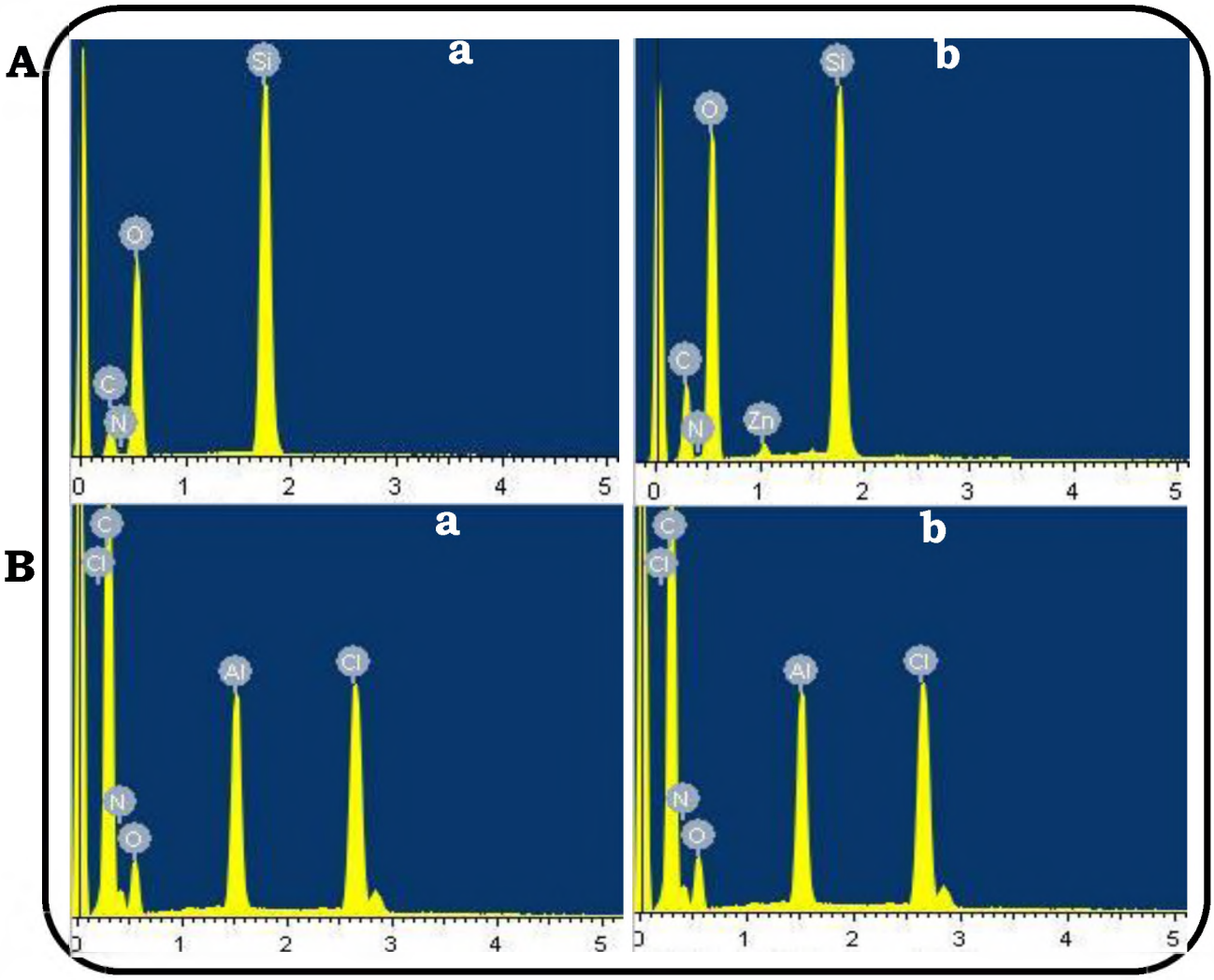

Figure 3.22: EDX spectra (A) SiNPs–APTES (20) (a), and 2b–SiNPs–APTES (20) (b); and (B) 5 (a), and 5–SiNPs (40) (b).

3.3.5 TEM Analysis

The morphologies of the NPs and their nanoconjugates were assessed using a transmission electron microscopy (TEM). SiNPs–APTES (20), **2b**–SiNPs–APTES (20), compound **3**, and compound **3** doped SiNPs (40) were used as examples, **Figure 3.23**. The SiNPs–APTES (20) were aggregated **(Figure 3.23A(a))** and on conjugation with **2b**, increased aggregation was observed **(Figure 3.23A(b))** and this could be attributed to π–π interaction of the MPcs onto adjacent SiNPs. The mean size for the SiNPs–APTES is 20 nm and 13 nm for the ZnO/SiNPs–APTES.

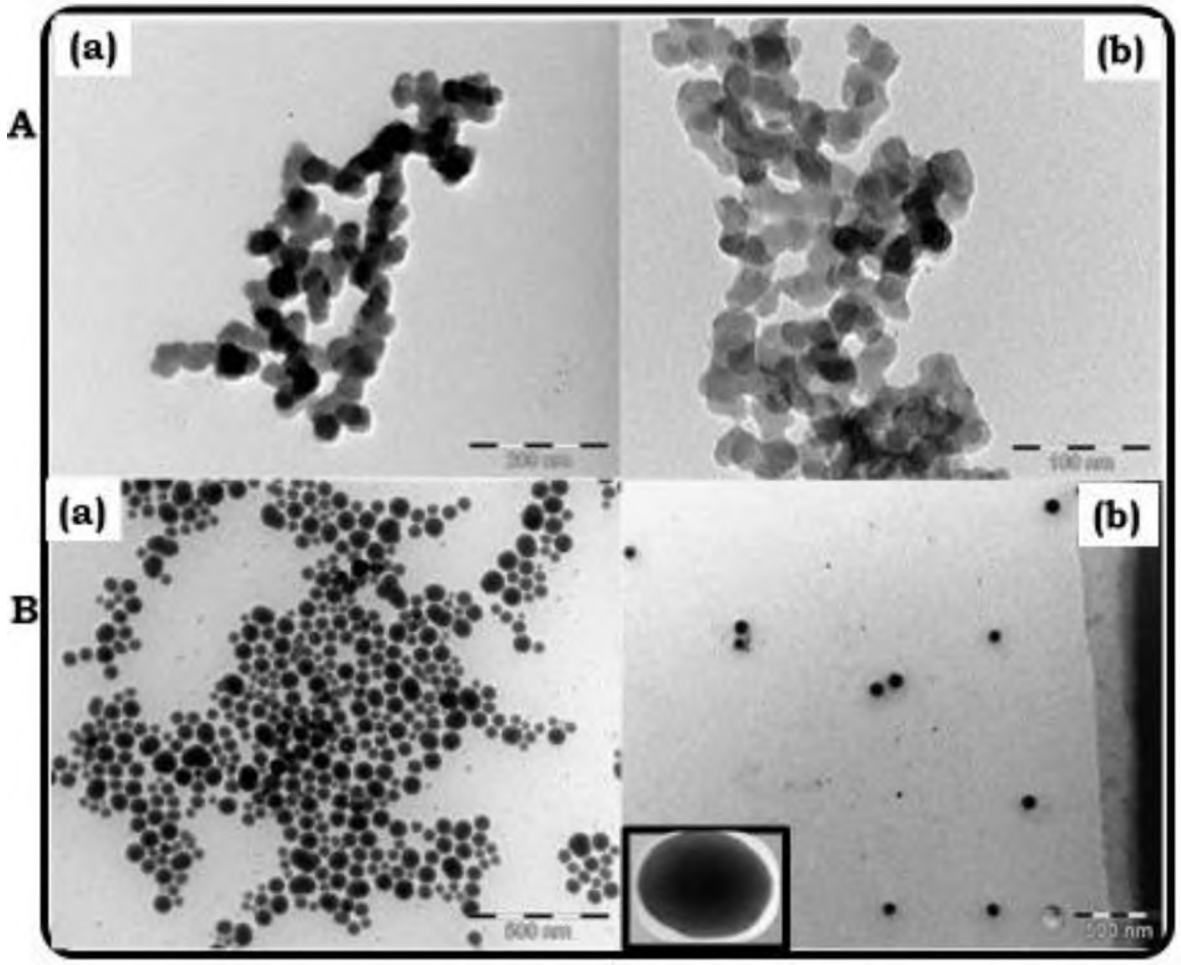

Figure 3.23: TEM micrographs (A) SiNPs–APTES (20) (a), and 2b–SiNPs–APTES (20) (b); and (B) Unmodified SiNPs (33) (a), and 3–SiNPs (60) (b). Inset = Isolated MPcs doped SiNPs.

The TEM micrographs of the unmodified SiNPs (33) alone showed a very distinct morphology with dispersed particle sizes **(Figure 3.23B(a))** and gave an average size of 33 nm. High dispersity was observed in the doped conjugates (using **3**–SiNPs (60) as an example) **(Figure 3.23B(a))** but the particle size of the conjugate was larger than that of the SiNPs alone **(Figure 3.23B)**, **Table 3.2**. The increase in size following conjugation could be to the interaction of the Pcs within the pores of SiNPs (hence aggregation). The largest size was obtained for **3**–SiNPs (60 nm), showing ease of aggregation of this non–peripherally substituted Pc when within the pores of SiNPs, **Table 3.2**. The sizes for **4**–SiNPs, **5**–SiNPs and **6**–SiNPs were 34 nm, 40 nm, and 39 nm respectively, **Table 3.2**. Similar trend in term of aggregation has earlier been reported for corroles grafted into SiNPs **[289]**. On close visual inspection of the TEM micrograph of the MPcs doped SiNPs (using the inset, **Figure 3.23B(b)**), two layers in their dispersed particles form were observed and this could serve as a good indication of the MPcs been grafted into the SiNPs. Similar trends were observed for QDs, AgNPs–Cyst (11.3) and AgAuNPs–Cyst (11.6) with their conjugates.

3.3.6 XRD Analysis

The XRD diffractograms of the respective NPs and their conjugates were measured. The cysteamine capped AgNPs and (using **10**–AgNPs–Cyst (11.3), as an example) showed five diffraction patterns which is typical of AgNPs with diffraction peaks at 2θ values of 38.47° (38.25°), 44.67° (44.44°), 64.70° (64.56°), 77.65° (77.47°), 81.77° (81.75°), values in the brackets are for **10**–AgNPs–Cyst

(11.3), **Figure 3.24A** (see also **Figure 3.3**). The last peak is weaker for **10**–AgNPs–Cyst (11.3) with appearance of a broad peak at 2θ = 20° which corresponds to the amorphous peak of Pcs **[290]**, **Figure 3.24A**.

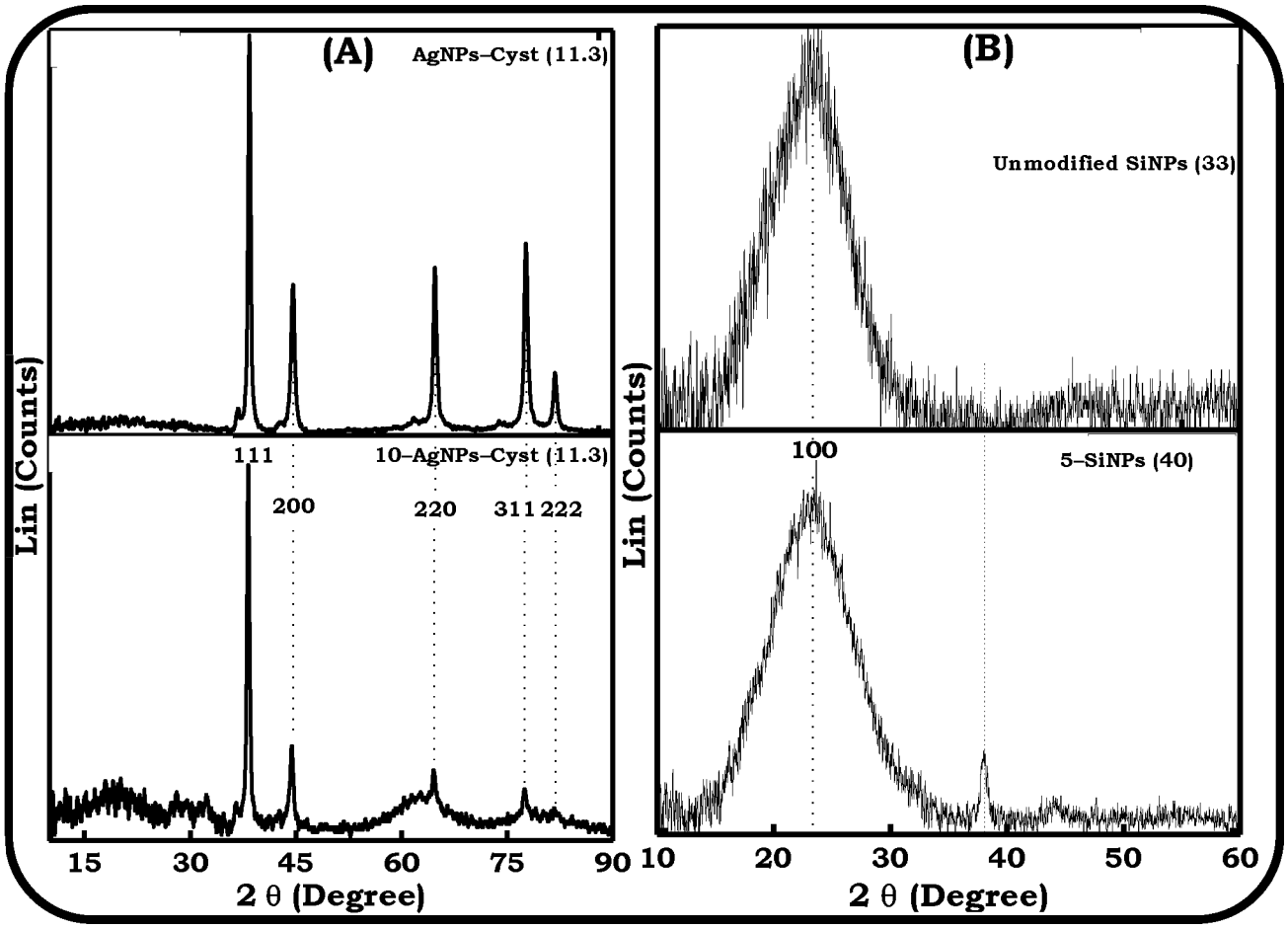

Figure 3.24: XRD diffractograms of (A) AgNPs–Cyst (11.3), and 10–AgNPs–Cyst (11.3); and (B) unmodified SiNPs (33), and 5–SiNPs (40) (Doped).

In addition, there is the attenuation of the AgNPs–Cyst (11.3) in the conjugate at plane 200 and broadening of the crystalline peaks of the AgNPs–Cyst (11.3) at planes 220, 311, 222. The observed changes in the NPs upon conjugation could be an indication of successful conjugation between the NPs and Pcs. QDs showed similar behaviour as AgNPs except for the predominant three broad diffraction

patterns at planes 110, 222, 311 (figures not shown). The unmodified SiNPs (33) showed its typical single broad peak at 2θ = 25° while its conjugate with compound **5** depicted similar diffraction pattern as the Pcs and SiNPs, this is expected because Pcs and SiNPs are known to show their only distinct diffraction peak between 2θ = 20°–27° **[290,291]**, **Figure 3.24B**.

3.3.7 Thermogravimetric Analysis

The thermal stability of the unmodified SiNPs (33) and its MPcs doped conjugates were assessed using a thermogravimetric analyzer at temperature range of 30 to 900 °C with heating rate of 10 °C min^{-1}, maintained under a steady N_2 flow rate of 20 mL min^{-1}. The stability of the unmodified SiNPs (33) decreased upon doping of the MPcs onto SiNPs, **Figure 3.25**. The loading efficiency was calculated as previously reported in the literature using TGA **[292]**. The total percent weight loss for the unmodified SiNPs alone was 26.2% at 900 °C, while that of the MPcs doped analogues were as follows: **3**–SiNPs (49.9%), **4**–SiNPs (43.5%), **5**–SiNPs (37.2%), **6**–SiNPs (36.3%). The loadings of the MPcs to the SiNPs were estimated to be 23.6% (**3**–SiNPs (60)), 17.3% (**4**–SiNPs (34)), 11% (**5**–SiNPs (40)), 10.1% (**6**–SiNPs (39)), **Table 3.4**. The non–peripheral substituted MPc (**3**–SiNPs (60)) showed a larger loading compared to the corresponding peripherally substituted MPcs (**4**–SiNPs (34)), suggesting ease of loading for non–peripheral substitution for compound **3**. This also supports the larger size for **3**–SiNPs (60) obtained by TEM.

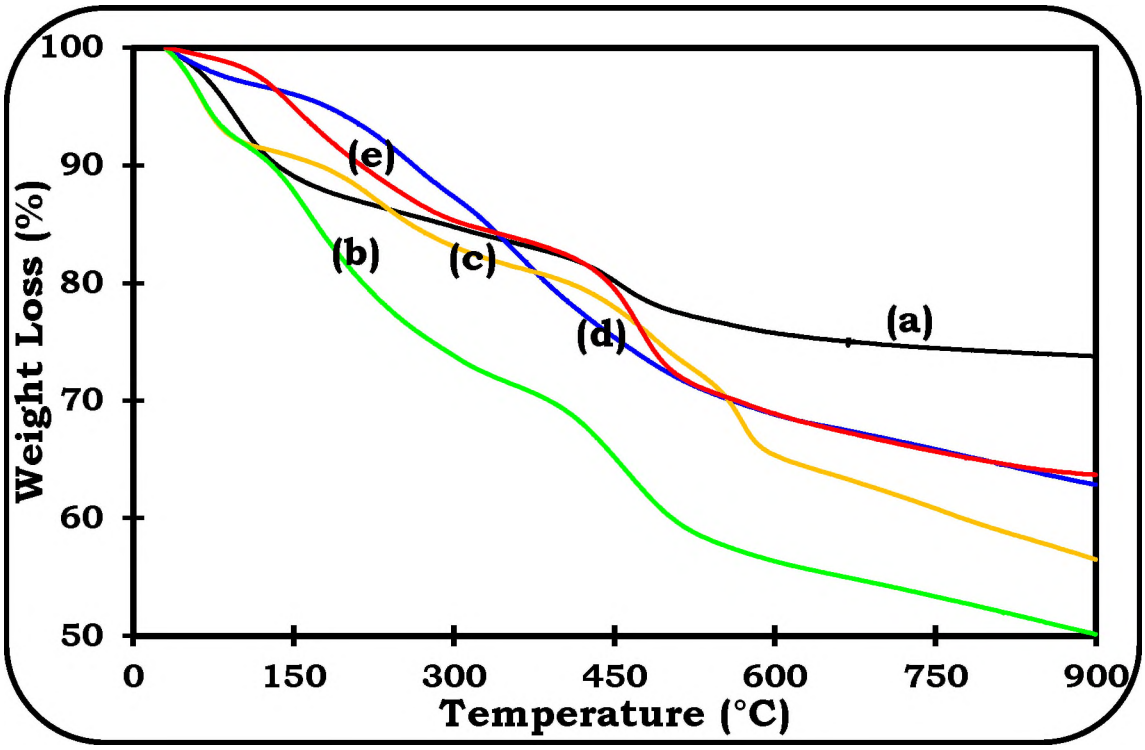

Figure 3.25: Thermogravimetric decomposition curves of (a) unmodified SiNPs (33), (b) 3–SiNPs (60), (c) 4–SiNPs (34), (d) 5–SiNPs (40), and (e) 6–SiNPs (39).

3.3.8 UV–Vis Absorption Spectra

The ground state electronic absorption spectra of all the compounds and their nanoconjugates were measured in solution. The representative spectra for the compounds and conjugates were selected as follows: compound **7** and **7**–CdTe/CdS/ZnS–GSH (5.2) (sulfonamide bond); compound **2b** and **2b**–SiNPs–APTES (20) (amide bond); compound **14** and **14**–CdSeTe/CdTeS/ZnSeS–MSA (7.3) (ester bond); compound **5** and **5**–SiNPs (40) (MPcs doped SiNPs), **Figure 3.26**.

For compound **7** and **7**–CdTe/CdS/ZnS–GSH (5.2), a significant hypsochromic shift in the absorption wavelength of the Q–band for compound **7** in the nanoconjugate compared to **7** alone was observed. In addition, there is an

enhancement in the absorption of **7** in the conjugate at ≤ 650 nm, attributed to the presence of QDs in the conjugates, **Figure 3.26A**. Shifts in the Q–band maxima may be linked to orientation of Pcs on the QDs as reported before for other chromophores **[293]**. Comparing the sulfonamide and amide bonds conjugates using **7**–CdTe/CdS/ZnS–GSH (5.2) and **6**–CdTe/CdS/ZnS–GSH as examples, hypsochromic shift was observed in the absorption Q–band of compound **7** in the former while compound **6** in the latter was relatively unchanged.

SiNPs–APTES (20) showed significant absorption around the B band region of compound **2b** and this was reflected in the spectra of the nanoconjugates (**2b**–SiNPs–APTES (20)) with enhanced absorption at ≤ 650 nm. There was no pivotal change in the Q–band maxima of the **2b** upon conjugation, **Figure 3.26B, Table 3.2**.

For compound **14** and **14**–CdSeTe/CdTeS/ZnSeS–MSA (7.3), the absorption spectra of the nanoconjugates showed slight enhancement ≤ 600 nm, which could be due to the presence of both QDs and Pcs, Figure **3.26C**.

Compound **5** in **5**–SiNPs (40) shows broad absorption bands in the 550 nm to 650 region, due to aggregation, **Figure 3.26D**. Aggregation in Pcs is judged by the broadening or split in the Q–band with the high energy band due to the so called "H" aggregates **[261]**. Aggregation of the Pcs embedded in silica nanoparticles has been reported with broadened Q–band as observed here **[294]**. Aggregation of the Pcs within the SiNPs could be due to the close proximity of the Pcs in the pores. Among the MPcs doped onto SiNPs, aggregation in **5**–SiNPs

(40) is more prominent compared to the other conjugates (figures not shown). This could be due to the easy replacement of the Cl on the axial position with OH leading to hydrogen bonding of two adjacent Al(OH)Pcs via axial hydroxyl groups as discussed before **[242]**.

The individual compounds showed their characteristics monomeric Q–band, in addition to their typical soret band. The absorption spectra of the conjugates were significantly enhanced at ≤ 650 nm. The observed enhancement could be attributed to the presence of the NPs and this was confirmed by comparing the compounds alone and in conjugates. No significant change was observed in the monomeric Q–band of the compounds upon conjugations except in some cases where shifts in Q–band were observed, for example, **7** in **7**–CdTe/CdS/ZnS–GSH 5.2), **Table 4.2**.

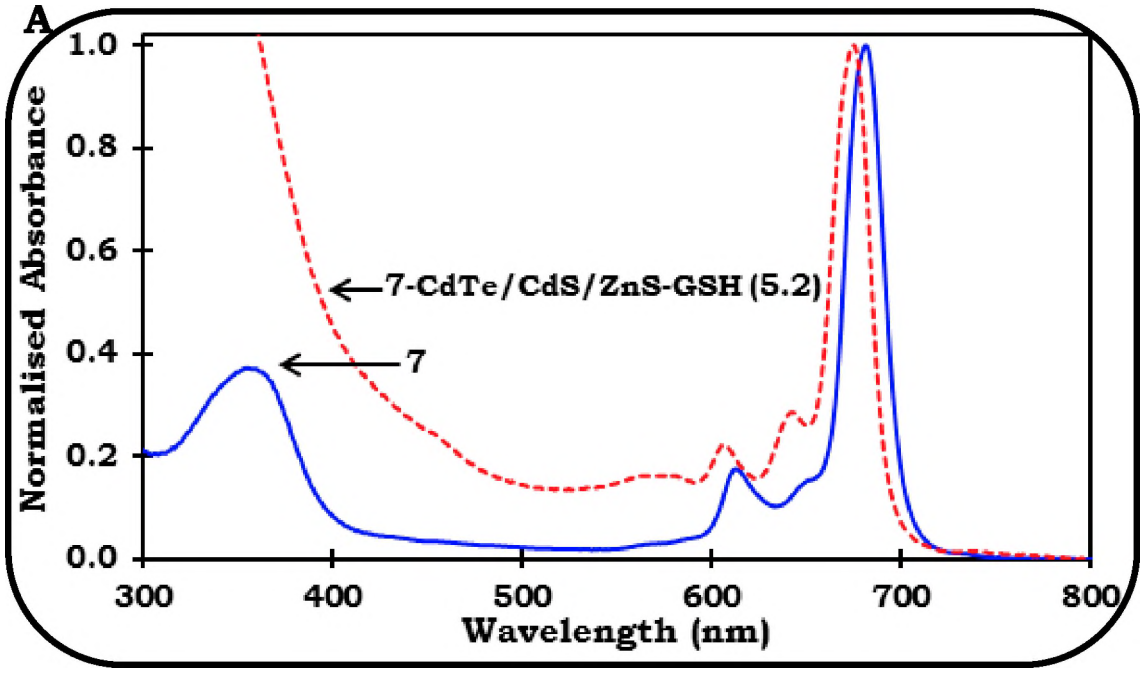

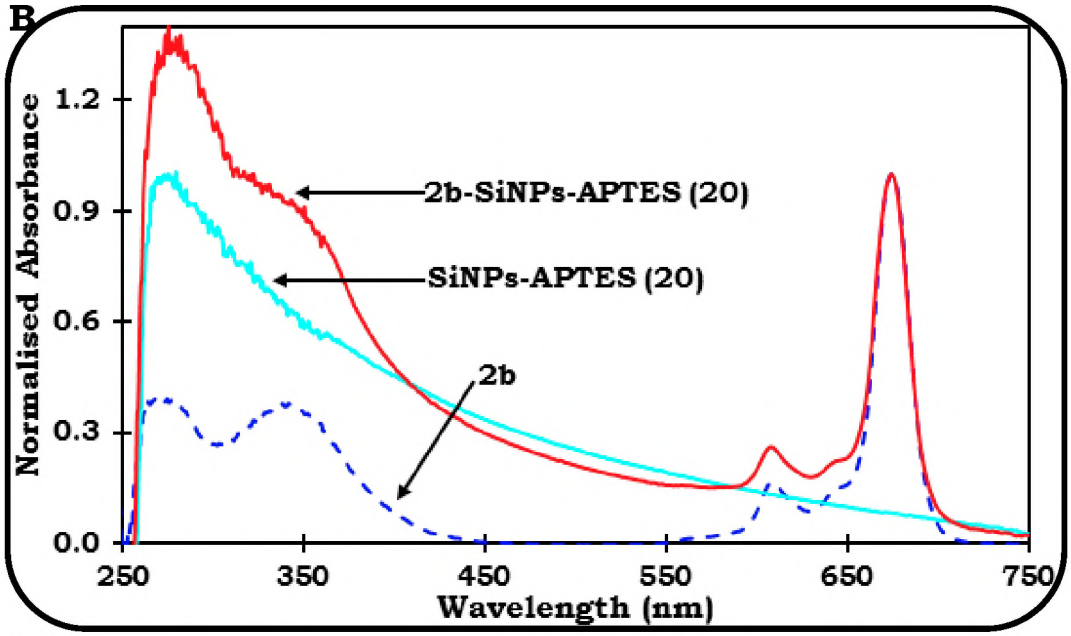
B
Normalised Absorbance
1.2
0.9
0.6
0.3
0.0
2b-SiNPs-APTES (20)
SiNPs-APTES (20)
2b
250
350
450
550
650
750
Wavelength (nm)

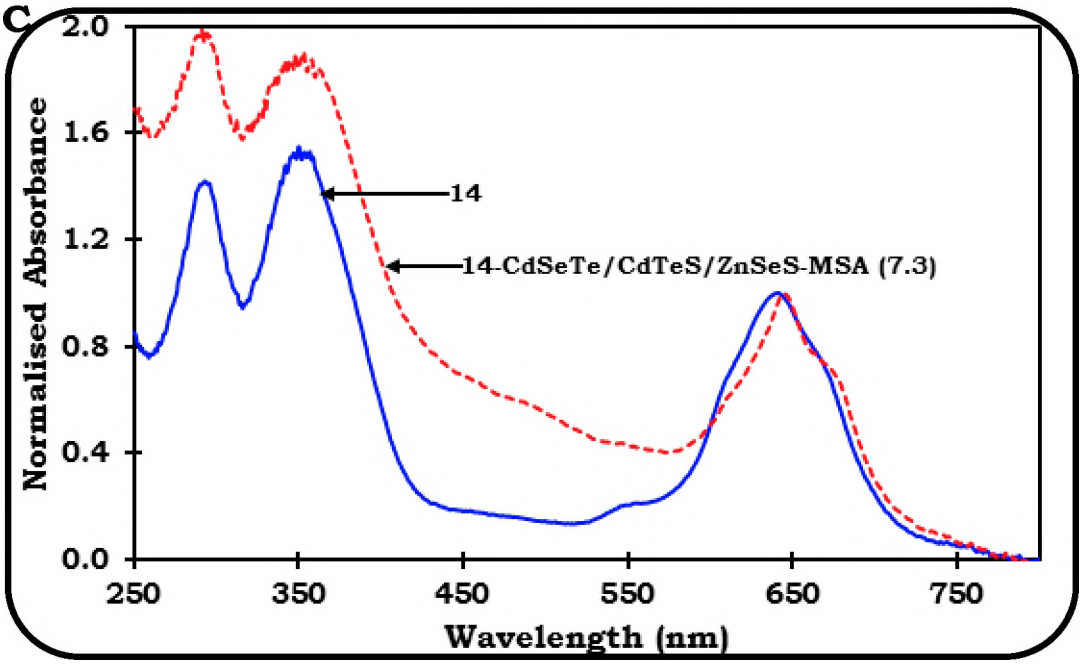
C
Normalised Absorbance
2.0
1.6
1.2
0.8
0.4
0.0
14
14-CdSeTe/CdTeS/ZnSeS-MSA (7.3)
250
350
450
550
650
750
Wavelength (nm)

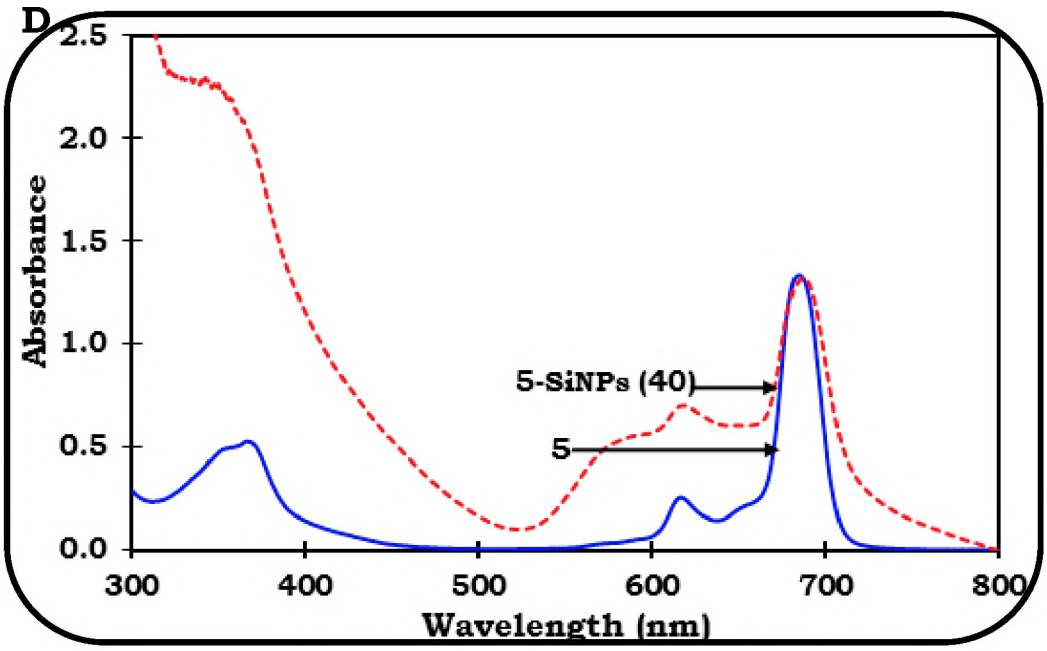

Figure 3.26: Absorption spectra of (A) compound 7 and its conjugate (sulfonamide bond), (B) compound 2b and its conjugate (amide bond), (C) 14 and its conjugates (ester bond), and (D) compound 5 and its conjugate (MPcs doped SiNPs).

3.4 MASS LOADING OF MPcs TO NPs

In addition to using TGA for MPcs doped onto SiNPs, the mass loading of the MPcs chemically bonded to NPs were estimated as reported in the literature using UV–Vis spectrometry **[152,292,295,296]**, representative data are shown in **Table 3.4**. The size of MPc is often ~1 nm while that of NPs are usually greater 2 nm. Thus, it is unlikely for more than one NPs to bind to a Pc from size consideration due possible straining of the Pc as a result of instability that might result from excessive loading onto a small molecule (Pc). But it is possible for more than one Pcs to bind to NPs. The mass loading of compound **7** in **7**–CdTe/CdS/ZnS–GSH (5.2) and **7**–CdTe/CdS/ZnS–GSH (6.3) were estimated to be 11.1% and 8.4%

respectively, **Table 3.4** implying less loading for the larger QDs with a smaller surface area. For **2b** and **2b**–SINPs–APTES (20), and **2b**–ZnO/SiNPs–APTES (13), the mass loading of **2b** to SiNPs–APTES (20) and ZnO/SiNPs–APTES (13) were 68.4% and 94.9% respectively. Thus, the larger SiNPs–APTES (20 nm) had a lower mass loading compared to the smaller ZnO/SiNPs–APTES (13 nm). The larger loading of **2b** to ZnO/SiNPs–APTES could be attributed to the large surface areas and pore sizes of the NPs. It has been reported that the mass loading of Pcs to NPs is dependent on the size, surface areas and pore sizes of the NPs **[297]**. For the SiNPs doped MPcs; as discussed above, the loadings of the MPcs to the SiNPs were estimated to be 23.6% (**3**–SiNPs (60)), 17.3% (**4**–SiNPs (34)), 11% (**5**–SiNPs (40)), 10.1% (**6**–SiNPs (39)). The non–peripheral substituted MPc (**3**–SiNPs (60)) showed a larger loading compared to the corresponding peripherally substituted MPcs (**4**–SiNPs (34)), suggesting ease of loading for non–peripheral substitution for compound **3**. It can be inferred that the NPs having large sizes recorded less efficient mass loading of the Pcs onto their surfaces due small surface areas and pore sizes which does not allow for high loading onto their surface **[297]**. The trend does not hold in some cases, for example, **8**–CdTe/ZnSe/ZnO–GSH (6.2, and 7.6), and **9**–CdTe/ZnS/ZnO–GSH (4.8).

Table 3.4: Mass loading efficiency (*Eff.*) of Pcs onto NPs.

Compounds	Loading *Eff.* (%)
2a–CdTe–GSH (2.4)	ND
2a–CdTe/CdS–GSH (3.1)	ND
2a–CdTe/CdS/ZnS–GSH (4.2)	25.0
2a–CdTe/CdS/ZnS–GSH (5.1)	16.7
2a–CdTe/CdS/ZnS–GSH (6.7)	12.5
2b–SiNPs–APTES (20)	68.4
2b–ZnO/SiNPs–APTES (13)	94.9
3–SiNPs (60) [Doped]	23.6
4–SiNPs (34) [Doped]	17.3
5–SiNPs (40) [Doped]	11.0
6–SiNPs (39) [Doped]	10.1
6–CdTe–GSH (2.4)	25.0
6–CdTe/CdS–GSH (3.1)	14.5
6–CdTe/CdS/ZnS–GSH (4.2)	11.1
6–CdTe/CdS/ZnS–GSH (5.1)	8.4
6–CdTe/CdS/ZnS–GSH (6.7)	6.3
6–CdTe–GSH (2.9)	24.8
6–CdTe/ZnO–GSH (4.6)	16.7
6–CdTeSe–GSH (3.6)	20.0

6–CdTeSe/ZnO–GSH (5.1)	20.0
6–CdTeSe/ZnO–GSH (6.5)	11.1
7–CdTe/CdS/ZnS–GSH (5.2)	11.1
7–CdTe/CdS/ZnS–GSH (6.3)	8.4
8–CdTe–GSH (3.2)	20.0
8–CdTe/ZnSe–GSH (4.1)	16.7
8–CdTe/ZnSe/ZnO–GSH (4.5)	10.0
8–CdTe/ZnSe/ZnO–GSH (6.2)	12.5
8–CdTe/ZnSe/ZnO–GSH (7.6)	17.1
9–CdTe–GSH (2.7)	20.0
9–CdTe/ZnS–GSH (4.1)	14.5
9–CdTe/ZnS/ZnO–GSH (4.8)	11.1
9–CdTe/ZnS/ZnO–GSH (5.8)	11.1
9–CdTe/ZnS/ZnO–GSH (8.9)	8.4

3.5 SUMMARY OF CHAPTER

The syntheses and characterizations of the functionalised nanoparticles and phthalocyanines as well as their conjugates were explicitly presented in this chapter.

The AgNPs–Cyst (11.3) and AgAuNPs–Cyst (11.6) showed their typical semi–crystalline diffraction patterns corresponding to the faced–centred cubic structure of metallic silver with planes at 111, 200, 220, 311, and

222. The QDs also showed their characteristic semi–amorphous diffraction patterns with 2θ values which are consistent with the zinc blend crystal and cubic structure at planes 111, 220 and 311. All the NPs showed spherical morphology with dispersed particle sizes evidenced by TEM micrographs. The AgNPs–Cyst (11.3) and AgAuNPs–Cyst (11.6) showed their typical absorption SPR peaks and the QDs depicted their characteristic size dependent absorption and emission spectra. The surface area and the pore sizes of the ZnO/SiNPs–APTES (13) were larger in comparison to the SiNPs–APTES (20).

The mononuclear asymmetrical and symmetrical phthalocyanines showed their typical symmetrical Q– and B– bands. The Pc macrocycles with heavy metals showed pivotal bathochromic shift in comparison to their light metal analogues. All the mononuclear compounds showed monomeric Q–band in solution. The absorption and excitation spectra of the compounds were similar, and mirror images of the emission spectra. Furthermore, the multinuclear asymmetrical and symmetrical phthalocyanines showed their typical absorption bands with the trisphthalocyanines showing bands similar to mononuclear Pcs except for the broad Q–bands while the bisphthalocyanines depicted the following bands: near infrared (NIR–), red valence (RV–), Q–, blue valence (BV–) and B–. In general, the Pc conjugates showed relatively unchanged Q–band compared to the Pcs alone with enhancement in their absorption spectra ≤ 650 nm.

The FT–IR and XPS spectra showed amide, sulfonamide, and ester bonds for the respective linkages which confirms successful formation of the conjugates.

CHAPTER FOUR

PHOTOPHYSICS AND PHOTOCHEMISTRY

These studies were done for compounds **2** to **10**. Compounds **1**, **11** to **14** were only studied for NLO properties, hence are not discussed in this chapter. For the photophysicochemical studies of the MPc compounds and their conjugates with ZnO/SiNPs–APTES (13) and QDs, heavy–atom effect due to spin–orbit coupling is expected to play an indispensable role in the photophysical behaviour of the Pcs and their conjugates. The spin–orbit coupling is known to be dependent on atomic numbers of metals. Hence, large atomic number often corresponds to high spin–orbit coupling. It is expected that Pcs containing heavy metal will show improved triplet state properties in comparison to their relatively light metal containing analogues. Similarly, when ZnO/SiNPs–APTES (13) and QDs are conjugated to the Pc compounds, the former are expected to improve their photophysical properties due to the heavy metal contribution from the NPs **[298]**.

4.1 FLUORESCENCE QUANTUM YIELD (Φ_F) AND LIFETIME (τ_F)

The Φ_F values of the quantum dots (QDs), metallophthalocyanines (Pcs) and their conjugates were determined as described in the literatures **[231,232]**. The fluorescence lifetime (τ_F) was determined using time correlated single photon counting set–up **[231,236]**.

4.1.1 Quantum dots

The Φ_F values of the QDs used in this work ranges from 0.02 to 0.94, **Table 4.1**. The QDs that were synthesized via the hydrothermal route showed significantly higher Φ_F and τ_F values in comparison to the ones obtained via the organometallic route. The CdSe–TOPO (3.8), CdSe/ZnS–TGA (4.0),

CdSeTe/CdTeS/ZnSeS–MSA (7.3) and CdSeTe/CdTeS/ZnSeS–TOPO (6.6) QDs were synthesized via the organometallic route while the others listed in the **Table 4.1** were synthesized via the hydrothermal route. Comparing CdSe/ZnS–TGA (4.0) and CdTe/ZnS–GSH (4.1) with relatively the same size, the latter afforded a higher Φ_F value (0.63) compared to the former which afforded a lower Φ_F value (0.02). The low Φ_F and τ_F values for the QDs obtained from the organometallic route could be attributed to the phase transfer process from lipophilic forms to hydrophilic forms which often results in quenching of fluorescence **[299,300]**.

In general, the binary QDs showed better Φ_F and τ_F values in comparison to their ternary counterparts and this could be attributed to the possible large surface defects and nonradiative decay in the ternary core QDs. Comparing CdTe–GSH (3.8) and CdTeSe–GSH (3.6), the former (0.30) afforded a higher Φ_F value compared to the latter (0.09), **Table 4.1**. Comparing CdTe/ZnO–GSH (4.6) and CdTeSe/ZnO–GSH (5.1), the former (0.36) afforded a higher Φ_F value compared to the latter (0.29). The effects of sizes cannot be ignored due to their role in the photophysical properties of QDs. The small QDs showed higher Φ_F values in comparison to the larger ones, for example, compare CdTe–GSH (2.7) with CdTe–GSH (3.2, 3.8), the exception of CdTe/CdS/ZnS–GSH (4.7) (0.39), and CdTe/CdS/ZnS–GSH (5.1) (0.62) where the latter afforded higher Φ_F value in comparison to the former, **Table 4.1**. The decrease in Φ_F values with increased particle size of the QDs could be attributed to possible larger surface trap which creates dangling bonds around QDs surface and non–radiative decay

probabilities in the larger QDs **[301]**. Previous studies have shown that the Φ_F values of QDs are dependent on the capping ligands employed for their surface modification **[301,302]**. Generally, the glutathione capped QDs showed the highest Φ_F values in comparison to the others used in this work, **Table 4.1**. All the QDs showed tri–exponential τ_F which is typical of QDs [**303–305**], the mean τ_F is shown in **Table 4.1**. The trends in τ_F followed the Φ_F in terms of particle size of the QDs. A typical decay curve for QDs is shown in **Figure 4.1**. No detectable emission was noticed for CdTe/CdTeS/ZnSeS–MSA but the TOPO capped analogue showed a detectable emission and the quenching of the emission of the former could be associated with the phase transfer from lipophilicity to hydrophilicity as earlier stated **[299,300]**.

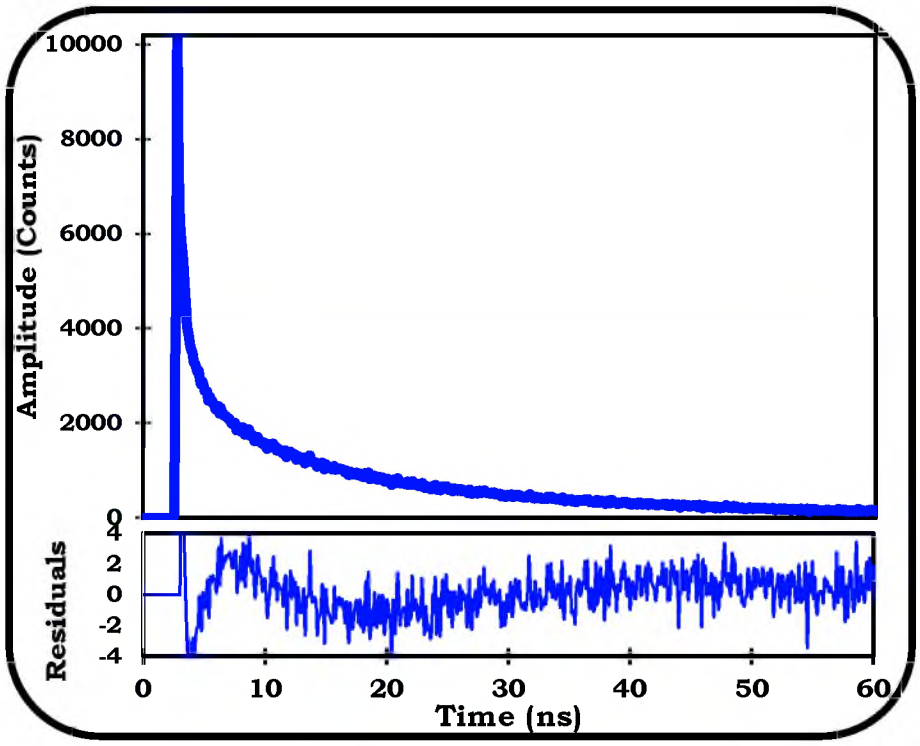

Figure 4.1: Fluorescence lifetime decay curve of quantum dots (using CdTe/ZnS–GSH (4.1) in water as an example).

Table 4.1: Photophysical parameters of quantum dots

QDs	MEDIA	$\Phi_{F\ (0.01)}$	τ_F (ns)
Core			
CdTe–TGA (2.8)	**Water**	0.60	22.81
CdTe–GSH (3.2)	**Water**	0.32	19.20
CdTe–GSH (3.8)	**Water**	0.30	20.50
CdTe–GSH (2.7)	**Water**	0.47	20.38
CdSe–TOPO (3.8)	**Chloroform**	0.19	39.79
CdTeSe–TGA (3.4)	**Water**	0.09	07.33
CdTeSe–GSH (3.6)	**Water**	0.09	17.82
Core/Shell			
CdSe/ZnS–TGA (4.0)	**Water**	0.02	6.28
CdTe/CdS–GSH (3.1)	**Water**	0.43	37.00
CdTe/ZnSe–GSH (4.1)	**Water**	0.32	20.10
CdTe/ZnS–GSH (4.1)	**Water**	0.63	24.63
CdTe/ZnO–TGA (4.0)	**Water**	0.07	08.23
CdTe/ZnO–GSH (4.6)	**Water**	0.36	35.69
CdTeSe/ZnO–TGA (4.7)	**Water**	0.25	18.04
CdTeSe/ZnO–TGA (6.6)	**Water**	0.10	14.64
CdTeSe/ZnO–GSH (5.1)	**Water**	0.29	31.10
CdTeSe/ZnO–GSH (6.5)	**Water**	0.14	25.35
Core/Shell/Shell			
CdTe/CdS/ZnS–GSH (3.2)	**Water**	0.94	36.26
CdTe/CdS/ZnS–GSH (4.5)	**Water**	0.70	30.25
CdTe/CdS/ZnS–GSH (4.7)	**Water**	0.39	28.06

CdTe/CdS/ZnS–GSH (5.1)	**Water**	0.62	28.89
CdTe/CdS/ZnS–GSH (5.2)	**Water**	0.32	21.46
CdTe/CdS/ZnS–GSH (6.3)	**Water**	0.08	13.66
CdTe/ZnSe/ZnO–GSH (4.5)	**Water**	0.42	25.62
CdTe/ZnSe/ZnO–GSH (6.2)	**Water**	0.29	17.1
CdTe/ZnSe/ZnO–GSH (7.6)	**Water**	0.20	13.9
CdTe/ZnS/ZnO–GSH (4.7)	**Water**	0.49	22.06
CdTe/ZnS/ZnO–GSH (5.8)	**Water**	0.33	19.90
CdTe/ZnS/ZnO–GSH (8.9)	**Water**	0.11	13.71
CdSeTe/CdTeS/ ZnSeS–TOPO (6.6)	**Chloroform**	0.10	33.55
CdSeTe/CdTeS/ ZnSeS–MSA (7.3)	**Water**	ND	ND

τ_F = Fluorescence lifetime, ND = Not Detected, values in the brackets represent the QDs sizes obtained by XRD

4.1.2 Metallophthalocyanines (MPcs)

The Φ_F of the Pcs were obtained by the excitation of the Pcs at the vibronic band absorption crossover wavelength with the standard. The Φ_F values of the asymmetrical compounds **2a** (0.18) and **2b** (0.16) were higher than that of compound **6** (0.10), **Table 4.2** and this could be attributed to the lack of symmetry coupled with less deactivation of the excited singlet state of the former thereby encouraging less population at the triplet state. Symmetry is known to promote intersystem crossing to the triplet state **[306]**. The Φ_F values of compounds **3** and **4** with same ring substituents but different point of ring substitution (α vs β) were 0.10 and 0.14 respectively with the latter (**4**, β) accounting for higher Φ_F value in comparison to the former (**3**, α) and this could

be due to peripheral substitution of compound **4** while the observed low Φ_F value of compound **3** could be attributed to the non–peripheral nature of the compound with red shifted Q–band **[262]** which sometimes results in low Φ_F values. The Φ_F values of compounds **4** (Zn) and **5** (Al) having same ring substituents were 0.14 and 0.28 respectively with the latter (**5**) accounting for higher Φ_F value in comparison to the former (**4**), **Table 4.2**. This could be ascribed to the presence of relatively light central metal (Al) in compound **5** compared to the heavy metal (Zn) in compound **4**. Heavy metals are known to promote intersystem crossing to the triplet state by deactivation of the excited singlet state **[298]**. Comparing compounds **4** (0.14) and **6** (0.10), the former (**4**) accounted for higher Φ_F value in comparison to the latter (**6**), **Table 4.2**. The Φ_F values of compounds **6** (Zn) and **8** (In) having similar ring substituents were 0.10 and 0.02, respectively with the former (**6**) accounting for a higher Φ_F value in comparison to the latter (**8**) and this could be adduced to the presence of less heavy metal (Zn) in compound **6** compared to the pronounced heavy metal (In) in compound **8**. Among the asymmetrical compounds **2a** (0.18), **2b** (0.16) and **10** (0.20), compound **10** accounted for the highest Φ_F value and this could be adduced to the presence of additional oxo bridge spacing in its molecular structure compared to the former, **Table 4.2**.

Typical fluorescence decay curves for MPcs are shown in **Figure 4.2**, using **3** and **5** as examples. The τ_F of MPc compounds followed similar trends to what

was observed for the Φ_F due to direct correlation between the Φ_F and τ_F. For example, the τ_F of compounds **3** and **4** were 2.55 ns and 3.01 ns respectively, with compound **4** accounting for higher τ_F value in comparison to compound **3** (**Figure 4.2**) corresponding to high Φ_F value.

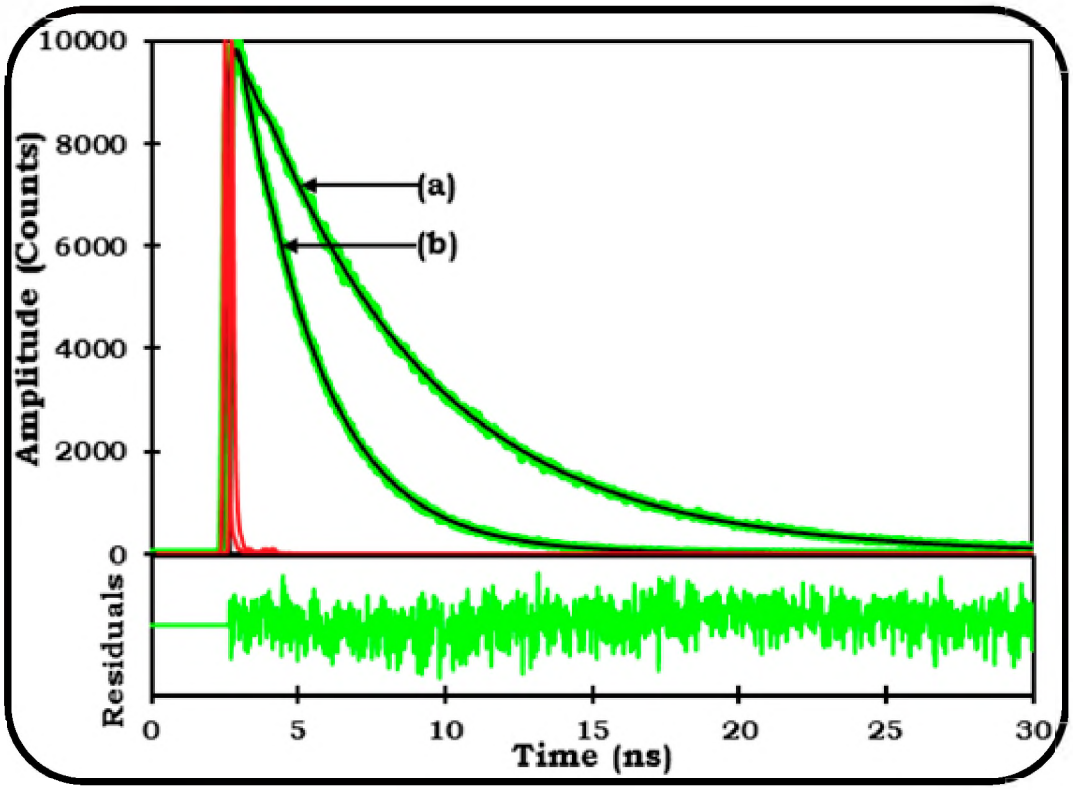

Figure 4.2: Fluorescence lifetime decay curves of 5 (a) and 3 (b) in DMSO.

The τ_F of compounds **4** (Zn) and **5** (Al) having similar ring substituents were 3.01 and 5.90 respectively, with the latter (**5**) accounting for higher τ_F in comparison to the former (**4**) due the heavy–atom effect of the former, **Figure 4.2**. The τ_F values of compounds **6** (Zn) and **8** (In) accounted for 3.00 ns and 2.43 ns respectively, with latter showing short τ_F in comparison to the former due to higher spin–orbit coupling in the latter. Comparing the τ_F values of asymmetrical

compounds **2a** (3.00 ns), **2b** (3.27 ns) and **10** (3.16 ns), compound **2b** accounted for the highest τ_F. Compound **10** accounted for the highest Φ_F but low τ_F in comparison to **2b**. A mono–exponential decay profile inferring one τ_F were observed for all the MPcs, which could be due to their monomeric forms in solution. The Pcs macrocycle with light metals showed higher Φ_F and τ_F values in comparison to their heavy metals counterparts and this could associated with the spin–orbit coupling of the latter which induces faster intersystem crossing to the triplet state, **Table 4.2**.

Table 4.2: Fluorescence quantum yield and lifetime parameters of the Pcs and the respective conjugates

Compounds	Media	Φ_F (0.01)	τ_F (ns)
2a	DMSO	0.18	3.00
2a–CdTe–GSH (2.4)	DMSO	0.17	3.00
2a–CdTe/CdS–GSH (3.1)	DMSO	0.17	3.00
2a–CdTe/CdS/ZnS–GSH (4.2)	DMSO	0.18	3.00
2a–CdTe/CdS/ZnS–GSH (5.1)	DMSO	0.19	3.00
2a–CdTe/CdS/ZnS–GSH (6.7)	DMSO	0.19	3.00
2b	DMSO	0.16	3.27
2b–HSA	DMSO	0.22	3.70
2b–Chitosan	DMSO	0.20	3.45
2b–SiNPs–APTES (20)	DMSO	0.23	3.63
2b–ZnO/SiNPs–APTES (13)	DMSO	0.17	3.11
3	DMSO	0.10	2.55
3–SiNPs (60) [Doped]	DMSO	0.10	2.70
4	DMSO	0.14	3.01
4–SiNPs (34) [Doped]	DMSO	0.15	3.05
5	DMSO	0.28	5.90
5–SiNPs (40) [Doped]	DMSO	0.29	5.89
6	DMSO	0.10	3.00
6–SiNPs (39) [Doped]	DMSO	0.10	3.01
6–CdTe–GSH (2.4)	DMSO	0.10	2.90
6–CdTe/CdS–GSH (3.1)	DMSO	0.10	2.90
6–CdTe/CdS/ZnS–GSH (4.2)	DMSO	0.11	2.90

6–CdTe/CdS/ZnS–GSH (5.1)	DMSO	0.12	2.90
6–CdTe/CdS/ZnS–GSH (6.7)	DMSO	0.12	2.90
6–CdTe–GSH (2.9)	DMSO	0.11	3.00
6–CdTe/ZnO–GSH (4.6)	DMSO	0.11	3.00
6–CdTeSe–GSH (3.6)	DMSO	0.11	3.00
6–CdTeSe/ZnO–GSH (5.1)	DMSO	0.11	3.00
6–CdTeSe/ZnO–GSH (6.5)	DMSO	0.11	3.00
7	PBS	0.13	5.10
7– CdTe/CdS/ZnS–GSH (5.2)	PBS	0.14	5.20
7– CdTe/CdS/ZnS–GSH (6.3)	PBS	0.14	5.20
8	DMSO	0.020	2.43
8–CdTe(3.2)–GSH (3.2)	DMSO	0.012	0.39
8–CdTe/ZnSe–GSH (4.1)	DMSO	0.016	0.38
8–CdTe/ZnSe/ZnO–GSH (4.5)	DMSO	0.017	0.22
8–CdTe/ZnSe/ZnO–GSH (6.2)	DMSO	0.014	0.35
8–CdTe/ZnSe/ZnO–GSH (7.6)	DMSO	0.017	0.25
9	PBS	0.27	4.68
9–CdTe–GSH (2.7)	PBS	0.25	4.61
9–CdTe/ZnS–GSH (4.1)	PBS	0.24	4.61
9–CdTe/ZnS/ZnO–GSH (4.8)	PBS	0.23	4.55
9–CdTe/ZnS/ZnO–GSH (5.8)	PBS	0.23	4.60
9–CdTe/ZnS/ZnO–GSH (8.9)	PBS	0.19	4.56
10	DMSO	0.20	3.16
10–AgNPs–Cyst (11.3)	DMSO	0.18	3.11
10–AgAuNPs–Cyst (11.6)	DMSO	0.18	3.13

4.1.3 MPc conjugates with NPs, chitosan and HSA

It is expected that QDs will enhance intersystem crossing to the triplet state, resulting in lower Φ_F and τ_F values. However, for compounds **2a** and **6**, there were no significant changes in the Φ_F or τ_F values in the presence of the QDs, **Table 4.2**. Decrease in the Φ_F values of compounds **8** and **9** were observed in the presence of GSH–QDs and this could be attributed to effect of more heavy metal in the GSH–QDs. The Φ_F value of compound **6** in **6**–CdTe–GSH (2.9), **6**–CdTe/ZnO–GSH (4.6), **6**–CdTeSe–GSH (3.6), **6**–CdTeSe/ZnO–GSH (5.1), and **6**–CdTeSe/ZnO–GSH (6.5) were relatively unchanged, **Table 4.2**. The Φ_F value of compound **2b** increased in its conjugates with ZnO/SiNPs–APTES (13), SiNPs–APTES (20), HSA, and chitosan. The observed increase in the Φ_F value of **2b**–SiNPs–APTES (20) and **2b**–ZnO/SiNPs–APTES (13) could be due to the structure of the silica–based NPs which allows for close grafting of the MPcs onto their surface, thereby increasing the efficiency of the fluorescence process **[307]**. In addition, **2b**–SiNPs–APTES (20) accounted for the highest Φ_F value among the conjugates and this could be attributed to extensive protection afforded to the MPcs by SiNPs–APTES (20). The high Φ_F value for **2b** in **2b**–HSA could be attributed to the presence of HSA in the conjugate which contains two tryptophan residues with intrinsic fluorescence properties **[308]**. The Φ_F values of the doped conjugates of compounds **3** to **6** onto SiNPs, were relatively unchanged in comparison to the MPcs. Compound **10** in conjugates with

cysteamine capped (AgNPs (11.3), and AgAuNPs (11.6)) showed a slight decrease in the Φ_F value of the conjugates. The trend in the τ_F of the MPcs in the conjugates with NPs, HSA and chitosan are similar to that of the Φ_F due to direct correlation between the Φ_F and τ_F. Bi–exponential decay profiles were obtained for the conjugates in some cases indicating two fluorescence lifetimes which could be attributed to different orientations of the MPcs around the NPs **[293]**.

4.2 TRIPLET (Φ_T) QUANTUM YIELD AND LIFETIME (τ_T)

The laser flash photolysis set–up was employed for the triplet state absorption measurements. Typical triplet decay curves of MPcs and their conjugates are shown in **Figure 4.3** using compound **10** and **10**–AgNPs–Cyst (11.3) as examples. The Φ_T and τ_T measurements of the MPcs were obtained by comparing the Q–band absorption crossover wavelengths between the standard and the MPcs or in conjugates. The crossover wavelengths served as the laser excitation source wavelength. The solution was introduced into a 1 cm path length UV–visible spectrophotometric cell and deaerated using argon for 15 min. Thereafter the solution was sealed and illuminated using an appropriate excitation laser source and detection wavelength leading to appearance of a time–evolved electronic absorption from the T_1–T_n state. The maximum triplet absorption detection wavelength was determined from the transient curves. The solutions were properly deaerated to avoid quenching of the triplet state absorption by atmospheric oxygen. Triplet quantum yield (Φ_T) is a measure of the efficiency of intersystem crossing (ISC) from the excited singlet state to the triplet state. ISC

involves forbidden T_1–S_0 transition to the triplet state and it can be obtained through spin–orbit charge transfer intersystem crossing (SOCT–ISC). For the SOCT–ISC mechanism to be achieved, the donor and acceptor orbitals need to be perpendicular and this is extensively dependent on the donor–bridge–acceptor charge separation. Compounds with the phenyl bridge have been reported to exhibit rapid intersystem crossing rates and this often accounts for highly populated triplet state absorption **[306]**. Φ_T is expected to be high when there is shortening of the τ_T and vice–versa **[309]**.

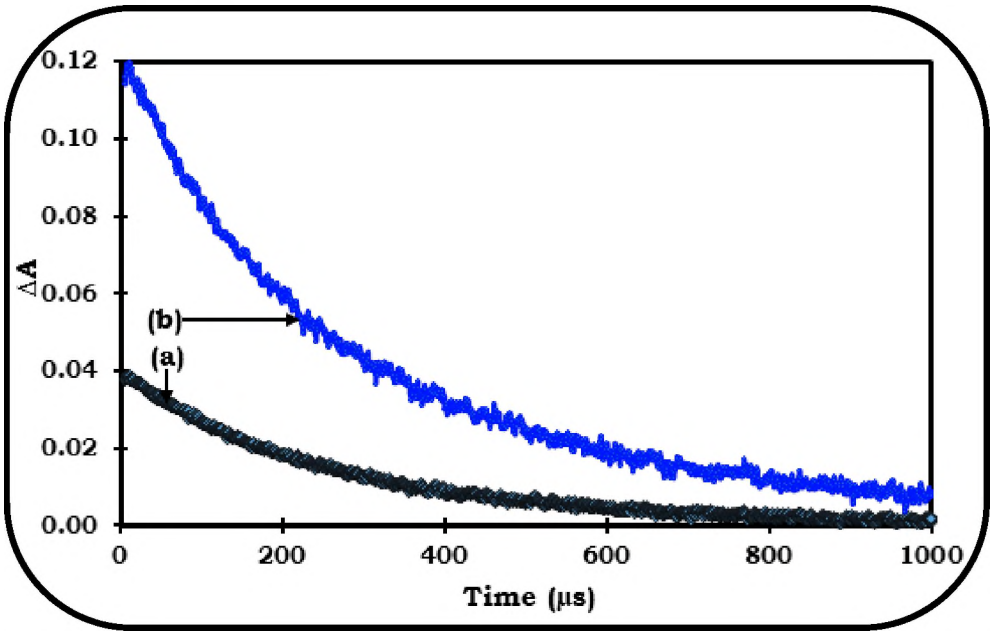

Figure 4.3: Excited triplet state absorption curve of compound 10 (a), and 10–AgNPs–Cyst (11.3) (b) in DMSO.

4.2.1 MPcs alone

The Pc macrocycles with heavy metals accounted for the highest Φ_T values in comparison to their light metal counterparts. This phenomenon could be associated with the spin–orbit coupling of the former which have strong

tendencies to deactivate the excited singlet state to promote rapid intersystem crossing (ISC) of the photosensitizers into the triplet state.

The Φ_T values of asymmetrical compounds **2a** (0.35) and **2b** (0.41) were lower than that of compound **6** (0.49) and this could be attributed to the presence of more phenyl bridges present on the latter which promotes faster ISC of compound **6** to the triplet state **[306]**, **Table 4.3**. The Φ_T values of compounds **3** (α) and **4** (β) were 0.71 and 0.85 respectively, with compound **4** showing higher Φ_T value in comparison to compound **3**. This could be due to more steric hindrance at the non–peripheral position (**3**) compared to the peripheral position (**4**). The higher Φ_T value for compound **4** compared to **3** does not match their Φ_F values. Compound **4** with high Φ_F value should have accounted for lower Φ_T value. The Φ_T values of compounds **4** (Zn) and **5** (Al) with same ring substituents but different central metals (Zn vs Al) were 0.85 and 0.22 respectively, with the former (**4**) accounting for higher Φ_T value in comparison to the latter **5**; this could be ascribed to the presence of heavy central metal (Zn) in compound **4** compared to the relatively light central metal (Al) in compound **5**. Comparing compounds **4** and **6**, the former (**4**) showed higher Φ_T value in comparison to the latter (**6**) and this is due to the low symmetry of the former (**4**) **[310]** due to the *tert*–butyl substituents, as discussed above.

The Φ_T values of compounds **6** (Zn) and **8** (In) with similar ring substituents were 0.49 and 0.68 respectively, with the latter accounting for higher Φ_T value in

comparison to the former and this could be adduced to the presence of less heavy metal (Zn) in compound **6** compared to the pronounced heavy metal (In) in compound **8**, **Table 4.3**. The Φ_T value of compound **7** was higher than what was obtained for compound **9** and this could be attributed to the magnitude of the acidity of **7** which could have lessened the effects of aggregation when in aqueous media compared to **9 [144,264]**.

When the Φ_T values of compounds **2a** (0.35), **2b** (0.41) and **10** (0.48) were compared, compound **10** accounted for the highest Φ_T value. This does not correspond to the large Φ_F value for **10**, since Φ_F and Φ_T are competing processes. As earlier stated, increase in Φ_T should correspond to decrease in τ_T **[309]**. In general, compounds with larger Φ_T values accounted for shorter τ_T values, for example, compounds **3** to **6** and **8**, **Table 4.3**. Furthermore, low Φ_T value is often accompanied by long τ_T **[309]** and this is seen in compounds **5**, **7**, and **9**.

Table 4.3: Triplet quantum yield and lifetime parameters of the Pcs and respective conjugates

Compounds	Media	$\Phi_{T\,(0.01)}$	τ_T(μs)
2a	DMSO	0.35	202
2a–CdTe–GSH (2.4)	DMSO	0.38	188
2a–CdTe/CdS–GSH (3.1)	DMSO	0.42	187
2a–CdTe/CdS/ZnS–GSH (4.2)	DMSO	0.46	171
2a–CdTe/CdS/ZnS–GSH (5.1)	DMSO	0.48	162
2a–CdTe/CdS/ZnS–GSH (6.7)	DMSO	0.51	145
2b	DMSO	0.41	161
2b–HSA	DMSO	0.42	273
2b–Chitosan	DMSO	0.46	277
2b–SiNPs–APTES (20)	DMSO	0.43	277
2b–ZnO/SiNPs–APTES (13)	DMSO	0.64	281
3	DMSO	0.71	247
3–SiNPs (60) [Doped]	DMSO	0.48	152
4	DMSO	0.85	160
4–SiNPs (34) [Doped]	DMSO	0.89	211
5	DMSO	0.22	594
5–SiNPs (40) [Doped]	DMSO	0.17	544
6	DMSO	0.49	238
6–SiNPs (39) [Doped]	DMSO	0.45	390
6–CdTe–GSH(2.4)	DMSO	0.52	193
6–CdTe/CdS–GSH (3.1)	DMSO	0.58	205
6–CdTe/CdS/ZnS–GSH (4.2)	DMSO	0.69	204

6–CdTe/CdS/ZnS–GSH (5.1)	DMSO	0.76	222
6–CdTe/CdS/ZnS–GSH (6.7)	DMSO	0.81	172
6–CdTe–GSH (2.9)	DMSO	0.51	279
6–CdTe/ZnO–GSH (4.6)	DMSO	0.57	276
6–CdTeSe–GSH (3.6)	DMSO	0.54	370
6–CdTeSe/ZnO–GSH (5.1)	DMSO	0.53	370
6–CdTeSe/ZnO–GSH (6.5)	DMSO	0.56	266
7	PBS	0.36	560
7–CdTe/CdS/ZnS–GSH (5.2)	PBS	0.59	68
7–CdTe/CdS/ZnS–GSH (6.3)	PBS	0.69	44
8	DMSO	0.68	56
8–CdTe–GSH (3.2)	DMSO	0.71	57
8–CdTe/ZnSe–GSH (4.1)	DMSO	0.81	67
8–CdTe/ZnSe/ZnO–GSH (4.5)	DMSO	0.93	69
8–CdTe/ZnSe/ZnO–GSH (6.2)	DMSO	0.86	48
8–CdTe/ZnSe/ZnO–GSH(7.6)	DMSO	0.76	58
9	PBS	0.32	450
9–CdTe–GSH (2.7)	PBS	0.37	315
9–CdTe/ZnS–GSH (4.1)	PBS	0.42	330
9–CdTe/ZnS/ZnO–GSH (4.8)	PBS	0.54	225
9–CdTe/ZnS/ZnO–GSH (5.8)	PBS	0.60	115
9–CdTe/ZnS/ZnO–GSH (8.9)	PBS	0.73	115
10	DMSO	0.48	268
10–AgNPs–Cyst (11.3)	DMSO	0.57	293
10–AgAuNPs–Cyst (11.6)	DMSO	0.80	301

4.2.2 MPc conjugates with NPs, chitosan and HSA

Significant improvement was observed in the Φ_T values for compounds **2a**, **6**, **7**, **8** and **9** in the presence of QDs and this could be attributed to the heavy–atom effect associated with QDs, **Table 4.3**. For compounds **2a**, **6**, **7**, and **9**, Φ_T values increase with the particle sizes of QDs and this could be due to increase in the number of heavy–atom associated with respective QDs based on the increase in the sizes. For **2b**–SiNPs–APTES (20), **2b**–chitosan and **2b**–HSA, had relatively unchanged or slightly increased Φ_T values compared to compound **2b** and this could be due to lack of heavy metal in the NPs and HSA. Comparing **2b**–ZnO/SiNPs–APTES (13) and **2b**–SiNPs–APTES (20), the former accounted for higher Φ_T value in comparison to the latter which could be attributed to heavy–atom effect of ZnO in the former. Comparing the Φ_T values of the doped conjugates of compounds **3** to **6** onto SiNPs, reduced Φ_T value of the MPcs were seen in the presence of SiNPs which could be attributed to aggregation except for **4**–SiNPs (34) which showed slight increase in its Φ_T value in comparison to **4** alone. A decrease in triplet quantum yields of Pcs in the presence of SiNPs has been observed in some cases **[86]**. Aggregated photosensitizers are known to be photo–inactive **[309]**. Compound **10** in conjugates with cysteamine capped (AgNPs (11.3), and AgAuNPs (11.6)) showed pivotal improvement in the Φ_T value of compound **10** due to heavy–atom effect, **Table 4.3**. For compounds **2a**, **6**, **7**, and **9** with QDs, decrease in τ_T values were observed with corresponding increase

in the Φ_T values upon conjugation, as earlier stated **[309]**. This is not observed for compound **8**. For **2b**–HSA, **2b**–chitosan, **2b**–SiNPs–APTES (20), and **2b**–ZnO/SiNPs–APTES (13); there is an increase in τ_T values in all cases even though there is no decrease in Φ_T values. The lengthening of the τ_T values may be due to the protection afforded the MPc (**2b**) by the NPs or biomolecule. For MPcs doped SiNPs, decreases in the Φ_T values accompanied by decrease in τ_T values for **3**, and **5** were observed. For **4**, increase in both Φ_T and τ_T values was observed; and for **6**, increase in τ_T values with decrease in Φ_T value as expected. The lengthening of triplet lifetime could reflect the protection of **4** from the environment within the pores of SiNPs. For **5**–SiNPs (40) and **3**–SiNPs (60), a decrease in Φ_T values is accompanied by a shortening of triplet lifetimes, this could be due to aggregation discussed above for these conjugates. For **6**–SiNPs (39), there is a lengthening of triplet lifetimes corresponding to the decrease in Φ_T value as expected.

The triplet absorption rate constants (*K*) of compounds **8** and **10** with their conjugates were determined as examples. The *K* value was employed to predict the amount of each MPcs or conjugates available at the excited triplet state. The fitting of triplet state data for *K* value determination was done at the best fit using equation 1.8, **Figure 4.4**. The *K* values of compounds **8** and **10** were 6.67×10^8 s^{-1} and 4.88×10^5 s^{-1} respectively, which correspond to higher triplet quantum yields for both **8** (0.68) and **10** (0.48). The observed higher *K* value of Compound

8 in comparison to **10** could be attributed to higher crowding at the T_1 resulting for **8** in faster transition from T_1 to T_2 which accounts for 0.68 of the total number of molecules (*N*) in transit between the T_1 to T_2.

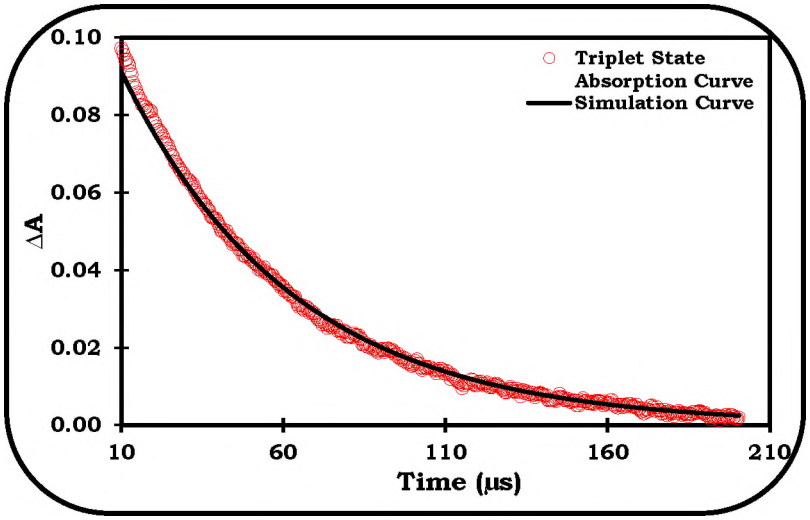

Figure 4.4: Fitted triplet decay curve for compound 8 in DMSO. ΔA = change in absorbance

It can be inferred that the heavy metal in compound **8** could have accounted for the high *K* and Φ_T values in comparison to **10**. The high *K* value for compound **8** in comparison to compound **10**, can further be explained with the SOCT–ISC mechanism. Compound **8** has more phenyl rings on its Pc macrocycle compared to **10**, hence, more of compound **8** will be present in the excited triplet state compared to **10**. The conjugates gave higher rate constants in comparison to the MPcs alone and this could be attributed to the high crowding of the triplet state by MPcs conjugates. The nanoconjugates showed improved *K* values with enhanced triplet quantum yields. For **10**–AgNPs–Cyst (11.3) and **10**–AgAuNPs–Cyst (11.6), the *K* values were 6.67×10^5 s^{-1} and 5.00×10^6 s^{-1} with corresponding triplet quantum yields of 0.57 and 0.80 respectively. **10**–AgNPs–Cyst (11.3) and

10–AgAuNPs–Cyst (11.6) had higher crowding at the T_1 state than **10** alone (4.88 $\times 10^5$ s^{-1}) resulting in faster transition between the T_1 to T_2 and this accounts for their high Φ_T values. The low Φ_T value obtained for compound **10** compared to its nanoconjugates could be due to low crowding at T_1 which facilitate slow transition from T_1 to T_2 while nanoconjugates involving compound **10** and AgAuNPs accounted for the largest *K* value which also reflected on their large Φ_T values and long τ_T.

4.3 SINGLET QUANTUM YIELD (Φ_Δ)

Singlet oxygen is formed through an energy transfer process between excited triplet state (T_1) of MPc (^{3}MPc*) and ground state molecular oxygen ($^3O_2$). The Φ_Δ value for a viable photosensitizer is dependent on the excited triplet state population and the effectiveness of energy transfer process. The singlet oxygen quantum yields of the MPc compounds and in conjugates were determined using either luminescence or photochemical method. The Φ_Δ obtained from either of the two methods are known to be similar **[311]**. Hence, this will not be differentiated in this work. The choice of the method was dependent on the absorption of the Pcs/conjugates compared to DPBF or ADMA (chemical quencher). In cases where intense interference of absorption of Pcs/conjugates with chemical quencher were observed, the luminescence method was employed. In the optical method, sodium azide is often utilized as the singlet oxygen quencher and it involves the time–resolved phosphorescence decay of singlet oxygen at 1270 nm **[239,240]** using equation 1.11 **[239]**:

$$I(t) = B \cdot \frac{\tau_D}{\tau_T - \tau_D} \cdot [Exp^{-t/\tau_T} - Exp^{-t/\tau_D}] \quad \textbf{(1.11)}$$

where I(t) is the phosphorescence signal intensity of $^1O_2$ at time t, τ_D is the lifetime of $^1O_2$, τ_T is the lifetime of the sample or standard at triplet state, and B is a coefficient involved in sensitizer concentration and $^1O_2$ quantum yield.

The Φ_Δ values of the MPcs can then be determined using equation 1.12:

$$\Phi_\Delta = \Phi_\Delta^{StD} \cdot \frac{B}{B^{StD}} \quad \textbf{(1.12)}$$

where Φ_Δ^{StD} is the singlet oxygen quantum yield of unsubstituted ZnPc standard in DMSO reference standard (Φ_Δ= 0.67 **[242]**), B and B^{StD} are the coefficients of the sample and standard, respectively. The coefficient of the standard was obtained by comparison of the singlet oxygen phosphorescence signal of unsubstituted ZnPc standard when alone and in the presence of sodium azide. The difference in the singlet oxygen phosphorescence decay of the standard alone and in the presence of sodium azide accounts for the coefficient value. Same procedure was repeated for the samples to obtain the sample coefficient.

4.3.1 MPcs alone

A typical spectra for singlet oxygen quantum yield determination using photochemical method is shown in **Figure 4.5** (using compound **10** as an example). No changes in the Q–band of the Pcs were observed indicating the photo–stability of the Pc compounds. The Φ_Δ value of asymmetrical compound

2a (0.20) was higher than what was observed for compounds **2b** (0.15) and **6** (0.17) which does not correspond to larger Φ_T of the latter. This could be attributed to the inefficient energy transfer of the excited triplet state for the latter to the ground state molecular oxygen.

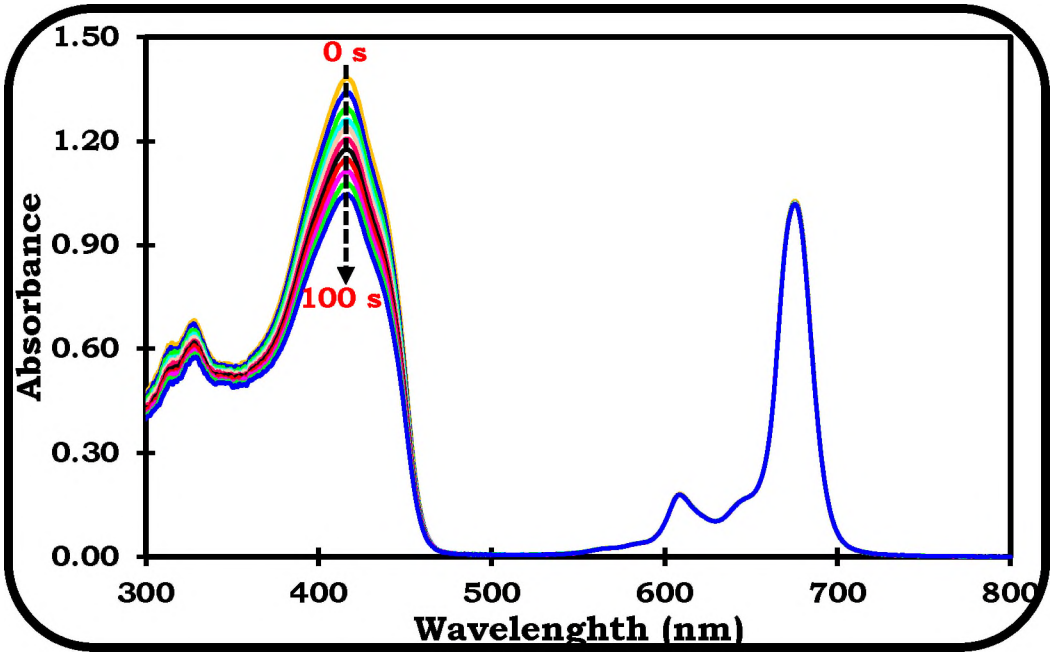

Figure 4.5: Representative spectra for singlet oxygen quantum yield determination using photochemical method. The spectra show the degradation of DPBF (6.0×10^{-5} M) in the presence of compound 10 (9.8×10^{-6} M) in DMSO.

The Φ_Δ values of compounds **3** (α) and **4** (β) were 0.30 and 0.60 respectively, corresponding to their high Φ_T values. The Φ_Δ values of compounds **4** (Zn) and **5** (Al) with same ring substituents were 0.60 and 0.14 corresponding to trends in Φ_T values as expected. In general, the trends in the Φ_Δ values correspond to the Φ_T values. For the MPcs alone, the S_Δ values range from 0.35 to 0.90 with **10** (0.96) accounting for the highest S_Δ value and **6** (0.35) accounted for the least S_Δ values, **Table 4.4**.

Table 4.4: Photophysicochemical parameters of the MPcs and their respective conjugates. **AlPcSmix in PBS was used as standard for compounds 7, 9 and their conjugates; and unsubstituted ZnPc in DMSO were used for the compounds 2 to 6, 8, 10 and their conjugates.**

Compounds	Media	Φ_T (0.01)	Φ_Δ (0.01)	S_Δ
2a	DMSO	0.35	0.20	0.57
2a–CdTe–GSH (2.4)	DMSO	0.38	0.26	0.68
2a–CdTe/CdS–GSH (3.1)	DMSO	0.42	0.29	0.69
2a–CdTe/CdS/ZnS–GSH (4.2)	DMSO	0.46	0.34	0.74
2a–CdTe/CdS/ZnS–GSH (5.1)	DMSO	0.48	0.35	0.73
2a–CdTe/CdS/ZnS–GSH (6.7)	DMSO	0.51	0.39	0.77
2b	DMSO	0.41	0.15	0.37
2b–HSA	DMSO	0.42	0.22	0.52
2b–Chitosan	DMSO	0.46	0.23	0.50
2b–SiNPs–APTES (20)	DMSO	0.43	0.17	0.40
2b–ZnO/SiNPs–APTES (13)	DMSO	0.64	0.25	0.39
3	DMSO	0.71	0.30	0.42
3–SiNPs (60) [Doped]	DMSO	0.48	0.30	0.63
4	DMSO	0.85	0.60	0.71
4–SiNPs (34) [Doped]	DMSO	0.89	0.44	0.49
5	DMSO	0.22	0.14	0.64
5–SiNPs (40) [Doped]	DMSO	0.17	0.15	0.88
6	DMSO	0.49	0.17	0.35
6–SiNPs (39) [Doped]	DMSO	0.45	0.43	0.96
6–CdTe–GSH (2.4)	DMSO	0.52	0.33	0.64
6–CdTe/CdS–GSH (3.1)	DMSO	0.58	0.22	0.38

6–CdTe/CdS/ZnS–GSH (4.2)	DMSO	0.69	0.36	0.52
6–CdTe/CdS/ZnS–GSH (5.1)	DMSO	0.76	0.27	0.36
6–CdTe/CdS/ZnS–GSH (6.7)	DMSO	0.81	0.42	0.52
6–CdTe–GSH (2.9)	DMSO	0.51	0.23	0.45
6–CdTe/ZnO–GSH (4.6)	DMSO	0.57	0.25	0.44
6–CdTeSe–GSH (3.6)	DMSO	0.54	0.30	0.56
6–CdTeSe/ZnO–GSH (5.1)	DMSO	0.53	0.29	0.55
6–CdTeSe/ZnO–GSH (6.5)	DMSO	0.56	0.27	0.48
7	PBS	0.36	0.34	0.94
7–CdTe/CdS/ZnS–GSH (5.2)	PBS	0.59	0.46	0.78
7–CdTe/CdS/ZnS–GSH (6.3)	PBS	0.69	0.49	0.71
8	DMSO	0.68	0.37	0.54
8–CdTe–GSH (3.2)	DMSO	0.71	0.41	0.58
8–CdTe/ZnSe–GSH (4.1)	DMSO	0.81	0.53	0.65
8–CdTe/ZnSe/ZnO–GSH (4.5)	DMSO	0.93	0.61	0.66
8–CdTe/ZnSe/ZnO–GSH (6.2)	DMSO	0.86	0.59	0.69
8–CdTe/ZnSe/ZnO–GSH (7.6)	DMSO	0.76	0.44	0.58
9	PBS	0.32	0.12	0.38
9–CdTe–GSH (2.7)	PBS	0.37	0.13	0.35
9–CdTe/ZnS–GSH (4.1)	PBS	0.42	0.12	0.29
9–CdTe/ZnS/ZnO–GSH (4.8)	PBS	0.54	0.14	0.26
9–CdTe/ZnS/ZnO–GSH (5.8)	PBS	0.60	0.20	0.33
9–CdTe/ZnS/ZnO–GSH (8.9)	PBS	0.73	0.38	0.52
10	DMSO	0.48	0.43	0.90
10–AgNPs–Cyst (11.3)	DMSO	0.57	0.39	0.68

10–AgAuNPs–Cyst (11.6)	DMSO	0.80	0.39	0.49

4.3.2 MPcs conjugates with NPs, chitosan and HSA

A representative singlet oxygen phosphorescence decay curve is shown using the luminescence method, **Figure 4.6** (using **6**–CdTe/CdS/ZnS–GSH (4.2) as an example).

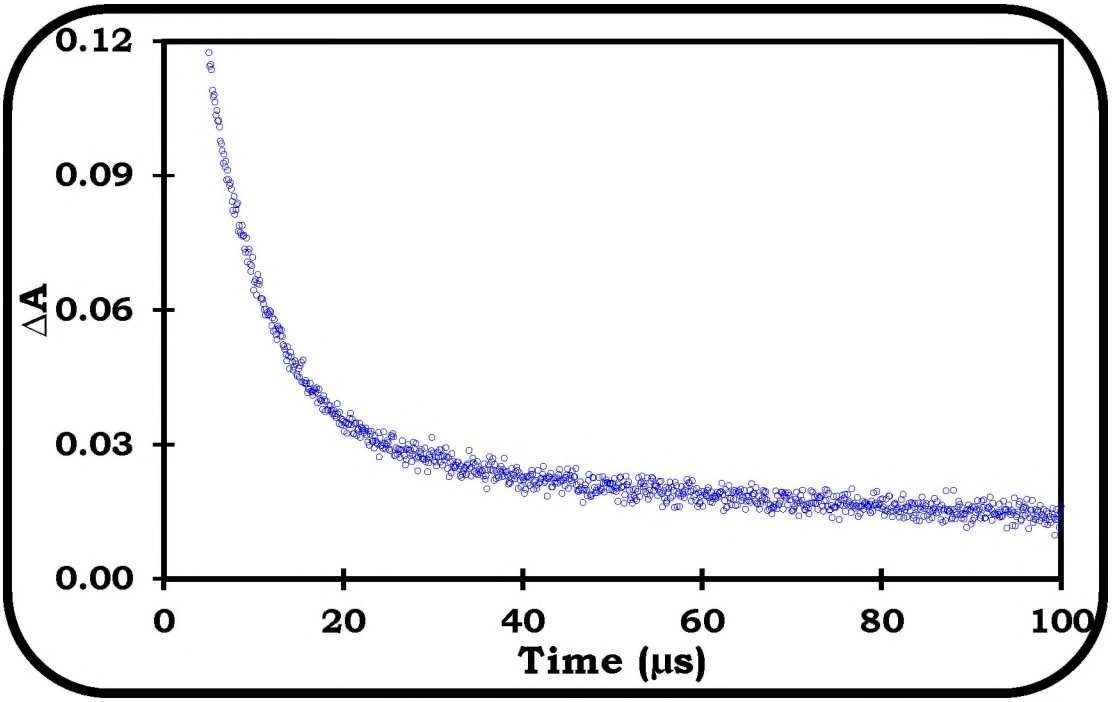

Figure 4.6: Representative singlet oxygen phosphorescence decay curve of 6–CdTe/CdS/ZnS–GSH (4.2). ΔA = change in absorbance at 1270 nm (arbitrary units)

The Φ_{Δ} values of compound **2a**, **6**, **7**, and **8** improved in the presence of QDs corresponding to the trends in Φ_{T} values. For **2a**, the largest QDs, accounted for the highest Φ_{Δ} value (0.39), corresponding to high Φ_{T} value. The Φ_{Δ} value of compound **2b** was slightly enhanced in the presence of ZnO/SiNPs–APTES (13), SiNPs–APTES (20), HSA, and chitosan. For **2b**–ZnO/SiNPs–APTES (13), the

ZnO/SiNPs–APTES (13) may have formed a charged species in the presence of excited Pcs. Upon excitation with visible light, an electron hole pair is formed in the highest occupied molecular orbital (HOMO) and lowest unoccupied molecular orbital (LUMO) of the phthalocyanine. The electron in the LUMO is then injected into the conduction band of ZnO **[312]**. This could reduce the population of the excited states. Hence, there is a mismatch between the Φ_T and Φ_Δ values with a high Φ_T value but low Φ_Δ value. Comparing the Φ_Δ values of doped conjugates of compounds **3** to **6** onto SiNPs, the Φ_Δ values of the MPcs were relatively unchanged for **3** and **5** in the presence of SiNPs. **6** in **6**–SiNPs showed significant increase in its Φ_Δ value in the conjugate and **4** showed a decrease. There is no correlation between the Φ_Δ and Φ_T values of some MPcs doped SiNPs conjugates. It has been suggested that doping of photosensitizers onto SiNPs may result in lack of energy transfer from the triplet state to the dissolved oxygen in the solvent **[313]**. For compound **9** in the presence of QDs, there is no significant increase in the Φ_Δ value except for the larger QDs. Compound **10** in conjugates with cysteamine capped (AgNPs (11.3), and AgAuNPs (11.6)) showed reduced Φ_Δ value in comparison to **10** alone. The decrease could be due to the screening effect as a result of the capping ligand on the NPs which might have prevented the ground state molecular oxygen from interacting with excited triplet state of the MPc conjugates **[314].** For the conjugates, the S_Δ values range from 0.26 to 0.96 with conjugates of **6**–SiNPs (0.96) accounting for the highest S_Δ value while **9**–CdTe/ZnS/ZnO–GSH (0.26)

accounted for the least S_{Δ} values which serve to indicate the possible inefficiency in the transfer of energy between the excited triplet state of the compounds to the ground state molecular oxygen.

4.4 PHOTODEGRADATION STUDIES

The photodegradation studies of compounds **6, 8,** and **10** with their conjugates were performed in air saturated solutions. A typical photodegradation curves are shown in **Figure 4.7** (using **10**–AgAuNPs–Cyst (11.6) as an example).

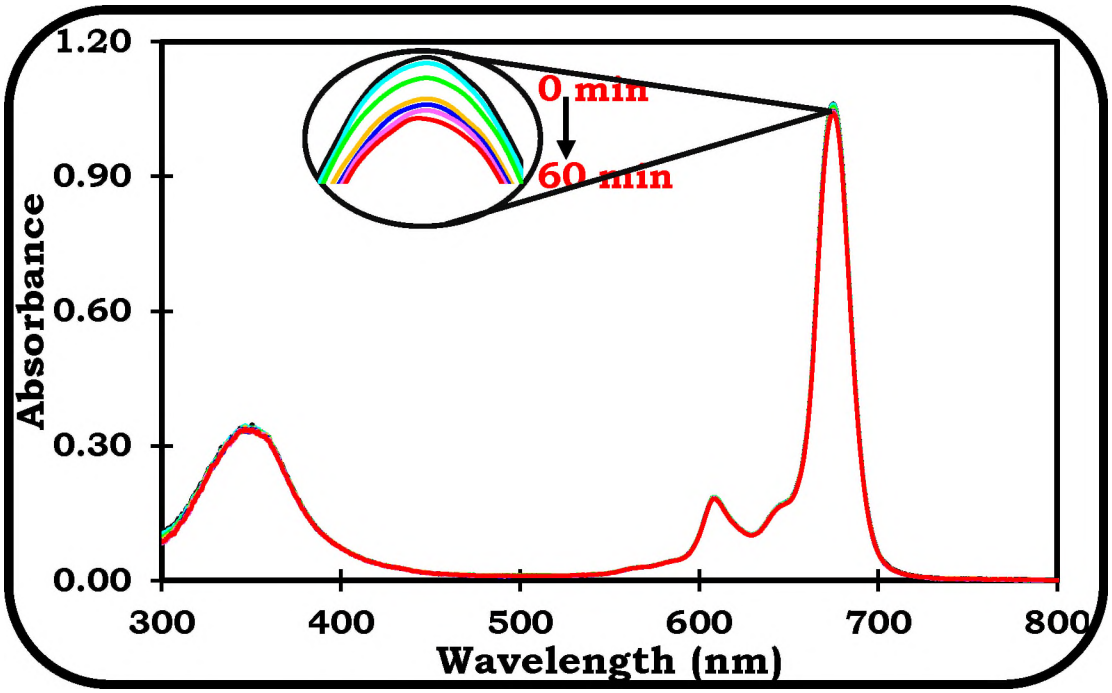

Figure 4.7: Representative spectra for photodegradation studies using 10–AgAuNPs–Cyst (11.6) in DMSO.

Photodegradation is caused by oxidative attack on the excited triplet state of phthalocyanines by singlet oxygen upon illumination. It is usually accompanied by depletion of the Pcs Q– and B– band without the formation of a new peak **[244]**.

Table 4.5: Photodegradation quantum yields of compounds 6, 8, and 10 with conjugates in DMSO

Samples	Φ_{Pd} (cm^{-2} s^{-1})
6	7.32×10^{-7}
6–CdTe–GSH (2.9)	2.04×10^{-7}
6–CdTe/ZnO–GSH (4.6)	1.84×10^{-7}
6–CdTeSe–GSH (3.6)	1.82×10^{-7}
6–CdTeSe/ZnO–GSH (5.1)	1.63×10^{-7}
6–CdTeSe/ZnO–GSH (6.5)	1.46×10^{-7}
8	4.35×10^{-6}
8–CdTe–GSH (3.2)	2.54×10^{-6}
8–CdTe/ZnSe–GSH (4.1)	5.52×10^{-6}
8–CdTe/ZnSe/ZnO–GSH (4.5)	9.22×10^{-6}
8–CdTe/ZnSe/ZnO–GSH (6.2)	6.56×10^{-6}
8–CdTe/ZnSe/ZnO–GSH (7.6)	4.94×10^{-6}
10	1.18×10^{-6}
10–AgNPs–Cyst (11.3)	1.57×10^{-6}
10–AgAuNPs–Cyst (11.6)	1.17×10^{-6}

The photodegradation quantum yields (Φ_{Pd}) of the Pcs and their conjugates were determined using equation 1.17, **Table 4.5**. All the compounds showed good photo–stability with values below 10^{-3} but the conjugates were observed to exhibit better photo–stability in comparison to the MPcs alone and this could be attributed to the close and compact protection afforded the MPcs by the NPs except in some cases where the compounds showed relatively higher Φ_{Pd} values,

for example: **6** in conjugates, **8** in **8**–CdTe–GSH (3.2), and **10** in **10**–AgAuNPs–Cyst (11.6), **Table 4.5**.

4.5 FÖRSTER RESONANCE ENERGY TRANSFER PARAMETERS (FRET)

The FRET studies of the following MPcs (**2a**, **6** to **9**) with GSH–QDs were performed in solution. To obtain efficient FRET process, there must be a close spectra overlap between the donor's fluorescence emission spectrum and the acceptor absorption spectrum. For all the compounds, the most efficient overlap of QDs to the MPcs was observed with the large QDs due to high bathochromic shift in the emission spectrum of the QDs, **Figure 4.8** (using **6** and QDs as examples).

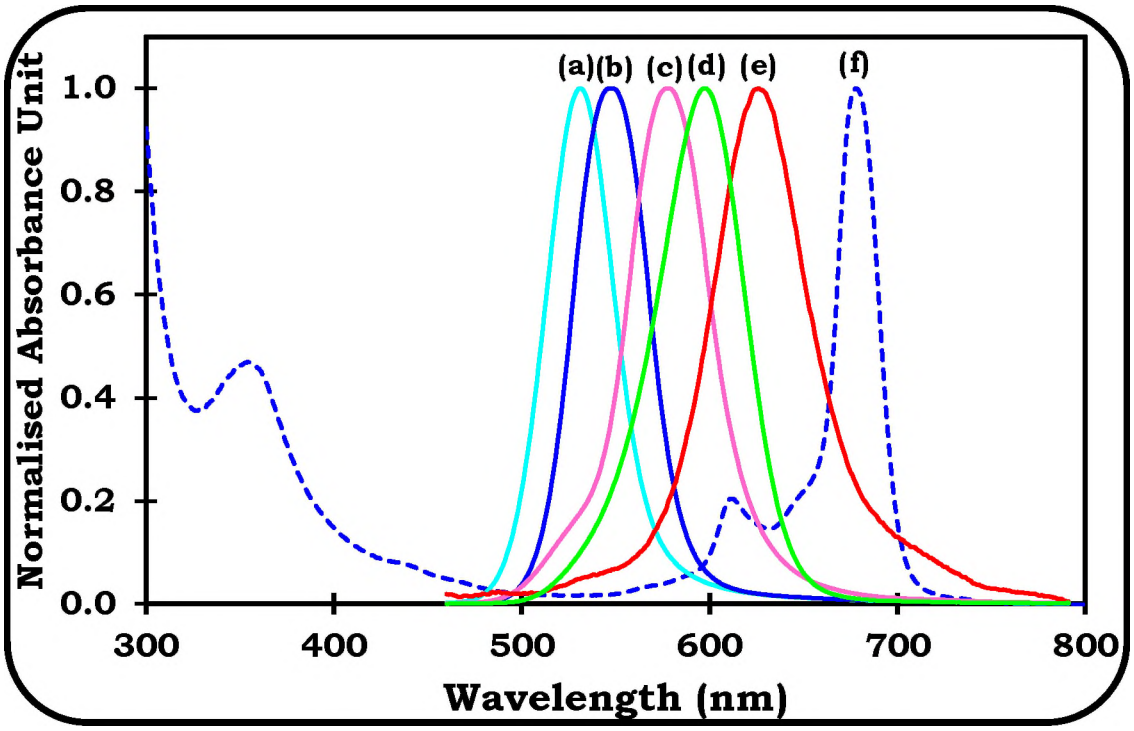

Figure 4.8: Normalised fluorescence spectra of glutathione capped {(a) CdTe(2.4), (b)CdTe/CdS (3.1), (c) CdTe/CdS/ZnS (4.2), (d) CdTe/CdS/ZnS (5.1), and (e) CdTe/CdS/ZnS (6.7)} at λ_{exc} = 450 nm and (f) absorption spectrum of compound 6.

The QDs alone and in the nanohybrids were excited at 450 nm where Pcs does not absorb. Upon excitation, there was a pivotal decrease in QDs emission intensity leading to induced emission intensity for the Pcs at 692 nm (**Figure 4.9**, using **6** and QDs as examples), due to FRET and other processes which deactivate the fluorescence of QDs. Similar trend was observed in the conjugates of **2a**, **7**, **8**, **9** and QDs. In all cases, J values and FRET efficiency increases with particle size for the same type of QDs. **Table 4.6**, r < R° in all cases, hence FRET *eff.* > 50%.

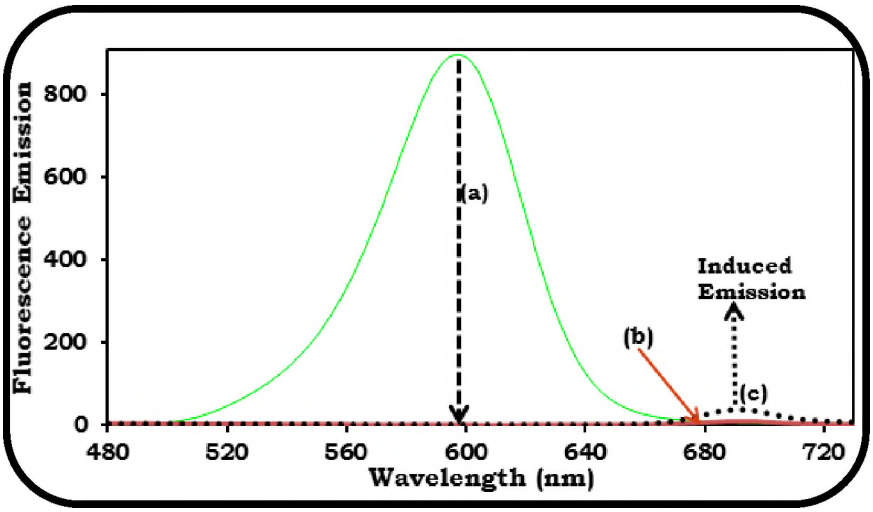

Figure 4.9: Emission Spectra of (a) CdTe/CdS/ZnS–GSH (5.1) ≈ [1.2 × 10^{-7}M] alone in water, (b) compound 6 alone in DMSO ≈ [2.8 × 10^{-7}M], and (c) 6–CdTe/CdS/ZnS–GSH (5.1) ≈ [3.7× 10^{-6}M] in DMSO at λ_{exc} = 450 nm).

It is pertinent to note that there are several factors reported (and are still under debate) that influence photoluminescence decrease for QDs other than FRET **[315–317]**. It has been reported that for QDs–porphyrin nanoconjugates, the major part of the observed quenching of QDs photoluminescence can neither be assigned to FRET nor to photoinduced charge transfer between the QDs and the porphyrin **[315]**.

Table 4.6: Forster resonance energy transfer of glutathione QDs nanohybrids

Samples	J(×10^{-13}cm^6)	R_o (×10^{-10}m)	r (× 10^{10}m)	*Eff.*
	DMSO			
2a–CdTe–GSH (2.4)	1.16	42	34.00	0.85
2a–CdTe/CdS–GSH (3.1)	2.12	47	32.00	0.91
2a–CdTe/CdS/ZnS–GSH (4.2)	2.93	53	36.00	0.96
2a–CdTe/CdS/ZnS–GSH (5.1)	4.86	54	32.00	0.96
2a–CdTe/CdS/ZnS–GSH (6.7)	8.90	67	38.00	0.97
6–CdTe–GSH (2.4)	1.59	43	29.92	0.89
6–CdTe/CdS–GSH (3.1)	2.70	48	32.23	0.92
6–CdTe/CdS/ZnS–GSH (4.2)	3.31	54	32.73	0.95
6–CdTe/CdS/ZnS–GSH (5.1)	4.47	58	34.12	0.96
6–CdTe/CdS/ZnS–GSH (6.7)	6.98	72	37.70	0.98
8–CdTe(3.2)–GSH (3.2)	1.40	42	37.08	0.68
8–CdTe/ZnSe–GSH (4.1)	2.33	46	40.33	0.68
8–CdTe/ZnSe/ZnO–GSH (4.5)	1.86	46	40.02	0.70
8–CdTe/ZnSe/ZnO–GSH (6.2)	2.59	46	39.43	0.71
8–CdTe/ZnSe/ZnO–GSH (7.6)	3.11	44	37.25	0.74
	PBS			
7–CdTe/CdS/ZnS–GSH (5.2)	4.86	52	40.00	0.85
7–CdTe/CdS/ZnS–GSH (6.3)	6.60	55	36.00	0.93

9–CdTe–GSH (2.7)	0.56	41.18	42.58	0.45
9–CdTe/ZnS–GSH (4.1)	1.13	48.58	46.01	0.58
9–CdTe/ZnS/ZnO–GSH (4.8)	2.89	54.49	49.50	0.64
9–CdTe/ZnS/ZnO–GSH (5.8)	4.07	54.01	48.00	0.67
9–CdTe/ZnS/ZnO–GSH (8.9)	5.20	46.85	40.68	0.70

4.6 SUMMARY OF CHAPTER

The photophysics and photochemistry of the MPcs and their conjugates were studied in solution. All the studied MPcs showed good photophysicochemical behaviour with relatively high triplet and singlet quantum yields. The Pc macrocycles with heavy central metals (Zn, In) exhibited higher triplet and singlet quantum yields in comparison to the ones with relatively light metal (Al) and this could be due to the heavy–atom effect obtained from the former. The MPcs conjugates with most of the NPs, HSA and chitosan showed improved triplet and singlet quantum yields in comparison to the MPcs alone. Screening effects could have prevented the interaction of the excited triplet state of the MPcs with the ground state molecular oxygen due inefficient energy transfer, resulting in lower Φ_{Δ} values. It can be inferred that the nanoconjugates of the MPcs and GSH–QDs had significant enhancement in their Φ_{T} and Φ_{Δ} values in comparison to the MPcs alone which is attributed to heavy–atom effect of the latter. It is pertinent to note that the improved Φ_{T} and Φ_{Δ} of the MPcs in the presence of the GSH–QDs when linked could afford efficacious

photosensitization which is pivotal for PDT in treatment of cancer. In addition, there is the effect of QDs sizes on the Φ_T and Φ_Δ of the MPcs. The elongation of the triplet lifetimes in some cases, could be ascribed to the protection afforded to the MPcs by the NPs.

CHAPTER FIVE

NONLINEAR OPTICAL PROPERTIES

5.1 NONLINEAR PARAMETERS

For the NLO studies, open aperture Z–scan technique was employed to measure the nonlinear absorption coefficient (β) from which imaginary third–order nonlinear susceptibility $\mathrm{Im}[\chi^{(3)}]$ and the limiting threshold were obtained. β measures the degree of nonlinear absorptivity and it depends on the population of molecules in the first excited triplet state (T_1) and the $\mathrm{Im}[\chi^{(3)}]$ measures the degree of polarizability in the materials when they are irradiated with light. Pc **1,** compounds **11**, **12**, **13**, **14** and their conjugates with semiconductor QDs were employed for NLO studies. Compounds **11** to **14** were selected for NLO studies due to their extensive π–electron conjugated ring system and heavy lanthanide central metal while the metal free Pc (**1**) was chosen due to its reduced symmetry which has the capacity to enhance its NLO properties. These properties have the tendency to significantly enhance their NLO behaviour **[115,116]**. The compounds were compared as follows: **11** with **12**, **13** with **14**; **11** with **13**; and **12** with **14**. Similar comparative studies were done on their nanoconjugates with QDs. The NLO properties of metal free Pc **1** and its conjugates were assessed as well.

5.1.1 Effect of extensive π–electron conjugate ring system

The effect of magnitude of π–electron conjugated ring system on the NLO properties of the compounds were evaluated using compounds **11** and **12**, **13** and **14**. The Z–scan open aperture curves of the compounds exhibited reverse

saturable absorption (RSA) which is typical of phthalocyanines. For RSA mechanism to occur, the excited state cross–section must be greater than the ground state cross section **[318,319]** and this is observed by the attenuation in the transmittance of the sample as it tends towards zero, **Figure 5.1**. It can be inferred that the compounds depicted reverse saturable absorption, **Figure 5.1**. The nonlinear transmittance of compounds **12** and **14** (triple deckers) was higher than their corresponding compounds **11** and **13** (double deckers). This trend is also seen in the obtained β_{eff} and $\mathrm{Im}[\chi^{(3)}]$ values, **Table 5.1**.

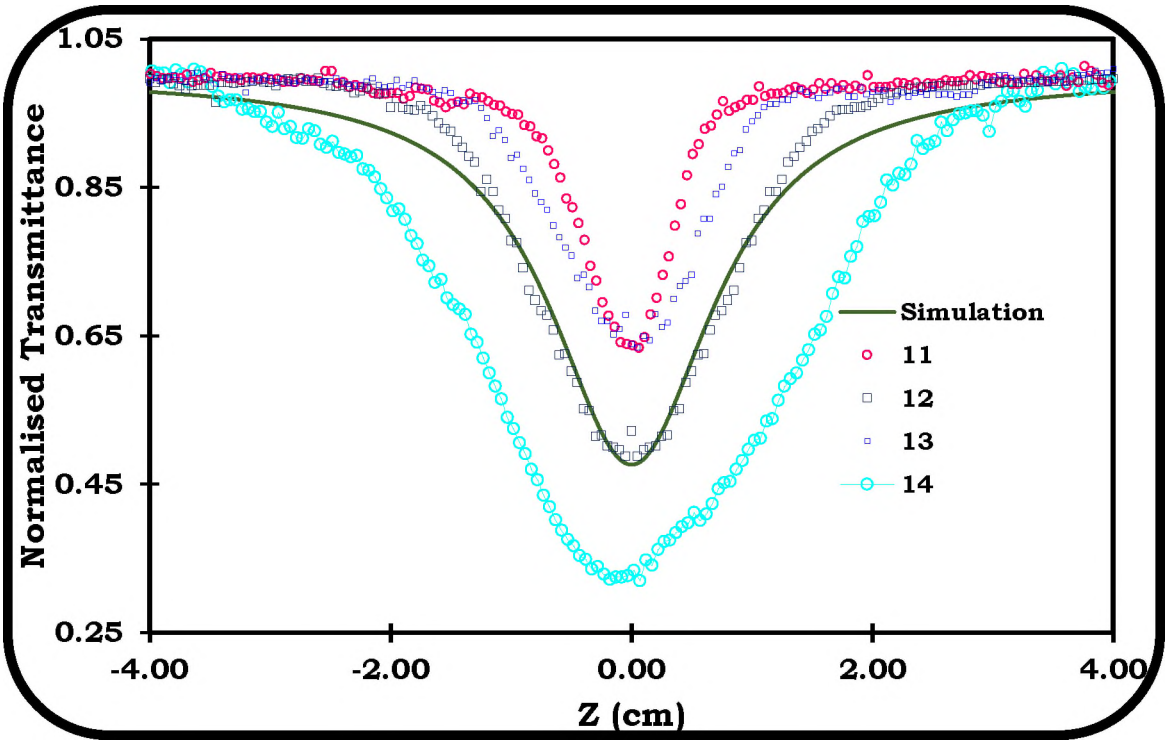

Figure 5.1: Open aperture Z-scan curves for the investigated multinuclear MPc compounds in DCM. All recorded at an absorbance of 2.5 at Q-bands wavelength in DCM at a pulse rate of 10 ns with I_o= ~ 0.33 GW·cm^{-2}

The marked phenomenon in the NLO responses could be attributed to the more expanded π–electron conjugated ring system of the triple deckers which is known to promote extensive optical nonlinearity **[116,150,197–199]**.

5.1.2 Effect of symmetry

The effect of symmetry on the NLO properties of the compounds were investigated using the following compounds (**11** and **13**) and (**12** and **14**). **13** is the asymmetrical counterpart of **11** and **14** is the asymmetrical counterpart of **12**. Comparing the symmetrical (**11**) and asymmetrical (**13**) double deckers, it can be observed that the symmetry of the respective compounds plays an indispensable role in their nonlinear transmittance as asymmetrical compound **13** depicted improved β_{eff} and $\mathrm{Im}[\chi^{(3)}]$ values in comparison to compound **11** with higher optical nonlinearity for **13** compared to **11**. Similar trends were observed in symmetrical (**12**) and asymmetrical (**14**) triple deckers with **14** accounting for higher β_{eff} and $\mathrm{Im}[\chi^{(3)}]$ in comparison to **12** with higher optical nonlinearity for **14** compared to **12**, **Table 5.1**. As earlier discussed, the symmetry of the compounds played critical roles in the NLO behaviour of the Pcs as lack of symmetry contributed to high performance of compounds **13** and **14**. Compound **14** accounted for the best NLO performance with the highest β_{eff} and $\mathrm{Im}[\chi^{(3)}]$ values, **Table 5.1**.

Table 5.1: Nonlinear optical data of phthalocyanines and their corresponding nanoconjugates studied in DCM. Compounds 11 to 14 and conjugates were studied at absorbance of 2.5 of their respective Q-band wavelength and I_0 = ~ 0.33 GW·cm^{-2}. Pc 1 and conjugates were studied at absorbance of 2.0 of their respective Q-band wavelength and I_0 = ~ 0.25 GW·cm^{-2}

Compounds	β_{eff} (m/W)	Im[$\chi^{(3)}$](esu)	I_{lim} (J·cm^{-2})
1	3.48×10^{-8}	2.98×10^{-11}	1.61
1–CdSe (S–M bond)	3.95×10^{-8}	3.38×10^{-11}	0.17
11	1.00×10^{-8}	8.57×10^{-12}	-[a]
11–CdSeTe/CdTeS/ZnSeS–TOPO (6.6) (mixed)	1.80×10^{-8}	1.54×10^{-11}	-[a]
12	2.40×10^{-8}	2.06×10^{-11}	0.92
12–CdSeTe/CdTeS/ZnSeS–TOPO (6.6) (mixed)	4.70×10^{-8}	4.03×10^{-11}	0.45
13	1.09×10^{-8}	9.34×10^{-12}	-[a]
13–CdSeTe/CdTeS/ZnSeS–MSA (7.3) (linked)	2.10×10^{-8}	1.80×10^{-11}	2.00
14	4.82×10^{-8}	4.13×10^{-11}	0.57
14–CdSeTe/CdTeS/ZnSeS–MSA (7.3) (linked)	4.90×10^{-8}	4.20×10^{-11}	0.42

[a] 50% attenuation of transmitted fluence is not achieved.

5.1.3 Effect of semiconductor quantum dots (QDs)

The effect of QDs on the NLO properties of compounds **11**, **12**, **13** and **14** were studied. The CdSeTe/CdTeS/ZnSeS–MSA (7.3) were covalently linked to asymmetrical compounds **13** and **14** while the CdSeTe/CdTeS/ZnSeS–TOPO

(6.6) were mixed with symmetrical compounds **11** and **12** due to lack of suitable point of attachments on both the QDs and Pcs.

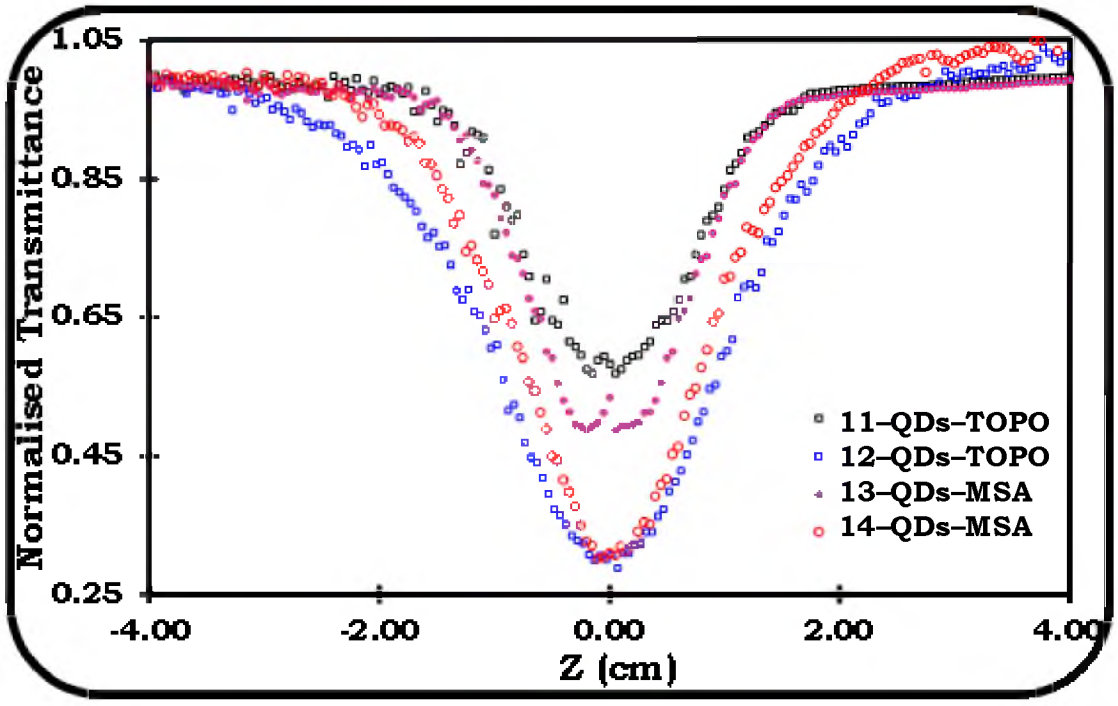

Figure 5.2: Open aperture Z–scan curves for the investigated nanoconjugates of multinuclear MPcs with QDs in DCM. All recorded at an absorbance of 2.5 at Q-bands wavelength in DCM at a pulse rate of 10 ns with I_o= ~ 0.33 GW·cm^{-2}. QDs = CdSeTe/CdTeS/ZnSeS.

The compounds exhibited enhanced optical nonlinearity in the presence of the QDs with more than 50% deep in their transmittance, **Figure 5.2**. A significant attenuation in the transmittance was observed for compounds **11**, **12**, **13**, **Figure 5.3**, not very clear for **14**.

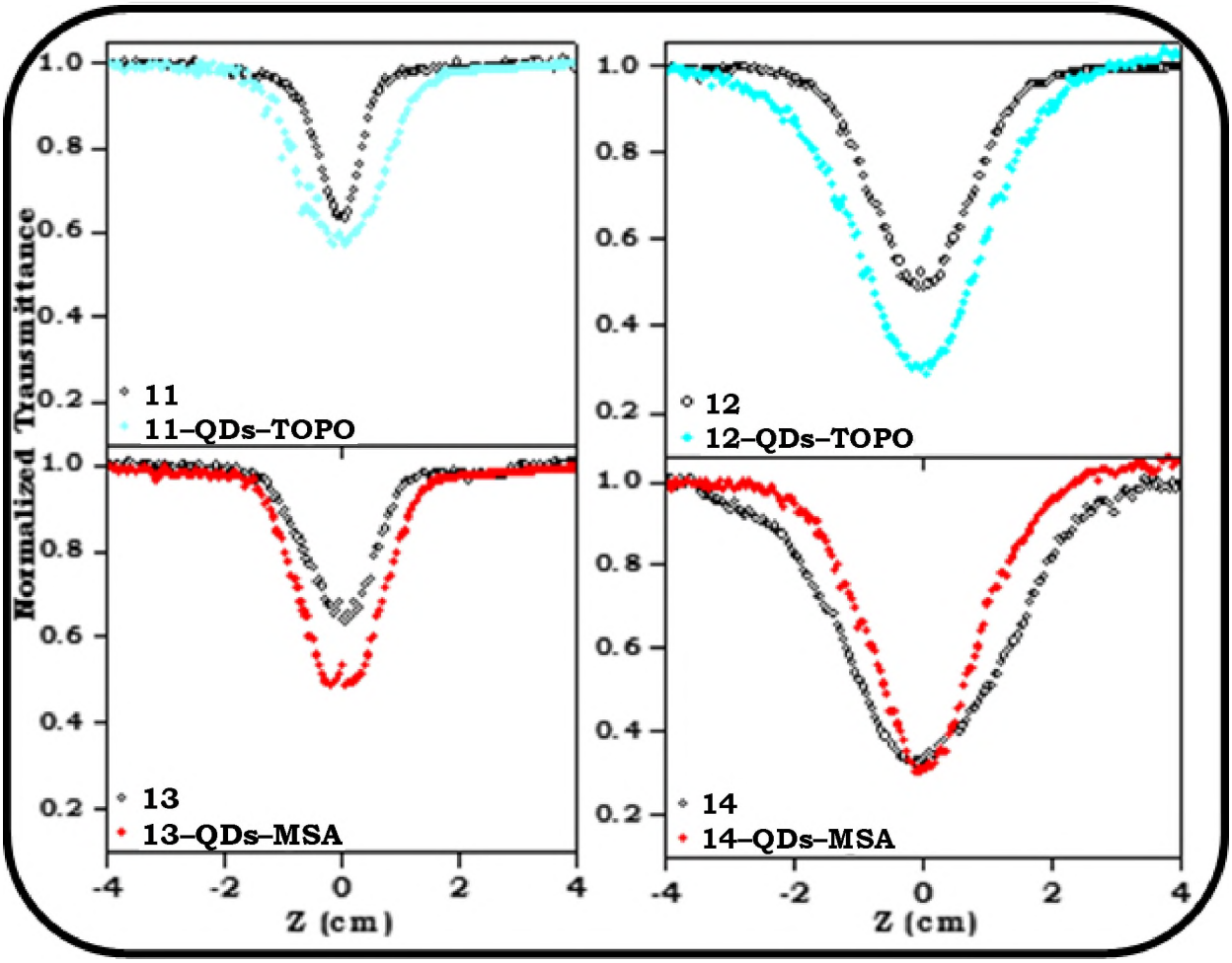

Figure 5.3: Open aperture Z-scan curves for the investigated multinuclear MPcs and their nanoconjugates. All recorded at an absorbance of 2.5 at Q-bands wavelength in DCM at a pulse rate of 10 ns with I_o= ~ 0.33 GW·cm^{-2}

The high β_{eff} and $\mathrm{Im}[\chi^{(3)}]$ values of the nanoconjugates in comparison to the compounds alone could be attributed to the heavy–atom effect associated with the QDs which encourages extensive population of the triplet state. In addition, QDs may contribute to NLO behaviour of Pcs through the free–carrier absorption (FCA) mechanism **[169]**. FCA is usually produced when excitation takes place at the wavelengths where there is linear absorption **[169]**.

An optical limiting material displays a decreasing transmittance as a function of the incident fluence. At low incident fluence, the material has a linear transmittance; while at some critical fluence or threshold, the transmittance changes abruptly, and leads to clamping of the output fluence at a constant value that would presumably be less than the amount required to damage the optical element. This critical point is referred to as the threshold limit intensity or fluence I_{lim}, which is typically referred to the energy where 50% transmittance is observed **[320]**. **Figure 5.4**, the double-decker compounds (**11** and **13**) failed to produce 50% transmittance while the triple-decker compounds (**12** and **14**) did afford required optical limiting. In the case of symmetrical compound **12**, the 50% threshold is achieved at 0.92 $J \cdot cm^{-2}$ input fluence, while the low-symmetry compound **14** reveals superior optical limiting characteristics with limiting threshold of 0.57 $J \cdot cm^{-2}$ at 50% of the transmittance, **Figure 5.4**, **Table 5.1**.

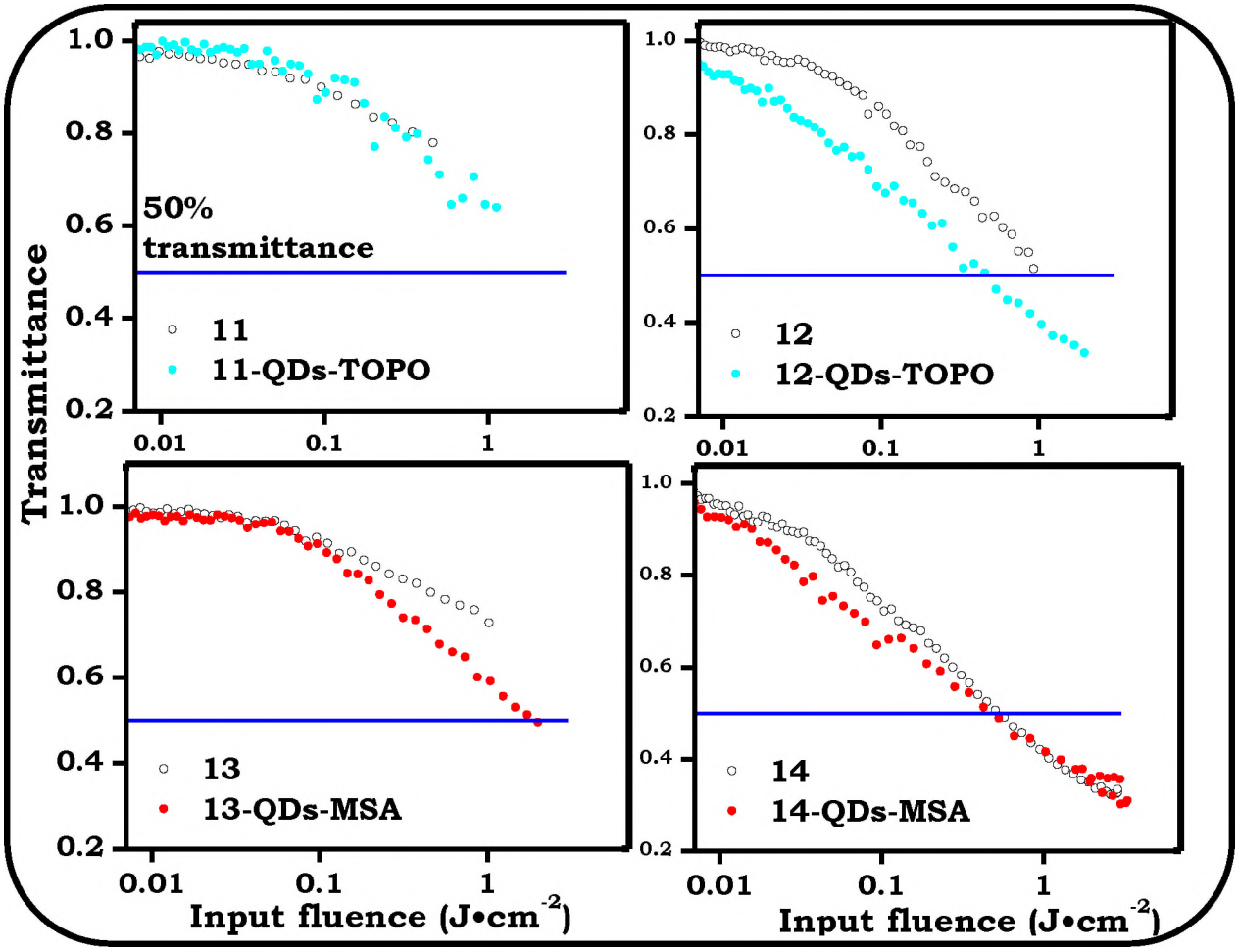

Figure 5.4: Input fluence versus transmittance curves of compounds alone and their nanoconjugates with QDs in DCM. All recorded at an absorbance of 2.5 at Q-bands wavelength in DCM at a pulse rate of 10 ns with I_o= ~ 0.33 GW·cm^{-2}

Again, further improvement of the I_{lim} value is achieved by the formation of composites with QDs, therefore, the composites of triple-deckers **12** and **14** with QDs showed improved I_{lim}, their properties exceed the ones of nano-carbon materials, such as fullerenes and graphene derivatives, making them promising components of optical limiting materials and devices **[318,319]**.

5.1.4 Pc 1 and nanoconjugates

Pc **1** was linked to QDs via S–M bond. **Figure 5.5** shows the open aperture Z-scan profile spectra of Pc **1** and **1**–CdSe–TOPO (3.8), recorded at 532 nm with 10 ns laser pulse in DCM. From the spectra, it can inferred that the Pc **1** and its nanoconjugate exhibited reverse saturable absorption (RSA) as is typical of phthalocyanines **[189,321,322]**. The normalized transmittance of **1**–CdSe–TOPO exhibited a deeper valley compared to Pc **1** alone.

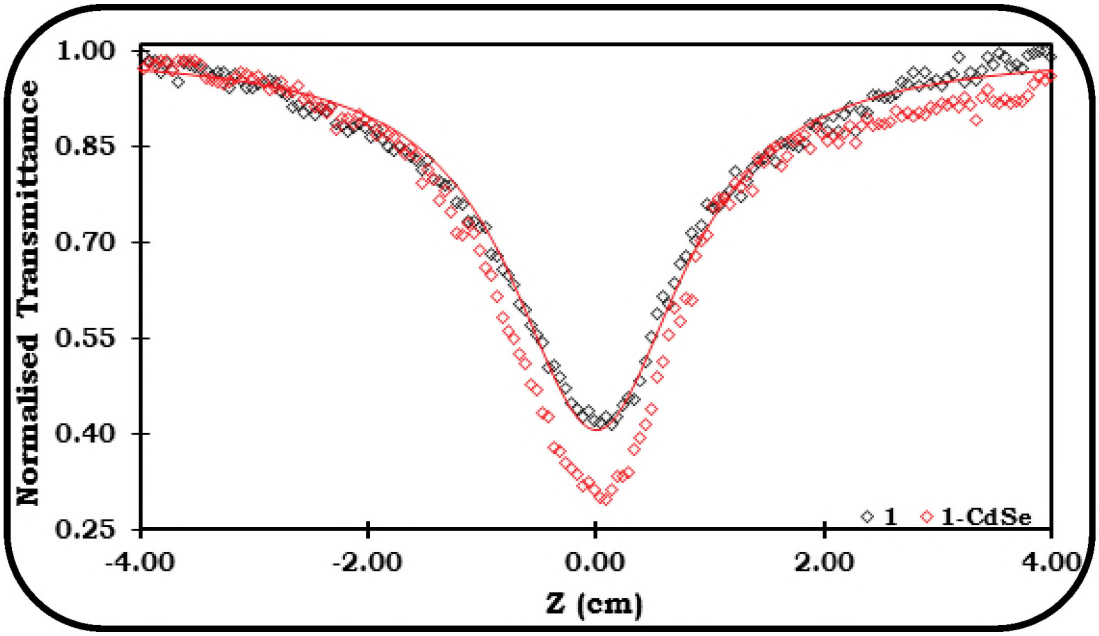

Figure 5.5: Open aperture Z-scan curves for compound 1 and 1–CdSe–TOPO (3.8). All measurements were performed in DCM (absorbance 2.0 at Q–band) at 532 nm with a pulse rate of 10 ns with I_o = ~ 0.25 GW.cm^{-2}.

The observed trend has earlier been described to be due to heavy–atom effect (spin–orbit coupling) associated with Cd–based QDs **[169]**. As earlier stated, a good optical limiting material must have high $I_m[\chi^{(3)}]$ and β_{eff}. There are improvements in the B_{eff}, and $Im[\chi^{(3)}]$ values for compound **1** in the presence of

QDs, **Table 5.1**. As stated above, QDs alone show NLO behavior which may be due FCA mechanism **[169]**. The combination of QDs and Pc **1** resulted in improved NLO behavior when compared to the Pc alone.

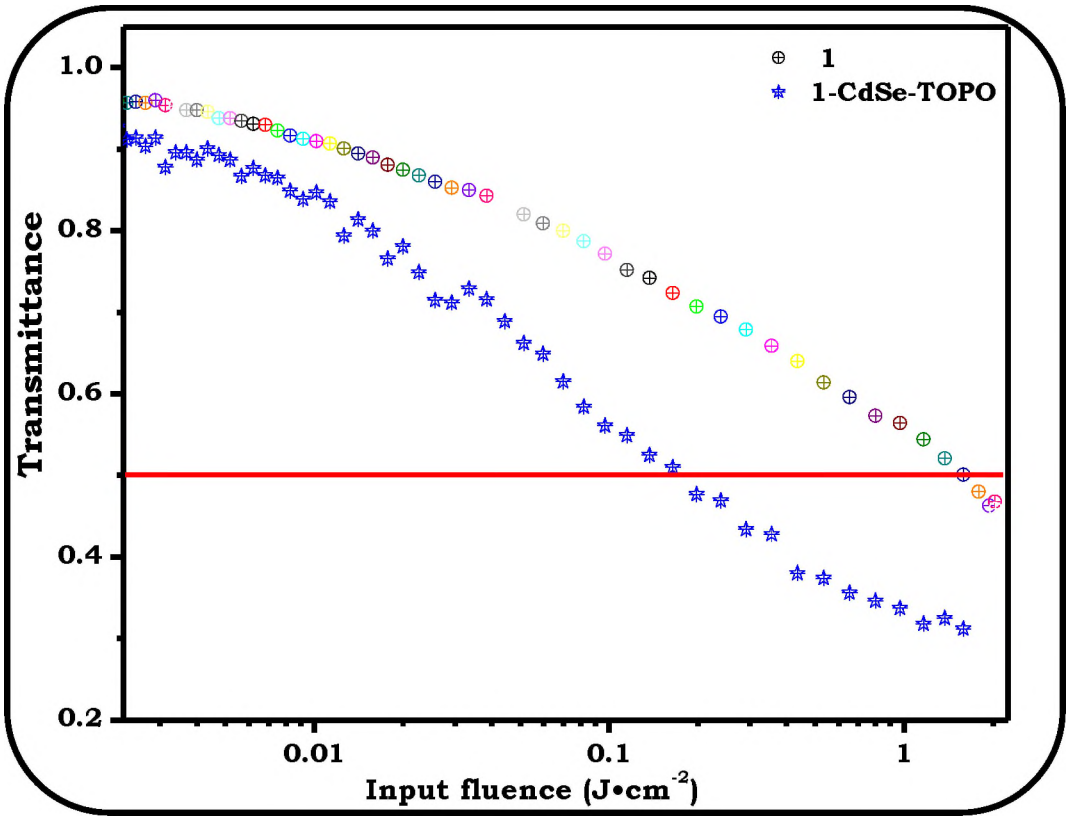

Figure 5.6: Input fluence versus output fluence curves for compound 1 and 1–CdSe–TOPO (3.8). All measurements were done in dichloromethane at an absorbance of 2.0 (Q–band) at 532 nm with a pulse rate of 10 ns with I_o = ~ 0.25 GW.cm^{-2}.

The lower the I_{lim} values the better is the material as an optical limiter. Plots of I_{in} against I_{out} are shown in **Figure 5.6**. The I_{lim} value decreased (**Table 5.1**) for **1**–CdSe–TOPO (3.8) in comparison to Pc **1** alone indicating superior optical limiting behaviour for the threshold.

5.2 SUMMARY OF CHAPTER

For all the compounds, the two-photon absorption mechanism was employed. The imaginary third–order nonlinear susceptibility $\mathrm{Im}[\chi^{(3)}]$ was calculated from the β_{eff}. $\mathrm{Im}[\chi^{(3)}]$ characterizes the response time of a nonlinear optical material, following the perturbation initiated by the intense laser pulses. A prospective optical limiting material must have high $\mathrm{Im}[\chi^{(3)}]$ and β_{eff}. Comparing triple–deckers with the corresponding double deckers (**12** with **11**, and **14** with **13**) in the absence of QDs, demonstrates that the β_{eff} and $\mathrm{Im}[\chi^{(3)}]$ values are higher for the triple decker compounds without unpaired electrons **[323]** (**Table 5.1**). It is pertinent to note that the loss of molecular symmetry in double decker **13** and triple decker **14** resulted in higher β_{eff} and $\mathrm{Im}[\chi^{(3)}]$ values in comparison to their symmetrical analogues (**11** and **12**, respectively) which is in agreement with the expected, based on previously reported studies **[253]**. Among the MPcs, the symmetrical and asymmetrical triple deckers showed the highest NLO behaviour while the low-symmetry compound **14** accounted for the best NLO behaviour alone and for the conjugates. The nanoconjugates of Pc **1** with QDs showed a better NLO activity in comparison to Pc **1** alone. The good performance observed with the nanoconjugate could be further attributed to the higher population in the excited state in comparison to the Pc compounds alone. The quality NLO behaviour exhibited by the respective compounds make them suitable nonlinear optical materials.

CHAPTER SIX

IN VITRO CYTOTOXICITY AND PHOTODYNAMIC THERAPY

The following compounds and their conjugates were tested against human breast adenocarcinoma cells (MCF–7) for *in vitro* dark toxicity studies; compound **2b** and its conjugates (**2b**–ZnO/SiNPs–APTES (13), **2b**–HSA, **2b**–SiNPs–APTES (20), and **2b**–chitosan); **6** and its conjugates (**6**–CdTe–GSH (2.9), **6**–CdTeSe/ZnO–GSH (5.1), and **6**–CdTeSe/ZnO–GSH (6.5)); **9** and its conjugates **9**–(CdTe/ZnS–GSH (4.7) and **9**–CdTe/ZnS/ZnO–GSH (5.8)); compound **10** and its conjugates (**10**–AgNPs–Cyst (11.3) and **10**–AgAuNPs–Cyst (11.6)). PDT activity was investigated on compound **2b** and its conjugates (**2b**–ZnO/SiNPs–APTES (13), **2b**–HSA, and **2b**–chitosan); and compound **10,** and its conjugates (**10**–AgNPs–Cyst (11.3) and **10**–AgAuNPs–Cyst (11.6)).

Conjugates of Pcs with QDs were not studied further for PDT since studies below showed that QDs when independently administered have high dark cytotoxicity.

6.1 *IN VITRO* DARK CYTOTOXICITY STUDIES

The cytotoxicity studies were used to evaluate the degree to which the molecules could cause cell death at varied concentration doses. All the cytotoxicity studies were performed in dark and are referred to as *in vitro* dark viability or cytotoxicity. *In vitro* dark cytotoxicity is undesirable for photosensitizers aimed for use in PDT. The lower the cell viability, the higher the dark cytotoxicity. The percent cell viabilities of the DMSO and PBS (used for making stock solution and 1.6% (v/v) in supplemented

DMEM), were similar with what was obtained in the control (supplemented DMEM alone) showing that DMSO or PBS have no cytotoxic effect on the cells at this concentration.

6.1.1 Semiconductor QDs

The percentage cell viability (representing active cells) data for all the QDs and conjugates are shown in **Table 6.1** except for CdTe/ZnS–GSH (4.1), CdTe/ZnS/ZnO–GSH (4.7), CdTe/ZnS/ZnO–GSH (8.9), and their conjugates with compound **9** which are shown in pictorial form **Figure 6.1**. The latter was not presented in **Table 6.1** due to differences in concentrations employed.

The concentrations of the QDs in **Figure 6.1** were estimated using method reported in the literature **[324]**. Equation 6.1–6.3:

$$D = (9.8127 \times 10^{-7})\lambda^3 - (1.7147 \times 10^{-3})\lambda^2 + (1.0064)\lambda - (194.84) \quad \textbf{(6.1)}$$

$$\varepsilon = 10043\ (D)^{2.12} \quad \textbf{(6.2)}$$

$$A = \varepsilon C L \quad \textbf{(6.3)}$$

where D is the diameter, λ is the wavelength, A is the absorbance at the peak position. C is the molar concentration (mol/L) of the nanocrystals. *L* is the path length (cm).

Table 6.1: Cytotoxicity (expressed as percent cell viability) of QDs, compounds 6 and nanoconjugates

Compounds	5 μg/mL (%)
TGA capped QDs	
CdTe–TGA (2.8)	36 ± 2
CdTe/ZnO–TGA (4.0)	48 ± 2
CdTeSe–TGA (3.4)	65 ± 2
CdTeSe/ZnO–TGA (4.7)	67 ± 2
CdTeSe/ZnO–TGA (6.6)	66 ± 2
CdSe/ZnS–TGA (4.0)	64 ± 2
GSH capped QDs and Conjugates	
CdTe–GSH (2.9)	65 ± 0
CdTe/ZnO–GSH (4.6)	60 ± 1
CdTeSe–GSH (3.6)	65 ± 1
CdTeSe/ZnO–GSH (5.1)	69 ± 1
CdTeSe/ZnO–GSH (6.5)	66 ± 3
Compound **6**	99 ± 15
6–CdTe–GSH (2.9)	76 ± 1
6–CdTeSe/ZnO–GSH (5.1)	72 ± 3
6–CdTeSe/ZnO–GSH (6.5)	77 ± 3

The GSH capped QDs showed less cytotoxic effects against MCF–7 cells (higher % viability) when compared to their corresponding TGA capped

analogues. This observation could be due to the fact that glutathione is a molecule known to serve as an essential co–factor in cellular metabolism **[325]**.

The addition of a shell to the core QDs resulted in increased % cell viability, hence the QDs are less toxic in the presence of the shell (with the exception of CdTe–GSH (2.9) and CdTe/ZnO–GSH (4.6)). CdTe/ZnS–GSH (4.1) and CdTe/ZnS/ZnO–GSH (8.9) showed cell viability above 50% at ≤ 2 μm while the CdTe/ZnS/ZnO–GSH (4.7) and CdTe/ZnS/ZnO–GSH (5.8) showed cell viability greater than 50% at ≤ 4 μm, **Figure 6.1A**. In general, the larger QDs were more toxic in comparison to the smaller ones except for CdTe/ZnS/ZnO–GSH (8.9) which showed minimal toxicity at ≤ 2 μm. Large QDs are known to have large surface defects **[301]** which have the tendency to allow the leaching of Cd^{2+} due to ineffective passivation. All the QDs showed % cell viabilities less than 50% at ≥ 8 μm.

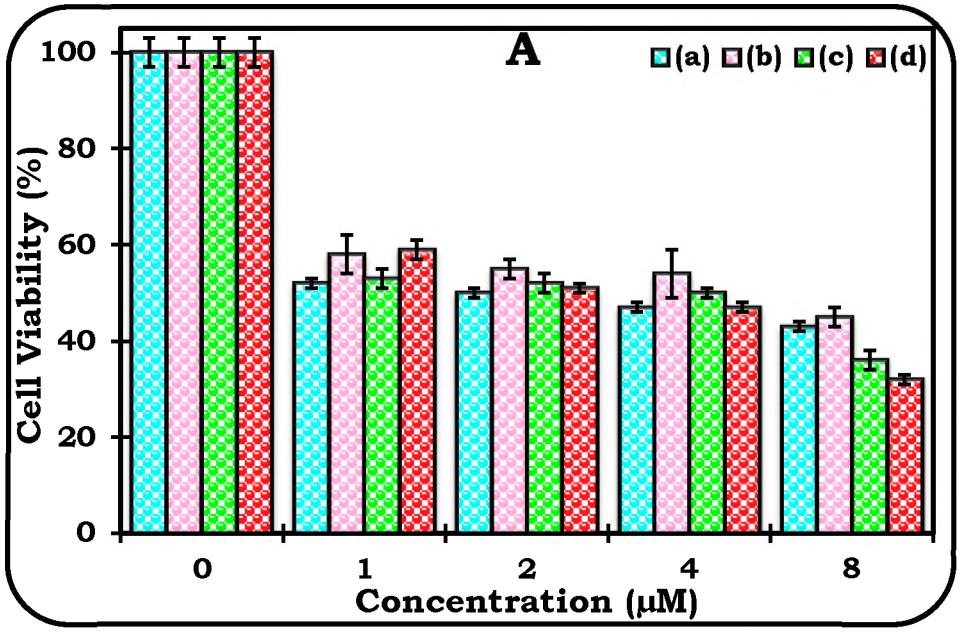

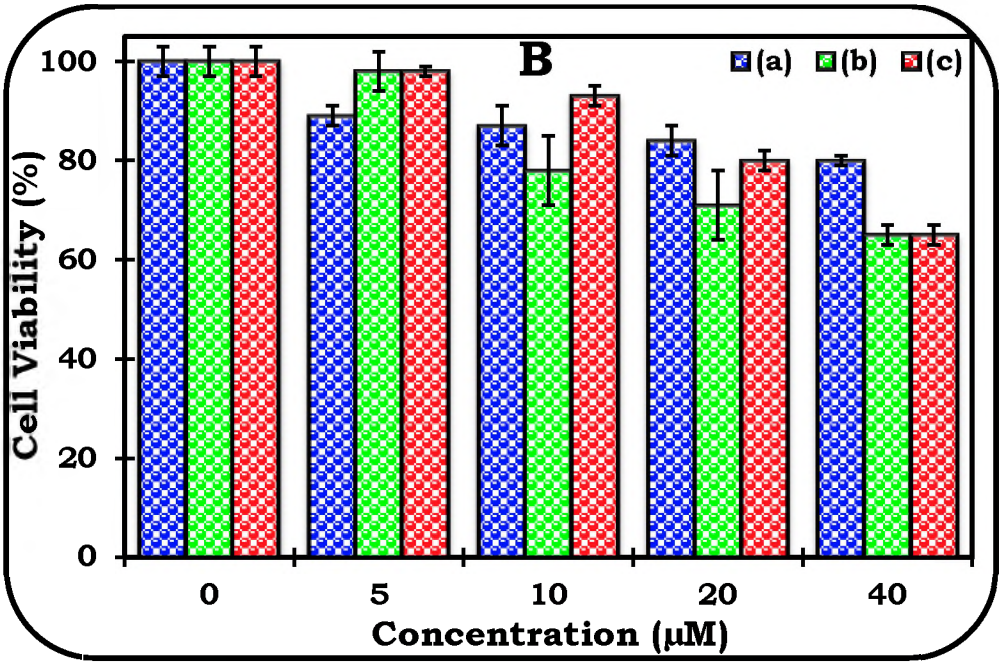

Figure 6.1: Histograms showing the percentage cell viability in the dark (A) CdTe/ZnS–GSH (4.1) (a), CdTe/ZnS/ZnO–GSH (4.7) (b), CdTe/ZnS/ZnO–GSH (5.8) (c), CdTe/ZnS/ZnO–GSH(8.9) (d); and (B) Compound 9 (a), 9–CdTe/ZnS/ZnO–GSH (4.7) (b), and 9–CdTe/ZnS/ZnO–GSH (5.8) (c).

6.1.2. Metallophthalocyanines and conjugates

The biomolecule (human serum albumin), chitosan and the NPs were studied when independently administered and in conjugates with Pcs. Chitosan and human serum albumin (HSA) when independently administered showed more than 50% cell viability at ≤ 57.1 μg/mL, **Figure 6.2A**. Of particular note is the increase in the cell viability of HSA above 100% which could be attributed to the fact that serum albumin forms part of the nutrient used in the culture DMEM for the cell culturing and this was thought to be due to an increase in the nutrient supplied to the cells, **Figure 6.2A**. ZnO/SiNPs–APTES (13) and SiNPs–APTES (20) exhibited

more than 50% cell viability at ≤ 28.6 µg/mL but the % cell viability reduced to less than 50% at 57.1 µg/mL, **Figure 6.2B**. AgNPs–Cyst (11.3) and AgAuNPs–Cyst (11.6) showed % cell viability greater than 50% within the tested concentration doses ≤ 29.8 µg/mL, **Figure 6.3**.

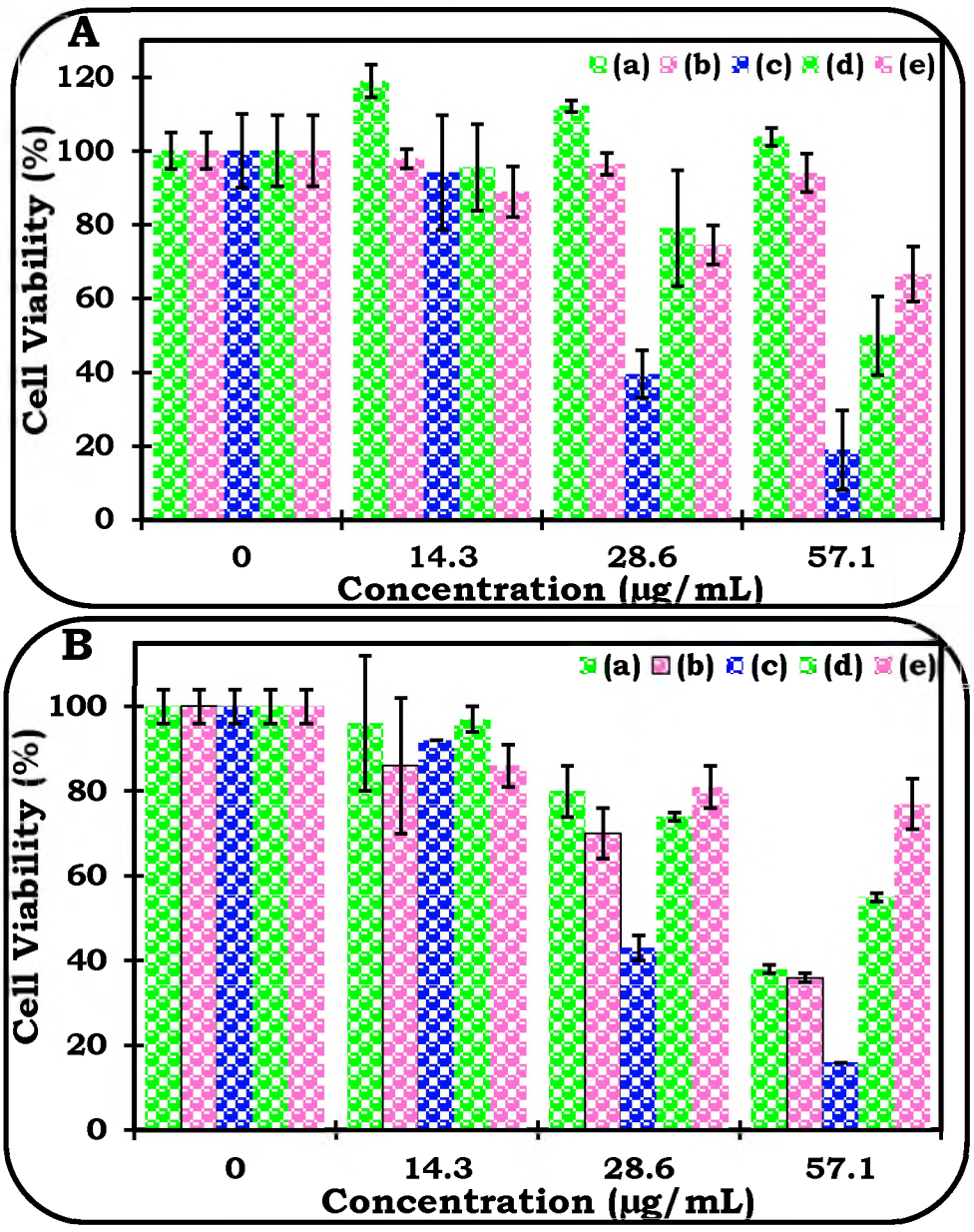

Figure 6.2: Histograms showing the percentage cell viability in the dark (A) HSA (a), Chitosan (b), 2b (c), 2b–HSA (d), 2b–Chitosan (e); and (B) SiNPs–APTES (20) (a), ZnO/SiNPs–APTES (13) (b), 2b (c), 2b–SiNPs–APTES (20) (d), and 2b–ZnO/SiNPs–APTES (13) (e).

Compound **2b** showed cell viability < 50% at ≥ 28.6 µg/mL (hence more dark toxicity), and the conjugates with chitosan, HSA and NPs accounted for more than 50% (hence less dark toxicity) at the same concentrations. This confirms reduced dark toxicity of compound **2b** in the presence of HSA and chitosan, **Figure 6.2A**. At the highest concentration of 57.1 µg/mL, both ZnO/SiNPs–APTES (13), and SiNPs–APTES (20) were toxic, though less toxic than compound **2b**, **Figure 6.2B**. Statistically significant differences were observed between compound **2b** alone, and its conjugates with ZnO/SiNPs–APTES (13), SiNPs–APTES (20), HSA and chitosan.

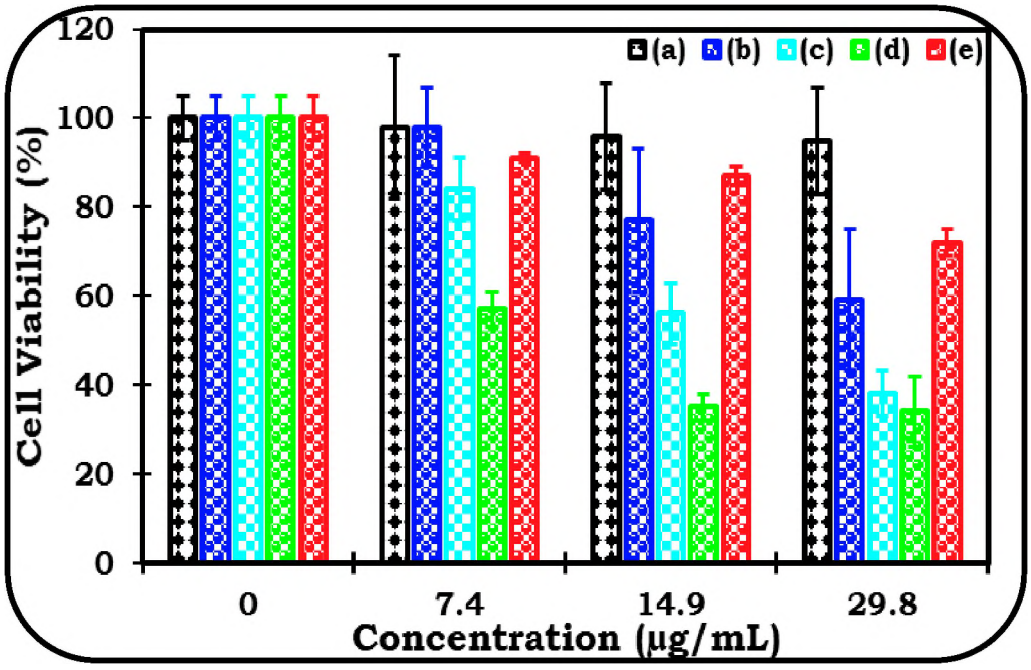

Figure 6.3: Histograms showing the percentage cell viability in the dark (a) AgNPs–Cyst (11.3), (b) AgAuNPs–Cyst (11.6), (c) Compound 10, (d) 10–AgNPs–Cyst (11.3), and (e) 10–AgAuNPs–Cyst (11.6).

Compound **6** exhibited more than 70% cell viability at 5 µg/mL and same trend was observed in its nanoconjugates with CdTe–GSH (2.9),

CdTeSe/ZnO–GSH (5.1) and CdTeSe/ZnO–GSH (6.5), **Table 6.1**. The % cell viability (related to active cells) of compound **6** and nanoconjugates were higher than what was observed for QDs alone indicating less dark cytotoxicity of QDs in the presence of compound **6** due to observed high numbers of active cells after treatment. Thus, the Pc compound appears to reduce the dark toxicity of QDs when combined (**6** and QDs), **Table 6.1**. Both compound **9**, and it conjugates with QDs (CdTe/ZnS–GSH (4.7) and CdTe/ZnS/ZnO–GSH (5.8)) showed more than 60% viable cells at ≤ 40 μm, **Figure 6.1B**. The % cell viabilities of compound **9**, and its conjugates with CdTe/ZnS–GSH (4.7) and CdTe/ZnS/ZnO–GSH (5.8) were higher than what was obtained for the QDs alone, **Figure 6.1A** indicating reduction in the dark cytotoxicity of QDs in the presence of compound **9**.

Compound **10** showed cell viability < 50% at 29.8 μg/mL and its conjugates, **10**–AgAuNPs–Cyst (11.6) showed % cell viability > 50% at ≤ 29.8 μg/mL and **10**–AgNPs–Cyst (11.3) showed < 50% at 29.8 μg/mL, **Figure 6.3**. Low cell viability corresponds to high dark toxicity. **10**–AgAuNPs–Cyst (11.6) showed lower dark toxicity compared to **10**–AgNPs–Cyst (11.3) and compound **10**. The dark toxicity followed the order: **10**–AgNPs–Cyst (11.3) > **10** > **10**–AgAuNPs–Cyst (11.6). The combination of compound **10** and AgAuNPs–Cyst (11.6) showed lower dark toxicity than the individual components at 14.9 and 29.8 μg/mL (**Figure 6.3**). Thus, compound **10** and AgAuNPs–Cyst (11.6) are better when combined than when administered independently. There were statistically significant

differences in the percent viability of the cells as the drug concentration increases.

6.2 *IN VITRO* PHOTODYNAMIC THERAPY STUDIES

The PDT activity of ZnO/SiNPs–APTES (13), HSA, chitosan, compound **2b** and conjugates were studied as examples at a fixed light dosimetry and varied drug concentrations. Illumination for PDT studies was obtained using a quartz lamp for **2b** and its conjugates which has been reported to be effective light source in the photo–irradiation of tumor cells **[326]**. A laser light source with excitation wavelength source of 680 nm was used for PDT studies for AgNPs–Cyst (11.3), AgAuNPs–Cyst (11.6), compound **10**, and their conjugates (**10**–AgNPs–Cyst (11.3) and **10**–AgAuNPs–Cyst (11.6)).

6.2.1 HSA, chitosan, and ZnO/SiNPs–APTES (13)

The PDT studies of the QDs and their conjugates were not done due to observed dark toxicity when administered in the absence of light. HSA and chitosan did not show any significant PDT activity as their % cell viability was more than 80% at ≤ 57.1 µg/mL, **Figure 6.4A**. ZnO/SiNPs–APTES (13) exhibited less than 50% cell viability at the highest concentration (57.1 µg/mL), **Figure 6.4B**. The observed PDT activity can be attributed to the fact that ZnO/SiNPs–APTES (13) are known to have anticancer activity as a result of reactive oxygen species produced upon excitation at a suitable wavelength **[62]**. AgNPs–Cyst (11.3) exhibited less than 50% cell viability

at the highest concentration (29.8 µg/mL) while AgAuNPs–Cyst (11.6) showed less than 50% cell viability at 14.9 µg/mL and 29.8 µg/mL, **Figure 6.5**. AgNPs and AgAuNPs are known to possess anticancer activity when excited at suitable wavelength **[20,327]**.

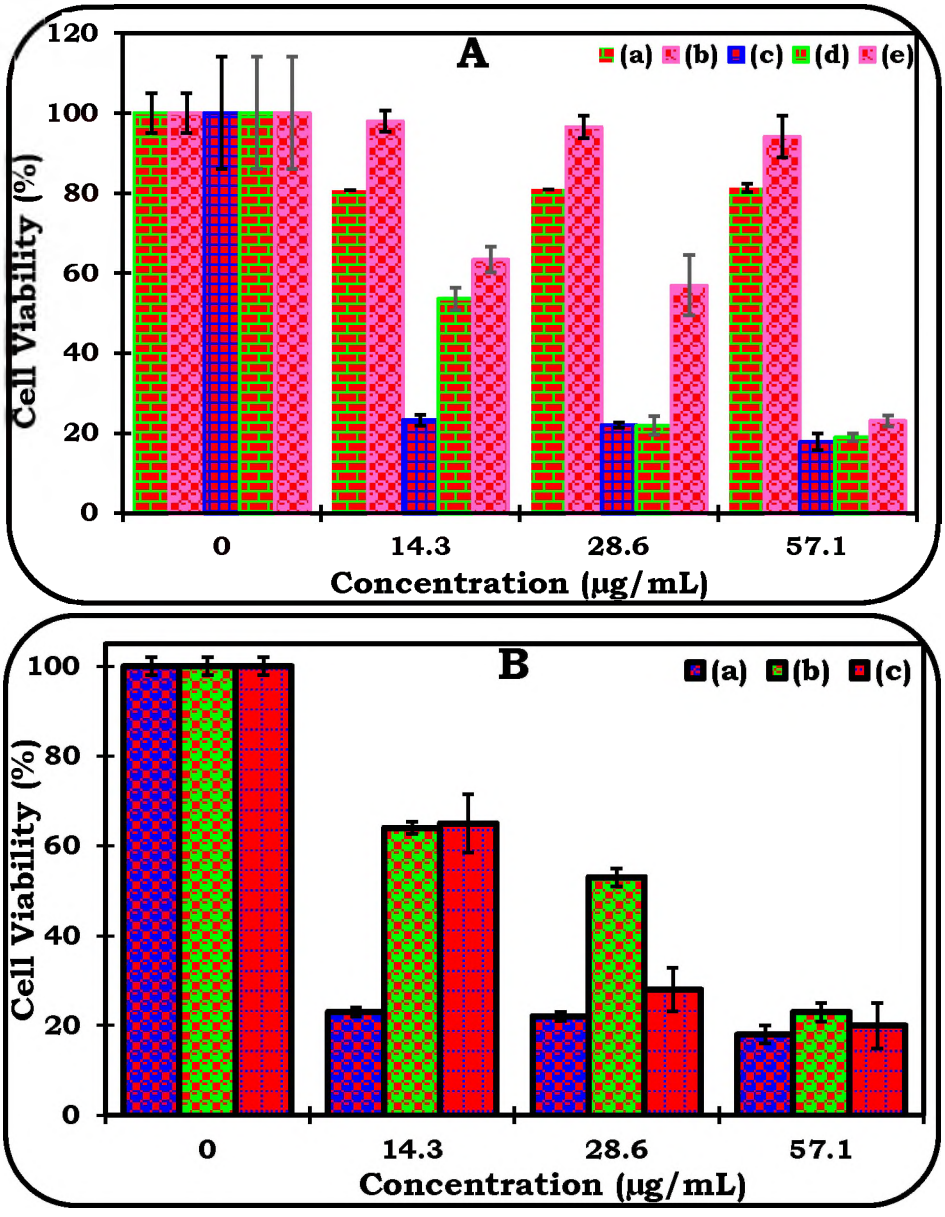

Figure 6.4: Histograms showing the percentage cell viability after illumination (A). HSA (a), Chitosan (b), Compound 2b (c), 2b–HSA (d), and 2b–Chitosan (e); and (B). 2b (a), ZnO/SiNPs–APTES (13) (b), and 2b–ZnO/SiNPs–APTES (13) (c).

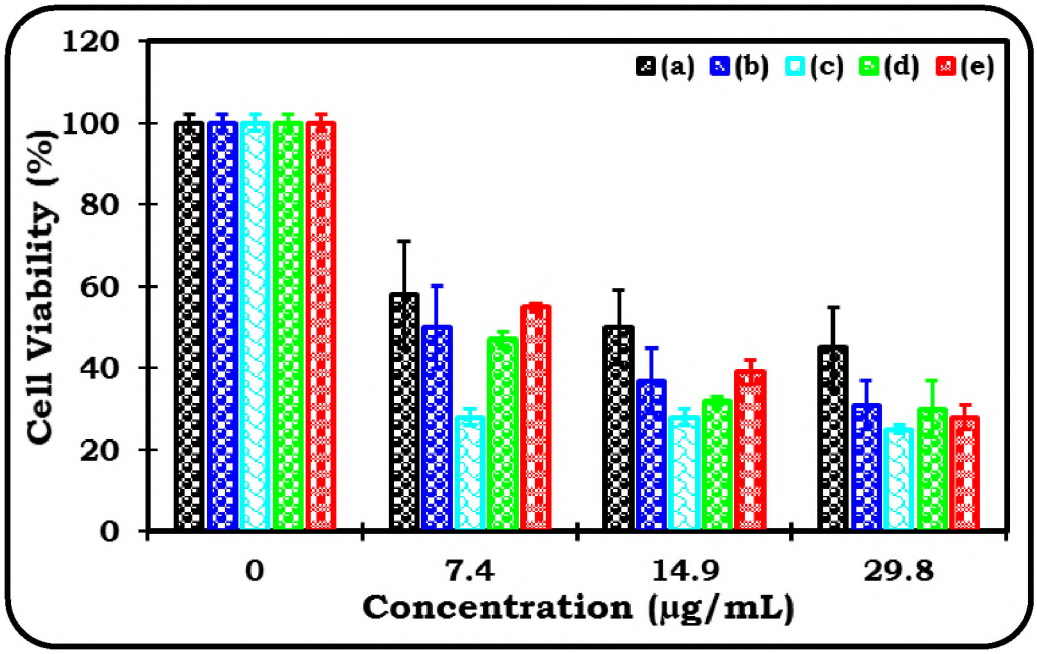

Figure 6.5: Histograms showing the percentage cell viability after illumination for (a) AgNPs–Cyst (11.3), (b) AgAuNPs–Cyst (11.6), (c) Compound 10, (d) 10–Cyst–AgNPs (11.3), and (e) 10–AgAuNPs–Cyst (11.6).

6.2.2 Metallophthalocyanines and conjugates

Comparing compounds **2b** and **10**, the cell viability of compound **2b** was less than 50% at ≥ 14.3 µg/mL and **10** accounted for less than 50% cell viability at ≥ 7.4 µg/mL, **Figure 6.4, and 6.5**. Compound **10** exhibited enhanced PDT activity in comparison to **2b** and this could be due to higher singlet oxygen generation by the former. The conjugates of **2b** with HSA, chitosan and ZnO/SiNPs–APTES (13) accounted for more than 50% cell viability at ≤ 14.3 µg/mL, inferring reduced PDT activity in comparison to **2b**, **Figure 6.4A**. The observed high PDT activity of compound **2b** could be due to its high dark toxicity, as earlier discussed. PDT activities of **2b**–ZnO/SiNPs–APTES (13), **2b**–HSA, **2b**–chitosan and compound **2b** were relatively better than that of ZnO/SiNPs–APTES (13),

HSA and chitosan alone, **Figure 6.4**. Comparing the conjugates, the PDT activity of **2b**–ZnO/SiNPs–APTES (13) and **2b**–HSA were better than **2b**–chitosan, **Figure 6.4**.

Statistically significant differences were observed between compound **2b** alone, and its conjugates with ZnO/SiNPs–APTES (13), HSA and chitosan, **Figure 6.4**. Compound **10** showed cell viability < 50% at (7.4–29.8) μg/mL and its conjugates with NPs (**10**–AgNPs–Cyst (11.3), and **10**–AgAuNPs–Cyst (11.6)) (**Figure 6.5**) showed similar trend but the PDT activity of compound **10** was higher than what was obtained in the conjugates. The high PDT activity of compound **10** is due to the dark toxicity and the higher singlet oxygen quantum yield, earlier stated, **Table 4.4**. The PDT activities of **10**–AgNPs–Cyst (11.3) and **10**–AgAuNPs–Cyst (11.6) at 29.8 μg/mL are slightly better than the NPs alone. **10**–AgAuNPs–Cyst (11.6) (**Figure 6.5**) showed minimal dark toxicity and efficacious PDT activity, hence the combinations of **10** with AgAuNPs–Cyst (11.6) is good for PDT but not when **10** is combined with AgNPs–Cyst (11.3) alone. There were statistically significant differences in the percentage viability of the cells as the drug concentration increases. Upon analysis of the triplicate replicate data of each concentration, no statistically significant difference was obtained as the p–values were > 0.05.

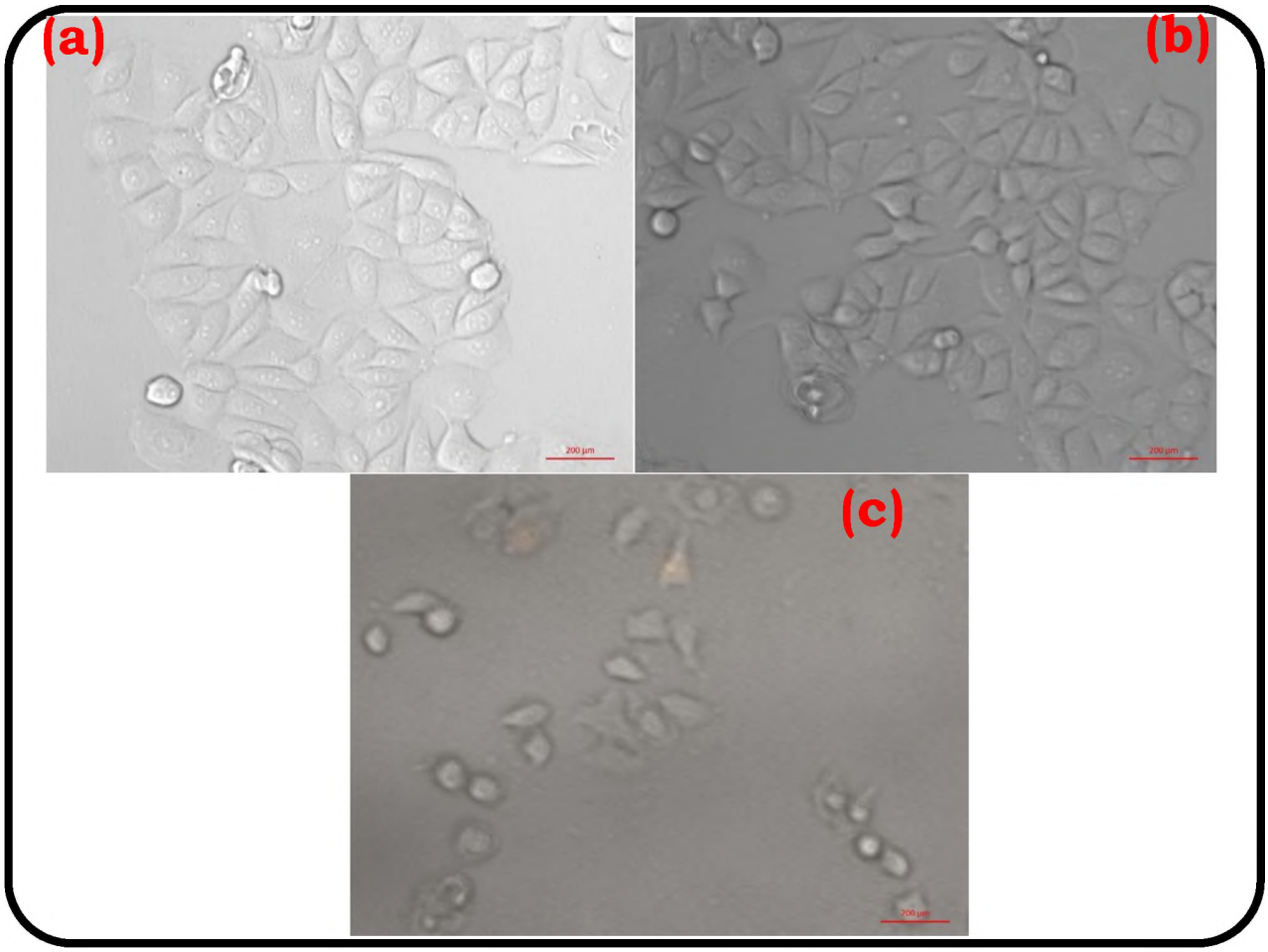

Figure 6.6: Photo-micrograph for cytotoxicity of MCF-7 cells at 200 µm magnification: (a) control cells (placebo cells), (b) 6–CdTeSe/ZnO–GSH (5.1), and (c) CdTe–TGA (2.8).

A visual inspection of the morphology of the placebo cells which served as control (in dark) and the treated cells showed a clear distinction with less viable cells in the Pcs, NPs and the conjugates (using **6**–CdTeSe/ZnO–GSH (5.1), CdTe–TGA (2.8) as an example) compared to the placebo cells, **Figure 6.6**.

6.3 SUMMARY OF CHAPTER

The *in vitro* dark cytotoxicity and photodynamic therapy studies of HSA, chitosan, nanoparticles, metallophthalocyanines and their conjugates were

tested against human breast adenocarcinoma cells (MCF–7 cells). The *in vitro* dark viability studies were performed at a physiological temperature and varied concentration doses while the *in vitro* PDT studies were done at different concentration doses and fixed illumination dosimetry.

The *in vitro* dark viability studies of various sizes and capping ligands of quantum dots at different concentrations, showed that the toxicity of QDs are dependent on the size and passivation as well as the concentrations. In general, the passivation of the QDs with suitable shells afforded reduction in their cytotoxicity with more than 50% cell viability at low concentrations. This could be associated with the size of the QDs as increase in sizes are often associated with loss/decomposition of the stabilizers due to longer heating time. Reduced cytotoxicity of the QDs were observed when linked to MPcs. At low concentrations, the AgNPs–Cyst (11.3) and AgAuNPs–Cyst (11.6) did not show any significant dark cytotoxicity as more than 50% cell viability was observed. Chitosan did not show any significant cytotoxic activity at tested concentrations while increase in the % cell viability of HSA above 100% was observed which could be attributed to the fact that serum albumin forms part of the nutrient used in the culture media and this was thought to be due to an increase in the nutrient supplied. The MPcs showed reduced cytotoxicity in the presence of NPs, chitosan and HSA.

The *in vitro* PDT studies of the ZnO/SiNPs–APTES (13), AgNPs–Cyst (11.3), AgAuNPs–Cyst (11.6), chitosan, HSA, MPcs and their conjugates were evaluated at a fixed illumination dosimetry. MPcs showed phenomenal PDT activity in

comparison to their corresponding conjugates with other components. Compound **10** showed a better anticancer activity in comparison to **2b** while **10**–AgAuNPs–Cyst (11.6) afforded the most efficacious PDT activity among the conjugates. The MPcs and conjugates showed better anticancer activity in comparison to the NPs, chitosan, and HSA.

CHAPTER SEVEN

CONCLUSIONS AND FUTURE PROSPECTS

7.1 GENERAL CONCLUSIONS

Mononuclear and multinuclear phthalocyanines (Pcs) were successfully synthesized and characterized with sundry analytical spectroscopic techniques. The syntheses of diverse nanoparticles (NPs) were achieved in this research work. The Pcs were covalently linked or mixed with NPs, HSA and chitosan. The morphologies of the NPs and their conjugates were assessed using transmission electron microscopy and X–ray diffractometer. FT–IR and X–ray photoelectron were used to confirm the successful formation of the amide or ester bond of the Pcs and NPs conjugates. Thermal stability of the compounds, NPs and their conjugates were confirmed with thermogravimetric analyzer and the surface area analysis of the SiNPs–APTES (20) and ZnO/SiNPs–APTES (13) were assessed using a surface analyzer. The purity of the compounds were confirmed with MALDI–TOF mass spectrometry, UV–Vis spectroscopy and elemental analysis. The results of the synthesized compounds were consistent with the predicted structures. The compounds showed good solubility in most solvents evidenced by their typical absorption bands.

The photophysics and photochemistry of the MPcs were assessed when alone and in conjugates with NPs, chitosan and HSA respectively. The Pc macrocycles with relatively light metal (Al) exhibited high Φ_F and τ_F while their heavy metal (Zn and In) analogues depicted low Φ_F and τ_F in comparison to the former. It is pertinent to note that the point of substitution also played a crucial role in the fluorescence property of the MPcs. The Φ_F and τ_F values of the MPcs were

relatively unchanged in the presence of NPs, HSA and chitosan except in some cases where reductions or increases were observed. Bi–exponential τ_F was observed in some cases in the conjugates. The Pc macrocycles with heavy metal (Zn and In) exhibited high Φ_T and τ_T in comparison to their relatively light metal (Al) analogues and this is associated with heavy–atom effect. The MPcs conjugates with ZnO/SiNPs–APTES (13) and QDs afforded significantly higher Φ_T and τ_T in comparison to their chitosan, HSA and SiNPs–APTES (20) analogues. Lengthening or shortening of the τ_T were observed in some cases. The trend in the Φ_F and Φ_T were consistent with low Φ_F corresponding to high Φ_T. The heavy atom and extended π conjugated system with phenyl ring corroborated the SOCT–ISC. Decreases in the Φ_T of the MPcs were observed in the presence of SiNPs and this was thought to be due to aggregation effects which are often responsible for photo–inactivation of the photosensitizers. The obtained Φ_Δ values of some of the MPc compounds were not consistent with the expected trends due to inconsistency between the Φ_T and Φ_Δ of the MPcs. Low Φ_Δ was observed in the MPcs in some cases. Similar trends were also observed in the conjugates. The low Φ_Δ could be adduced to inefficiency in the energy transfer between the excited triplet state photosensitizer and ground state molecular oxygen.

The optical nonlinearities of the multinuclear MPcs resulted in high β_{eff} and third order hyperpolarizabilities. The asymmetrical multinuclear Pcs showed better

NLO behaviour in comparison to their symmetrical analogues. Improvements were observed in the conjugates of the MPcs when linked or mixed with quantum dots which could be attributed to spin–orbit coupling and free–carrier absorption mechanism often associated with QDs. The metal free di–thiol Pc and conjugate with QDs also showed good NLO behaviour.

The *in vitro* cytotoxicity of the passivated QDs were relatively innocuous at the tested concentration while reduced cytotoxicity was observed when the QDs were linked with Pcs. The MPcs and their conjugates showed relative toxicity at very high concentrations. The photodynamic therapy studies of the MPcs and their conjugates showed significant activity at the tested concentrations. Reduced PDT activity was observed in the conjugates in comparison to the MPcs alone except for the conjugates of **10**–AgAuNPs–Cyst (11.6) which showed similar activity as the MPc but minimal dark cytotoxicity which is essential for PDT.

7.2 FUTURE PROSPECTS

Efforts will be made to utilize different lanthanide metals for the multinuclear MPcs and their NLO activity will be assessed in solution or when embedded on solid support. In addition, the photophysical behaviour of the multinuclear Pcs will be evaluated. Further assessment of the *in vitro* cytotoxicity and PDT activity of the compounds will be undertaken using different cancer cells. The employment of confocal microscopy and Xcelligence system will further provide more information on the cytotoxicity and phototoxicity of the photosensitizers. Effort will be made to synthesize water soluble MPcs and their possible

conjugation to small biomolecules to evaluating their photochemistry and PDT activities. Compound **10** and conjugates with AgAuNPs–Cyst (11.6) showed efficacious PDT activity, efforts will be made to further investigate its mode of action.

[1] A. Ambrosi, F. Airò, A. Merkoçi, Anal. Chem., 82 (2010) 1151.

[2] G.F. Zheng, W.L. Daniel, C.A. Mirkin, J. Am. Chem. Soc., 130 (2008) 9644.

[3] X.Y. Xu, D.G. Georganopoulou, H.D. Hill, Mirkin C. A, Anal. Chem., 79 (2007) 6650.

[4] X. Gao, Y. Cui, R.M. Levenson, L.W. Chung, S. Nie, Nat. Biotechnol., 22 (2004) 969.

[5] A.D. Yoffe, Adv. Phys., 50 (2001) 5.

[6] H. Mader, X. Li, S. Saleh, M. Link, P. Kele, O.S. Wolfbeis, Ann. N.Y. Acad. Sci., 1130 (2008) 218.

[7] J.L. Vivero-Escoto, R.C. Huxford–Phillips, W. Lin, Chem. Soc. Rev., 41 (2012) 2673.

[8] S.C. Feifel, F. Lisdat, J. Nanobiotechnol., 9 (2011) 59.

[9] M. Nyk, D. Wawrzynczyk, J. Szeremeta, M. Samoc, Appl. Phys. Lett., 100 (2012) 041102.

[10] X.F. Li, M. Li, J.H. Yang, X.Y. Li, T.J. Hu, J.S. Wang, R.Y. Sui, X.T. Wu, L.N. Kong, J. Phys. Chem. Solids, 75 (2014) 441.

[11] M. Ahmad, E. Ahmed, Z.L. Hong, X.L. Jiao, T. Abbas, N.R. Khalid, Appl. Surf. Sci., 285 (2013) 702.

[12] N. Venkatram, D.N. Rao, M.A. Akundi, Opt. Express, 13 (2005) 867.

[13] R.B. Martin, M.J. Meziani, P. Pathak, J.E. Riggs, D.E. Cook, S. Perera, Y.P. Sun, Opt. Mater., 29 (2007) 788.

[14] S. Wang, N. Mamedova, N. Kotov, W. Chen, J. Studer, Nano Lett., 2 (2002) 817.

[15] N. Narband, S. Tubby, I. P. Parkin J. Gil-Tomas, D. Ready, Curr. Nanosci., 4 (2008) 409.

[16] C. Fasciani, J. Silvero, M.A. Anghel, G.A. Argüello, M.C. Becerra, J.C. Scaiano, J. Am. Chem. Soc., 136 (2014) 17394.

[17] N.F. Gamaleia, E.D. Shishko, G.A. Dolinsky, A.B. Shcherbakov, A.V. Usatenko, V.V. Kholin, Exp. Oncol., 32 (2010) 44.

[18] ASTM E 2456-06 "Terminology for Nanotechnology." ASTM International, 2006.

[19] B. Duncan, C. Kim, V.M. Rotello, J. Con. Rel., 148 (2010) 122.

[20] A. El-Hussein, I. Mfouo-Tynga, M. Abdel-Harith, H. Abrahamse, J. Photochem. Photobiol. B., 153 (2015) 67.

[21] J. Nam, N. Won, H. Jin, H. Chung, S. Kim, J. Am. Chem. Soc., 131 (2009) 13639.

[22] M.E. Wieder, D.C. Hone, M.J. Cook, M.M. Handsley, J. Gavrilovic, D.A. Russell, Photochem. Photobiol. Sci., 5 (2006) 727.

[23] D. Graham, K. Fauldsa, W.E. Smith, Chem. Commun., (2006) 4363.

[24] Y. Cheng, A.C. Samia, J.D. Meyers, I. Panagopoulos, B. Fei, C. Burda, J. Am. Chem. Soc., 130 (2008) 10643.

[25] D. Demberelnyamba, M. Ariunaa, Y. K. Shim, Int. J. Mol. Sci., 9 (2008) 864.

[26] W. Jiang, B.Y.S. Kim, J.T. Rutka, W.C.W. Chan, Nat. Nanotech., 3 (2008) 145.

[27] X. Ma, Y. Wu, S. Jin, Y. Tian, X. Zhang, Y. Zhao, L. Yu, X.J. Liang, ACS Nano., 5 (2011) 8629.

[28] P.K. Jain, X. Huang, I.H. El-Sayed, M.A. El-Sayed, Accounts Chem. Res., 41 (2008) 1578.

[29] X. Huang, I.H. El-Sayed, W. Qian, M.A. El-Sayed, J. Am. Chem. Soc., 128 (2006) 2115.

[30] J. Kim, S. Park, J.E. Lee, S.M. Jin, J.H. Lee, I.S. Lee, I. Yang, J.S. Kim, S.K. Kim, M.H. Cho, T. Hyeon, Angew. Chem., 118 (2006) 7918.

[31] S. Liu, G. Chen, P.N. Prasad, M.T. Swihart, Chem. Mater., 23 (2011) 4098.

[32] W. Jia, E.P Douglas, F. Guo, W. Sun, Appl. Phys. Lett., 85 (2004) 6326.

[33] M. Bruchez, Moronne M, P. Gin, S. Weiss, A.P. Alivisatos, Science 281 (1998) 2013.

[34] W.C. Chan, S. Nie, Science, 281 (1998) 2016.

[35] J.K. Jaiswal, S.M. Simon, Trends Cell Biol., 14 (2004) 497.

[36] H.Y. Ramírez, C.H. Lin, C.C. Chao, Y. Hsu, W.T. You, S.Y. Huang, Y.T. Chen, H.C. Tseng, W.H. Chang, S.D. Lin, S.J. Cheng, Phys. Rev. B, 81 (2010) 245324.

[37] B.A. Rzigalinski, J.S. Strobl, Toxicol. Appl. Pharmacol., 238 (2009) 280.

[38] A.M. Smith, S. Nie, Nat. Biotechnol., 27 (2009) 732.

[39] Z. Gu, L. Zou, Z. Fang, W. Zhu, X. Zhong, Nanotechnology, 19 (2008) 135604.

[40] C.H. Soo, W. Liu, P. Misra, E. Tanaka, J.P. Zimmer, I.B. Itty, M.G. Bawendi, J.V. Frangioni, Nat. Biotechnol., 25 (2007) 1165.

[41] Y. Su, Y. He, H. Lu, L. Sai, Q. Li, W. Li, L. Wang, P. Shen, Q. Huang, C. Fan, Biomaterials, 30 (2009) 19.

[42] F. Zhang, D. Yi, H. Sun, H. Zhang, J. Nanosci. Nanotechnol., 14 (2014) 1409.

[43] Y. Wang, Z. Tang, M.A. Correa-Duarte, I. Pastoriza-Santos, M. Giersig, N.A. Kotov, L.M. Liz-Marzan, J. Phys. Chem. B, 108 (2004) 15461.

[44] H.F. Qian, L. Li, J.C. Ren, Mater. Res. Bull., 40 (2005) 1726.

[45] H. Seo, S.W. Kim, Chem. Mater., 19 (2007) 2715.

[46] H. He, X. Sun, X. Wang, H. Xu, Luminescence, 29 (2014) 837.

[47] A.M. Derfus, W.C.W. Chan, S.N. Bhatia, Nano. Lett., 4 (2004) 11.

[48] A.M. Smith, H. Duan, A.M. Mohs, S. Nie, Adv. Drug Delivery Rev., 60 (2008) 1226.

[49] T.S. Hauck, R.E. Anderson, H.C. Fischer, S. Newbigging, W.C.W. Chan, Small, 6 (2010) 138.

[50] L. Ye, K.T. Yong, L.W. Liu, I. Roy, R. Hu, J. Zhu, H.X. Cai, W.C. Law, J.W. Liu, K. Wang, J. Liu, Y. Liu, Y. Hu, X. Zhang, M.T. Swihart, P.N. Prasad, Nat. Nanotechnol., 7 (2012) 453.

[51] A.C.S. Samia, X. Chen, C. Burda, J. Am. Chem. Soc., 125 (2003) 15736.

[52] T. Pons, N. Lequeux, B. Mahler, S. Sasnouski, A. Fragola, B. Dubertret, Chem. Mater., 21 (2009) 1418.

[53] Y. Liu, J. Yu, J. Colloid Interface Sci., 351 (2010) 1.

[54] Z. Yuan, Q. Ma, A. Zhang, Y. Cao, J. Yang, P. Yang, J. Mater. Sci., 47 (2012) 3770.

[55] V.A.L. Roy, A.B. Djurisic, W.K. Chan, J. Cao, H.F. Lui, C. Surya, Appl. Phys. Lett., 83 (2003) 141.

[56] Z.S. Wang, C.H. Huang, Y.Y. Huang, Y.J. Hou, P.H. Xie, B.W. Zhang, H.M. Cheng, Chem. Mater., 13 (2001) 678.

[57] C. Feldmann, Adv. Fundam. Mater., 13 (2003) 101.

[58] R. Wu, C.S. Xie, Mater. Res. Bull., 39 (2004) 637.

[59] M. Kitano, M. Shiojiri, Powder Technol., 93 (1997) 267.

[60] G.M. Hamminga, G. Mul, J.A. Moulijn, Chem. Eng. Sci., 59 (2004) 5479.

[61] V.P. Kamat, R. Huehn, R. Nicolaescu, J. Phys. Chem. B, 106 (2002) 788.

[62] H. Zhang, B. Chen, H. Jiang, C. Wang, H. Wang, X. Wang, Biomaterials, 32 (2011) 1906.

[63] D. Zaouk, Y. Zaatarb, R. Asmarb, J. Jabbourd, Microelectr. J., 37 (2006) 1276.

[64] A. Joseph, G.L Praveen, K. Abha, G.M Lekha, S. George, J. Lumin., 132 (2012) 1999.

[65] R.K. Iler, In The Colloid Chemistry of Silica and Silicates. Cornell University Press, Ithaca, New York, 1955.

[66] Y. Xia, B. Gates, Y. Yin, Y. Lu, Adv. Mater., 12 (2000) 693.

[67] K. Sathiyamoorthy, C. Vijayan, S. Varma, Langmuir, 24 (2008) 7485.

[68] A. Bitar, N. M. Ahmad, H. Fessi, Abdelhamid Elaissari, Drug Discov. Today, 17 (2012) 1147.

[69] Y. Jin, A. Li, S.G. Hazelton, S. Liang, C.L. John, P.D. Selid, D.T. Pierce, J.X. Zhao, Coord. Chem. Rev., 253 (2009) 2998.

[70] K.S. Finnie, J.R. Bartlett, C.J.A. Barbe, L. Kong, Langmuir, 23 (2007) 3017.

[71] P. Couleaud, V. Morosini, C. Frochot, S. Richeter, L. Raehm, J.O. Durand, Nanoscale, 2 (2010) 1083.

[72] T. Doussineau, S. Trupp, G.J. Mohr, J. Colloid Interface Sci., 339 (2009) 266.

[73] S. Santra, K. Wang, R. Tapec, W. Tan, J. Biomed. Opt., 6 (2001) 160.

[74] F. Figueira, J.A.S. Cavaleiro, J.P.C. Tomé, J. Porphyr. Phthalocya., 15 (2011) 517.

[75] J.L. Vivero-Escoto, Y.T. Huang, Int. J. Mol. Sci., 12 (2011) 3888.

[76] S. Kim, T.Y. Ohulchanskyy, H.E. Pudavar, R.K. Pandey, P.N. Prasad, J. Am. Chem. Soc., 129 (2007) 2669.

[77] S. Zhu, J. Xiang, X. Li, S. Shen, H. Lu, J. Zhou, W. Xiong, B. Zhang, X. Nie, M. Zhou, K. Tang, G. Li. Biotechnol. Appl. Biochem., 39 (2004) 179.

[78] C. Kneuer, M. Sameti, U. Bakowsky, T. Schiestel, H. Schirra, H. Schmidt, C. Lehr, Bioconjugate Chem., 11 (2000) 926.

[79] D. Luo, E. Han, N. Belcheva, W.M. Saltzman, J. Control. Release, 95 (2004) 333.

[80] M.N.R. Kumar, M. Sameti, S.S. Mohapatra, X. Kong, R.F. Lockey, U. Bakowsky, G. Lindenblatt, H. Schmidt, C. Lehr, J. Nanosci. Nanotechnol., 4 (2004) 876.

[81] W. Tan, K. Wang, X. He, X.J. Zhao, T. Drake, L. Wang, R.P. Bagwe, Med. Res. Rev., 24 (2004) 621.

[82] G. Yao, L. Wang, Y. Wu, J. Smith, J. Xu, W. Zhao, E. Lee, W. Tan, Anal. Bioanal. Chem., 385 (2006) 518.

[83] T.Y. Ohulchanskyy, I. Roy, L.N. Goswami, Y. Chen, E.J. Bergey, R.K. Pandey, A.R. Oseroff, P.N. Prasad, Nano. Lett., 7 (2007) 2835.

[84] J. Qian, A. Gharibi, S. He, J. Biomed. Opt., 3 (2009) 1507.

[85] I.I. Slowing, B.G. Trewyn, V.S.Y. Lin, J. Am. Chem. Soc., 129 (2007) 8845.

[86] A. Fashina, E. Amuhaya, T. Nyokong, Spectrochim. Acta. A Mol. Biomol. Spectrosc., 140 (2015) 256.

[87] R.P. Bagwe, C. Yang, L.R. Hilliard, W. Tan, Langmuir, 20 (2004) 8336.

[88] W. Stöber, A. Fink, E. Bohn, J. Colloid Interface Sci., 26 (1968) 62.

[89] A.B.P. Lever, H.J. Emeleus, A.G. Sharpe (Eds), In: Advances in Inorganic Chemistry and Radiochemistry, Academic Press, New York, 7 (1965) 28.

[90] N.B. McKeown, In: Phthalocyanine Materials–Synthesis, Structure and Function, Cambridge University Press, 1998.

[91] K. Kadish, Kevin M. Smith, Roger Guilard (eds), In The Porphyrin Handbook, Academic Press, San Diego CA, USA, 15 (2003).

[92] F.H. Moser, A.I. Thomas, In: The Phthalocyanines Manufacture and Application, CRC Press, Boca Raton FL, 2 (1983).

[93] K. Sakamoto, E. Okumura, R. Hirohashi, In: Phthalocyanine as Functional Dyes, IPC, Tokyo, Japan, 2004.

[94] G. de la Torre, P. Vazquez, T. Torres, Chem. Rev., 104 (2004) 3723.

[95] J.J. Cid, J.H. Yum, S.R. Jang, M.K. Nazeeruddin, E. Martinez–Ferrero, E. Palomares, J. Ko, M. Graetzel, T. Torres, Angew. Chem. Int. Ed., 46 (2007) 8358.

[96] D. Gu, Q. Chen, X. Tang, F. Gan, S. Shen, K. Liu, H. Xu, Opt. Commun., 121 (1995) 125.

[97] S. Campidelli, B. Ballesteros, A. Filoramo, D. Diaz, G. de la Torre, T. Torres, G.M.A. Rahman, E.C. Aminur, D. Kiessling, F. Werner, V. Sgobba, D.M. Guldi, C. Cioffi, M. Prato, J.P. Bourgoin, J. Am. Chem. Soc., 130 (2008) 11503.

[98] P. Gregory, In: High-Technology Applications of Organic Colourants, Plenum Press, New York, (1991) 7.

[99] I. Okura, In: Photosensitization of Porphyrins and Phthalocyanines, Gordon and Breach, Amsteldijk, Netherlands, (2001) 151.

[100] D. Dini, M. Hanack. In: Phthalocyanines Properties and Materials. The Porphyrin Handbook, K.M. Kadish, K.M. Smith, R. Guilard (Eds.), Academic Press New York, 17 (2003) 107.

[101] E. Ben-Hur, W.S. Chan, In: Phthalocyanines in Photobiology and their Medical Applications. The Porphyrin Handbook, K.M. Kadish, K.M. Smith, R. Guilard (Eds.), Academic Press, New York, 19 (2003) 1.

[102] P. Gregory, J. Porphyr. Phthalocya., 4 (2000) 432.

[103] S. Makarov, C. Litwinski, E.A. Ermilov, O. Suvorova, B. Röder, D. Wöhrle, Chem. Eur. J., 12 (2006) 1468.

[104] Z. Odabaş, A. Altındal, A.R. Özkaya, M. Bulut, B. Salih, Ö. Bekaroğlu, Polyhedron, 26 (2007) 3505.

[105] N. Shibata, B. Das, M. Hayashi, S. Nakamura, T. Toru, J. Fluorine Chem., 130 (2009) 1164.

[106] T.V. Dubinina, S.A. Trashin, N.E. Borisova, I.A. Boginskaya, L.G. Tomilova, N.S. Zefirov, Dyes Pigm., 93 (2012) 1471.

[107] V. Pushkarev, M. Breusova, E. Shulishov, Y.V. Tomilov, Russ. Chem. Bull. Int. Ed., 54 (2005) 2087.

[108] N. Ishikawa and Y. Kaizu, Chem. Phys. Lett., 203 (1993) 472.

[109] N. Ishikawa, Y. Kaizu, Coord. Chem. Rev., 226 (2002) 93.

[110] N.B. Mckeown, J. Painter, J. Mater. Chem., 4 (1994) 1153.

[111] L.F. Levey, H. Stephen, J. Chem. Soc., (1931) 79.

[112] F. Dumoulin, M. Durmuş, V. Ahsen, T. Nyokong, Coord. Chem. Rev., 254 (2010) 2792.

[113] V.N. Nemykin, E.A. Lukyanets, ARKIVOC, I (2010) 136.

[114] M.S. Rodríguez-Morgade, G. de la Torre, T. Torres, in The Porphyrin Handbook, K.M. Kadish, K.M. Smith, R. Guilard (Eds.), Academic Press, Elsevier Science, 15 (2003) 99.

[115] C.C. Byeon, M.M. McKerns, W. Sun, T.M. Nordlun, C.M. Lawson, Appl. Phys. Lett., 84 (2014) 5174.

[116] M.J.F. Calvete, D. Dini, S.R. Flom, M. Hanack, R.G.S. Pong, J.S. Shirk, Eur. J. Org. Chem., (2005) 3499.

[117] Y. Liu, Y. Xu, D. Zhu, T. Wada, H. Sasabe, L. Liu, W. Wang, Thin Solid Films, 244 (1994) 943.

[118] Y. Liu, D. Zhu, T. Wada, A. Yamada, H. Sasabe, Heterocyclic Chem., 31 (1994) 1017.

[119] C.F. van Nostrum, R.J.M. Nolte, Chem. Comm., (1996) 2385.

[120] M. Ando, Y. Mori, Chem. Abstr., 113 [1990] 255558c.

[121] N. Kobayashi, R. Kondo, S.I. Nakajima, T. Osa, J. Am. Chem. Soc., 112 (1990) 9640.

[122] T. Yonekura, T. Ohsaka, F. Kitamura, K. Tokuda, J. Porphyr. Phthalocya., 9 (2005) 54.

[123] B. Zhu, X. Zhang, M. Han, P. Deng, Q. Li, J. Mol. Struct., 1079 (2015) 61.

[124] I.P. Kalashnikova, V.V. Kalashnikov, L.G. Tomilova, Russ. Chem. Bull., Int. Ed., 58 (2009) 1413.

[125] T.V. Dubinina, K.V. Paramonova, S.A. Trashin, N.E. Borisova, L.G. Tomilova, N.S. Zefirov, Dalton Trans., 43 (2014) 2799.

[126] J. Jiang, J. Xie, M.T.M. Choi, Y. Yan, S. Sun, D.K.P. Ng, J. Porphyr Phthalocya., 3 (1999) 322.

[127] K.P. Unnikrishnan, J. Thomas, V.P.N. Nampoori, C.P.G. Vallabhan, Syn. Met., 139 (2003) 371.

[128] K.P. Unnikrishnan, J. Thomas, V.P.N. Nampoori, C.P.G. Vallabhan, Chem. Phys., 279 (2002) 209.

[129] T. Ceyhan, M.A. Özdag, B. Salih, M.K. Erbil, A. Elmalı, A.R. Özkaya, Ö. Bekaroglu, Eur. J. Inorg. Chem., (2008) 4943.

[130] X. Wang, C.L. Liu, Q.H. Gong, Y.Y. Huang, C.H. Huang, J.Z. Jiang, Appl. Phys. A, 75 (2002) 497.

[131] S. Saydam, E. Yılmaz, F. Bag˘cı, H. Gül Yag˘lıog˘lu, A. Elmalı, B. Salih, Ö. Bekarog˘lu, Eur. J. Inorg. Chem., (2009) 2096.

[132] H.G. Yaglıoglu, M. Arslana, S. Abdurrahmanoglu, H. Unverc, A. Elmalia, O. Bekaroglud, J. Phys. Chem. of Solids, 69 (2008) 161.

[133] K.E. Sekhosana, T. Nyokong, Opt. Mat., 47 (2015) 211.

[134] K.E. Sekhosana, T. Nyokong, Inorg. Chim. Acta., 450 (2016) 87.

[135] K.E. Sekhosana, E. Amuhaya, S. Khene, T. Nyokong, Polyhedron, 85 (2015) 347.

[136] K.E. Sekhosana, E. Amuhaya, T. Nyokong, Inorg. Chim. Acta., 426 (2015) 221.

[137] T. Fukuda, K. Ono, S. Homma, N. Kobayashi, Chem. Lett., 32 (2003) 736.

[138] T. Nyokong, In: Functional Phthalocyanine Molecular Materials, Structure and Bonding, J. Jiang (Eds.), Springer, New York, 135 (2010) 45.

[139] N. Kobayashi, H. Ogata, N. Nonaka, E. A. Luk'yanets. Chem. Eur. J., 9 (2003) 5123.

[140] N. Kobayashi, H. Konami, In Phthalocyanines: Properties and Application, C. C. Leznoff, A.B.P. Lever (Eds.), VCH, New York, 4 (1999).

[141] L. Edwards, M. Gouterman, J. Mol. Spectrosc., 33 (1970) 292.

[142] A. Henrikson, M. Soundbom, Theor. Chim. Acta., 27 (1972) 213.

[143] M. Gouterman, In: The Porphyrins, Part A. Physical Chemistry, D. Dolphin (Ed.), Academic Press, New York, 3 (1978).

[144] C.G. Claessens, U. Hahn, T. Torres, Chem. Rec., 8 (2008) 75.

[145] A.B. Karpo, V.E. Pushkarev, V.I. Krasovskii, L.G. Tomilova, Chemical Phys. Lett., 554 (2012) 155.

[146] R. Wang, R. Li, Y. Li, X. Zhang, P. Zhu, P.C. Lo, D. K. P. Ng, N. Pan, C. Ma, N. Kobayashi, J. Jiang, Chem. Eur. J., 12 (2006) 1475.

[147] C. Huang, Y. Zhang, J. Sun, Y. Bian, D. P. Arnold, J. Porphyr. Phthalocya., 17 (2013) 673.

[148] N. Kobayashi, Coord. Chem. Rev., 227 (2002) 129.

[149] A.J. Martynov, E.A. Safonova, Y.G. Gorbunova, A.Y. Tsivadze, Russ. J. Inorg. Chem., 55 (2010) 347.

[150] N. Ishikawa, Y. Kaizu, Chem. Phys. Lett., 228 (1994) 625.

[151] R. Rousseau, R. Aroca, M. L. Rodríguez-Méndez, J. Mol. Struct., 356 (1995) 49.

[152] L. Li, J.F. Zhao, N. Won, H. Jin, S. Kim, J.Y. Chen Nanoscale Res. Lett., 7 (2012) 386.

[153] C. Tshangana, T. Nyokong, J. Fluoresc., 25 (2015) 199.

[154] K.E. Sekhosana, E. Antunes, T. Nyokong, Polyhedron, 54 (2013) 294.

[155] S. D'Souza, E. Antunes, T. Nyokong, Inorganica. Chimica. Acta., 367 (2011) 173.

[156] W. Chidawanyika, C. Litwinski, E. Antunes, T. Nyokong, J. Photochem. Photobiol. A: Chem., 212 (2010) 27.

[157] O.L. Osifeko, T. Nyokong, Dyes Pigm., 131 (2016) 186.

[158] J. Britton, E. Antunes, T. Nyokong, J. Photochem. Photobiol. A: Chem., 312 (2010) 1.

[159] S. Moeno, E. Antunes, S. Khene, C. Litwinski, T. Nyokong, Dalton Trans., 39 (2010) 3460.

[160] S. D'Souza, E. Antunes, C. Litwinski, T. Nyokong, J. Photochem. Photobiol. A: Chem., 220 (2011) 11.

[161] N. Masilela, T. Nyokong, J. Photochem. Photobiol. A: Chem., 247 (2012) 82.

[162] K.E. Sekhosana, E. Antunes, S. Khene, S. D'Souza, T. Nyokong, J. Lumin., 136 (2013) 255.

[163] O. Adegoke, T. Nyokong, Syn. Met., 188 (2014) 35.

[164] O. Adegoke, E. Antunes, T. Nyokong, J. Photochem. Photobiol. A: Chem., 257 (2013) 11.

[165] O. Adegoke, T. Nyokong, J. Fluoresc., 23 (2013) 963.

[166] O. Adegoke, T. Nyokong, J. Lumin., 146 (2014) 275.

[167] V.M. Blas-Ferrando, J. Ortiz, V. González-Pedro, R.S. Sánchez, I. Mora-Seró, F. Fernández-Lázaro, Á. Sastre-Santos, Chem. Commun., 51 (2015) 1732.

[168] S. Khene, T. Nyokong, Microchem. J., 99 (2011) 478.

[169] K. Sanusi, S. Khene, T. Nyokong, Opt. Mater., 37 (2014) 572.

[170] K. Sanusi, T. Nyokong, Opt. Mater., 38 (2014) 17.

[171] J. Britton, M. Durmus, S. Khene, V. Chauke, T. Nyokong, J. Porphyr. Phthalocya., 17 (2013) 691.

[172] R. Lin, L. Zhou, Y. Lin, A. Wang, J.H. Zhou, S.H. Wei, Spectroscopy, 26 (2011) 179.

[173] B. Zhao, J.J. Yin, P.J. Bilski, C.F. Chignell, J.E. Roberts, Y.Y. He, Toxicol. Appl. Pharmacol. 241 (2009) 163.

[174] K. Sanusi, J.M. Stone, T. Nyokong, New J. Chem., 39 (2015) 1665.

[175] Q.F. Zhuang, J.E. Wang, Z.J. Zhu, F. Feng, Z.X. Wang, Chin. J. Anal. Chem., 39 (2011) 1567.

[176] H.G. Baldovi, V.M. Blas-Ferrando, J. Ortiz, H. Garcia, F. Fernández-Lázaro, A. Sastre-Santos, Chem. Phys. Chem., 17 (2016) 1579.

[177] A.N. Gowda, M. Kumar, A.R. Thomas, R. Philip, S. Kumar, ChemistrySelect, 1 (2016) 1361.

[178] N. Nombona, K. Maduray, E. Antunes, A. Karsten, T. Nyokong, J. Photochem. Photobiol. B: Biol., 107 (2012) 35.

[179] N. Masilela, E. Antunes, T. Nyokong, J. Porphyr. Phthalocya., 17 (2013) 417.

[180] C. Shena, S. Songa, L. Zanga, X. Kang, Y. Wena, W. Liua, L. Fua, J. Hazardous Mat. 177 (2010) 560.

[181] J.D. Huang, P.C. Lo, Y.M. Chen, J.C. Lai, W.P. Fong, D.K. Ng, J. Inorg. Biochem., 100 (2006) 946.

[182] Y. Li, T.M. Pritchett, J. Huang, M. Ke, P. Shao, W. Sun, J. Phys. Chem. A., 112 (2008) 7200.

[183] C. Ma, D. Tian, X. Hou, Y. Chang, F. Cong, H. Yu, X. Du, G. Du, Synthesis, 5 (2005) 0741.

[184] J. Metz, O. Schneider, M. Hanack, Inorg. Chem., 23 (1984) 1065.

[185] K. Sakamoto, E. Ohno, Prog. Org. Coat., 31 (1997) 139.

[186] R. Philip, G.R. Kumar, P. Mathur, S. Ghosh, Chem. Phys. Lett., 313 (1999) 719.

[187] J.E. Riggs, Y.P. Sun, J. Phys. Chem., A, 103 (1999) 485.

[188] J.W. Perry, K. Mansour, S.R. Marder, K.J. Perry, D. Alvarez, I. Choong, Opt. Lett., 19 (1994) 625.

[189] L. De Boni, S.D. Corrêa, C.R. Mendonça, In Advances in Lasers and Electro Optics, ed. N. Costa and A. Cartaxo, INTECH, Croatia, 838 (2010).

[190] R.W. Boyd, Nonlinear Optics, 2nd ed. Academic, San Diego, 2003.

[191] G. de laTorre, P. Vazquez, F. AgullLopez, T. Torres, Chem. Rev., 104 (2004) 3723.

[192] Y. Chen, M. Hanack, Y. Araki, O. Ito, Chem. Soc. Rev., 34 (2005) 517.

[193] R.L. Sutherland, Handbook of Nonlinear Optics, Marcel Dekker, New York, NY, 2nd ed., 2003.

[194] G. de la Torre, M. Nicolau, T. Torres, In Supramolecular Photosensitive and Electroactive Materials; H.S. Nalwa, Ed.; Academic Press: San Diego, CA, 2001; K.M. Kadish, K.M. Smith, R. Guilard, Eds. Porphyrin and Phthalocyanine Handbook; Academic Press: Boston, MA, 11–20 (2003).

[195] J.S. Shirk, R.G.S. Pong, S R. Flom, H. Heckmann and M. Hanack, J. Phys. Chem., 104 (2000) 1438.

[196] J.L. Bredas, C. Adant, P. Tackx, A. Persoons, B.M. Pierce, Theoretical and Experimental Aspects Chem. Rev., 94 (1994) 243.

[197] X. Wang, C.L. Liu, Q.H. Gong, Y.Y. Huang, C.H. Huang, Opt. comm., 197 (2001) 83.

[198] L. De Boni, L. Gaffo, L. Misoguti, C.R. Mendonça, Chem. Phys. Lett., 419 (2006) 417.

[199] L. Chen, R. Hu, J. Xu, S. Wang, X. Li, S. Li, G. Yang, Spectrochim. Acta A Mol. Biomol. Spectrosc., 105 (2013) 577.

[200] H.S. Nalwa, J.S. Shirk, In: Phthalocyanines Properties and applications, Eds. Leznoff CC, A.B.P. Lever, VCH Publishers, Inc., New York, 4 (1996) 83.

[201] H.L. Wang, D.D. Qi, Z. Xie, W. Cao, K. Wang, H. Shang, J.J. Jiang, Chem. Commun., 49 (2013) 889.

[202] H. Shang, H. Wang, K. Wang, J. Kan, W. Cao, J. Jiang, Dalton Trans., 42 (2013) 1109.

[203] Y.R. Shen, In The Principles of Nonlinear Optics, Wiley, New York, 1984.

[204] M.B. Ballesteros, G. de la Torre, A. Shearer, A. Hausmann, M. Herranz, D.M. Guldi, T. Torres, Chem. Eur. J., 16 (2010) 114.

[205] K.E. Sekhosana, E. Amuhaya, T. Nyokong, Polyhedron, 105 (2016) 159.

[206] N. Shenga, Z. Yuana, J. Wanga, W. Chena, J. Sunc, Y. Bian, Dyes Pigm., 95 (2012) 627.

[207] F. Li, Z. He, M. Li, P. Lu, Mater. Lett., 111 (2013) 8.

[208] Y. Chen, L. Gao, M. Feng, L. Gu, N. He, J. Wang, Y. Araki, W.J. Blau, O. Ito, Mini Rev. Org. Chem., 6 (2009) 55.

[209] I. Rosenthal, Photochem. Photobiol., 53 (1991) 859.

[210] R. Bonnett, In Chemical Aspects of Photodynamic Therapy, Gordon and Breach Science Publishers, Amsterdam, (2000).

[211] S.L. Marcus, W.R. McIntyre, Expert Opin. Emerg. Drugs, 7 (2002) 321.

[212] J.G. Levy, Trends Biotechnol., 13 (1995) 14.

[213] T.J. Dougherty, J. Photochem. Photobiol., 58 (1993) 895.

[214] V.V. Sokolov, E.F. Stranadko, N.N. Zharkova, R.I. Iakubovskaia, E.V. Filonenko, T.A. Astrakhankina, Vop. Onkol., 41 (1995) 134.

[215] A.S. Sobolev, E.F. Stranadko, Int. Photodyn., 1 (1997) 2.

[216] M. Ochsner, J. Photochem. Photobiol. B Biol., 32 (1996) 3.

[217] J.R. Sounik, B.D. Rihter, W.E. Ford, M.A.J. Rodgers, M.E. Kenney, Proc. SPIE, 1426 (1991) 340.

[218] M. Soncin, A. Busetti, R. Biolo, G. Jori, G. Kwag, Y.S. Li, M.E. Kenney, M.A.J. Rodgers, J. Photochem. Photobiol. B Biol., 42 (1998) 202.

[219] A.E. Peaston, M.W. Leach, R.J. Higgins, J. Am. Vet. Med. Assoc., 202 (1993) 1261.

[220] K. Miller, B. Bartos, A. Rück, E. Schmidt, R. Steiner, R. Hautmann (Eds), Investigative Urology 3, Springer Berlin Heidelberg, (1989) 153.

[221] D. Frackowiak, A. Planner, A. Waszkowiak, A. Boguta, R. Ion, K. Wiktorowicz, J. Photochem. Photobiol. A Chem., 141 (2001) 101.

[222] D.E. Dolmans, D. Fukumura, R.K. Jain, Nat. Rev. Cancer, 3 (2003) 380.

[223] L.V. Uspenskii, L.V. Chistov, E.A. Kogan, V.B. Loshchenov, I. Ablitsov, V.K. Rybin, D.I. Shiktorov, N.F. Serbinenko, I.G. Semenova, Khirurgiia (Mosk) 2 (2000) 38.

[224] E.F. Stranadko, M.I. Garbuzov, V.G. Zenger, A.N. Nasedkin, N.A. Markichev, M.V. Riabov, I.V. Leskov, Vestn. Otorinolaringol. 3 (2001) 36.

[225] E.V. Filonenko, V.V. Sokolov, V.I. Chissov, E.A. Lukyanets, G.N. Vorozhtsov, Photodiagnosis Photodyn. Ther. 5 (2008) 187.

[226] J.D. Miller, E.D. Baron, H. Scull, A. Hsia, J.C. Berlin, T. McCormick, V. Colussi, E. Malcolm, A.E. Kenney, K.D. Cooper, N.L. Oleinick, Toxicol. Appl. Pharmacol., 224 (2007) 290.

[227] Z. Huang, Photodiagnosis Photodyn. Ther., 5 (2008) 285.

[228] E. Ben-Hur, R. Kol, R. Marko, E. Riklis, I. Rosenthal, Int. J. Radiat. Biol. 54 (1988) 21.

[229] Z. Jablonski, Phys., 94 (1935) 38.

[230] P.W. Atkins, In Physical Chemistry, P.W. Atkins (Ed.), Oxford University Press, Oxford, 6th ed., 17 (1998).

[231] J.R. Lakowicz, In Principles of Fluorescence Spectroscopy, 3rd ed., Kluwer Academic/Plenum Publishers, New York, 2006.

[232] S. Fery–Forgues, D. Lavabre, J. Chem. Educ., 76 (1999) 1260.

[233] A. Ogunsipe, J.Y. Chen, T. Nyokong, New. J. Chem., 28 (2004) 822.

[234] K. Ishii, N. Kobayashi, In The Porphyrin Handbook, K.M. Kadish, K.M. Smith, R. Guilard, (Eds.), Elsevier Science, New York, 16, 102 (2003) 1.

[235] J. Fu, X.Y. Li, D.K.P. Ng, C. Wu, Langmuir, 18 (2002) 3843.

[236] A.G. Ryder, S. Power, T.J. Glynn, J.J. Morrison, Proc. SPIE, 4529 (2001) 102.

[237] T.H. Tran–Thi, C. Desforge , C. Thiec, S.J. Gaspard, Phys. Chem., 93 (1989) 1226.

[238] L. De boni, E. Piovesan, L. Gaffo. C. R. Mendonca. J. Phys. Chem. A., 112 (2008) 6803.

[239] M. Niedre, M.S. Patterson, B.C. Wilson, J. Photochem. Photobiol. 75 (2003) 382.

[240] H. Li, T.F. Guarr, J. Chem. Soc. Chem. Commun. (1989) 832.

[241] R.A. Keller, S.G. Hadley, J. Chem. Phys., 42 (1965) 238.

[242] N.A. Kuznetsova, N. Gretsova, O. Yuzhakova, V. Negrimovsky, O. Kaliya, E. Luk'yanets, Russ. J. Gen. Chem., 71 (2001) 36.

[243] M.S. Patterson, S.J. Madsen, R. Wilson, J. Photochem. Photobiol. B: Biol., 5 (1990) 69.

[244] T. Nyokong, E. Antunes, In the handbook of porphyrin science: Kadish KM, Smith KM, Guilard R (Eds.). Academic Press New York, 7 (2010) 247.

[245] J.S. Hsiao, B.P. Krueger, R.W. Wagner, T.E. Johnson, J.K. Delaney, D.C. Mauzerall, G.R. Fleming, J.S. Lindsey, D.F. Bocian, R.J. Donohoe, J. Am. Chem. Soc., 118 (1996) 11181.

[246] E.Z. Chong, D.R. Matthews, H.D. Summers, K.L. Njoh, R.J. Errington, P.J. Smith, J. Biomed. Biotechnol. 54169 (2007) 1.

[247] H. Du, R.A. Fuh, J. Li, L.A. Cockan, J.S. Lindsey, PhotochemCAD: J. Photochem. Photobiol., 68 (1998) 141.

[248] J.G. Young, W. Onyebuagbu, J. Org. Chem., 55 (1990) 2155.

[249] M. Ambroz, A. Beeby, A.J. McRobert, M.S.C Simpson, R.K. Svensen, D. Phillips, J. Photochem, Photobiol. B, 9 (1991) 87.

[250] N. Masilela, T. Nyokong, J. Photochem. Photobiol. A, 223 (2011) 124.

[251] P. Modisha, E. Antunes, J. Mack, T. Nyokong, Int. J. Nanosci., 12 (2013) 1350010.

[252] O. Adegoke, T. Nyokong, P. B. C. Forbes, Opt. Mater. (Amst)., 46 (2015) 548.

[253] J. Britton, A. G. Martynov, D. Oluwole, Y. G. Gorbunova, A. Y. Tsivadze, T. Nyokong, J. Porphyr. Phthalocya., 20 (2016) 1296.

[254] G. Anilkumar, H. Nambu, Y. Kita, Org. Process Res. Dev., 6 (2002) 190.

[255] I. Chambrier, M.J. Cook, D.A. Russell, Synthesis, (1995) 1283.

[256] L. Luca, G. Giacomelli, J. Org. Chem., 73 (2008) 3967.

[257] X. Brokmann, L. Coolen, M. Dahan, J.P. Hermier, Phys. Rev. Lett., 93 (2004) 107403.

[258] R. Jenkins, R. Snyder, Introduction to X-Ray Powder Diffractometry, Wiley, 1996.

[259] J. Chen, Q. Gan, S. Li, F. Gong, Q. Wong, Z. Yang, S. Wong, H. Xu, J.S. Ma, G. Yang, J. Photochem. Photobio. A Chem., 207 (2009) 58.

[260] A.Y. Tolbin, V.E. Pushkarev, G.F. Nikitin, L.G. Tomilova, Tetrahedron Lett., 69 (2009) 4848.

[261] T. Nyokong, H. Isago, J. Phthalocya. Porphyr. 8 (2004) 1083.

[262] Y. Zorlu, U. Kumru, Ü. İşci, B. Divrik, E. Jeanneau, F. Albrieux, Y. Dede, V. Ahsen, F. Dumoulin, Chem. Commun., 51 (2015) 6580.

[263] N. Kobayashi, T. Furuyama, K. Satoh, J. Am. Chem. Soc. 133 (2011) 19642.

[264] R. Edrei, V. Goofried, J.E. van Lier, S. Kimel, J. Phthalocya. Porphyr., 2 (1998) 191.

[265] S. Alpugan, U. Isci, F. Albrieux, C. Hirel, A.G. Gurek, Y. Bretonniere, V. Ahsen, F. Dumoulin, Chem. Commun. 50 (2014) 7466.

[266] M.M. Ayhan, A. Singh, C. Hirel, A.G. Gürek, V. Ahsen, E. Jeanneau, I. Ledoux-Rak, J. Zyss, C. Andraud, Y. Bretonnière, J. Am. Chem. Soc. 134 (2012) 3655.

[267] M.M. Ayhan, A. Singh, E. Jeanneau, V. Ahsen, J. Zyss, I. Ledoux-Rak, A. G. Gürek, C. Hirel, Y. Bretonnière, C. Andraud, Inorg. Chem., 53 (2014) 4359.

[268] V.E. Pushkarev, A.Y. Tolbin, F.E. Zhurkin, N.E. Borisova, S.A. Trashin, L.G. Tomilova, N.S. Zefirov, Chem. Eur. J., 18 (2012) 9046.

[269] J. Jiang, D.K.P. Ng, Acc. Chem. Res. 42 (2009) 79.

[270] V.E. Pushkarev, L.G. Tomilova, V.N. Nemykin, Coord. Chem. Rev. 319 (2016) 110.

[271] Y.G. Gorbunova, L.A. Lapkina, A.G. Martynov, I.V. Biryukova, A.Y. Tsivadze, Russ. J. Coord. Chem., 30 (2004) 245.

[272] I.V Nefedova, Y.G. Gorbunova, S.G. Sakharov, A.Y. Tsivadze, Russ. J. Inorg. Chem., 50 (2005) 204.

[273] V.E. Pushkarev, E.V. Shulishov, Y.V. Tomilov, L.G. Tomilova, Tetrahedron Lett., 48 (2007) 5269.

[274] V.E. Pushkarev, L. G. Tomilova, Y. V Tomilov, Russ. Chem. Rev., 77 (2008) 875.

[275] K. Takahashi, Y. Tomita, Y. Hada, K. Tsubota, M. Handa, K. Kasuga, K. Sogabe, T. Tokii, Chem. Lett., (1992) 759.

[276] K. Takahashi, M. Itoh, Y. Tomita, K. Nojima, K. Kasuga, K. Isa, Chem. Lett., (1993) 1915.

[277] K. Takahashi, J. Shimoda, M. Itoh, Y. Fuchita, H. Okawa, Chem. Lett., 2 (1998) 173.

[278] A. Robertson, M. Ikeda, M. Takeuchi, S. Shinkai, Bull. Chem. Soc. Jpn., 74 (2001) 883.

[279] W. Su, M. Bao, J. Jiang, Vib. Spectrosc., 39 (2005) 186.

[280] S. Kahlal, A. Mentec, A. Pondaven, M. L'Her, J.-Y. Saillard, New J. Chem., 33 (2009) 574.

[281] N. Ishikawa, Y. Kaizu, Chem. Phys. Lett., 228 (1994) 625.

[282] N. Ishikawa, J. Porphyrins Phthalocya., 5 (2001) 87.

[283] D.P. Arnold, J. Jiang, J. Phys. Chem. A, 105 (2001) 7525.

[284] A.G. Martynov, Y.G. Gorbunova, Polyhedron, 29 (2010) 391.

[285] A.G. Martynov, Y.G. Gorbunova, A.Y. Tsivadze, Dalton Trans., 40 (2011) 7165.

[286] K.P. Birin, Y.G. Gorbunova, A.Y. Tsivadze, Magn. Reson. Chem., 48 (2010) 505.

[287] C.D. Wagner, W.M. Riggs, L.E. Davis, J.F. Moulder, G.E. Muilenberg (Ed.), Handbook of X-ray Photoelectron Spectroscopy, 1979.

[288] C.D. Wagner, A.V. Naumkin, A. Kraut-Vass, J.W. Allison, C.J. Powell, J.R. Rumble, NIST standard Reference Database 20, version 3.4 (web version) (http:/srdata.nist.gov/xps/) 2003.

[289] J.F.B. Barata, A.L. Da-Silva, M. Garcia, P. M. S. Neves, J. A. S. Cavaleiro, T. Trindade, RSC. Adv. 3 (2013) 274.

[290] A.W. Snow, J.R. Griffith, N.P. Marullo, Macromolecules, 17 (1984) 1614.

[291] L.P. Singh, S.K. Bhattacharyya, G. Mishra, S. Ahalawat, Appl. Nanosci. 1 (2011) 117.

[292] P. Huang, Z. Li, J. Lin, D. Yang, G. Gao, C. Xu, L. Bao, C. Zhang, K. Wang, H. Song, H. Hu, D. Cui, Biomaterials 32 (2011) 3447.

[293] C.D. Geddes, J.R. Lakowicz, J. Fluoresc., 12 (2002) 121.

[294] N.C.L. Zeballos, M.C.G. Vior, J. Awruch, L.E. Dicelio, Dyes Pigm., 113 (2015) 145.

[295] E. Secret, M. Maynadier, A. Gallud, M. Gary-Bobo, A. Chaix, E. Belamie, P. Maillard, M.J. Sailor, M. Garcia, J.-O. Durand, F. Cunin, Chem. Commun., 49 (2013) 4202.

[296] O. Hocine, M. Gary-Bobo, D. Brevet, M. Maynadier, S. Fontanel, L. Raehm, S. Richeter, B. Loock, P. Couleaud, C. Frochot, C. Charnay, G. Derrien, M. Smaihi, A. Sahmoune, A. Morere, P. Maillard, M. Garcia, J.O. Durand, Int. J. Pharm., 402 (2010) 221.

[297] M. Bouchoucha, R.C. Gaudreault, M.A. Fortin, Adv. Funct. Mater., 24 (2014) 5911.

[298] Y. Shimzu, T. Azumi, J. Phy. Chem., 86 (1982) 22.

[299] V.V. Breus, C.D. Heyes, G.U. Nienhaus, J. Phys. Chem. C, 111 (2007) 18589.

[300] J.A. Kloepfer, S.E. Bradforth, J.L. Nadeau, J. Phys. Chem. B, 109 (2005) 9996.

[301] X.W. Sun, J. Chen, J.L. Song, D.W. Zhao, W.Q. Deng, W. Lei, Opt. Express, 18 (2010) 1296.

[302] L.M. Maestro, C. Jacinto, U. Rocha, M.C. Iglesias-de la Cruz, F. SanzRodriguez, A. Juarranz, J.G. Solé, D. Jaque, J. Appl. Phys. **111** (2012) 023513.

[303] Y-F. Liu, J-S. Yu, J. Colloid Interf. Sci. **333** (2009) 690.

[304] X. Wang, L. Qu, J. Zhang, X. Peng, M. Xiao, Nano Lett. **3** (2003) 1103.

[305] M. Sanz, M.A. Correa-Duarte, L.M. Liz-Marzan, A. Douhal, **196** (2008) 51.

[306] M.T. Colvin, A.B. Ricks, A.M. Scott, D.T. Co, M.R. Wasielewski, J. Phys. Chem. A, 116 (2012) 1923.

[307] S. Bonacchi, D. Genovese, R. Juris, M. Montalti, L. Prodi, E. Rampazzo, M. Sgarzi and N. Zaccheroni, Top. Curr. Chem., 300 (2011) 93.

[308] A. Papadopoulou, R.J. Green, R.A. Frazier, J. Agric. Food Chem., 53 (2005) 158.

[309] J.R. Darwent, I. McCubbin, D. Phillips, Faraday Trans., 78 (1982) 347.

[310] K. Ishii, H. Itoya, H. Miwa, M. Fujitsuka, O. Ito, N. Kobayashi, J. Phys. Chem., 109 (2005) 5781.

[311] D. Wöhrle, O. Suvorova, R. Gerdes, O. Bartels, L. Lapok, N. Baziakina, S. Makarov, A. Slodek, J. Porphyr. Phthalocya. 8 (2004) 1020.

[312] K. Nonomura, T. Loewenstein, E. Michaelis, D. Wöhrle, T. Yoshida, H. Minoura, D. Schlettwein, Phys. Chem. Chem. Phys. 8 (2006) 3867.

[313] H.S. Muddana, T.T. Morgan, J.H. Adair, P.J. Butler, Nano. Lett. 9 (2009) 1559.

[314] E.I. Sagun, E.I. Zenkevich, V.N. Knyukshuto, A.M. Shulga, D.A. Starukhin, C. von Borczyskowski, Chem. Phys., 275 (2002) 211.

[315] C.L. Takanishi, E.A. Bykova, W. Cheng, J. Zheng, Brain. Res., 1091 (2006) 132.

[316] E.I. Zenkevich, A.P. Stupak, D. Kowerko, C. Borczyskowski, J. Chem. Phy., 406 (2012) 21.

[317] T. Blaudeck, E.I. Zenkevich, F. Cichos, C. von Borczyskowski, J. Phys. Chem. C, 112 (2008) 20251.

[318] G.L. Wood, M.J. Miller, A.G. Mott, Opt. Lett. 20 (1995) 973.

[319] S. Fu, X. Zhu, G. Zhou, W,-Y. Wong, C. Ye, W.-K Wong, Z. Li, Eur. J. Inorg. Chem. (2007) 2004.

[320] P. Chen, X. Wu, X. Sun, J. Lin, W. Ji, K. L. Tan, Phys. Rev. Lett. 82 (1999) 2548.

[321] K. Sanusi, E. K. Amuhaya, T. Nyokong, J. Phys. Chem. C, (2014) 7057.

[322] G. de la Torre, P. Vazquez, F. Agullo-Lopez, T. Torres, J. Mater. Chem., 8 (1998) 1671.

[323] S.V. Rao, P.T. Anusha, L. Giribabu, S.P. Tewari, Pramana-J. Phys. 75 (2010) 1017.

[324] W.W. Yu, L. Qu, W. Guo, X. Peng, Chem. Mater., 15 (2003) 2854.

[325] A. Pompella, A. Visvikis, A. Paolicchi, V. Tata, A.F. Casini, Biochem. Pharmacol., 66 (2003) 1499.

[326] M. Alexiades-Armenakas, Laser-mediated photodynamic therapy Clin. in Dermatol., 24 (2006)16.

[327] I. Mfouo-Tynga, A. El-Hussein, M. Abdel-Harith, H. Abrahamse, Int. J. Nanomedicine, 9 (2014) 3771.

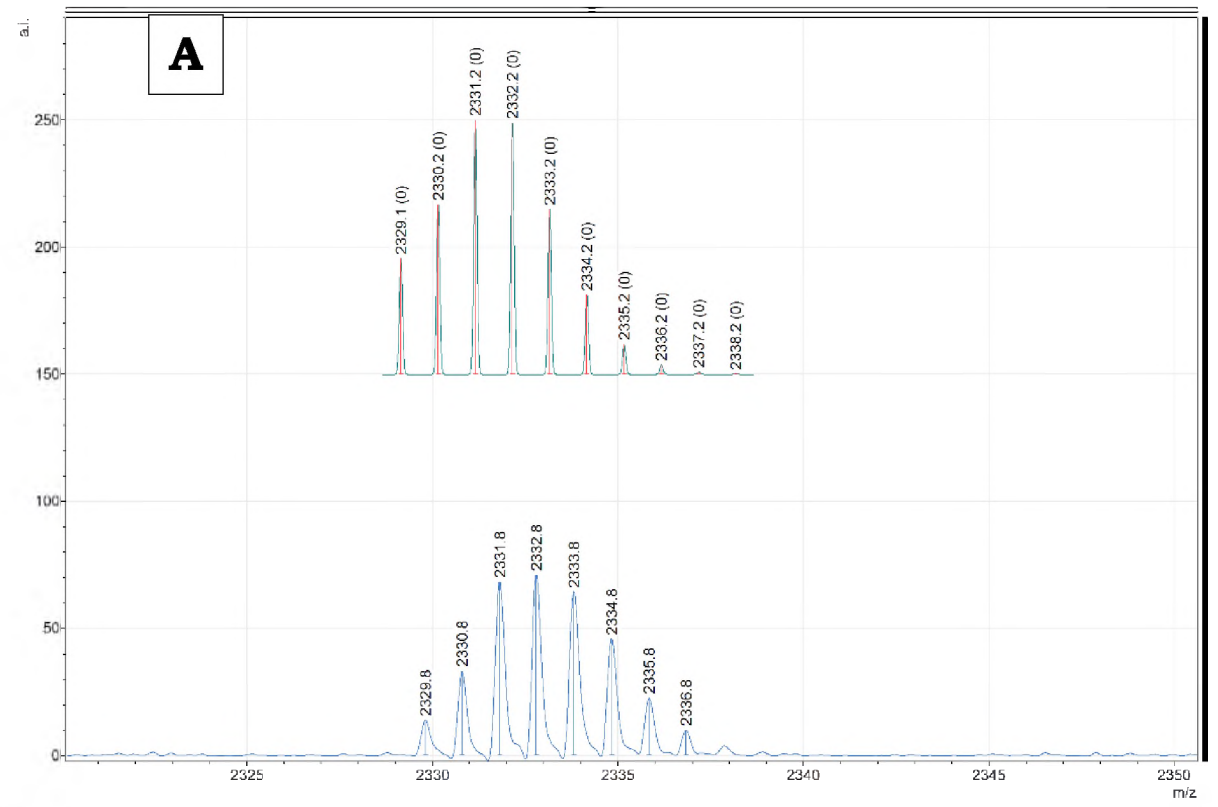
A
a.i.
250
200
150
100
50
0
2329.1 (0)
2330.2 (0)
2331.2 (0)
2332.2 (0)
2333.2 (0)
2334.2 (0)
2335.2 (0)
2336.2 (0)
2337.2 (0)
2338.2 (0)
2328.8
2330.8
2331.8
2332.8
2333.8
2334.8
2335.8
2336.8
2325
2330
2335
2340
2345
2350
m/z

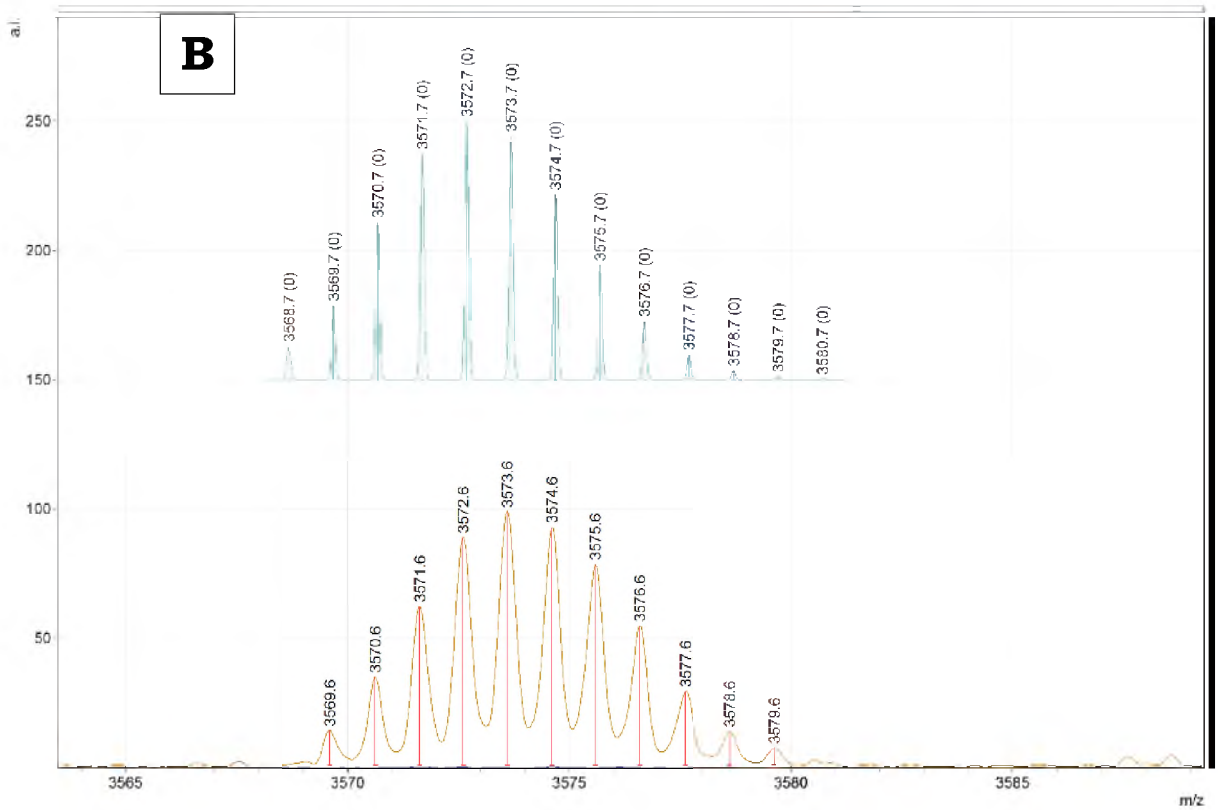
B
a.i.
250
200
150
100
50
3568.7 (0)
3569.7 (0)
3570.7 (0)
3571.7 (0)
3572.7 (0)
3573.7 (0)
3574.7 (0)
3575.7 (0)
3576.7 (0)
3577.7 (0)
3578.7 (0)
3579.7 (0)
3580.7 (0)
3569.6
3570.6
3571.6
3572.6
3573.6
3574.6
3575.6
3576.6
3577.6
3578.6
3579.6
3565
3570
3575
3580
3585
m/z

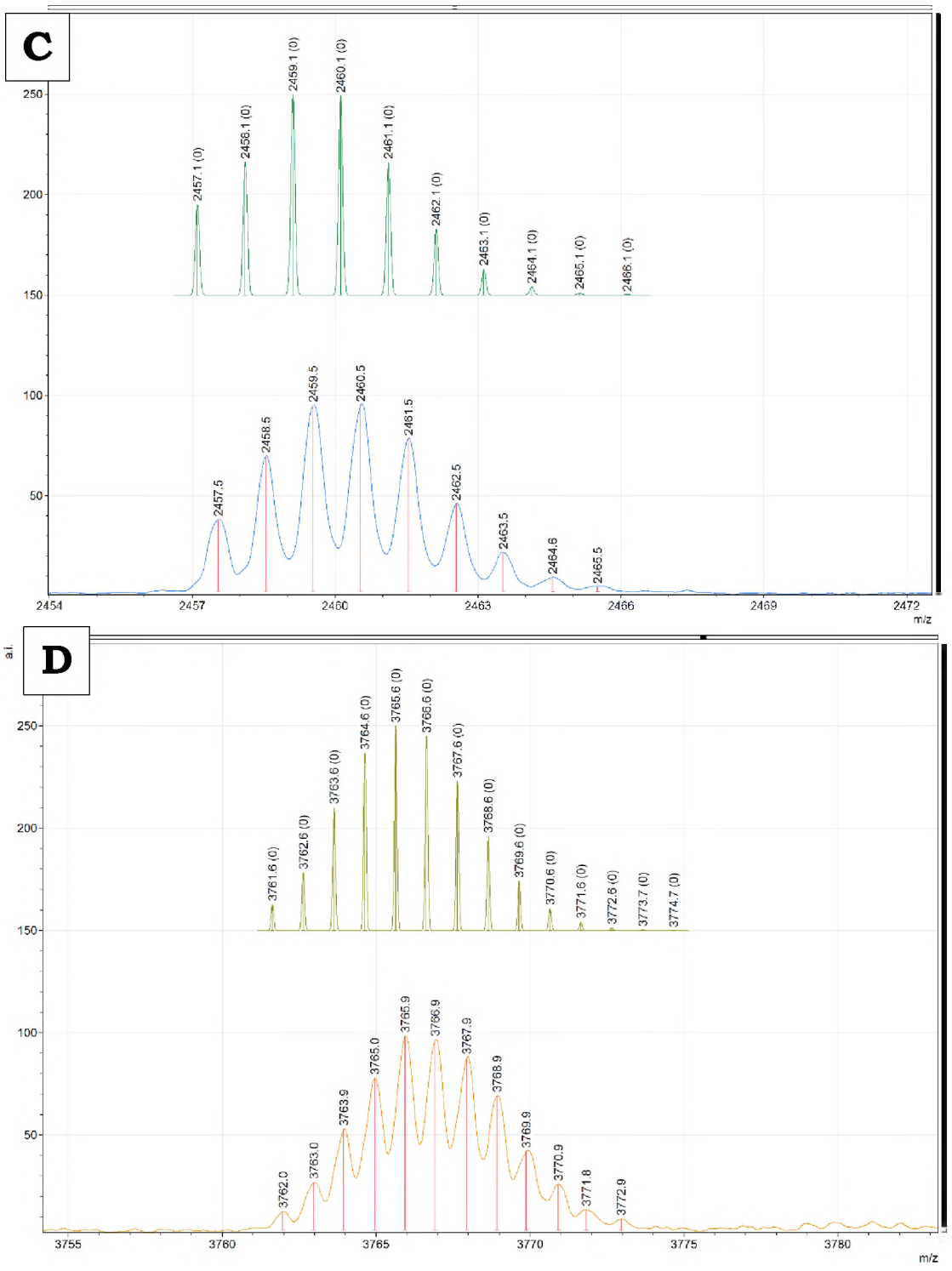

Appendix 1: Observed isotopic distributions (bottom) of molecular ion $[M+H]^+$ in MALDI–TOF mass spectra (calculated = top) (A). compound 11 $C_{128}H_{161}EuN_{16}O_{16}$ (top), (B). compound 12 $C_{192}H_{241}Eu_2N_{24}O_{24}$ (top), (C). compound 13 $C_{128}H_{161}EuN_{16}O_{24}$ (top), and (D). compound 14 $C_{192}H_{241}Eu_2N_{24}O_{36}$ (top)